Black holes in cosmological spacetimes and alternative theories of gravity

by

Maxence Corman

A thesis
presented to the University of Waterloo
in fulfillment of the
thesis requirement for the degree of
Doctor of Philosophy
in
Physics

Waterloo, Ontario, Canada, 2023

Examining Committee Membership

The following served on the Examining Committee for this thesis. The decision of the Examining Committee is by majority vote.

External Examiner: Richard Easther
Professor, Faculty of Science, Physics, University of Auckland

Supervisor(s):   William E. East
Adjunct Faculty, Dept. of Physics and Astronomy, University of Waterloo
Faculty, Perimeter Institute for Theoretical Physics

Niayesh Afshordi
Professor, Dept. of Physics and Astronomy, University of Waterloo
Associate Faculty, Perimeter Institute for Theoretical Physics

Internal Member: Robert Mann
Professor, Dept. of Physics and Astronomy, University of Waterloo
Affiliate, Perimeter Institute for Theoretical Physics

Internal-External Member: Ben Webster
Associate Professor, Dept. of Mathematics, University of Waterloo
Associate Faculty, Perimeter Institute for Theoretical Physics

Other Member(s):   Matthew C. Johnson
Professor, Dept. of Physics and Astronomy, York University
Associate Faculty, Perimeter Institute for Theoretical Physics

Author's Declaration

This thesis consists of material all of which I authored or co-authored: see Statement of Contributions included in the thesis. This is a true copy of the thesis, including any required final revisions, as accepted by my examiners.

I understand that my thesis may be made electronically available to the public.

Statement of Contributions

The material presented in this thesis was largely written by myself and is based on co-authored publications to which I made significant contributions.

Chapter 2 comes from [110] written in collaboration with Will East and Matthew Johnson. Chapters 4 and 5 are based on [111] and [112], and were both written in collaboration with Justin Ripley and Will East. Chapter 3 was written in collaboration with Will East and is based on [109].

Abstract

This thesis is dedicated to the study of spacetimes surrounding black holes within the context of cosmology, high energy physics and modified theories of gravity. We do this by applying and adapting modern numerical relativity techniques to probe the inhomogeneous and strong field regime in a number of different scenarios.

The first application we consider is the nonlinear evolution of unstable flux compactifications in a low-energy limit of string theory. Going beyond stationary solutions and their perturbations, we find rich dynamics, in some cases finding that the evolution from an unstable homogeneous state to a stable warped compactification can serve as a toy-model for slow-roll inflation, while in other cases finding solutions that eventually evolve to a singular state.

We then apply the methods for numerically evolving scalar fields coupled to the Einstein field equations to address several problems in early universe cosmological scenarios. We study the conditions under which inflation can arise from very inhomogeneous initial conditions. To do so, we introduce and compare several different ways of constucting initial data with large inhomogeneities in both the scalar field and time derivative profiles, by solving for the coupled Einstein constraint equations. We then study the evolution of various classes of initial conditions in both single- and two-field inflationary models. In some of the cases studied, the initial gradient and kinetic energy are much larger than the inflationary energy scale such that black holes can form. Taken together, our results suggest inflation can arise from highly inhomogeneous conditions.
Using the same numerical techniques, we study the nonlinear classical dynamics and evolutions of black holes in a particular nonsingular bouncing cosmology. We find that for sufficiently large black holes the black hole apparent horizon can disappear during the contraction phase. Despite this, we show that most of the local cosmological evolution remains largely unaffected by the presence of the black hole. For all the cases explored, the black hole's event horizon persists throughout the bounce, suggesting the nonsingular bouncing model under study is fairly robust to large perturbations.

Finally, we use and further develop a novel formulation of the Einstein field equations for evolving a large class of modified theories of gravity. We use this formulation to study the nonlinear dynamics of binary black hole mergers in a specific class of theories, where the black holes acquire a scalar charge. We consider quasi-circular inspirals with different mass-ratios, varying the coupling parameter introducing deviations from General Relativity and quantifying the impact on the emitted scalar and gravitational waveforms. We also compare our numerical results to analytic post-Newtonian calculations of the radiation emitted during the inspiral.

Acknowledgements

In hindsight, my PhD was a bit of a struggle at time but mostly a lot of fun. I really enjoyed my time in Waterloo and the reason for such a joyful journey is most likely all the people I met along the way. The list is so long, I can't thank everyone but I will at least give it a try.

I would not have been able to complete this thesis without the support and guidance of my advisor Will East. Will, I can't thank you enough for taking me in as your student and being so patient with the erratic person I can be. I am honestly so grateful for all the time you spent sharing your ideas and invaluable knowledge with me. I would not get so excited (or frustrated) when I see a convergence plot if it wasn't for you.

I would also like to thank the other members of my advisory committee: Daniel Siegel, Niayesh Afshordi and Matt Johnson as well as Richard Easther for taking the time to examine this thesis. I do want to give a special thanks to Matt Johnson for being such a great mentor. Matt, thank you for your support in my very first project as a PhD student but also later on for being such a source of inspiration and encouragement. I feel very lucky to have Justin Ripley as a collaborator. It's been really fun to work with you and I hope we will meet in person soon.

I also wish to thank the Strong Gravity group at PI for having something to look forward to on a Wednesday afternoon. I really enjoyed our meetings and learned a great deal from them. I am particularly grateful to Erik Schnetter for always being so helpful when it came to coding issues and Luis Lehner for his scientific and career advice but more so for always being so enthusiastic about science.

During my time in Waterloo, I made so much more friends than I could ever have hoped for. I thank Pablo for his support in all fronts. You were so helpful in my first months as a PhD student, but also a great friend. I thank Anna, Schuyler, Mike, Fiona, Finn and Lei for being my sports buddies. I thank Alex, Benji, Rami, both Laura's, Celine, Aman, Michael and Luciano. I am so grateful to have met you all. Special thanks to Dhruv for staying in Waterloo during the pandemic, I have so many good memories. Finally, thank you to Hanna, Kristine and Soham for being like family to me. I am especially grateful to Hanna and her family for sponsoring me in all my endeavors. I am so grateful you introduced me to XC skiing, roller blading, Dallas, Coffee in the Morning & Whiskey All Night Long and so much more (I miss you every day).

I would also like to thank my father for never giving up on trying to understand my research, my mother for being such a role model and my sisters, les Mirabelles and Elise for reminding me there is more than Physics in life. Je vous aime.

I also want to express my gratitude to the Academic, IT and Bistro staff at PI. Special thanks to Maïté, Angela, Josh, Craig and Ishan. My life at PI would not have been the same without you.

Finally, I really should apologize to Nils for putting up with me this whole time. Thank you for all the hugfest, potatoing and quality time. Thank you for sharing my excitement

for hockey, skiing, canoeing and meesei. Thank you for being my techno buddy during the pandemic. Thank you for being such an engaged co-pilot. But really thank you for seeing past all the jpp moments and following me in all my endeavors even though you know I rarely think things through. Coucou.

Table of Contents

List of Figures

xix

List of Tables

Chapter 1

Introduction

1.1 Motivation

The theory of General Relativity (GR) is one of the greatest achievements of modern physics. More than a century after its formulation, the theory remains to date the most accurate description of gravitational physics at all scales. GR fits observations from our solar system to the entire cosmological model of the universe and more recently Gravitational Waves (GW) from astronomical sources (see [333] for a review of experimental tests of GR before the detection of GWs).

Yet, there are both theoretical and observational reasons to believe that GR is incomplete. On the theoretical side, GR itself is not consistent with quantum mechanics because it breaks down at very small length scales. In particular, the theory is non-renormalizable but also exhibits physical singularities such as those inside black holes and at the big bang. It is believed that GR and Quantum Field Theory should be limits of a, yet to be determined, complete fundamental theory of quantum gravity. On the experimental side, there are open problems that could be associated with deviations from GR, the most important ones regard cosmology: observations have shown that $\sim 25\%$ of the mass-energy content of the universe is in the form of a pressureless dark matter component that does not interact electromagnetically, and $\sim 70\%$ of the energy content of the universe is filled with dark energy which accounts for the observed late time acceleration of our universe. These observations together with GR as a mathematical foundation gave birth to the current standard model of cosmology, also known as the ΛCDM model, where 'CDM' stands for 'Cold Dark Matter' and Λ the inclusion of a cosmological constant associated with dark energy. Although this theory describes much of what we observe, including the existence and structure of cosmic microwave background as well as the large-scale structures we observe in distribution of galaxies, the origin of dark matter and energy within this model is still currently unknown. Further assuming that the universe satisfies the cosmological principle, which states that at least on large scales the universe is *homogeneous* and *isotropic*, the ΛCDM model makes use of the Friedmann-Lemaitre-Robertson-Walker (FLRW) met-

ric (which we will introduce in more detail below) to describe the expanding universe. While the ΛCDM model fits all cosmological observations to their current precision, it does not predict or even just explain why the universe began with nearly homogeneous, spatially flat and isotropic conditions. It turns out that if one assumes a FLRW metric all the way to the Big Bang, then observations of the cosmic microwave background and large-scale structures would require very special and finely-tuned initial conditions. This is often referred to as the *homogeneity* and *flatness* problem in cosmology or simply the problem of initial conditions. The question that early universe cosmologies would then like to address is: can we find a physical mechanism that generically explains the initial flatness and homogeneity of the universe? It is also worth pointing out that the inclusion of the cosmological constant gives rise to the cosmological constant problem: why is the observed value of the cosmological constant so small compared to the one predicted from quantum field theory?

These open questions have prompted many researchers to consider deviations from GR or at the very least continue to test our theory of gravity. The study of extreme regimes, naturally encountered in early universe cosmology, high energy physics and spacetimes surrounding compact objects is a particularly promising target to probe for deviations of GR. The discovery of gravitational waves in 2015 provided us with a new very powerful tool to test GR in the highly relativistic strong field regime previously inaccessible to other experiments and observations. Since then LIGO and Virgo have detected over ninety black hole mergers [8], two binary neutron star mergers [3, 7] and two neutron-star black hole binary mergers [9], all testing Einstein's gravity in regimes never tested before [2, 346, 36, 5, 199, 10, 198, 296, 329, 227, 271]. So far no deviation from GR has been detected. The continued improvement in sensitivity of current GW observatories, and planning of the future generation of ground- and space-based GW observatories conceived to begin operations in the 2030s, will resolve signals with a far greater precision and open up new observational windows, revealing invaluable information about the underlying theory that describes their generation and propagation. Together with highly precise observations across the electromagnetic spectrum we are in an unprecedented position to detect a deviation from GR.

There are two distinct approaches that have been developed to test for departures from GR in the strong field regime [1]. In the top-down approach, we modify the theory at the fundamental level and make predictions that can be tested observationally. In the bottom-up approach, we use a phenomenological description of the observations in an attempt to discover clues for how to modify the theory at the fundamental level. Both approaches have strengths and weaknesses. The former approach to testing gravity is very attractive because it not only guarantees testing predictions of a fundamental modification to gravity, but also allows for the parameters of the same theory to be constrained by a wide range of observations in the electromagnetic and gravitational wave spectrum as well as covering small and large scales. However, there is a clear non-technical drawback in this

---

[1]Note these approaches to testing a theory are very general and in fact the bottom-up approach was used when constructing the standard model of elementary particles

approach, namely it requires choosing one fundamental theory out of the many possibilities. Moreover, ideally one would like to maximize the amount of information we obtain from the data, in order to not miss any unexpected physics. But maybe more importantly, the real technical challenge with following this approach to test gravity in the highly dynamical strong field regime (where linear treatments fail) is that it requires numerically solving the Einstein field equations or modifications thereof. In fact, there are very few alternative theories of gravity that are on an equal theoretical footing to GR, in the sense of being able to give a full prediction of what happens given some initial data or in other words many modified theories of gravity do not have a well-posed initial value formulation[2]. Given this, one might wish to follow the bottom-up approach instead, where one parameterize the deviations from GR in a generic way, simplifying the modelling drastically. However, if one does detect a deviation from GR using the bottom-up approach, then one will still need the top-down approach to understand which theory can lead to such deviation. Clearly, both approaches are then worth pursuing. In this thesis, we follow the top-down approach. In particular, we study black holes both in early universe scenarios and string inspired modified theories of gravity. The use of black holes instead of other compact objects such as neutron stars is particularly important, as one does not need to deal with uncertainties associated with astrophysical matter. This allows us to probe the highly dynamical and relativistic regime of gravity in a clean way.

In the remainder of this chapter, we first briefly review the Einstein equations along with the form they take in homogeneous and isotropic spacetimes. We then review the formulation of the Einstein equations we use in our numerical simulations of GR and extensions thereof. We close this chapter with an outline of the remainder of the thesis.

Throughout this thesis, unless stated otherwise, we make use of geometric units where $G = c = 1$. For the exception of chapter 2 we work in four spacetime dimensions, with metric signature $(-+++)$. When working in four spacetime dimensions, we use lower-case Greek letters $(\mu, \nu, ...)$ to denote spacetime indices and Latin letters $(i, j, k, ...,$ although t is reserved for the time coordinate index) to denote spatial indices. The Riemann tensor is $R^{\alpha}{}_{\beta\gamma\delta} = \partial_{\gamma}\Gamma^{\alpha}_{\beta\delta} - \cdots$.

We sometimes use the same notation to refer to different quantities and explicitly say so when this is the case. In general H is always used to refer to the Hubble parameter and a the scale factor, but depending on the context it might be computed differently. The notation we use is always fully consistent within a single chapter. Derivatives with respect to coordinate time, harmonic time, proper time and when applicable scalar fields are usually denoted by a *dot* or *prime*. Similarly the notation is fully consistent within a particular chapter.

---

[2]A theory admits a well-posed initial value formulation if given initial data that satisfies the constraint equations, there exists a unique solution to the equations of motion that depends continuously on the initial data. A sufficient condition for a theory to be well-posed is that there should exist a formulation of the equations of motion which is strongly hyperbolic (see e.g. [232, 141, 305] for further details on well-posedness and hyperbolicity).

1.2 The Einstein equations

In GR, spacetime is a four-dimensional curved manifold with a Lorentzian metric $g_{\mu\nu}$ and the dynamics of $g_{\mu\nu}$ are prescribed by the Einstein equations

$$G_{\mu\nu} = 8\pi T_{\mu\nu}, \tag{1.1}$$

where $T_{\mu\nu}$ is the stress-energy tensor of the matter and $G_{\mu\nu}$ is the Einstein tensor

$$G_{\mu\nu} \equiv R_{\mu\nu} - \frac{1}{2}Rg_{\mu\nu}. \tag{1.2}$$

Here $R_{\mu\nu} \equiv R^{\alpha}_{\mu\alpha\nu}$ is the Ricci tensor and $R \equiv g^{\alpha\beta}R_{\alpha\beta}$ the Ricci scalar, both obtained from the Riemann tensor $R^{\alpha}_{\beta\gamma\delta}$ which encodes the curvature of spacetime and can be computed from

$$R^{\alpha}_{\beta\gamma\delta} = \partial_{\gamma}\Gamma^{\alpha}_{\beta\delta} - \partial_{\delta}\Gamma^{\alpha}_{\beta\gamma} + \Gamma^{\alpha}_{\gamma\mu}\Gamma^{\mu}_{\delta\beta} - \Gamma^{\alpha}_{\delta\mu}\Gamma^{\mu}_{\gamma\beta} \tag{1.3}$$

where $\Gamma^{\alpha}_{\beta\gamma}$ are the Christoffel symbols

$$\Gamma^{\alpha}_{\beta\gamma} = \frac{1}{2}g^{\alpha\mu}\left(\partial_{\beta}g_{\mu\gamma} + \partial_{\gamma}g_{\beta\mu} - \partial_{\mu}g_{\beta\gamma}\right). \tag{1.4}$$

It is sometimes useful to rewrite the field equations in the equivalent form

$$R_{\mu\nu} = 8\pi\left(T_{\mu\nu} - \frac{1}{2}Tg_{\mu\nu}\right), \tag{1.5}$$

where $T \equiv g^{\mu\nu}T_{\mu\nu}$ is the trace of the stress-energy tensor. Written in their most general form, in an arbitrary coordinate system, the Einstein equations are thus a set of ten coupled, non-linear, second-order partial differential equations for the metric.

The field equations (1.1) can also be derived from a variational principle where the Lagrangian for the gravitational field is simply the Ricci scalar. The GR action with a cosmological constant then reads

$$\mathcal{S}_{\mathrm{GR}} = \int d^4x\sqrt{-g}\left[\frac{R - 2\Lambda}{16\pi} + \mathcal{L}_M\right], \tag{1.6}$$

where g is the determinant of the metric tensor $g \equiv \det g_{\mu\nu}$ and $\mathcal{L}_M$ is the matter Lagrangian density. Variation of the action (1.6) with respect to the metric gives the Einstein field equations above (1.1) where the stress-energy tensor is defined as

$$T_{\mu\nu} \equiv -\frac{2}{\sqrt{-g}}\frac{\delta L_M}{\delta g^{\mu\nu}} \tag{1.7}$$

where $L_M = \sqrt{-g}\mathcal{L}_M$ is the matter Lagrangian. Modifications to GR in the top-down approach are introduced at the level of the action and therefore this will be the starting point for any theoretical model we consider in this thesis.

1.2.1 The homogeneous background cosmology

Contemporary cosmological models, the ΛCDM model included, are based on the cosmological principle which states that our universe is essentially the same everywhere at least on sufficiently large scales, where local variations in density are averaged over. The validity of this very simple assumption has been confirmed by a number of different observations, such as number counts of galaxies and observations of the diffuse X-ray and γ-ray backgrounds, but perhaps more importantly by observations of the cosmic microwave background [281, 317, 14]. Although we know that the cosmic microwave background is not perfectly smooth, the deviations from homogeneity are of the order of 10^{-5}. Therefore, much of what we understand about the cosmic evolution from very early times to the current stages of the universe as we observe it today comes from FLRW models plus cosmological perturbation theory. We now briefly review the zeroth order approximation to the evolution of the real, lumpy universe.

Assuming the cosmological principle or equivalently assuming that the universe is homogeneous and isotropic on large scales one is lead to the FLRW metric line element to describe geometry of spacetime [87],

$$ds^2 = -d\tau^2 + a^2(\tau) \left(\frac{dr^2}{1 - kr^2} + r^2 \left(d\theta^2 + \sin^2\theta d\phi^2 \right) \right) \tag{1.8}$$

where τ is the proper (physical) time, $a(\tau)$ is the time-dependent scale factor representing the relative size of spacelike hypersurfaces at different times, and $k \in \{-1, 0, +1\}$ determines the geometry of these spatial surfaces: negatively curved, flat and positively curved, respectively. r is the comoving radius, related to the proper (physical) distance through the relation $R = a(\tau)r$.

Provided we assume a FLRW metric, the dynamics of the universe is completely determined by the evolution of the scale factor. The form the scale factor takes is dictated by the matter content of the universe via the Einstein field equations (1.1). Assuming a perfect fluid description of the universe, the stress-energy tensor is

$$T_{\mu\nu} = (\rho + P)u_\mu u_\nu + P g_{\mu\nu}, \tag{1.9}$$

where u^μ is the four-velocity of fluid (normalized so that $u^\mu u_\mu = -1$) and ρ and P the energy density and pressure in the rest frame of fluid. In particular, in a frame that is comoving with fluid we may take $u^\mu = (1, 0, 0, 0)$ such that for the FLRW metric $T^\mu_\nu = \text{diag}(-\rho, P, P, P)$. The Einstein field equations, assuming the FLRW metric and a perfect fluid energy-momentum source with equation of state $P(\rho)$, then take the form of two coupled, non-linear ordinary differential equations, also known as the Friedmann equations

$$H^2 = \frac{8\pi\rho}{3} - \frac{k}{a^2} \tag{1.10}$$

and

$$\frac{\ddot{a}}{a} = -\frac{4\pi}{3}\left(\rho + 3P\right) \tag{1.11}$$

where an overdot denotes a derivative with respect to proper time and $H \equiv \frac{\dot{a}}{a}$ is the Hubble parameter and denotes the expansion rate of the FLRW spacetime.

In the standard Big Bang model of cosmology, the universe has been expanding as described by the FLRW model since $t = 0$. However, as was already mentioned earlier, if we assume a FLRW model all the way to the initial singularity then this leads to the homogeneity and flatness problem. The horizon problem arises from the fact that if one solves for the evolution of the scale factor using the Friedmann equations, then one can show that the comoving horizon[3] grows monotonically with time which implies that comoving scales entering the horizon today were far outside the horizon at the time of last scattering. The question is then, how does one explain the near-homogeneity of the CMB temperature on scales containing a priori many causally independent regions? The flatness problem arises from the observation that the universe is geometrically nearly flat, yet assuming a FLRW cosmology the departure from flat Euclidean space diverges with time. Therefore, in the standard Big Bang cosmology the near-flatness observed today would require extremely fined-tuned initial conditions.
The goal of early universe cosmologists is to then come up with a theory that explains the near inhomogeneity and flatness on the period of last scattering dynamically or in other words without fine tuning.

Cosmic inflation, a period of accelerated expansion in the early universe, [320, 177, 246, 19, 247] has been proposed as a solution to the horizon and flatness problems. Both problems of the standard Big Bang cosmology arise because in a FLRW universe the comoving Hubble radius $(aH)^{-1}$ is strictly increasing. Since H is approximately constant while a grows exponentially during inflation we find that the comoving Hubble radius decreases as required (see e.g. [44] for a review of inflationary cosmology). Besides solving the problem of initial conditions in cosmology, inflation also explains the origin of the large-scale structures in the universe. The inflationary paradigm, is embedded in many theories, the predictions of which can then be tested against the large amount of observational data on the cosmic microwave background. However, although inflation has become widely accepted as the theory that explains the nearly scale-invariant, Gaussian and adiabatic scalar perturbations in the cosmic microwave background, it remains a hypothesis and many open questions remain (see e.g. [71] for some of the conceptual problems of inflationary cosmology). We will challenge the conditions under which inflation can begin in chapter 3 of this thesis. A proposed alternative to cosmic inflation is the idea that the universe underwent a bounce: a transition from a stage of contraction to expansion

---

[3]The comoving horizon, also referred to as particle horizon, describes the maximum distance that light could have travelled to an observer in the age of the universe. It represents the furthest distance from which we can retrieve information from the past and so defines the size of the observable universe at the present epoch. The physical size of the particle horizon is given by the scale factor multiplied by the elapsed conformal time.

[161, 72, 268, 43, 70]. In contrast to inflation, in bouncing models the Hubble radius typically shrinks ultra-rapidly during the contracting phase while the scale factor is nearly constant, resolving the smoothness problem. The flatness problem is resolved because the curvature of the universe is exponentially suppressed during the contracting phase (see e.g. [194] for more details on how bouncing cosmologies resolve the problems of initial conditions). In bouncing cosmologies the nature of the structure formation mechanism depends on the specific bouncing model being considered. In chapter 4 we focus on a specific bouncing model where the transition from contraction to expansion happens at sub-Planckian energies, and study its robustness to the presence of black holes.

1.2.2   Formulation of the Einstein equations

The particular formulation (by which we mean the choice of gauge and inclusion of appropriate gauge-fixing terms in the equations of motion) of the Einstein equations that we use in the first three chapters of this thesis is the generalized harmonic formulation [157, 292]. In this formulation, the gauge degrees of freedom are specified by introducing the source functions which determine the covariant d'Alembertian of the coordinates, $H^\mu = \Box x^\mu$. Promoting the source functions to independent quantities one can rewrite the Einstein field equations (1.1) as

$$
\begin{aligned}
g^{\mu\nu}\partial_\mu\partial_\nu g_{\alpha\beta} \ &+ \ \partial_\beta g^{\mu\nu}\partial_\mu g_{\alpha\nu} + \partial_\alpha g^{\mu\nu}\partial_\mu g_{\beta\nu} + \partial_\alpha H_\beta + \partial_\beta H_\alpha - 2H_\nu \Gamma^\nu_{\alpha\beta} + 2\Gamma^\mu_{\nu\beta}\Gamma^\nu_{\mu\alpha} \\
&= \ -8\pi\left(2T_{\alpha\beta} - g_{\alpha\beta}T\right).
\end{aligned}
\tag{1.12}
$$

Since the source functions H_μ are four independent functions, one needs to specify four additional equations for them. In this thesis, we only consider gauge conditions where the source functions are some function of the metric and spacetime coordinates, such that the evolution equation for the metric is manifestly hyperbolic. In this formulation, the evolution equations are reduced to first order in time so that there are 28 fundamental variables $\{g_{\mu\nu}, H_\mu, \partial_t g_{\mu\nu}, \partial_t H_\mu\}$. Introducing the constraint functions C^μ

$$
C^\mu \equiv H^\mu - \Box x^\mu,
\tag{1.13}
$$

which are identically zero for any solution of the Einstein field equations (1.1), one can show using the contracted Bianci identity and conservation of stress-energy tensor, that C^μ obeys the following homogeneous wave equation

$$
\Box C^\mu = -R^\mu_\nu C^\nu.
\tag{1.14}
$$

This means that if one begins with initial data satisfying both $C^\mu = 0$ (which we ensure by setting $H^\mu = \Box x^\mu$ on initial time slice) and $\partial_t C^\mu = 0$, then while evolving $g_{\mu\nu}$ with (1.12), (1.14) guarantees that $C^\mu = 0$ will be satisfied for all time or in other words $g_{\mu\nu}$ will solve the Einstein field equations (1.1). When evolving the equations numerically, this statement will only be true up to truncation error. In practice, we ensure that C^μ converges to zero

7

(by evolving a given simulation run at different resolutions) for any particular evolution system we use. Such a convergence test provides a nontrivial check that our numerical solution is indeed converging to a solution of the Einstein field equations. When evolving black hole spacetimes, we add constraint damping terms to the equations as in [176, 293]. Equivalent to enforcing $\partial_t C^\mu = 0$ at $t = 0$ is to make sure that the usual Hamiltonian and momentum constraint equations are satisfied on the initial time slice. To summarize, evolving the Einstein equations in the generalized harmonic formulation consists of: first constructing initial data for $\{g_{\mu\nu}, \partial_t g_{\mu\nu}\}$ that satisfies the constraint equations to then evolve the metric according to (1.12) and the source functions according to an appropriate choice of gauge. In this thesis, we will also include matter which we evolve according to its equations of motion.

In the last chapter of the thesis we study a modified theory of gravity, called Einstein-scalar-Gauss-Bonnet (ESGB) gravity which is a representative example of a Horndeski theory of gravity. Horndeski theories of gravity are the most general class of classical scalar-tensor theories that lead to second order equations of motion, making them a particularly attractive alternative to GR [188]. As was already mentioned above, one technical challenge that has prevented finding fully nonlinear solutions to many Horndeski theories of gravity, has been the lack of a well-posed initial value formulation for such theories. However, it was recently shown that the equations of motions for Horndeski theories of gravity possess a well-posed initial value formulation when using the so-called modified generalized harmonic (MGH) formulation, so long as the coupling parameter introducing beyond-GR corrections is much smaller than all the other length scales in system under study, which is also referred to as the weakly-coupled regime [230, 229]. We briefly review the MGH formulation and refer the reader to [230, 229] for more details.

Assuming a Lorentzian spacetime, one starts by introducing two auxiliary (inverse) Lorentzian metrics $\tilde{g}^{\mu\nu}$ and $\hat{g}^{\mu\nu}$ such that the causal cone of the inverse of physical metric $g^{\mu\nu}$ is strictly inside the causal cone of $\tilde{g}^{\mu\nu}$, and the latter is strictly inside the causal cone of $\hat{g}^{\mu\nu}$. Raising and lowering indices is always performed with the spacetime metric $g_{\mu\nu}$, so e.g. $\hat{g}^{\mu\nu} \equiv g^{\mu\alpha} g^{\nu\beta} \hat{g}_{\alpha\beta}$. We also define $\tilde{g} \equiv \tilde{g}^{\mu\nu} g_{\mu\nu}$ and $\hat{g} \equiv \hat{g}^{\mu\nu} g_{\mu\nu}$.

The MGH formulation imposes the following gauge condition on the coordinates x^μ:

$$
\begin{aligned}
C^\mu &\equiv H^\mu - \tilde{g}^{\alpha\beta} \nabla_\alpha \nabla_\beta x^\mu \\
&= H^\mu + \tilde{g}^{\alpha\beta} \Gamma^\mu_{\alpha\beta} = 0.
\end{aligned}
\tag{1.15}
$$

Just like in the generalized harmonic formulation, H^μ are the (as-yet unspecified) source functions that, along with $\tilde{g}^{\alpha\beta}$, determine the gauge degrees of freedom, and C^μ (which remember will generally not be exactly zero in a given numerical solution) the constraint functions.

One next defines the modified generalized harmonic equations of motion

$$
E^{\mu\nu} - \hat{P}_\beta{}^{\alpha\mu\nu} \nabla_\alpha C^\beta - \frac{1}{2}\kappa \left(n^\mu C^\nu + n^\nu C^\mu + \rho n^\alpha C_\alpha g^{\mu\nu}\right) = 0,
\tag{1.16}
$$

where $E^{\mu\nu}$ are the equations of motion derived from varying the metric (i.e. the equations of motion before gauge fixing), n^μ is a timelike vector (with respect to $g^{\mu\nu}$, $\tilde{g}^{\mu\nu}$, and $\hat{g}^{\mu\nu}$), and

$$\hat{P}_\beta{}^{\alpha\mu\nu} \equiv \frac{1}{2}\left(\delta_d^\mu \hat{g}^{\nu\alpha} + \delta_\beta^\nu \hat{g}^{\mu\alpha} - \delta_\beta^\alpha \hat{g}^{\mu\nu}\right). \tag{1.17}$$

We here include the constraint damping terms with the constants κ and ρ [176]. Note Eq. 1.16 is slightly different from Ref. [229] where $\nabla_\alpha C^\beta$ is replaced by $\partial_\alpha C^\beta$. We choose the form used here for consistency with the standard generalized harmonic formulation introduced earlier, but either way the principal part, and therefore the hyperbolicity results are the same.

In the MGH formulation the coordinates x^μ obey a hyperbolic equation with characteristics determined by $\tilde{g}^{\mu\nu}$ as opposed to the physical metric in generalized harmonic formulation (1.13). Furthermore, if one takes the divergence of (1.16) and assumes $\nabla_\mu E^{\mu\nu} = 0$, we obtain the modified version of (1.14)

$$-\frac{1}{2}\hat{g}^{\mu\alpha}\nabla_\mu\nabla_\alpha C^\nu - \hat{g}^{\alpha\nu}R_{\beta\alpha}C^\beta - \left(\nabla_\mu \hat{P}_\beta{}^{\alpha\mu\nu}\right)\left(\nabla_\alpha C^\beta\right) - \frac{1}{2}\kappa\nabla_\mu\left(n^\mu C^\nu + n^\nu C^\mu \rho n^\alpha C_\alpha g^{\mu\nu}\right) = 0. \tag{1.18}$$

This implies that the constraint violating modes C^μ satisfy a hyperbolic equation with characteristics determined by $\hat{g}^{\mu\nu}$ instead of physical metric. If we set $\tilde{g}^{ab} = \hat{g}^{ab} = g^{ab}$, one can show that the MGH formulation reduces to the generalized harmonic formulation. In the context of Horndeski theories of gravity, the latter does not admit a well-posed initial value formulation [277, 276]. The reason for this can be traced to the fact that in the generalized harmonic formulation the unphysical pure gauge and constraint violating modes both propagate at the speed of light i.e. are degenerate with the characteristic speed of physical solutions. Introducing a modification of the usual generalized harmonic formulation such that the pure gauge modes propagate along the null cone of $\tilde{g}^{\mu\nu}$ and the gauge-condition violating modes along the null cone of $\hat{g}^{\mu\nu}$ instead of the null cone of physical metric, and choosing the auxiliary metrics such that the three null cones do not intersect, we ensure that the three different types of solutions propagate with different speeds. One can show that this formulation of GR is strongly hyperbolic and remains so when turning on Horndeski terms [229]. Finally, we note that picking a gauge in the MGH formulation is equivalent to choosing the functional form of the auxiliary metrics $\tilde{g}^{\mu\nu}$ and $\hat{g}^{\mu\nu}$, as well as choosing the source functions H^μ.

1.3 Summary and outline of thesis

The rest of the thesis is as follows.

In chapter 2 we consider string theory as a candidate theory of quantum gravity. Key to this program is explaining why we cannot experimentally probe the extra spatial dimensions invoked to make string theory a consistent theory. Despite many advances, including systematic linear treatments of perturbations of the solutions in such compactifications, there remain many open problems regarding the rich dynamics of these solutions. It is known that some of these solutions are sometimes perturbatively unstable but determining the endpoint of such instabilities requires a fully nonlinear treatment of the equations, a daunting task given the difficulty of solving the Einstein equations in four dimensions, let alone ten. We describe an evolution code to probe the strong field regime and determine the end state of such linear instabilities. In some cases we show that initially homogeneous compactifications are unstable to forming stable inhomogeneous solutions. In other scenarios, we show that the transition to a dynamically more favored state can serve as a toy-model for inflation, suggesting that perhaps our universe arose from the dynamical re-adjustment of the shape of a compactification. We also find a regime where unstable solutions overshoot perturbatively stable solutions to evolve towards a singular state, forming trapped regions in the process and resulting in a crunch of the effective four-dimensional spacetime.

As mentioned earlier the inflationary paradigm, invoked to explain the flatness and nearly isotropic nature of the universe we observe today, has so far been consistent with observational tests. However, while it is true that if inflation begins it will smoothen out and flatten any inhomogeneities, it is less understood whether inflation can start from general initial conditions. In order to study whether inflation can occur for arbitrary anisotropic and inhomogeneous initial conditions, one needs to carry numerical simulations. This question has been studied in the past using general relativistic simulations in full 3+1D with large initial inhomogeneities in the scalar field profile and gravity sector, but ignoring inhomogeneities in the velocity profile of the inflaton for simplicity of the numerical implementation. In chapter 3 we extend the methods and software for constructing initial data describing a universe dominated not only by the gradient but also kinetic energy of the inflaton. Numerically evolving these initial conditions, we find that even when the wavelength of the perturbations is of the order of the initial Hubble length such that overdense regions collapse to form black holes, these are quickly inflated out by the expanding spacetime and inflation eventually begins. We discover that large gradients can mitigate the disruptive effects of a non-zero initial velocity profile, rendering inflation more robust than one would naively expect from homogeneous calculations.

As mentioned in the first part of this introduction, a proposed alternative to inflation is that the universe underwent a transition from contraction to expansion at sub-Planckian energies, a nonsingular bounce. One outstanding question is the viability of such models in the inhomogeneous and non-perturbative regime. In particular, what is the fate of black holes, if present, in nonsingular bouncing cosmologies. One might worry that the bounce, requiring general relativity coupled to exotic matter or modifications to gravity, will reverse gravitational collapse possibly leading to a naked singularity. Alternatively the bounce could fail to happen in the vicinity of the black hole. In chapter 4, we adapt

the techniques from numerical relativity and consider the first numerical evolution of black holes through a nonsingular bouncing cosmology. We find that for sufficiently large black holes in comparison to the minimum Hubble radius, the black hole and cosmological horizons collide and temporarily disappear during the contracting phase. Regardless, we show that most of the local cosmological evolution remains largely unaffected by the presence of the black hole, making nonsingular bouncing models robust to large inhomogeneities.

A common feature of many proposed modifications to GR is that they show the strongest effects in the presence of the shortest curvature lengths. Gravitational waves emitted during the merger of compact objects, neutron stars and black holes, are therefore a particularly promising target to find corrections to GR. Despite the potential for discovery, high-precision inspiral-merger-ringdown waveform models are currently lacking in theories introducing modifications to gravity. In chapter 5 we use the modified generalized harmonic formulation described earlier to perform a detailed study of binary black hole mergers in a specific theory, Einstein-scalar-Gauss-Bonnet gravity, introducing deviations from general relativity at small curvature length scales. Different variants of this particular theory give rise to black hole solutions with scalar charge, the merger of which produces gravitational signals that differ qualitatively from GR, while still passing weak field tests. We quantify the dephasing of the gravitational signal as compared to GR, the latter being a promising feature to be compared with current GW observations. We find that analytic predictions of the waveform, currently used for model dependent tests of general relativity in the weak field regime, are lacking the accuracy to place meaningful constraints on our theory of gravity, emphasizing the need for fully nonlinear evolutions as a benchmark for analytic approaches.

Finally, we conclude in chapter 6 and discuss some directions for future work.

11

Chapter 2

Nonlinear dynamics of flux compactification

2.1 Introduction

As mentioned in Chapter 1, the standard cosmological model invokes accelerated expansion of the Universe at late times, in the current epoch of dark energy domination and at early times when including an inflationary era. Determining the physical mechanism(s) responsible for the accelerated expansion of the Universe is among the most important challenges in modern cosmology. One proposed framework for tackling this is string/M-theory, where the mechanisms responsible for dark energy and inflation would ideally just be one feature of a complete description of gravity and the standard model of particle physics.

A major complication in developing these phenomenological connections are the extra spatial dimensions invoked to make string theory a consistent quantum theory of gravity. There are two dominant paradigms for explaining why we cannot experimentally probe extra spatial dimensions: they are small (compactification [217, 226]) or the standard model degrees of freedom are constrained to move in only four dimensions (the braneworld scenario [26, 298, 299]). The specific choice of compactification or realization of the braneworld scenario has implications for phenomenology, dictating the particle content and vacuum structure, as well as the types and strengths of interactions, in the effectively four-dimensional theory that results. The proliferation of four-dimensional theories (known as the string theory landscape [322]) intertwines string theory with cosmology in many fundamental ways. In this chapter, our main point of contact will be the evolution of the size and shape of a compactification, which (in this picture) are part of our cosmological history, and can provide the physical mechanism for inflation and dark energy.

What dynamics might be associated with extra dimensions? In the simplest scenario, the Universe remains effectively four-dimensional and small deformations of the extra dimensions correspond to a set of fields known as Kaluza Klein (KK) modes. Even this is

highly non-trivial, requiring the addition of various sources of energy momentum (such as q-form gauge fields, branes, etc.) to stabilize the size and shape of the compactification, and verifying that the resulting four-dimensional effective theory has the desired properties. Beyond studying linear perturbations of such static stable configurations, very little is known about the dynamics associated with extra dimensions. This is not surprising given the difficulties in solving Einstein's equations in four dimensions, let alone ten. Nevertheless, a better understanding is necessary to fully understand cosmology in theories with extra dimensions, and in particular address questions such as: How was the Universe we observe selected from the many possibilities? What features of our Universe are accidental, and which are inevitable (e.g. fixed by special initial conditions or symmetries)? Why are there only three large spatial dimensions?

To make progress in this direction, we focus on a simple model that retains many of the important features of the low-energy limit of string theory: Einstein-Maxwell theory in D-dimensions with a positive cosmological constant and a q-form gauge field [1]. Freund and Rubin [149] showed that this theory admits solutions in which the extra dimensions are compactified on a sphere, stabilized against collapse by the positive curvature of the compactification and a homogeneous configuration of the gauge field over the sphere. If a positive bulk cosmological constant is included [63], it is possible to find solutions in $D = p + q$ dimensions that are a product space of p-dimensional anti-de Sitter, Minkowski or de Sitter space and a q-dimensional sphere. The size of the compact sphere and the magnitude of the four dimensional cosmological constant are adjusted with the number of units of flux of the q-form gauge field wrapping the q-sphere. This simple model figures prominently in the AdS/CFT correspondence [256], serves as a simple example of flux compactifications in string theory [123, 116], and has been employed to study the cosmological constant problem [116, 88, 77, 28], flux tunneling [15, 57, 75, 56], and dimension-changing transitions [106, 234, 88, 58], among other phenomena. Another interesting feature of the Einstein-Maxwell model is that in addition to spherical compactifications, it also admits stable solutions where the compact space is inhomogeneous, or "warped" [223, 224, 242, 114]. In string constructions, warped extra dimensions are essential in models that address the hierarchy between the gravitational and electroweak scales [165], dark energy [209], and cosmic inflation (e.g. [208]). A complete understanding of the dynamical generation of such structure is an important missing component of the cosmology of these models.

In the Einstein-Maxwell model, the linear stability and mass spectrum of the Freund-Rubin solutions were studied in refs. [118, 223, 224, 242, 76, 186]. Their analysis showed that the stability of the solution to small perturbations depends on the relative value of the flux density or Hubble parameter compared to the cosmological constant as well as on the dimension of the internal manifold. There are two types of dynamical instabilities:

- The *total volume instability* can be attributed to homogeneous perturbations ($\ell = 0$

---

[1]see Appendix A.3 for a comparison of the theory considered here to the more realistic 10 dimensional type IIB supergravity (SUGRA)

modes) of the internal space and arises whenever the density of flux lines warping the q-sphere is too small, or equivalently, when the Hubble expansion rate of the external de Sitter space is too large causing the internal manifold to either grow or shrink. The endpoint of this instability was found to be either decompactification to empty D-dimensional de Sitter space or flow in towards a different configuration where total flux integrated over the compact space is the same but the volume is smaller hence flux density larger [234].

- The *warped instability* arises when $q \geq 4$ (in contrast to the volume instability which already exists when $q \geq 2$) and is due to inhomogeneous perturbations. Mathematically, this instability is due to a mode that couples the metric and flux (with $\ell \geq 2$ angular dependence) and in turn deforms the internal space. One expects that if some configuration is unstable for a given total flux, then this may signal the presence of another more stable configuration with the same flux. Indeed refs. [223, 242, 114] numerically constructed stationary warped solutions and ref. [224] studied their perturbative stability. But their connection to the inhomogeneous instability has not been determined, so it is not known whether these are the endpoint of the instability.

Note that when $q \geq 5$, all of the Freund-Rubin solutions are linearly unstable to one or both types of instability.

The goal of this chapter is to go beyond studying stationary or homogeneous solutions, and their linear perturbations, by performing full nonlinear evolutions of perturbed Freund-Rubin and warped compactifications. We do this by applying modern numerical relativity techniques to probe the inhomogeneous and strong field regime, as has been done for a number of different cosmological scenarios, e.g. [159, 330, 127, 126, 105], though here we study inhomogeneities in a compact extra dimension. We find rich dynamics, in some cases finding evolution from unstable to stable stationary warped solutions, though in other cases finding that unstable solutions evolve towards a singular state (even in some cases overshooting stable stationary solutions). We comment on some features of the cosmology seen by four-dimensional observers, and motivate the use of the cosmological apparent horizon as a useful measure of the four dimensional Hubble parameter. The solutions we study provide an important proof-of-principle that numerical relativity could be a powerful tool for exploring new phenomena in cosmologies with extra spatial dimensions.

2.2 Flux compactifications in Einstein-Maxwell theory

In this chapter, we focus on solutions to Einstein-Maxwell theory in $D = p + q$ spacetime dimensions with a D-dimensional cosmological constant Λ_D and a q-form flux that wraps q compact dimensions, leaving p uncompactified dimensions. The starting point for the

theory is then the following $D = p + q$-dimensional action

$$S = \int d^p x d^q y \sqrt{-g} \left[\frac{1}{2}{}^{(D)}R - \Lambda_D - \frac{1}{2q!}\mathbf{F}_q^2 \right] \tag{2.1}$$

where unlike in the rest if this thesis we use units with $M_D = c = 1$, where $M_D \equiv (8\pi G_D)^{-1/(D-2)}$ is the D-dimensional Planck mass, ${}^{(D)}R$ is the D-dimensional scalar curvature, and $\mathbf{F}_q = F_{M_1...M_q}$ is a q-form. Note this choice of units is not conventional, but it leaves us the freedom to fix Λ_D.

The Einstein equations which follow from the action (2.1) are a generalization of the Einstein equations in four dimensions (1.1) to D dimensions

$$G_{MN} = {}^{(D)}R_{MN} - \frac{1}{2}{}^{(D)}R g_{MN} = T_{MN} \tag{2.2}$$

where the stress-energy tensor is

$$T_{MN} = \frac{1}{(q-1)!}F_{MP_2...P_q}F_N^{P_2...P_q} - \frac{1}{2q!}\mathbf{F}_q^2 g_{MN} - \Lambda_D g_{MN} \tag{2.3}$$

with $\mathbf{F}_q^2 = F_{M_1...M_q}F^{M_1...M_q}$. The equations governing the q-form in the absence of sources are

$$\nabla_{[N}F_{MP_2...P_q]} = \nabla^M F_{MP_2...P_q} = 0 . \tag{2.4}$$

Throughout the chapter we will use $M, N, \ldots$ to denote indices that run over the $D-$dimensions, $\overline{m}, \overline{n}, \ldots$ for $(D-1)$-dimensional spatial indices, $\mu, \nu, \ldots$ for $p = 4$-dimensional spacetime indices, and $\alpha, \beta, \ldots$ for q-dimensional spatial indices.

The simplest flux compactifications of Einstein Maxwell theory are the Freund-Rubin solutions [149]: product spaces $\mathcal{M}_p \times S_q$, where $\mathcal{M}_p$ is a maximally symmetric p-dimensional spacetime and S_q is a q-dimensional sphere. In this chapter, we investigate solutions that are warped along a single internal direction, the polar angle θ. That is, we study solutions such that the p-dimensional external space is homogeneous in the uncompactified spatial dimensions with a warp factor depending on θ, and the q-dimensional compact space has the topology of a sphere with $q - 1$ azimuthal symmetries. With these symmetries, the metric takes the form:

$$\begin{aligned} ds^2 &= -(N^2 - \beta_\theta \beta^\theta)dt^2 + \gamma_{xx}(\theta, t)d\vec{x}_{p-1}^2 + 2\gamma_{\theta\theta}(\theta, t)\beta^\theta dt d\theta \\ &\quad + \gamma_{\theta\theta}(\theta, t)d\theta^2 + \gamma_{\phi_1\phi_1}(\theta, t)d\Omega_{q-1}^2 \end{aligned} \tag{2.5}$$

where $d\Omega_{q-1}^2 = d\phi_1^2 + \sin^2\phi_1 d\Omega_{q-1}^2$, $N(\theta, t)$ is the lapse and $\beta^\theta(\theta, t)$ is by symmetry the only non-zero component of the shift vector.

The q-form flux is time-dependent and non-uniformly distributed in the θ-direction,

$$\begin{aligned} \mathbf{F}_q &= Q_B(\theta, t)J(\theta, \phi_1, \ldots, \phi_{q-1})d\theta \wedge \cdots \wedge d\phi_{q-1} \\ &\quad - NQ_E(\theta, t)J(\theta, \phi_1, \ldots, \phi_{q-1})dt \wedge d\phi_1 \wedge \cdots \wedge d\phi_{q-1} \end{aligned} \tag{2.6}$$

where $J(\theta, \phi_1, ..., \phi_{q-1}) = \sin^{q-1}\theta \sin^{q-2}\phi_1 ... \sin\phi_{q-2}$ and $Q_B(\theta, t)$ and $Q_E(\theta, t)$ represent the magnetic and electric flux strengths, respectively.

In the remainder of this section, we review a variety of features of flux compactifications in Einstein-Maxwell theory. In section 2.2.1, we define several quantities that will be useful in describing solutions. In section 2.2.2, we outline how to describe the cosmology of the non-compact space. In section 2.2.3, we review the Freund-Rubin solutions and their stability. Finally, in section 2.2.4, we review the warped compactifications of refs. [223, 224]. The reader interested in going directly to the results can proceed to section 2.4.

2.2.1   Characterizing the solutions

We now define a few quantities which are helpful in describing the solutions presented below. The compact space is characterized by the volume of the internal q-sphere

$$\mathbf{Vol}_{S^q} \equiv \int \sqrt{\gamma_q} d^q y = \int \sqrt{\gamma_q} d\theta \wedge d\phi_1 \wedge ... \wedge d\phi_{q-1} \ , \tag{2.7}$$

the total number of flux units, which is a conserved quantity obtained by integrating the flux density over the internal q-sphere,

$$n \equiv \int_{S_q} \mathbf{F}_q \ , \tag{2.8}$$

and the aspect ratio

$$\epsilon = \frac{\int_0^\pi \sqrt{\gamma_{\theta\theta}(\theta, t)} d\theta}{\pi \sqrt{\widetilde{\gamma}_{\phi_1\phi_1}(\pi/2, t)}} \ , \tag{2.9}$$

defined such that spherical solutions have $\epsilon = 1$, oblate solutions have $\epsilon < 1$ and prolate solutions have $\epsilon > 1$.

As a visualisation tool, we also plot the internal metric as an embedding in $q + 1$ Euclidean dimensions. The internal metric $ds^2 = \gamma_{\theta\theta} d\theta^2 + \widetilde{\gamma}_{\phi_1\phi_1} \sin^2\theta d\Omega_{q-1}^2$ is the induced metric on the surface

$$
\begin{aligned}
x_1 &= \int_{\pi/2}^\theta d\theta' \sqrt{\gamma_{\theta'\theta'}(\theta', t) - [\partial_{\theta'}(\widetilde{\gamma}_{\phi_1\phi_1}(\theta', t)^{1/2}\sin\theta')]^2} \\
x_2 &= \widetilde{\gamma}_{\phi_1\phi_1}(\theta, t)^{1/2}\sin\theta\cos\phi_1 \\
x_3 &= \widetilde{\gamma}_{\phi_1\phi_1}(\theta, t)^{1/2}\sin\theta\sin\phi_1\cos\phi_2 \\
&\vdots \\
x_q &= \widetilde{\gamma}_{\phi_1\phi_1}(\theta, t)^{1/2}\sin\theta\ldots\sin\phi_{q-2}\cos\phi_{q-1} \\
x_{q+1} &= \widetilde{\gamma}_{\phi_1\phi_1}(\theta, t)^{1/2}\sin\theta\ldots\sin\phi_{q-2}\sin\phi_{q-1} \ .
\end{aligned}
$$

2.2.2 The lower dimensional cosmology

If one hopes to make contact with the observable Universe, it is necessary to determine the effective four-dimensional cosmology sourced by evolution of the compact extra dimensions. The standard approach is via the procedure of "dimensional reduction", where one integrates the action over the compact extra dimensions and identifies a four-dimensional gravitational sector and a set of moduli fields associated with properties of the compactification, such as the total volume (see e.g. refs. [119, 165] for an approach most relevant to the present context). This approach has several limitations. Perhaps most importantly, because one must identify a set of coordinates to integrate over, dimensional reduction is intrinsically gauge dependent. Furthermore, gauge dependence arises when identifying the four-dimensional gravitational sector and moduli fields; it is typically feasible to do so only in special coordinate systems where the symmetries of the spacetime are manifest. Without prior knowledge of the "right" coordinate system, it is typically only possible to study small perturbations (see e.g. refs. [166, 151]). In the context of numerical relativity, one does not have complete freedom to dictate the coordinate system most convenient for dimensional reduction: in general, it is necessary to specify the gauge dynamics in a way that leads to well-posed evolution, while avoiding coordinate singularities. Another challenge is that in the typical approach to dimensional reduction, the goal is to find a set of equations of motion for the four-dimensional variables, while our starting point is the solution itself. Given a solution and not the four-dimensional equations of motion, it may not be possible to unambiguously identify the appropriate four-dimensional variables. These subtleties motivate an alternative approach based on the geometrical properties of the solutions themselves, which we now outline. Note, to make contact with the observable universe we assume $p = 4$.

To motivate our approach, let us recall some properties of the standard FLRW solution in four dimensions:

$$ds^2 = -N^2(t)dt^2 + a^2(t)(dx^2 + dy^2 + dz^2) \ . \tag{2.10}$$

The extrinsic curvature of spatial slices is $K_{ii} = -a(da/d\tau)$, with $d/d\tau \equiv (1/N)d/dt$, for $i = x$, y and z, and the trace is

$$K = 3K^x{}_x = -\frac{d \ln \mathrm{Vol}_3}{d\tau} = -\frac{3}{a}\frac{da}{d\tau} \equiv -3H. \tag{2.11}$$

where H is the Hubble parameter and $\mathrm{Vol}_3 = \sqrt{\gamma} = a^3$ is the normalized volume enclosed by a congruence of comoving geodesics. Note that these equalities are contingent on the time slicing chosen here, which preserves the homogeneity of the FLRW solution. In this cosmological slicing, the trace of the extrinsic curvature (or equivalently the expansion of comoving timelike geodesics) determines the Hubble parameter. Another useful geometrical quantity is the area of the cosmological apparent horizon. We define the cosmological apparent horizon as a surface where the null expansion vanishes. (This is analogous to how

17

apparent horizons can be used to define black hole horizons on a specific timeslice[2].) In an expanding FLRW universe, the coordinate radius of the cosmological apparent horizon is simply the comoving Hubble radius $r_H = (aH)^{-1}$, yielding an area:

$$\mathcal{A}_C = 4\pi a^2 r_H^2 = 4\pi H^{-2} \tag{2.12}$$

Therefore, we see that both the extrinsic curvature and the area of the cosmological apparent horizon can be used as alternative definitions of the Hubble parameter:

$$H = -\frac{K}{3} = \sqrt{\frac{4\pi}{\mathcal{A}_C}} \, , \tag{2.13}$$

where again the equivalence with the usual definition of the Hubble parameter is contingent on choosing a cosmological slicing.

How does this picture generalize to the present context, where we have compact extra dimensions? The trace of the intrinsic curvature in this case depends on the position in the compact space and contains terms associated with the expansion of the volume in the compact space:

$$K(\theta, t) = 3K^x{}_x + K^\theta{}_\theta + (q-1)K^{\phi_1}{}_{\phi_1} = -\left(\frac{d\ln \text{Vol}_3}{d\tau} + \frac{d\ln \text{Vol}_q}{d\tau}\right) \tag{2.14}$$

where for a general slicing, $d/d\tau \equiv (1/N)(\partial_t - \mathcal{L}_\beta)$, where the last term is the Lie derivative with respect to the shift vector. The observers associated with a general time slicing will not necessarily follow geodesics in the full D-dimensional spacetime, and restricting to geodesic slicing can be problematic due to the appearance of coordinate singularities. This aside, there are other subtleties associated with finding an effective four-dimensional Hubble parameter from the extrinsic curvature. If we were to use the trace of the extrinsic curvature, note that this includes expansion of both the compact and non-compact space. Should one simply use $-K^x{}_x$, which characterizes the expansion in the non-compact dimensions, or some combination of the expansion in the compact and non-compact space? In addition, the expansion is not homogeneous in the extra dimensions, so one must define the correct measure of integration over the compact space to obtain the expansion seen by an "average" cosmological observer.

Some insight to these questions can be gained by investigating the properties of the cosmological apparent horizon, which as we outlined above, can be used to define the Hubble parameter in a four-dimensional FLRW Universe. For surfaces of constant time and (uncompactified) radius $r \equiv \sqrt{x^2 + y^2 + z^2}$ with unit inward (outward) normal $s^{\bar{m}}$ the inward (outward) null expansion

$$\Theta_\pm = D_{\bar{m}} s^{\bar{m}} + K_{\bar{m}\bar{n}} s^{\bar{m}} s^{\bar{n}} - K \tag{2.15}$$

---

[2]We define various quasi-local notions of black hole and cosmological horizons in appendix C.2.

18

vanishes on the surface

$$r_H = \frac{\pm 2}{\sqrt{\gamma_{xx}}} \frac{1}{(K^x{}_x - K)} . \tag{2.16}$$

A marginally inner trapped surface with $\Theta_- = 0$ and $\Theta_+ > 0$ is a generalization of the de Sitter horizon, while the marginally outer trapped surface with $\Theta_+ = 0$ and $\Theta_- < 0$ that occurs for contracting spacetimes is more similar to that of a black hole apparent horizon[3].

The area of the cosmological apparent horizon is obtained by integrating over the compact space

$$\mathcal{A}_{\mathrm{C}}(t) = \int d\theta d\phi_1 \cdots d\phi_{q-1} \sqrt{\gamma_q} \, 4\pi r_H^2 \gamma_{xx} \tag{2.17}$$

$$= \int d\theta d\phi_1 \cdots d\phi_{q-1} \sqrt{\gamma_q} \, 4\pi \left(\frac{2}{K^x{}_x - K} \right)^2 . \tag{2.18}$$

Note that this is a $q + 2$ dimensional area with units of L^{q+2} where L is some length scale. One can also use this area as a measure of entropy:

$$\mathcal{S} \equiv 2\pi \mathcal{A}_{\mathrm{C}} , \tag{2.19}$$

where we recall that in our units $M_D \equiv (8\pi G_D)^{-1/(D-2)} = 1$. The connection between the area of the apparent horizon and gravitational entropy is related to the thermodynamic interpretation of Einstein's equations [200, 274] and has been considered for black holes (e.g. ref. [184]) and cosmological spacetimes (e.g. refs. [152, 81, 154]). In ref. [224], it was shown that for a subset of the solutions we consider below, the entropy as defined above is a useful indicator of stability. In particular, for solutions at fixed conserved flux, the stable solution has the highest entropy. Note that since this analysis is entirely classical, one could simply use the area of the cosmological horizon as a measure of stability. As for a purely four-dimensional FLRW Universe, a Hubble parameter can be defined by

$$\frac{H}{M_4} \equiv \pm \sqrt{\frac{4\pi}{\mathcal{A}_{\mathrm{C}}}} \tag{2.20}$$

where we take the positive (negative) sign when the inward (outward) null expansion vanishes. In our results below where we wish to examine the effective four-dimensional cosmology, we will use this definition of the Hubble parameter. Finally, we define the four-dimensional Planck mass as

$$M_4^2 \equiv \int d\theta d\phi_1 \cdots d\phi_{q-1} \sqrt{\gamma_q(t=0,\theta)} , \tag{2.21}$$

---

[3]Though we note that the usual definition of apparent horizon in the context of dynamical black hole spacetimes typically includes an extra condition specifying that the surface be outermost, or be at the boundary between a trapped and untrapped region, that excludes the cosmological setting we study here. See appendix C.2 for more details

where γ_q refers to the background solution.

It is useful to examine the Hamiltonian constraint equation in order to make a more direct connection with the effective four-dimensional theory. This is given by

$$K^2 - K_{\bar{m}\bar{n}}K^{\bar{m}\bar{n}} = 2\rho - {}^{(D-1)}R \tag{2.22}$$

where $\rho = n^N n^M T_{MN}$ and ${}^{(D-1)}R$ is the intrinsic curvature on spatial slices. The extrinsic curvature term decomposes as follows

$$
\begin{aligned}
K_{\bar{m}\bar{n}}K^{\bar{m}\bar{n}} - K^2 &= -6\left(\frac{K^x{}_x - K}{2}\right)^2 + \frac{1}{2}(K^\theta{}_\theta)^2 + \frac{(q+3)(q-1)}{4}(K^\phi{}_\phi)^2 \\
&+ \left(K^\theta{}_\theta + \frac{q-1}{2}K^\phi{}_\phi\right)^2 .
\end{aligned} \tag{2.23}
$$

Note that choosing to isolate the factor of $(K^x{}_x - K)/2$, which appeared in the expression for the cosmological apparent horizon, nicely splits the extrinsic curvature term into negative definite and positive definite components. Re-arranging the Hamiltonian constraint equation we obtain:

$$\left(\frac{K^x{}_x - K}{2}\right)^2 = \frac{1}{3M_4^2}\rho_{\text{eff}}(\theta, t) \tag{2.24}$$

where we have defined

$$
\begin{aligned}
\rho_{\text{eff}}(\theta, t)/M_4^2 &\equiv \rho - \frac{1}{2}{}^{(D-1)}R + \frac{1}{4}(K^\theta{}_\theta)^2 + \frac{(q+3)(q-1)}{8}(K^\phi{}_\phi)^2 \\
&+ \frac{1}{2}\left(K^\theta{}_\theta + \frac{q-1}{2}K^\phi{}_\phi\right)^2 .
\end{aligned} \tag{2.25}
$$

Equation (2.24) has the form of the Friedmann equation. The expression for the apparent horizon area eq. (2.17) can be used to define the measure of integration over the Hamiltonian constraint equation to give a four-dimensional Friedmann equation. In particular,

$$H(t)^2 = \frac{1}{3M_4^2}\langle\rho_{\text{eff}}(t)\rangle = \frac{4\pi M_4^2}{\mathcal{A}_{\text{C}}(t)} , \tag{2.26}$$

where H is defined as in eq. (2.20) and

$$\langle\rho_{\text{eff}}(t)\rangle \equiv M_4^2\left[\int d\theta d\phi_1\cdots d\phi_{q-1}\sqrt{\gamma_q}\,(\rho_{\text{eff}}(\theta, t))^{-1}\right]^{-1} . \tag{2.27}$$

Note that with these definitions, the square of the Hubble parameter is inversely proportional to the entropy, so a stability criterion based on maximizing the entropy (or synonymously, the area) is equivalent to one that minimizes this definition for the Hubble parameter.

For completeness, and because it will be useful in characterizing the properties of the solutions presented below, we sketch the standard procedure of dimensional reduction; further details can be found in appendix A.1. We begin with the D-dimensional action in ADM form:

$$S \;=\; \frac{1}{2} \int d^4x d^q y \sqrt{-g} \left[K_{\bar{m}\bar{n}} K^{\bar{m}\bar{n}} - K^2 + {}^{(D-1)}R - 2\Lambda_D - \frac{1}{q!}\mathbf{F}_q^2 \right] \;. \qquad (2.28)$$

The goal is to find an effective action for the four-dimensional metric variables and moduli fields, which can be identified with integrals of combinations of metric functions over the compact space (e.g. the volume). Schematically, for spacetimes that are homogeneous in the three large dimensions, the various terms in the action contribute as follows:

- $K_{\bar{m}\bar{n}} K^{\bar{m}\bar{n}} - K^2$: The extrinsic curvature term contains time derivatives of the metric functions, and therefore contains the 4-D Ricci scalar and kinetic terms for moduli fields.

- ${}^{(D-1)}R$: The Ricci scalar on spatial slices contains spatial derivatives of the metric functions on the compact space. With our assumption that the metric is independent of the three large dimensions, there are no contributions to the 4-D Ricci scalar. This term therefore contributes only to the potential for moduli fields.

- $2\Lambda_D + \mathbf{F}_q^2/q!$: The cosmological constant and flux terms contribute to the potential for moduli fields.

Here, we focus on the extrinsic curvature term; additional details for specific examples can be found in appendix A.1. Factoring the extrinsic curvature term as in Eq. (2.23), we have

$$S = \frac{1}{2} \int d^4x d^q y \sqrt{\gamma_q} N \gamma_{xx}^{3/2} \left[-6 \left(\frac{K^x{}_x - K}{2} \right)^2 + \dots \right] \qquad (2.29)$$

Comparing this to the action for four dimensional FLRW solutions, one can try to equate:

$$\sqrt{-g(t)} \; M_4^2 H(t)^2 = \int d^q y \sqrt{\gamma_q} N \gamma_{xx}^{3/2} \left(\frac{K^x{}_x - K}{2} \right)^2 \qquad (2.30)$$

For a convenient metric ansatz, one can explicitly identify $\sqrt{-g(t)}$, M_4^2 and $H(t)^2$; we outline several examples in appendix A.1. A nice feature of the decomposition of the extrinsic curvature we have chosen is that it contains the combination of metric functions that yield a dimensionally reduced action in the four dimensional Einstein frame (e.g. the conformal frame where M_4 is constant). For solutions with warping there are some subtleties in finding a unique four-dimensional metric determinant and Hubble parameter which we discuss in appendix A.1. In the more general cases we consider below, where we do not have complete freedom to specify a gauge where the metric functions take a convenient form, it is not possible to unambiguously identify the four dimensional Hubble parameter. We therefore utilize the geometrical definition of the Hubble parameter based on the area of the apparent horizon in Eq. 2.20.

2.2.3 Freund-Rubin branch

In this chapter, we consider the nonlinear evolution of perturbations to two classes of stationary solutions of the theory described above. Namely, we consider the homogeneous Freund-Rubin solutions and warped solutions with a θ-dependence. In the symmetric Freund-Rubin solution, a q-form flux uniformly wraps the extra dimensions into a q-sphere,

$$\mathbf{F}_q = \rho_B \mathbf{vol}_{S^q} \tag{2.31}$$

where ρ_B is the magnetic flux density and $\mathbf{vol}_{S^q} = \epsilon$ is the volume element on the internal q-sphere. The direct product condition guarantees that the p extended dimensions form an Einstein space. Restricting to the trivial case of a maximally symmetric extended de Sitter spacetime,

$$ds^2 = -dt^2 + e^{2Ht}d\vec{x}^2_{p-1} + L^2 d\Omega^2_q \tag{2.32}$$

where L is the radius of q-sphere, H is the Hubble parameter (2.20) and in the particular case where $p = 4$, $d\vec{x}^2_{p-1} = dx^2 + dy^2 + dz^2$ is the usual 3-Cartesian element.

The Maxwell equations are trivially satisfied, while the Einstein equations (2.2) enforce algebraic relations between the parameters $\{\rho_b, H, L\}$

$$\Lambda_D = \frac{(p-1)^2}{2}H^2 + \frac{(q-1)^2}{2}L^{-2} \tag{2.33}$$

$$\rho^2_B = -(p-1)H^2 + (q-1)L^{-2} \tag{2.34}$$

such that if we fix units with $\Lambda_D = 1$, we are left with one free parameter describing the Freund-Rubin solutions. This parameter can be taken to be the total number of flux units (2.8)

$$n \equiv \int_{S_q} \mathbf{F}_q = \rho_b \mathbf{Vol}_{S_q} \ , \tag{2.35}$$

where the latter equality is specific to the Freund-Rubin solution. From (2.33) and (2.34), we can see that there can be more than one solution for a given value of n. Figure 2.1 shows these different solutions in $(H/M_4, n)$ space. Focusing on the spherical solutions with aspect ratio $\epsilon = 1$, the figure indicates that below some value $n_{\max}$, there exists two solutions, a small and a large volume branch. As we will see below, the former is stable to the total-volume instability ($\ell = 0$), but may be unstable to the warped instability ($\ell \geq 2$), while the latter is unstable to the total-volume instability, with the end point being decompactification or flow towards the small volume solution. For $n \geq n_{\max}$, there is no solution.

The effective potential

In order to give some intuition for the stability of the flux compactification solutions, we can go back to the dimensional reduction procedure of section 2.2.2, and considering the
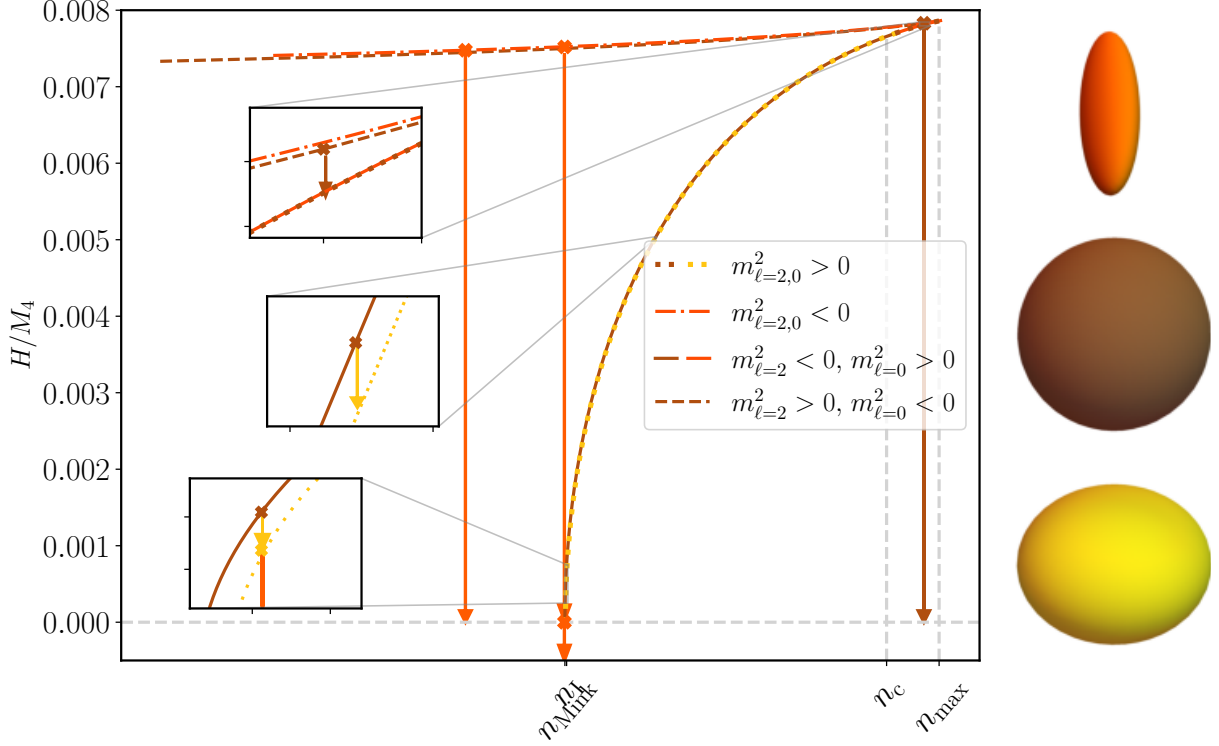
Figure 2.1: A cartoon of the Freund-Rubin and ellipsoidal solutions in the $(H/M_4, n)$ plane for $\Lambda_D = 1$ and $q = 4$. For each value of the conserved flux number (2.8), there are two solutions: a symmetric solution where the compact space is spherical with an aspect ratio $\epsilon = 1$ (indicated in brown), and a warped solution where the internal manifold is oblate with $\epsilon < 1$ (yellow) or prolate with $\epsilon > 1$ (orange). We find three critical values of n. First, for $n_{\text{Mink}} < n < n_{\text{max}}$ there are two Freund-Rubin and two warped solutions: On the Freund-Rubin branch there is a small and a large volume branch perturbatively stable or unstable to the volume instability ($m_{l=0}^2 > 0$ or $m_{l=0}^2 < 0$) respectively. At $n = n_{\text{max}}$ the two branches merge and annihilate. On the warped branch there is one solution on the large Hubble warped branch, perturbatively unstable to the warped instability ($m_{l=2}^2 < 0$) and a solution on the small Hubble warped branch. At $n = n_c$ the small Hubble warped branch intersects the small volume Freund-Rubin branch and the two branches are marginally stable to the warped instability ($m_{l=2}^2 = 0$). Whenever the ellipsoidal solution has $\epsilon > 1$ it is also perturbatively unstable. Arrows indicate the specific nonlinear solutions we discuss in section 2.4. They all point towards a solution with smaller effective Hubble rate and higher entropy (area). For a small range $n_{\text{Mink}} \leq n < n_I$, solutions tend to a state where $H/M_4 < 0$, the cosmological implications of which are discussed in section 2.4.2

23

source terms in eq. (2.28), think of the radius L of the sphere as a four-dimensional radion field, living in an effective potential given by

$$\frac{V(L)}{M_4^4} = \frac{1}{2} \left(\frac{L_0}{L}\right)^q \left(-\frac{q(q-1)}{L^2} + 2\Lambda_D + \frac{1}{M_4^4}\frac{n^2}{L^{2q}}\right) \qquad (2.36)$$

The details of the derivation can be found in appendix A.1.1. From left to right, the three terms represent the spatial curvature, the higher dimensional vacuum energy, and the energy density of the flux, respectively. The flux term is repulsive, and tends to push the sphere to larger radius, but the curvature of the compact space is attractive, such that the interaction of these two terms can form a minimum of the potential where the radius of the q-sphere can be stabilized, yielding a four-dimensional vacuum.

Each allowed value of n, p and q defines a set of allowed radion potentials or landscape of lower dimensional theories. The potential for fixed $q = p = 4$ and $\Lambda_D > 0$ is sketched in figure 2.2 for a number of values of n. As we saw in the previous subsection, the number of extrema depends on the value of n. For small enough n, the effective potential has a minimum and a maximum corresponding to the small and large volume branches, respectively. The extrema merge at $n = n_{\max} = 81\pi^2/\left(\sqrt{2}\Lambda_8^{3/2}\right)$ and above this value there is no solution. Note that for small enough n the four-dimensional vacua are negative, but as n increases, they eventually become positive, which is important for cosmological solutions. To derive this effective potential, we assumed the shape of the compact space is fixed. However, we will see below that minima of the effective potential in figure 2.2 can be unstable maxima in other directions of the field-space that correspond to shape mode fluctuations.

Stability

We now briefly review linear perturbations around Freund-Rubin solutions, restricting to scalar-type perturbations with respect to, not only the p-dimensional external de Sitter space, but also the $SO(q)$ symmetry of the background internal space. The full perturbative spectrum was studied in refs. [76, 186], and we defer the reader to those references for a more complete analysis. We write the perturbed metric as

$$\delta g_{\mu\nu} = -\frac{1}{p-2}g_{\mu\nu}\bar{h}Y_\ell(\theta) , \qquad \delta g_{\alpha\beta} = \frac{1}{q}g_{\alpha\beta}\bar{h}Y_\ell(\theta) \qquad (2.37)$$

which tells us that the q-sphere is deformed with the shape of a $m = 0$ spherical harmonic $Y_\ell(\theta)$ and some amplitude $\bar{h}$.

The perturbed field strength is

$$\delta F_{\alpha_1...\alpha_q} = -\bar{a}\rho_B\epsilon_{\alpha_1...\alpha_q}\lambda_\ell Y_\ell(\theta) , \qquad \delta F_{\beta\beta_2...\beta_q} = \nabla_\beta\bar{a}\rho_B\epsilon^\alpha_{\beta_2...\beta_q}\nabla_\alpha Y_\ell(\theta) \qquad (2.38)$$

where $\lambda_\ell = \ell(\ell + q - 1)/L^2 > 0$ is the eigenvalue of the spherical harmonic, $\Box_y Y_\ell(\theta) = -\lambda_\ell Y_\ell(\theta)$ (recalling that y refers to the q-dimensional coordinates) and $\bar{a}$ is a dimensionless
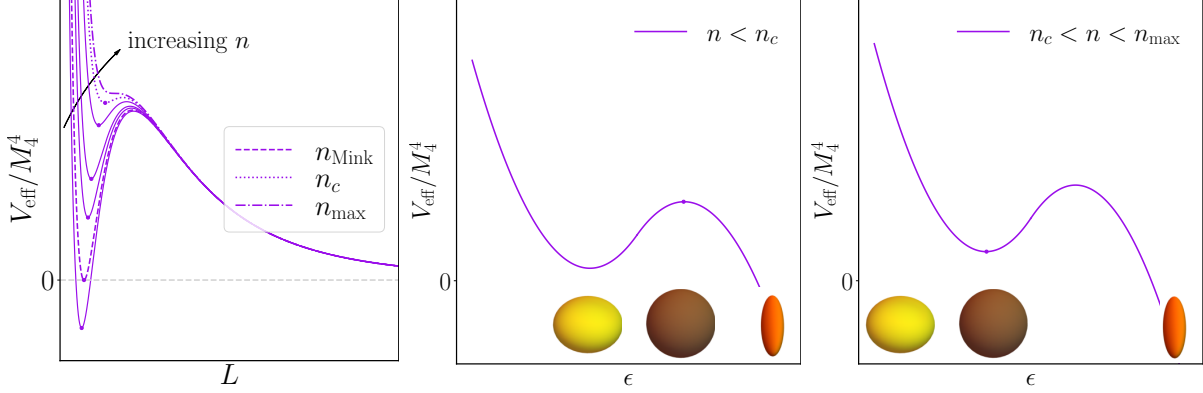
Figure 2.2: Left: The effective radion potential eq. (2.36) for $\Lambda_D > 0$ and successively larger values of n from bottom to top, assuming the compact space is spherically symmetric. The extrema correspond to the Freund-Rubin solutions. For small n, the effective potential has a maximum ($m_{\ell=0}^2 < 0$ and always de Sitter) and minimum ($m_{\ell=0}^2 > 0$ and de Sitter or anti-de Sitter). At $n = n_{\max}$ the solutions disappear. Right: Schematic of the effective potential for a fixed radius (minimum of $V_{\text{eff}}(L)$), but changing ellipticity. We find that the effective potential tends to $+\infty/-\infty$ as the internal manifold becomes increasingly oblate or prolate, respectively. The Freund-Rubin solution is at a maximum ($m_{\ell=2}^2 < 0$) when the corresponding warped solution is oblate, and a minimum ($m_{\ell=2}^2 > 0$) when the warped solution is prolate. Some solutions escape the potential well of oblate solution to roll in the prolate direction.

function. Note that the equations require that $\bar{h}$ and $\bar{a}$ shift in opposite directions (sign $\bar{a} = -\text{sign}(\bar{h})$), which physically means that whenever the internal radius gets larger, the flux density also gets larger (sign $\delta F_{\alpha_1...\alpha_q} = -\text{sign } \delta g_{\alpha\beta}$). Linearizing the Einstein-Maxwell system, we obtain a set of ordinary, coupled, second-order differential equations for the fluctuations, the spectrum of which can be found by diagonalization. We find two channels of instabilities, the first due to the homogeneous mode, the so-called volume-instability, and the second due to the inhomogeneous mode, the so-called warped instability.

We first consider homogeneous ($\ell = 0$) fluctuations in the total volume of the internal manifold. The equation of motion is

$$\Box_x \bar{h}(x) = \frac{1}{L^2}\left(-2(q-1) + \frac{q(p-1)}{p+q-2}\rho_B{}^2 L^2\right)\bar{h}(x) \tag{2.39}$$

(recalling that x refers to the p-dimensional coordinates), which implies that the mode has positive mass when

$$\rho_B{}^2 L^2 > \frac{2(q-1)(p+q-2)}{q(p-1)} \tag{2.40}$$

or alternatively, using eqs. (2.33)–(2.34), when

$$H^2 \leq \frac{2\Lambda_D(p-2)}{(p-1)^2(p+q-2)}, \qquad \text{or} \quad \rho_B^2 \geq \frac{2\Lambda_D}{(p-1)(q-1)} \ . \tag{2.41}$$

25

This implies that if the density of the flux lines wrapping the extra dimensions is too small, or the Hubble parameter of the external space is too large, then there can be an instability where the total volume of the internal manifold uniformly grows or shrinks, but the shape of the compactified sphere is fixed. Stable de Sitter solutions are on the small-volume branch, while unstable ones are on the large volume branch and correspond to a maximum of the effective potential.

Now looking at the coupled scalar sector, which will be the main focus of this chapter, then when $q \geq 4$, perturbations with polar number $\ell \geq 2$ can be unstable. Mathematically, this instability arises from the coupling of the metric and flux perturbations, their equations of motion being

$$\Box_x \begin{pmatrix} \tilde{h} \\ \tilde{a} \end{pmatrix} = \left[\frac{1}{L^2} \begin{pmatrix} -q\frac{q-1}{p+q-2}\rho_B{}^2 L^2 & 0 \\ 0 & 0 \end{pmatrix} + M \right] \begin{pmatrix} \tilde{h} \\ \tilde{a} \end{pmatrix} \tag{2.42}$$

where M is a 2×2 matrix given by

$$M = \frac{1}{L^2} \begin{pmatrix} -L^2\lambda - 2(q-1) + q\rho_B{}^2 L^2 - 2\frac{q-1}{q}L^2\lambda & \frac{-4}{\rho_B{}^2 L^2}\frac{q-1}{q}L^2\lambda(L^2\lambda + q) \\ \frac{q-1}{q}\rho_B{}^2 L^2 & -L^2\lambda + 2\frac{q-1}{q}L^2\lambda \end{pmatrix} \tag{2.43}$$

where $\tilde{h} = \bar{h} - 2\lambda_\ell a$ and $\tilde{a} = \rho_B\bar{a}$.

The mode will be stable provided the eigenvalues of M are positive, which for $\ell \geq 2$ implies

$$\rho_B{}^2 L^2 < \frac{\ell(\ell + q - 1) - 2q + 2}{2(q-2)}\frac{p+q-2}{p-1} , \tag{2.44}$$

or equivalently when

$$H^2 \geq \frac{2\Lambda_D\left((p-1)q^2 - (3p-1)q + 2\right)}{q(q-3)(p-1)^2(p+q-2)}, \qquad \text{or} \quad \rho_B^2 \leq \frac{4\Lambda_D}{q(q-3)(p-1)} . \tag{2.45}$$

Taking $p = 4$, one finds that for $q = 2$ or $q = 3$, de Sitter vacua are only unstable to the $\ell = 0$ mode. For $q = 4$, the only excited mode to develop a negative mass is $\ell = 2$. For $q \geq 5$, all de Sitter solutions are unstable to $\ell = 0$ or $\ell = 2$ fluctuations. Note that the case of $q = 4$ is interesting because it has a window of stability in the range of fluxes allowed by eqs. (2.40) and (2.44). The warped instability signals the presence of a new branch of deformed solutions, which we describe next.

2.2.4 Warped branch

In the previous section, we described the symmetric Freund-Rubin solutions, and saw that there is a critical value of n above which inhomogeneous perturbations develop a tachyonic

mass. This suggests that there may be other warped solutions obeying the Einstein-Maxwell system of equations. References [223, 242, 114] constructed stationary prolate or oblate topological spheres numerically, and ref. [224] studied their linear stability. One way to describe such warped solutions is by the following metric ansatz

$$ds^2 = e^{2\phi(\tilde{\theta})}\left[-dt^2 + e^{2ht}d\vec{x}_{p-1}^2\right] + e^{-\frac{2p}{q-2}\phi(\tilde{\theta})}(d\tilde{\theta}^2 + a(\tilde{\theta})^2 d\Omega_{q-1}^2) \qquad (2.46)$$

and flux

$$F_q(\tilde{\theta}) = b\, a(\tilde{\theta})^{q-1}e^{-\frac{2p(q-1)\phi(\tilde{\theta})}{(q-2)}}\sin^{-(q-1)}(\tilde{\theta})\; J(\tilde{\theta}, \phi_1, ..., \phi_{q-1})\; d\tilde{\theta} \wedge ... \wedge d\phi_{q-1} \qquad (2.47)$$

where the internal coordinate $\tilde{\theta}$ lies in the finite interval $\tilde{\theta}_- < \tilde{\theta} < \tilde{\theta}_+$, with $\tilde{\theta}_{-/+}$ designating the two poles [223], and where b and h are constants such that $b = \rho_B$ and $h = H$ whenever one recovers the Freund-Rubin solution with $\phi(\tilde{\theta}) = 0$ and $a(\tilde{\theta}) = L$. Note that eq. (2.46) can be put in the form of eq. (2.5), provided one performs the following coordinate transformation

$$\theta \to \frac{\tilde{\theta}}{L} + \frac{\pi}{2} \qquad (2.48)$$

where $L = 2\tilde{\theta}_+/\pi$. The inhomogeneous flux, eq. (2.47), automatically satisfies Maxwell's equations and the Bianchi identity. Plugging in our ansatz, the Einstein equations give us two equations involving second derivatives of the metric

$$\phi'' = (p-1)h^2 e^{-\frac{2(D-2)\phi}{q-2}} - (q-1)\frac{a'}{a}\phi' + e^{-\frac{2p\phi}{q-2}}\frac{1}{(D-2)}\left(-2\Lambda_D + (q-1)b^2 e^{-2p\phi}\right) \qquad (2.49)$$

$$\frac{a''}{a} = -\phi'^2 \frac{p(D-2)}{(q-2)^2} - a^{-2} + \frac{a'^2}{a^2} \qquad (2.50)$$

and one equation involving first derivatives

$$(q-1)(q-2)\frac{a'^2}{a^2} = (q-2)(q-1)a^{-2} + \frac{p(D-2)}{q-2}\phi'^2 + p(p-1)h^2 e^{-\frac{2(D-2)\phi}{q-2}} - 2e^{\frac{-2p}{q-2}\phi}\Lambda_D$$
$$+ b^2 e^{\frac{-2p(q-1)}{q-2}\phi}, \qquad (2.51)$$

where the prime denotes the derivative with respect to $\tilde{\theta}$. Using the procedure outlined in ref. [224], we solve these equations, and hence construct warped solutions. We refer the reader to ref. [224] for more details. Note that we assume that the internal space is symmetric about the equator since the linear analysis shows that the first mode to become tachyonic is quadrupolar ($\ell = 2$). Figure 2.3 shows the two one-parameter families of solutions, namely the trivially warped Freund-Rubin solutions, and the non-trivially warped solutions, in the $(b^2/\Lambda_D, h^2/\Lambda_D)$ (left) and (ϵ, n) (right) planes. This figure shows that the two branches intersect at a single point $(b_{cr}{}^2/\Lambda_D, h_{cr}{}^2/\Lambda_D) = (0.36, 0.052)$ where the only solution is the trivial one, and the compact space is a perfect sphere. For values of $b < b_{cr}$, the internal compact space is prolate, while for values $b > b_{cr}$, it is oblate. This is particularly important as, according to eq. (2.45), this critical point coincides with the point at which the $\ell = 2$ mode of the Freund-Rubin branch becomes massless. In other words, the warped branch emanates from the marginally stable Freund-Rubin solution, as one would expect.
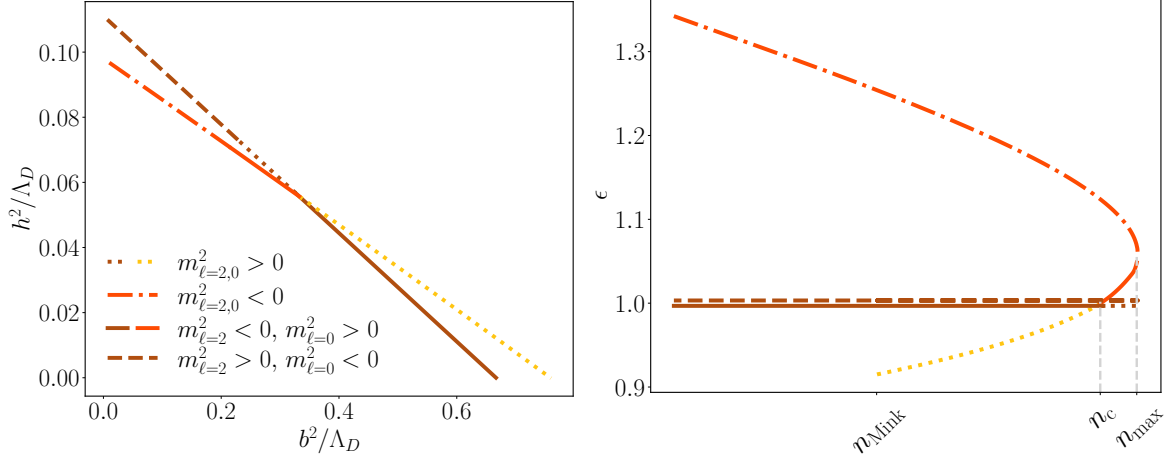
Figure 2.3: Two branches of solutions to (2.49) in the $(b^2/\Lambda_D, h^2/\Lambda_D)$ (left) and (ϵ, n) plane (right). The brown lines represent the Freund-Rubin branch, while the yellow (oblate) and orange (prolate) lines represent the interpolation of warped solutions reconstructed numerically. The two branches intersect at $({b_{cr}}^2/\Lambda_D, {h_{cr}}^2/\Lambda_D) = (0.36, 0.052)$. The linestyle reflects the perturbatively unstable modes for the two branches. See figure 2.1 for more details.

Stability

The spectrum for scalar perturbations of the warped solutions was studied in [224]. Computing the eigenspectrum in a similar way to the Freund-Rubin solutions, one finds that the marginal stability of the warped solutions coincides with the marginal stability of the Freund-Rubin branch. In particular, for the $\ell = 2$ mode, when h^2 satisfies the first inequality given by eq. (2.45), then the eigenvalue of the warped branch is positive, while the eigenvalue of the Freund-Rubin solution becomes negative. In other words, in the low Hubble regime, where the Freund-Rubin branch is unstable to inhomogeneous excitations, the warped branch is perturbatively stable. Conversely, the warped branch is unstable to inhomogeneous perturbations in the regime where the Freund-Rubin branch is stable. Additionally, the mass squared of the warped branch is larger than that of the symmetric branch in the regime where the latter is unstable, which in turn implies that the warping of the internal compact space stabilizes the shape mode of the compact space.

Alternatively, one can use a thermodynamic argument. Recall that the entropy is defined by eq. (2.19), where H is defined by the cosmological apparent horizon (see appendix A.1 for an explicit derivation for the warped metric ansatz). As shown in [224], the thermodynamic stability of these solutions agrees with their dynamical stability. In other words, when $n_c < n < n_{\max}$, where $n_c = 32\sqrt{3}\pi^2/\Lambda_8^{3/2} = 0.97 n_{\max}$, the small volume Freund-Rubin branch has a smaller Hubble parameter, or larger entropy (area), and hence is thermodynamically preferred. On the other hand, when $n < n_c$, the warped branch has smaller Hubble or larger entropy and is thermodynamically preferred. This is shown in

figure 2.1. At the linear level, the dynamical and thermodynamic stability of the Freund-Rubin solutions determine the shape and stability of the warped solutions. Reference [114] sketched an effective potential that neatly encapsulates this behaviour. In the effective theory described by eq. 2.36, only the radius of the solution is treated as a dynamical radion field. If we now allow the shape of the compact space to vary as well, we must treat the aspect ratio as a dynamical field, and extend the effective potential to be a function of L and ϵ. Minima of the potential in the L direction are now minima or maxima in the ϵ direction depending on whether the solution is stable or unstable to shape fluctuations which in turn depends on its conserved flux number. Reference [114] argued that this effective potential is captured by a cubic potential schematically drawn in figure (2.2), and that the effective potential asymptotes to $V \to +\infty$ in the oblate direction and $V \to -\infty$ in the prolate direction. Intuitively, one would expect that in the direction of decreasing ϵ, the equatorial radius is increasing, and flux is concentrating there such that the solution eventually settles to a minimum. On the other hand, as ϵ increases, the equatorial radius will decrease and the flux concentrates at the poles. Having no flux to support the equator, the sphere collapses to zero radius and the potential (2.36) tends to $V \to -\infty$. What happens to the solution as it rolls down the potential is unclear. In the next section, we verify this general picture nonlinearly and study the endpoint of the solutions. The evolution and endpoints of the unstable solutions are summarized in figure 2.1.

2.3   Numerical implementation

We evolve the Einstein equations using the generalized harmonic formulation introduced in 1.2.2. We choose our evolution variables according to a space-time decomposition of the metric. See appendix A.2 for the evolution variables and equations of motion.

To numerically evolve the system, we discretize in time and θ. To avoid solving the equations directly on the poles we use a shifted grid

$$\theta_j = \frac{j + 1/2}{N_\theta}\pi, \qquad j = 0, \ 1, \ldots, \ N_\theta - 1 \ . \tag{2.52}$$

We expand the evolution variables as a sum of sines or cosines, depending on the parity of the function around the pole, and use pseudospectral methods to calculate the spatial derivatives. The variables are evolved in time using fourth-order Runge-Kutta time stepping. High-frequency spectral noise is reduced by applying an exponential filter [255]. This filter is applied to the coefficients of every derivative function and directly to the coefficients of the solution at the end of each time step. The coordinate freedom is fixed by choosing the source functions. These are set to be such that the shift is driven to zero and the lapse remains approximately constant when the solution remains close to the background solution. This avoids extra dynamics coming solely from gauge transitions (as opposed to physical instability).

29

During the evolution, we search for, and in some cases find, trapped regions: points where both (i.e. the nominally "inward" and "outward") null geodesics moving in the θ direction must have the same sign for the derivative with respect to the affine parameter $d\theta/d\lambda$. In such cases, we excise a causally disconnected region bounded by such a point where the null geodesics are both ingoing, and instead use fourth order finite difference stencils to calculate derivatives, and Kreiss-Oliger dissipation to reduce the high-frequency noise [233]. In this way, we continue to evolve the spacetime outside the trapped regions.

We construct initial data describing perturbed Freund-Rubin or stationary warped solutions. To do this, we take the background metric on the initial time slice and add the perturbation given by eq. (2.37) with some specified amplitude. We then solve for the initial electric and magnetic forms using the Hamiltonian and momentum constraints (hence our perturbed solutions still exactly satisfy the constraints). This procedure gives rise to a slightly perturbed flux number, although close enough to background value to not affect the properties relevant for assessing stability. See appendix A.4 for results illustrating that we start with sufficiently small perturbations so as to be in the linear instability regime, as well as numerical convergence.

In the case where the background solution is a warped solution, we construct the background solution using the procedure described in section 2.2.4. Note that most of the solutions presented below are for $q = 4$, where only the $\ell = 0$ or $\ell = 2$ modes can be perturbatively unstable. We therefore only consider $\ell = 0$ or $\ell = 2$ perturbations, leaving the investigation higher modes in solutions with more dimensions for future work.

2.4 Results

We now present our numerical solutions, restricting to $p = 4$ to make contact with cosmology.

2.4.1 Total volume instability of Freund-Rubin solutions

We begin with a discussion of the total volume instability, which affects Freund-Rubin solutions on the large volume branch. We obtain results similar to ref. [234], which studied the cases where the dimensionality of the q-sphere was two or three. In those cases, the homogeneous mode is the only one excited, and hence the inhomogeneous perturbations ($\ell > 0$) can be set to zero. Here, our initial conditions are Freund-Rubin solutions on the large volume branch in theories with $q = 4$. Note that for $q = 4$, the small volume branch is vulnerable to the warped instability, but the large volume branch is not. This guarantees that, at least initially, time evolution does not break the spherical symmetry of the compact space.

In the absence of the warped instability, we can understand the time evolution entirely from the perspective of the four dimensional effective theory (see appendix A.1 for further

details): Einstein gravity with a scalar field describing the radius of the compact sphere that evolves in the potential depicted in figure 2.2. Our initial condition lies at the maximum of the effective potential, and the evolution will take the solution either to the potential minimum (corresponding to the $dS_p \times S_q$ solution on the small-volume branch) or to a solution that decompactifies to $D = p + q$ dimensional de Sitter space.

We find that the results of the full nonlinear evolution away from the large volume Freund-Rubin solutions are as expected from the four dimensional effective theory. A small positive perturbation to the total volume leads to decompactification while a small negative perturbation evolves toward the stable small-volume $dS_p \times S_q$ solution. For the solutions that decompactify, we confirm that the curvature scalar asymptotes to what is expected for $D = p + q$ dimensional de Sitter space with a cosmological constant Λ_D, i.e.

$$^{(D)}R = \frac{2D\Lambda_D}{D-2} \ . \tag{2.53}$$

The evolution does not lead to any significant growth away from homogeneity as the solution decompactifies, as expected based on the absence of the perturbative warped instability on the large volume branch.

For a negative total volume perturbation, the solution eventually settles to the small volume $dS_p \times S_q$ solution with the same conserved flux n as the initial condition. This end state has slightly smaller radius and a slightly lower Hubble parameter (as computed from eq. (2.20)) compared to the initial large volume Freund Rubin solution. In the left panel of figure 2.4, we show the Hubble parameter as a function of the proper time at the equator, defined by $d\tau = \alpha(t, \theta = \pi/2)dt$ (though here the solutions remain homogeneous and the value of θ is irrelevant), where it can be seen that the evolution smoothly connects the large and small volume solutions. A cosmological observer in four dimensions would observe a brief period of quasi-de Sitter expansion, followed by pure de Sitter evolution. In the center and right panels of figure 2.4, we plot the slow-roll parameters defined by:

$$\epsilon_{\rm sl} \equiv -\frac{1}{H^2}\frac{dH}{d\tau_{\rm eq}}, \qquad \eta_{\rm sl} \equiv \epsilon_{\rm sl} - \frac{1}{2H\epsilon_{sl}}\frac{d\epsilon_{\rm sl}}{d\tau_{\rm eq}} \ . \tag{2.54}$$

Both remain less than one over the duration of $\mathcal{N} = H_0\tau_{\rm eq} \sim 5$ e-folds. This implies that the transition from the large to the small-volume branch describes a short bout of slow-roll inflation. The evolution described here therefore serves as a toy model of inflation as driven by the volume modulus of a compactification. Solutions for other choices of the flux n are qualitatively similar.

2.4.2 Warped instability of Freund-Rubin solutions

We now move on to study perturbations that excite the warped instability of Freund-Rubin solutions on the small volume branch. Recall that the small volume solutions are stable to the total volume instability (in the four dimensional effective theory they sit at

31
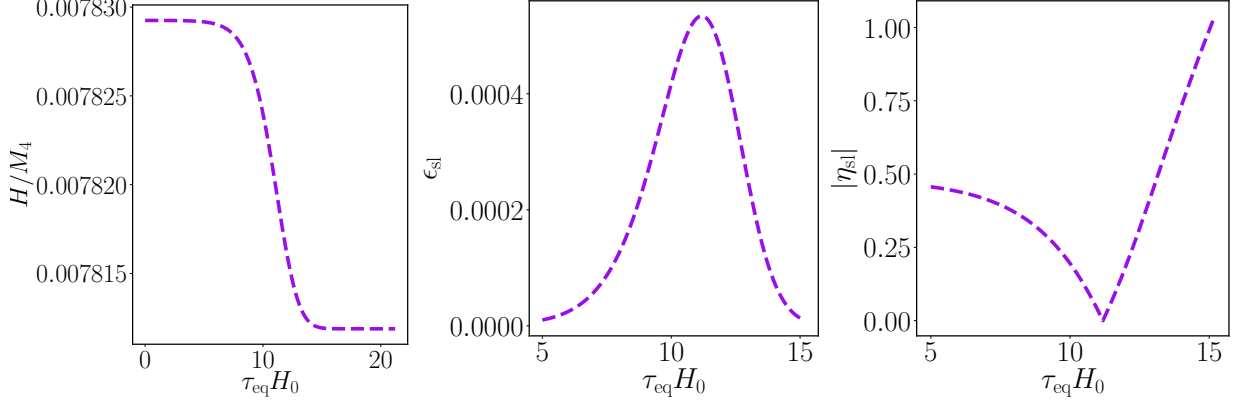
Figure 2.4: Sample solution on the large volume branch with $p = q = 4$, $\Lambda_D = 1$, $H_0/M_4 = 0.0078$ and an initial $\ell = 0$ perturbation. Left: The effective Hubble rate, H/M_4, flows to the solution with the same value of n on the small volume branch. The slow roll parameters ϵ_{sl} (middle) and η_{sl} (right) during the transition. All plots are shown as a function of proper time (in particular as measured at $\theta = \pi/2$, though here the solutions remain homogeneous).

a minimum of the effective potential), but when $q \geq 4$ they may be vulnerable to the warped instability. We focus on the case where an 8-dimensional spacetime is compactified down to four dimensions, and the internal manifold has the topology of a 4-sphere. This is an interesting scenario because, as we saw in Sec. 2.2.3, it features both a window of stability $n_c < n < n_{max}$ in the range of fluxes allowed by eqs. (2.40) and (2.44), as well as perturbatively unstable solutions for $n < n_c$. For initial conditions, we start from a small volume Freund-Rubin solution with an $\ell = 2$ perturbation; this is the only unstable mode in the linear regime.

Linearly stable solutions: $n_c < n < n_{max}$

We first explore the range of fluxes $n_c < n < n_{max}$ where the Freund-Rubin solution is linearly stable to both homogeneous and inhomogeneous perturbations. Although sufficiently small perturbations should decay, we can ask what will happen if one adds a sufficiently large homogeneous ($\ell = 0$) or inhomogeneous ($\ell = 2$) perturbation of the form given by eq. (2.37). In particular, appealing to the effective potential picture, it is not hard to imagine that the solution, originally sitting at the minimum of the potential well, will be kicked out, provided the perturbation is sufficiently large.

For large $\ell = 0$ perturbations, we expect the solution to reach the maximum of the effective potential after which it will decompactify. Indeed we find that when the size of the perturbation is such that the initial volume of the perturbed solution exceeds its large volume value it will decompactify.

In the effective potential depicted in the right panel of figure 2.2, one can think of

the potential maximum as corresponding to the stationary but unstable prolate solution on the warped branch with the same value of the conserved flux n as the small-volume Freund-Rubin solution. Adding $\ell = 2$ perturbations of increasing size, one eventually approaches a configuration close to this unstable prolate solution. Once the size of the perturbation exceeds this point, we expect the solution to become increasingly prolate. However, since the effective potential for the aspect ratio ϵ is only qualitative, we do not have a concrete prediction for the end-state. Likewise, with no stable warped solution to flow to, thermodynamic arguments are not of much help in determining the end-state. Note that we still put in an initial perturbation to the metric of the form given by eq. (2.37) (but with nonlinear corrections to the q-form through the constraints, as described in section), even as we consider large perturbations beyond the linear regime.

In figure 2.5, we show the evolution of the aspect ratio for a stable Freund-Rubin solution when perturbed with successively larger $\ell = 2$ perturbations. As expected, perturbations given by eq. (2.37) with sufficiently small h decay. However, there is a critical initial amplitude above which the solution evolves to become more and more prolate. As this threshold is approached (around $\bar{h} \sim 0.2$), the instability timescale (after a brief transient where the aspect ratio undergoes a few damped oscillations) increases—consistent with the initial condition approaching a maximum in the effective potential. Beyond the threshold, as the compactification becomes increasingly prolate, the compactified (but not uncompactified) volume rapidly decreases, as can be seen in figure 2.5. By adding higher numerical resolution, we can reach higher aspect ratios and smaller compactified volumes (which have higher magnitudes of the scalar curvature) before the evolution breaks down, but at all resolutions we see no evidence that the solution is asymptoting to some non-singular state. As we will see below, this behaviour seems to be generic for solutions where the internal space becomes prolate. Note that as the prolate solutions evolve to their ultimately singular end, the four dimensional effective theory, and the effective potential depicted in figure 2.2 eventually are no longer valid. The effective potential in the prolate direction is therefore only indicative of the general direction of evolution.

Linearly unstable solutions: $n < n_c$

We now discuss the evolution of Freund-Rubin solutions that are linearly unstable to $\ell = 2$ perturbations, which have a flux less than the critical value $n < n_c$. As illustrated in figure 2.1, and outlined in the previous sections, at each flux $n_{\text{Mink}} < n < n_c$ there exists a linearly unstable Freund-Rubin solution, as well as a corresponding linearly stable oblate warped solution with the same flux. The warped solution being thermodynamically preferred (e.g. with a higher entropy/lower Hubble parameter), these solutions are a natural candidate for the end point of the instability [224, 114]. This expectation is reflected in the effective potential for the aspect ratio sketched in the middle panel of figure 2.2. The Freund-Rubin solution is at the maximum of the effective potential, and a negative $\ell = 2$ perturbation would cause the solution to evolve towards the oblate warped solution at the potential minimum. Sampling initial conditions with a wide range of fluxes, we find that
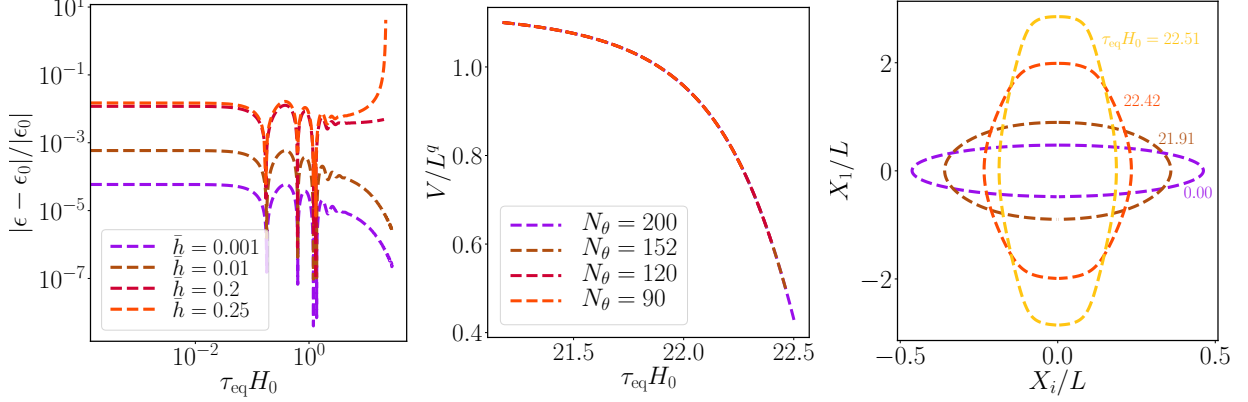
Figure 2.5: A sample solution on the small volume branch with $p = q = 4$, $\Lambda_D = 1$, $H_0/M_4 = 0.0077$ and an $\ell = 2$ perturbation. Left: The relative difference between the aspect ratio of the sample solution and the background Freund-Rubin solution for successively larger perturbations. Middle: The q-dimensional volume of the internal space for successively higher resolutions for initial data with $(\ell, \bar{h}) = (2, 0.3)$. Right: Several snapshots of the embedding of internal space for initial data with $(\ell, \bar{h}) = (2, 0.3)$.

the endpoint of the $\ell = 2$ Freund-Rubin instability (in the $-\epsilon$ direction) is in most cases the stable warped solution with corresponding flux. The notable exceptions occur in a window of flux between $n_{\text{Mink}} < n < n_I = 435.56$, where the end state is instead a crunching prolate solution. We discuss these solutions in more detail below. The confirmation of the thermodynamic arguments in previous literature, with interesting exceptions, is one of our primary results.

To explicitly verify that the endpoints of the Freund-Rubin instability are indeed the stable warped solutions, in figure 2.6 we show the volume of the compact space (left) and the aspect ratio (middle) of the numerical solutions at late times (dots) compared to the corresponding quantities for the warped solutions (dashed line) from section 2.2.4. The agreement is excellent. Note that the warped solutions have roughly the same internal volume as the symmetric solution they evolve from. In figure 2.6, we also plot the instability timescale measured from the linear regime of the numerical evolution, which grows as the flux is increased. We can understand this as follows. The Hubble parameter for the Freund-Rubin and warped solution match at n_c. Therefore, as n increases, the extrema of the effective potential in the ϵ direction merge, and the curvature at the maximum goes to zero—we therefore expect an increasing instability timescale as $n \to n_c$.

We now focus on the specific example shown in figure 2.7 to illustrate the transition between an initially unstable spherical solution and its endpoint, a stable oblate solution. In the left panel we show the entropy, which increases monotonically as expected. There are interesting step-like features in the evolution which persist at increasing resolution, and are therefore not likely to be numerical artifacts. In the middle panel we show the Hubble parameter, which decreases monotonically over the course of ~ 5 e-folds to its asymptotic
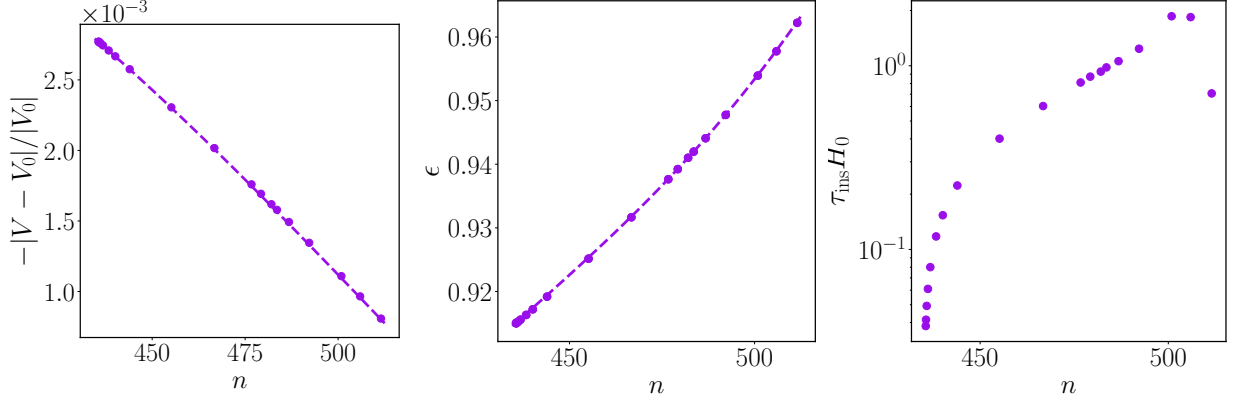
Figure 2.6: The volume (left), aspect ratio (middle) and ratio of instability timescale to e-fold period (right) of warped solutions with $n_I < n < n_c$ on the small volume branch for the special case $p = q = 4$. We find that in this regime each unstable symmetric solution evolves to an ellipsoidal solution with $\epsilon < 1$, which has roughly the same internal volume but lower effective potential. The dashed lines represent the interpolation of stationary solutions constructed as described in section 2.2.4, while the dots represent the end states of evolving a symmetric solution with an $\ell = 2$ perturbation. For the aspect ratio, the maximum of the difference is $\sim 10^{-4}$.

value. We show the embedding of the compact space in the right panel. Note that the flux is distributed on the ellipsoid the way you would expect it from the linear analysis. We found in section 2.2.3 that the unstable mode has inversely correlated flux $\bar{a}$ and shape $\bar{h}$ components, and similarly we find that whenever the radius gets larger, the flux density does too, such that, for an oblate solution, the flux is concentrated around the equator. This makes intuitive sense, as a region of larger radius implies higher curvature, and hence a larger flux density to support the region against collapse.

For the choice of flux in figure 2.7, the transition between the spherical and oblate solution occurs over the span of ~ 5 e-folds. As noted above, the instability timescale increases with n. Therefore, an interesting question is whether the transition period can persist over a larger number of e-folds. In this case, the four-dimensional effective theory includes a period of slow-roll leading to an asymptotic regime of pure de Sitter expansion [4]. In figure 2.8, we show the maximum value that the slow-roll parameter $\epsilon_{\rm sl}$ (defined in eq. 2.54) takes during the evolution (left) as well as the elapsed number of e-folds during the transition. To be more precise, we define the number of e-folds between the initial (i) Freund-Rubin and final (f) stationary warped solution as $N = \int_i^f H \, d\tau_{\rm eq}$ [5], where the time at which the slow-roll period starts (ends) is defined as when the Hubble factor differs by 10^{-4} relative to its initial (final) value (indicated by grey dashed lines in figure 2.7). We see

---

[4]Note that one is usually interested in computing the number of e-folds from a de Sitter phase to a universe with a small or zero cosmological constant, rather than to another de Sitter phase with smaller but comparable expansion rate.

[5]Note N is used to refer to the lapse in the rest of the chapter and thesis.
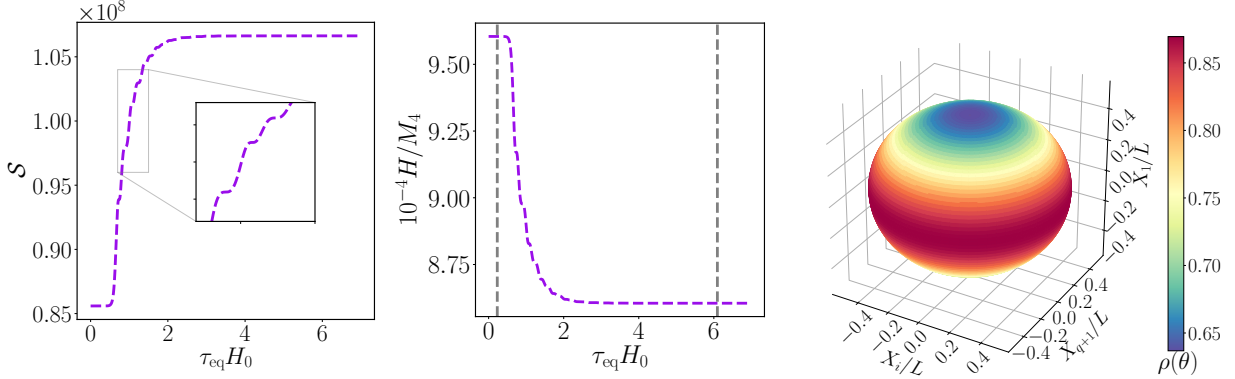
Figure 2.7: A sample solution on the small volume branch with $p = q = 4$, $\Lambda_D = 1$, $H_0/M_4 = 0.00096$, $n = 436.13$ and an initial $\ell = 2$ perturbation. Left: The effective entropy which is increasing between the two stationary solutions. Middle: The effective four-dimensional Hubble rate eq. (2.20), with grey lines indicating the approximate initial and final times of the transition period, as defined in the text. Right: The three dimensional projection of the embedding of internal space at $\tau_{\mathrm{eq}}H_0 = 8.6$. The color shows the flux density.

that it is possible to get $\sim$ 10–100 e-folds of slow-roll inflation as $n \to n_c$. We conclude that the evolution of unstable Freund-Rubin solutions provides a viable toy model for slow-roll inflation in flux compactifications. One interesting application of these solutions is to use the full higher dimensional picture to explicitly compute the effect of extra dimensions on the spectrum of linear scalar and tensor perturbations. This would make contact with phenomenology and cosmological observables such as the cosmic microwave background. We defer this and other possible explorations to future work.

So far, the linear analysis has been very good at predicting what happens in the full nonlinear case. But this is not always true. In the range of flux $n_{\mathrm{mink}} < n < n_I = 435.56$ we find that while the solution does transition to the corresponding oblate solution briefly, but does not settle there. Rather, it oscillates between the oblate and nearly spherical solution before running away to prolate values. In figure 2.9, we illustrate this behaviour for a limiting case where the external spacetime is Minkowski. There it can be seen that after a brief period where the internal space is oblate, the solution transitions to being more and more elongated, with the flux concentrating around the poles. In this case (in contrast to the prolate solutions discussed above), we find regions where the characteristics are ingoing, which allows us to excise a region around the poles and continue the evolution. We find that the spacetime curvature blows up, and the scale factor and equatorial circumference both tend to zero, consistent with a crunch.

Note that for the Minkowski spacetime, there are no oblate solutions with the same value of n, so it is not surprising that the solution goes prolate. However other solutions with $n_{\mathrm{mink}} < n < n_I$ have a solution on the oblate branch, and yet show the same behaviour as the Minkowski solution. We can understand this as follows. First, recall from

36
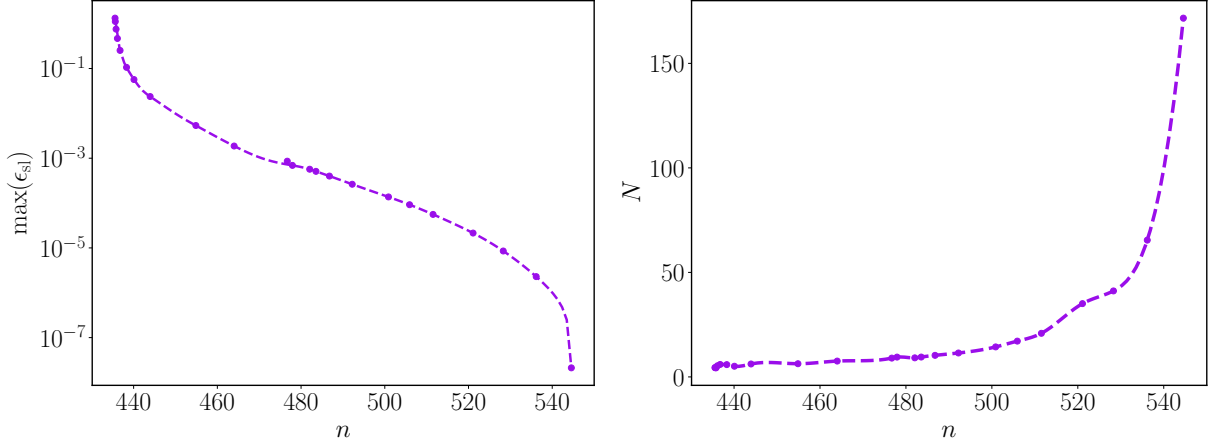
Figure 2.8: For unstable Freund-Rubin solutions with $n_I < n < n_c$ we plot the maximum value the slow-roll parameter $\epsilon_{\rm sl}$ takes during the evolution (left) and the number of e-folds of expansion in the four-dimensional effective theory elapsed during the transition to the stable warped end-point (right).

figure 2.6 that as n is decreased to approach n_I, the instability timescale decreases. Hence, in the language of the effective potential picture, the velocity approaching the minimum of potential will be larger, and there will be a greater tendency to overshoot, and, due to nonlinear effects, eventually roll back up the potential towards larger ϵ. The smaller the flux, the shorter the timescale of instability, and we observe that solutions undergo fewer oscillations about the oblate solution as the flux is decreased. The Hubble parameter decreases monotonically, passing through zero as the solutions roll back up the potential to increasing ϵ. As H goes through zero, the expanding marginally inner trapped cosmological horizon becomes infinite and disappears, and a marginally outer trapped horizon appears and begins contracting. Again, this is consistent with a crunch.

To further probe the validity of the effective potential picture, we consider perturbations around initially oblate solutions in this flux range. As shown in the right panel of figure 2.10, small perturbations decay (consistent with the linear stability), but modestly larger perturbations cause the solution to become prolate, undergoing the same fate as the corresponding initially spherical solutions. This implies the existence of a potential barrier about the oblate solutions.

Finally, we study initially prolate solutions to determine their fate. We expect that, in the range of flux where there is a corresponding solution on the small volume branch, they will undergo the same fate as the solutions that started out spherical or oblate but were kicked out the potential well. The left and middle panels of figure 2.11 show two such solutions, which indeed become extremely prolate as the equatorial radius shrinks to zero. Another interesting regime is the one with $n < n_{\rm Mink}$. As one can see from figure 2.1, these solutions do not have a Freund-Rubin solution they could have flowed from, hence they are distinct from the evolutions considered so far. The right panel of

37
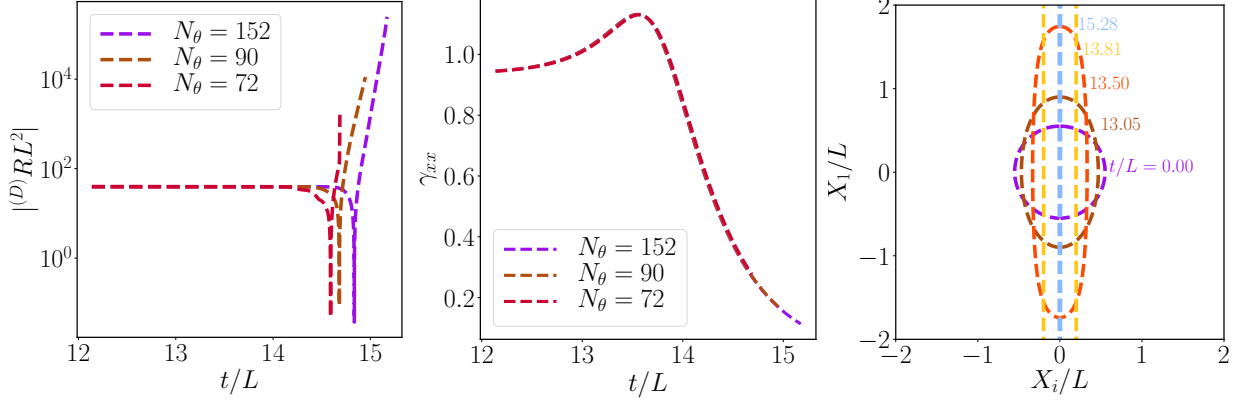
Figure 2.9: End state of solution on small volume Freund-Rubin branch with $p = q = 4$, $\Lambda_D = 1$, $n = n_{\text{Mink}}$ and an initial $\ell = 2$ perturbation for different resolutions. The D-dimensional curvature scalar which becomes negative at the end (left), scale factor at the equator (middle) and embedding of internal space (right).

figure 2.11 shows the embedding of the compact space for such a solution. Those solutions become not only very oblate but also extremely large in volume. Around the equator, the flux density approaches zero, and the expansion rate approaches that expected from the decompactified D-dimensional de Sitter solution. However, the internal space remains very inhomogeneous. We are unable to continue the evolution indefinitely, as tracking the distorted shape and differing expansion rates requires higher and higher numerical resolution. However, we do not find any singular behaviour before then. This distorted shape is qualitatively different from any of the solutions considered above.

Finally, we briefly report on higher dimensional spaces where $q \geq 5$. Exploring a few cases with $q = 5$, we find similar behaviour to the case where $q = 4$. In particular, we find a range of flux where the Freund-Rubin solution is only unstable to the total volume instability, and another where it is unstable to the warped instability only. In the latter case, we again find a range of the parameter space where the unstable solutions flow towards stable stationary oblate solutions, but outside that range the solutions will, in a similar way to the solutions shown in figure 2.9, become increasingly prolate forming trapped regions in the process and eventually crunching. However, it is important to note that for $q \geq 5$, the range of the inequalities in eqs. (2.40) and (2.44) overlap, and hence none of the Freund-Rubin solutions are stable. For future work, it would thus be interesting to see which instability dominates in this overlap region of the parameter space. Additionally, in contrast to $q = 4$, when $q \geq 5$, higher ℓ modes can be unstable, which in theory would result into further breaking of the symmetry of the compact sphere.

38
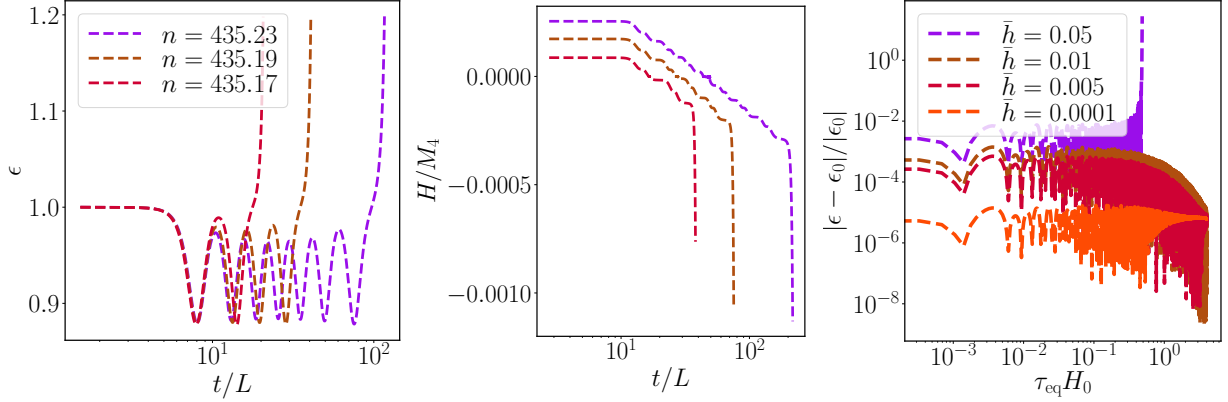
Figure 2.10: The aspect ratio (left) and effective Hubble rate (middle) for a few initially spherical solutions with $n < n_I$. The relative difference in the aspect ratio from the background value for a sample solution on the small Hubble warped branch with $p = q = 4$, $\Lambda_D = 1$ and $H_0/M_4 = 1.3 \times 10^{-5}$ and successively larger $\ell = 2$ perturbations (right).

2.5 Conclusions

Despite extensive study of the linear stability and mass spectrum of Freund-Rubin like solutions, very little is known about their nonlinear evolution and dynamical formation. In this work we have explored how such solutions might be generated and evolve. The starting point for this flux compactification scenario was the product space of a p-dimensional de Sitter space and a q-dimensional (in some cases warped) topological sphere. Provided we fix the higher dimensional constant Λ_D and the dimension of the internal manifold, the properties and stability of the p-dimensional vacua and the compact space, will depend on the number of flux units of the q-form field strength wrapping the sphere or the Hubble parameter of the extended dimensions. For each value of the conserved flux number $n < n_{\max}$ there are four solutions. Homogeneous solutions can be classified into two branches, a large volume branch, unstable to the $\ell = 0$ scalar sector and a small volume branch unstable to the $\ell = 2$ mode for $n < n_c < n_{\max}$. On the stationary warped branch one finds the so-called large Hubble branch, unstable to the $\ell = 2$ mode for $n < n_{\max}$, and the small Hubble warped branch which is stable to the $\ell = 2$ mode for $n < n_c$ but unstable for $n_c < n < n_{\max}$.

To gain some understanding of the parameter space and dynamics, we studied the evolution of initially small perturbations around those stationary solutions. We find, in agreement with previous studies that, for any dimensionality of the sphere, solutions on the large volume branch either decompactify to empty D-dimensional de Sitter space with cosmological constant Λ_D or flow to the solution on the small volume branch with the same number of flux units but a smaller volume, and hence large enough flux density to stabilize the sphere against collapse.

We show that within the regime where the small volume Freund-Rubin solution is
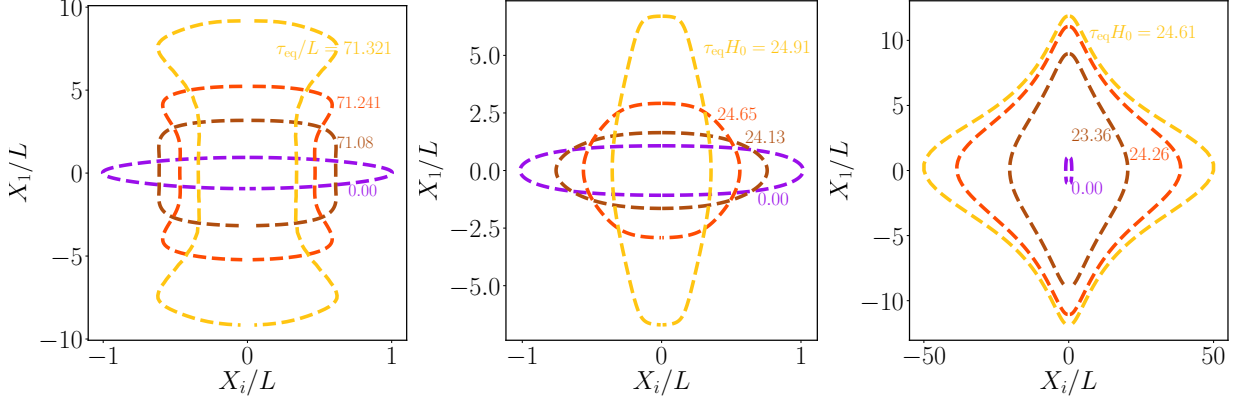
Figure 2.11: Sample solutions on the large Hubble warped branch with $p = q = 4$, $\Lambda_D = 1$, $(H_0/M_4, n) = (1.3 \times 10^{-5}, 435.23)$ (left), $(H_0/M_4, n) = (0.0077, 529.29)$ (middle) and $(H_0/M_4, n) = (0.0075, 402.11)$ (right) where recall $n_{\mathrm{Mink}} = 435.16$.

unstable to the $\ell = 2$ scalar mode, when $n_I < n < n_c$ the solutions flow to the corresponding solution on the small Hubble warped branch. The end point of the instability is a stationary oblate solution where the flux is concentrated in a band around the equator. We do not find any other instabilities and conclude this is the final endpoint of the solution, at least under our symmetry assumptions. However, for $n < n_I$, but still within the regime where the small volume Freund-Rubin branch is unstable, we find that the solution overshoots the linearly stable oblate solution, flowing towards an increasing prolate solution, where the flux concentrates at the poles of the sphere. The equator of the q-sphere is unsupported by flux, and the equatorial radius shrinks to zero size in finite time, forming trapped regions around the poles in the process. The four-dimensional spacetime undergoes a crunch.

Finally, regarding the end state of solutions on the large Hubble branch with $n < n_{\mathrm{Mink}}$, we find that the volume of the internal space grows, while the shape become increasingly oblate, but with cuspy feature at the poles. The expansion rate remains inhomogeneous, as there is no solution on the small Hubble branch with the same number of flux units.

It follows from the above that the warping of the compact space may stabilize initially unstable configurations. This spontaneous symmetry breaking of the internal space to more dynamically favoured configurations is a very natural phenomenon in cosmology. In the case of the Jeans instability, configurations with high mass density suffer from a gravitational instability. This symmetry breaking instability is ultimately cut-off by nonlinear terms leading to structure formation. Other analogous examples include the Gregory-Laflamme instability [174].

There are a number of directions in which one could expand on this study. While here we assumed that only one of the spatial degrees of freedom in the internal space were excited, it would be interesting to allow additional symmetries either in the compactified, or uncompactified dimensions, to be broken. Another possible avenue would be to study the case where the external space is anti-de Sitter, with potential applications to the AdS/CFT

40

correspondence. Here, we have focused on a simple model in order to gain insight into open questions surrounding extra dimensions and spherical compactifications. For example, there has been much debate and conjecture regarding the circumstances under which it is possible to have periods of exponential expansion in compactified scenarios [100, 275]. The general methods presented here could be used to explore this issue in scenarios that are dynamical and inhomogeneous.

Chapter 3

Starting inflation from inhomogeneous initial conditions with momentum

3.1   Introduction

As was mentioned in 1.1 cosmic inflation has been proposed as a solution to some of the fine-tuning problems of Standard Big Bang cosmology. But in order for inflation to be a successful explanation for the observed homogeneity of the universe on large scales, it should be able to arise from generic, inhomogeneous initial conditions. Inhomogeneities will not necessarily spoil inflation in models where inflation naturally begins at nearly Planckian densities, [247, 248, 249, 244, 245], though this has not be studied in detail[1]. The most recent observations of the cosmological microwave background motivate studying of the problem of initial conditions in low energy scale inflation, in which the potential energy density is much below the Planckian scale [16, 13, 244, 215, 245, 212]. Here, we focus on the effects of large inhomogeneities on the onset of inflation, both in scenarios where it occurs at nearly Planckian and sub-Planckian energy scales, using evolutions in fully nonlinear GR.

This question has been studied using tools from numerical relativity in a number of papers [237, 73, 169, 170, 168, 239, 171, 238, 117, 127, 105, 66, 104, 33, 202], complementing work evolving inhomogeneous fields on homogeneous spacetimes [17, 18, 236, 20, 135],

---

[1]The reasoning is as follows (see [244] for more details): Suppose we have a universe with Planckian density, then the sum of the kinetic, gradient and potential energy density is of the order unity in Planckian units. There are *a priori* no constraints on the value the scalar field takes in this domain, but typically one expects that this value , ϕ_p, is such that the potential energy is $2V(\phi_p) = 1$. Therefore typical conditions are such that the initial conditions correspond to $\dot{\phi}^2 \sim (\partial_i \phi)^2 \sim 2V(\phi) = \mathcal{O}(1)$. If $\dot{\phi}^2 \sim +(\partial_i \phi)^2 \lesssim 2V(\phi)$ in domain under consideration then inflation begins and the gradient and kinetic energy become much smaller than the potential energy which ensures the continuation of inflation. We will confirm this picture numerically in chapter 3.3 of this thesis.

and using analytic techniques [40, 225, 113] (see [69] for a short review on the topic). Focusing on more recent work, [127] showed that large field inflation is robust to simple inhomogeneous initial conditions even when the initial gradient energy is many orders of magnitude larger than the vacuum energy density, provided that the universe is initially expanding everywhere and that the scalar field range remains within the slow-roll regime. Reference [127] also included cases with large inhomogeneities that give rise to the formation of black holes, but showed that inflation can succeed even then. This happens because while the overdense scalar field regions collapse into black holes, the underdense regions evolve into voids that become dominated by the inflationary potential energy at later times such that inflation may begin. This line of research was then extended in two ways: [105, 33, 202, 201] expanded the classes of inflationary models under investigation and [105, 104, 202] the classes of inhomogeneities. In [105], inhomogeneities in both the scalar field profile and the extrinsic curvature were explored. In particular, the initial expansion was assumed to take the following simple form $K(\vec{x}) = -C\phi(\vec{x}) + K_0$ where $C > 0$ is a free parameter and K_0 is an integration constant and the initial velocity of scalar field was given by some constant such that the momentum constraint is trivially satisfied. In this ansatz, the initial hypersurface contains regions of local expansion and contraction. It was shown that as long as the spacetime is on average initially expanding, then inflation will occur in some patch even if other parts of the spacetime might collapse. Reference [104] investigated inhomogeneities in the transverse traceless part of the extrinsic curvature, $A_{ij}^{TT} \neq 0$, and found that these initial perturbations, roughly corresponding to gravitational radiation, initially reduce the total number of e-folds as the amplitude is increased, but that this reduction saturates and that in general the amplitude of the scalar perturbations remains the main driver of the onset of inflation. The effect of initial inhomogeneities in the scalar kinetic energy, but with constant field profile, such that the scalar momentum density was initially zero, was studied in [202].

In order to carry out such evolutions of various classes of initial conditions to determine whether they eventually lead to an exponentially expanding spacetime, one must begin with initial data that satisfies the constraint part of the Einstein equations. In practice, this requires specifying the values of various metric and matter components on the initial time slice in such a way that they satisfy the Hamiltonian and momentum constraint equations. However, all of the abovementioned studies are similar in that they rely on special choices of initial conditions that ensure the momentum constraint is trivially satisfied. The addition of momentum in the initial conditions is not only natural, but also interesting to pursue since, if the initial velocity of the inflaton were large enough, it could prevent the onset of inflation[2]. Solving the momentum constraint, in addition to the Hamiltonian constraint is highly non-trivial, not only because it requires solving three additional coupled non-linear elliptic equations, but also because it is challenging to separate freely specifiable versus constrained degrees of freedom in a manner where the underlying physical interpretation

---

[2]Note that in simulations of cosmic bubble collisions [203, 330], where inflation starts inside the bubble (some time after the initial conditions are specified), both the scalar field and its conjugate momentum are usually non-trivial.

of the free data is transparent, while also ensuring that a unique solution exists. If we over-restrict the system, no solutions to the constraint equations will exist, also known as the problem of *existence*. On the other hand, if we do not restrict the system sufficiently, there may be multiple nearby solutions, where even if the solutions are physically the same (this is not always the case, e.g. [288] for an example) our numerical solver might not converge to a single one. This so-called problem of local *uniqueness* is very relevant in cosmology [160], and has implications for how matter source terms in the momentum and Hamiltonian constraint are specified, as discussed below. In addition, a standard trick to choose which variables to set, and which to solve for, while ensuring the solution is unique, is to perform a conformal decomposition of the energy and momentum density. However, this does not extend straightforwardly to scalar fields since the energy and momentum density are functions of the scalar field and its time and spatial derivatives.

In this work, we solve both the Hamiltonian and momentum constraint equations for non-trivial inhomogeneities in the momentum density of the scalar field, considering scenarios where the time derivative of scalar field has a large homogeneous value, as well as scenarios where it has large spatial variations. We solve the equations using the conformal thin-sandwich (CTS) formalism [342], making using of the code described in [131], but without using the usual conformal rescaling of the matter terms. We find that our new scheme gives greater control over the initial conditions in the matter sector. We then study the evolution of several classes of initial conditions that have non-trivial inhomogeneities in the scalar field momentum density and have not been previously studied in the literature. We consider scenarios where the length scale of the inhomogeneities is comparable to the initial effective Hubble radius and (i) the initial scalar gradient and kinetic energy are comparable and much larger than the inflationary energy scale; (ii) the initial scalar gradient, kinetic energy, and potential energy are all comparable (as might arise in large field inflationary models where inflation begins at nearly Planckian densities); and (iii) in two-field inflationary models where the scalar fields are non-interacting. Our results for (i) are, broadly speaking, in agreement with previous analyses that assumed a vanishing initial velocity profile for scalar field. However, we also show that when the initial kinetic energy of scalar field is such that a homogeneous universe will fail to inflate, the addition of gradient energy can slow the scalar field before it reaches the end of the inflationary plateau. We attribute this to an increased initial expansion rate and non-negligible pull-back force due to the presence of gradients in the inflaton. Our results suggest that large gradients can mitigate the disruptive effect of a non-zero initial scalar velocity profile. Our results for (ii) show that in cases where the kinetic, gradient, and potential energy are all comparable, the universe will rapidly transition to exponential expansion, typically without forming collapsing regions. Finally, we extend our methods to the study of the effects of adding inhomogeneities to cosmological scenarios where the universe undergoes two stages of inflation Taken together, our results suggest inflation can arise from highly inhomogeneous conditions.

The remainder of this chapter is as follows. We discuss the inflationary models we use in section 3.2. Our approach to solving the constraint equations on the initial time slice

is outlined in section 3.2.1 and 3.2.2. We comment on the existence and uniqueness of our solutions in 3.2.3. Our numerical methods and diagnostics for evolving the Einstein equations and matter are described in section 3.2.4. Our results are presented in section 3.3, and we conclude in section 3.4. In appendix B.1, we discuss our numerical implementation in more detail, while in appendix B.2, we provide more details on the construction of our initial data.

Unlike in Chapters 1, 4 and 5, we use units with $M_P \equiv 8\pi G = c = 1$.

3.2 Theory

In this chapter, we consider inflationary theories with one or two canonical scalar fields, ϕ and θ[3], both minimally coupled to Einstein gravity, such that the action is given by

$$S = \int d^4x \ \sqrt{-g} \left(\frac{1}{2}R - g^{\mu\nu}\partial_\mu\phi\partial_\nu\phi - g^{\mu\nu}\partial_\mu\theta\partial_\nu\theta - 2V(\phi,\theta) \right) \tag{3.1}$$

where $V(\phi,\theta)$ the potential energy function. In most of the cases, we will consider single-field inflation by setting $\theta = 0$. In all cases, we assume that the scalar fields do not interact, such that $V(\phi,\theta) = V_\phi(\phi) + V_\theta(\theta)$. The Einstein equations that follow from the action (3.1), are then given by (1.1) where the stress-energy tensor is

$$T_{\mu\nu} = T_{\mu\nu}^{(\phi)} + T_{\mu\nu}^{(\theta)} \tag{3.2}$$

with

$$T_{\mu\nu}^{(\phi)} = g_{\mu\nu}\left[-\partial_\alpha\phi\partial^\alpha\phi - 2V_\phi(\phi)\right] + 2\partial_\mu\phi\partial_\nu\phi \ , \tag{3.3}$$

and similarly for θ. The equation of motion for each individual field is then

$$\Box\phi = V_\phi', \quad \Box\theta = V_\theta' \tag{3.4}$$

where $'$ is used to denote the partial derivative with respect to corresponding scalar field. In general, each field will undergo inflation when its potential energy density is greater than the sum of its kinetic and gradient energy density. Assuming the universe is spatially homogeneous, ϕ will undergo inflation if $V_\phi > 0$ and the slow-roll parameters satisfy:

$$\epsilon_v = \left(\frac{V_\phi'}{2V_\phi}\right)^2 \ll 1, \quad \eta_v = \frac{1}{2}\left|\frac{V_\phi''}{V_\phi}\right| \ll 1, \tag{3.5}$$

in which case the field is slowly rolling. The condition $\epsilon_v \ll 1$ implies that the potential energy density driving inflation is roughly constant, $\rho_{V_\phi} \equiv 2V_\phi \approx$ const., while $\eta_v \ll 1$ ensures that inflation persists for a number of e-folds.

---

[3]Note that θ was used to refer to the polar angle on q-sphere in chapter 2

3.2.1 Initial conditions: metric

We wish to specify initial data on a spacelike hypersurface Σ_t parameterized by t that is consistent with the Einstein equations. We formulate the problem using the Arnowitt-Deser-Misner (ADM) formalism, and decompose the metric into a spatial metric γ_{ij}, lapse N, and shift vector β^i as

$$ds^2 = -N^2 dt^2 + \gamma_{ij}(dx^i + \beta^i dt)(dx^j + \beta^j dt) \; , \tag{3.6}$$

and write the extrinsic curvature as

$$K_{ij} = -\frac{1}{2}\mathcal{L}_{\vec{n}}\gamma_{ij} \; , \tag{3.7}$$

where the Lie derivative $\mathcal{L}$ is taken with respect to the timelike unit normal to slices of constant coordinate time $n^\mu = (1/N, -\beta^i/N)$. The initial data for the metric and matter sector cannot be freely and independently specified, but must satisfy the momentum and Hamiltonian constraint equations

$$^{(3)}R + K^2 - K^{ij}K_{ij} = 2\,\rho \; , \tag{3.8}$$

$$D_j K^{ij} - D^i K = p^i \; , \tag{3.9}$$

where $K = \gamma^{ij}K_{ij}$, $^{(3)}R$, and D_i are, respectively, the extrinsic curvature scalar, Ricci scalar, and covariant derivative associated with γ_{ij}, $\rho \equiv n^\mu n^\nu T_{\mu\nu}$ is the energy density, and $p^i \equiv -\gamma^{i\mu}n^\nu T_{\mu\nu}$ is the momentum density as measured by an Eulerian observer with four-velocity n^μ.

In the 3+1 decomposition, initial data for the Einstein and matter equations are then a set of 20 functions representing N, β^i, γ_{ij}, K_{ij}, ρ, and p^i on the initial time slice that together satisfy the constraint equations.

We use a modified version of the CTS method [342], implemented in [131], as a prescription to separate freely specifiable from constrained degrees of freedom in such a way that the underlying physical interpretation of the free data is transparent. We outline the key features below, and refer the reader to [131] for more details. In the CTS formalism, the approach is to perform a conformal decomposition of the spatial metric and extrinsic curvature in order to introduce quantities that can be specified in a more well-motivated way. Introducing the conformal factor Ψ, we can define a number of conformal quantities as

$$\tilde{\gamma}_{ij} \;\equiv\; \Psi^{-4}\gamma_{ij} \tag{3.10}$$

$$\hat{A}^{ij} \;\equiv\; \Psi^{10}\left(K^{ij} - \frac{1}{3}K\gamma^{ij}\right)$$

$$\;=\; \frac{1}{2\tilde{N}}\left[\dot{\tilde{\gamma}}^{ij} + (\mathbb{L}\beta)^{ij}\right] \tag{3.11}$$

where the time-derivative of the conformal metric $\dot{\tilde{\gamma}}^{ij} \equiv \Psi^4 \left(\dot{\gamma}^{ij} - \frac{1}{3}\gamma^{ij}\gamma_{kl}\dot{\gamma}^{kl} \right)$ is traceless by construction. The conformal lapse $\tilde{N}$ is related to the lapse by $\tilde{N} \equiv \Psi^{-6}N$, while $\tilde{R}$ and $\tilde{D}$ are the Ricci scalar and covariant derivative with respect to $\tilde{\gamma}_{ij}$, and $\mathbb{L}$ is the corresponding conformal Killing operator, defined by

$$(\mathbb{L}\beta)^{ij} \equiv \tilde{D}^i\beta^j + \tilde{D}^j\beta^i - \frac{2}{3}\tilde{\gamma}^{ij}\tilde{D}_k\beta^k \ . \tag{3.12}$$

With these definitions, the constraint equations become an elliptic condition for Ψ, and three elliptic equations for β^i:

$$\tilde{D}_i\tilde{D}^i\Psi - \frac{1}{8}\tilde{R}\Psi + \frac{1}{8}\hat{A}_{ij}\hat{A}^{ij}\Psi^{-7} - \frac{1}{12}K^2\Psi^5 + \frac{1}{4}\rho\Psi^5 = 0, \tag{3.13}$$

$$\tilde{D}_j\hat{A}^{ij} - \frac{2}{3}\Psi^6\tilde{D}^iK - \Psi^{10}p^i = 0 \ . \tag{3.14}$$

In the CTS formalism, one then usually proceeds by specifying initial data for the free data

$$\tilde{\gamma}_{ij}, \quad \dot{\tilde{\gamma}}_{ij}, \quad K, \quad \tilde{N}, \quad \rho, \quad p^i \tag{3.15}$$

(or some conformally rescaled version of ρ and p^i), and solving the four elliptic equations for the shift β^i and conformal factor Ψ. We emphasize that in the CTS method, one is in principle free to choose any values for the free data for which a solution can be found. We now outline and motivate our choice of free data for the case of inhomogeneous conditions in an initially expanding universe filled with two (unless otherwise stated) scalar fields and periodic boundary conditions [4].

For simplicity, we choose the spatial metric on the initial time slice to be conformally flat, $\gamma_{ij} \equiv \Psi^4\tilde{\gamma}_{ij} = \Psi^4\delta_{ij}$, $\tilde{N} = 1$, and set the trace of the extrinsic curvature K to be constant, while the transverse-traceless part $\dot{\tilde{\gamma}}^{ij}$ is set to zero (loosely this is equivalent to setting the gravitational wave background to zero). In principle, K is a free parameter, representing a uniform expansion rate across the initial hypersurface. However, we also have to satisfy an integrability condition for the Hamiltonian constraint

$$\mathcal{I}_\mathcal{H} \equiv \int \left(\tilde{D}_i\tilde{D}^i\Psi - \frac{1}{8}\tilde{R}\Psi + \frac{1}{8}\hat{A}_{ij}\hat{A}^{ij}\Psi^{-7} - \frac{1}{12}K^2\Psi^5 + \frac{1}{4}\rho\Psi^5 \right) dV = 0 \ . \tag{3.16}$$

For a periodic domain, if we approximate the conformal factor to be roughly unity, this requires $K^2/3$ to be close to the initial energy density averaged over the initial hypersurface. For two scalar fields, this reduces to

$$K = -\left[\frac{3}{\text{Vol}} \int \left((\partial_t\phi)^2 + \tilde{\gamma}^{ij}\partial_i\phi\partial_j\phi + 2V_\phi(\phi) + (\partial_t\theta)^2 + \tilde{\gamma}^{ij}\partial_i\theta\partial_j\theta + 2V_\theta(\theta) \right) dV \right]^{1/2} \tag{3.17}$$

---

[4]Our simulation domain is periodic with coordinate length L[5], the largest wavelength of the perturbations in the scalar field, in each direction. This can either be seen as a convenient boundary condition for an infinite universe, or in scenarios where inflation starts slightly below Planckian densities, as describing a universe with toroidal topology.

where ϕ and θ are the values of scalar fields on the initial time slice and $\partial_t\phi$ and $\partial_t\theta$ are specified up to some conformal factor. The minus sign gives us an initially uniformly expanding universe with Hubble parameter $H_0 = -K/3$ (a positive K would imply a contracting universe). In the special case of a homogeneous scalar field profile, this choice of initial data gives a Friedman-Lemaitre-Robertson-Walker (FLRW) solution.

We now describe the choice of free data in the matter sector. We will restrict the discussion to a single field, say ϕ, but keep in mind that the same definitions and assumptions apply to the other field θ.

3.2.2   Initial conditions: matter

In the case of a scalar field, the quantities to be specified on the three dimensional spatial hypersurface are the scalar field ϕ and its time derivative $\partial_t\phi$. We thus rewrite the energy density at some time and any point in the hypersurface as the sum of the kinetic, gradient, and potential energy densities,

$$\rho = \eta^2 + \gamma^{ij}\partial_i\phi\partial_j\phi + 2V_\phi(\phi) \tag{3.18}$$

and the momentum density as

$$p^i = -2\,\eta\,\gamma^{ij}\partial_j\phi \tag{3.19}$$

where η is the conjugate momentum [6] defined by

$$\eta \equiv n^\mu\nabla_\mu\phi = \frac{1}{N}\left(\partial_t\phi - \beta^i\partial_i\phi\right). \tag{3.20}$$

Clearly, the technical challenge here is to choose which quantities to specify in such a way that not only does a unique solution exist, but also such that the values for the quantities can be physically motivated. The fundamental quantities we freely specify are the initial scalar field profile and a non-trivial velocity profile defined below. We comment on the existence and uniqueness of our solutions in section 3.2.3. The inhomogeneous initial conditions for the scalar field profile are chosen to be such that on the initial time slice,

$$\phi(t=0,\vec{x}) = \phi_0 + \delta\phi_x\sin(kx) + \delta\phi_y\sin(ky) + \delta\phi_z\sin(kz) \tag{3.21}$$

where $\vec{x} = (x,y,z)$ is the spatial coordinate of hypersurface labelled by the time coordinate t, $k = 2\pi/L$ is the wavenumber and $\vec{\delta\phi} = (\delta\phi_x, \delta\phi_y, \delta\phi_z)$ is a measure of the amplitude of the initial inhomogeneities which in general can be different in each direction, but we will only consider $\delta\phi = \delta\phi_x = \delta\phi_y = \delta\phi_z$. The maximum total amplitude of the fluctuations about ϕ_0 is then $\Delta\phi = \sqrt{\delta\phi_x^2 + \delta\phi_y^2 + \delta\phi_z^2} = \sqrt{3}\delta\phi$. For simplicity, we do not consider different amplitudes in the different spatial directions, or additional scalar field variations

---

[6]The conjugate momentum can be interpreted as the velocity of scalar field as seen by a fiducial observer whose worldline is orthogonal to the constant time hypersurfaces Σ_t, i.e., an observer with four-velocity n^μ.

at smaller wavelengths. In [127], including these was found not to qualitatively affect the results. We fix the (coordinate) length of the simulation domain in each direction to be equal to the wavelength L, and consider various ratios of this lengthscale to the initial Hubble scale (including gradient and all other energy contributions). The initial conditions of the scalar field depend on the amplitude of the inhomogeneities $\delta\phi$ and the potential $V(\phi_0)$ which sets the background inflationary Hubble scale.

We explore the effects of inhomogeneities on both single-field and two-field inflationary models. When studying single-field inflation, we consider two types of inflationary potentials, both of which are large field models, i.e., the inflaton needs to traverse a super-Planckian range in field space for there to be a sufficient period of inflation. The first potential we consider is a simple quadratic potential,

$$V(\phi) = m^2\phi^2 \ . \tag{3.22}$$

Although strongly disfavored by the most recent observations [16, 13], we do not expect our conclusions to be dependent on the shape of the potential, since the key feature is the flatness of potential and super-Planckian distance in field space to the minimum of potential (see [33] for a study of the effects of the potential shape on inhomogeneous inflation). To confirm this, we do, however, also look at the T-shaped potential,

$$V(\phi) = 3m^2\alpha \tanh^2\left(\frac{\phi}{\sqrt{6\alpha}}\right) \tag{3.23}$$

describing a class of so-called α-attractors, motivated by supergravity and string theory [211, 214] and consistent with the most recent BICEP/KECK data [212]. The two-field model we will consider is given by

$$V(\phi,\theta) = M^2\phi^2 + 3m^2\alpha \tanh^2\left(\frac{\theta}{\sqrt{6\alpha}}\right) \tag{3.24}$$

where $M \gg m$. Here, inflation can start at $M^2\phi^2 = O(1)$ if all gradient and kinetic terms are much smaller than $V_\phi(\phi)$ [245]. When the period of inflation driven by ϕ ends, a second stage of inflation driven by θ begins. Our choice of two-field model is motivated by the recently proposed α-attractor generalization [213, 68] of the hybrid inflation scenario [250]. Although this scenario describes an inflaton field θ, interacting with a Higgs-type field ϕ, one can show that the fields become decoupled in the large field limit, in which case the inflationary model reduces to the two-field model studied here.

Going back to the initial conditions on the velocity profile the scalar field, we find three distinct ways of specifying well motivated initial data, which we now describe.

1. *Uniform initial time derivative of scalar field.*
   The first method is to specify the time derivative of the scalar field, which for simplicity we assume to be constant on the numerical domain

$$\partial_t\phi(t=0,\vec{x}) = \omega\delta\phi \tag{3.25}$$

where $\delta\phi \sim O(1)$. The sign of the parameter ω determines whether the scalar field moves up or down the inflationary potential. In particular, when $\omega < 0$, the field is driven towards the minimum of the inflationary potential, which could cause an early end to inflation. We will thus give particular attention to this scenario.

We emphasize that, although the time derivative of the scalar field is constant, after the Hamiltonian and momentum constraints are solved for Ψ and β^i, the reconstructed physical energy and momentum density are inhomogeneous. While the reconstruction of the physical energy densities is unambiguous, the lack of ability to specify a particular configuration for ρ and its individual components is inconvenient. This motivates another way of specifying initial data.

2. *Spatially varying conjugate momentum: conformal rescaling.*
   Here, the trick is to specify a rescaled conjugate momentum, defined as

$$\tilde{\eta} = \Psi^2 \eta. \tag{3.26}$$

This ensures that if the conformal gradient energy, $\tilde{\gamma}^{ij}\partial_i\phi\partial_j\phi$ and kinetic energy $\tilde{\eta}^2$ have a chosen ratio, then so will the physically reconstructed quantities following the solution of the constraints. In other words, the ratio of the initial kinetic and gradient energies is not modified by solving for the shift and conformal factor in CTS formalism. The ansatz for $\tilde{\eta}$ is chosen to be spatially varying, although with fixed negative sign on the entire domain

$$\tilde{\eta} = -k\delta\phi\sqrt{\cos^2(kx) + \cos^2(ky) + \cos^2(kz)}. \tag{3.27}$$

such that the scalar field initially moves down the inflationary potential. We note that this initial data breaks the symmetry of the energy density about the origin.

3. *Spatially varying conjugate momentum: analytical solution.*
   Finally, instead of solving the momentum and Hamiltonian constraints using the CTS formalism, a third approach is to, following [159, 336], choose initial data such that the momentum constraint is analytically satisfied. We then use the Hamiltonian constraint to solve for the conformal factor. We outline the main assumptions of this construction here, and refer the reader to appendix B.2 for more details.

The initial data for the spatial metric and extrinsic curvature scalar is specified the same way as above, but the lapse and shift are chosen to be $N = 1$ and $\beta^i = 0$. The initial data for the scalar field profile is obtained by specifying $\phi(t = 0, \vec{x})$ according to (3.29) below, and the conjugate momentum by specifying

$$\hat{\eta} = \Psi^6 \eta = \Psi^6 \partial_t \phi \tag{3.28}$$

where it is important to note that $\hat{\eta}$ has a different scaling with the conformal factor from $\tilde{\eta}$ introduced above (3.28) and that the last step assumes $N = 1$ and $\beta^i = 0$.

Given those assumptions, the momentum constraint is then solved by the following ansatz

$$\hat{\eta}(x) \;=\; \frac{1}{\sqrt{2}} \left[\hat{\eta}_0 + \delta\hat{\eta}_x \cos(kx) + \delta\hat{\eta}_y \cos(ky) + \delta\hat{\eta}_z \cos(kz) \right], \qquad (3.29)$$

$$\phi(x) \;=\; \frac{1}{\sqrt{2}} \left[\hat{\phi}_0 + \delta\hat{\phi}_x \cos(kx) + \delta\hat{\phi}_y \cos(ky) + \delta\hat{\phi}_z \cos(kz) \right] \qquad (3.30)$$

and a particular solution for $\hat{A}^{ij}$ given in eqn. (B.4). This allows the reconstructed $\partial_t \phi(t = 0, \vec{x})$ to take both positive and negative values in the domain. For this study, we will further assume $\delta\hat{\eta} = \delta\hat{\eta}_x = \delta\hat{\eta}_y = \delta\hat{\eta}_z$ and $\delta\hat{\phi} = \delta\hat{\phi}_x = \delta\hat{\phi}_y = \delta\hat{\phi}_z$.

Figure 3.1 shows two-dimensional spatial slices of the scalar field and time derivative of scalar field which we typically evolve .
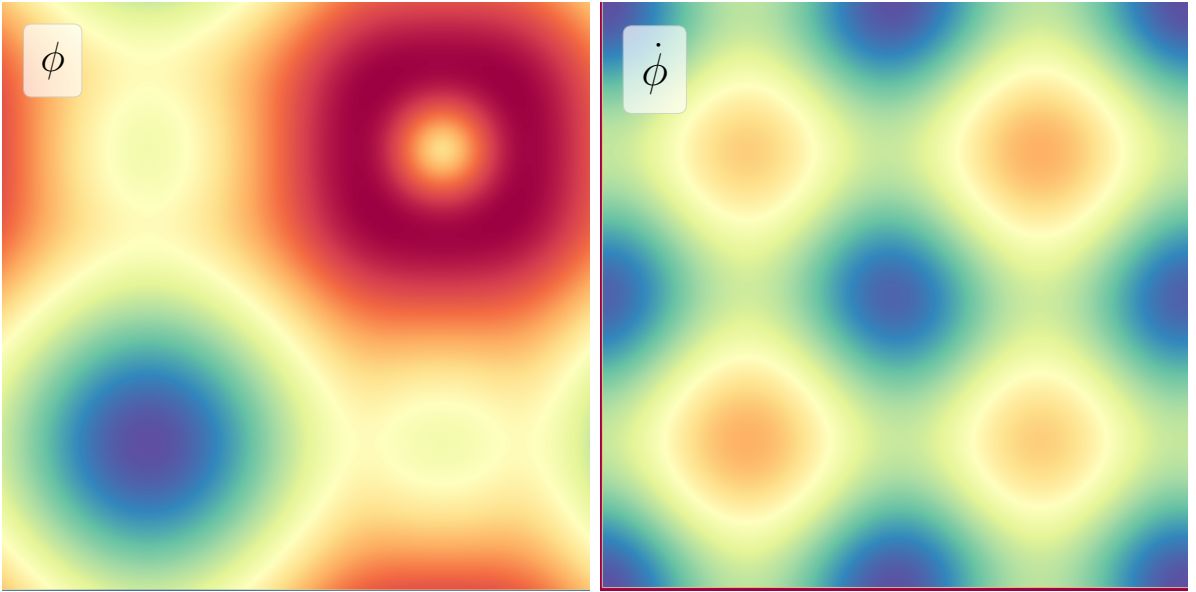
Figure 3.1: Two-dimensional spatial slices showing the scalar field and its time derivative on the initial timeslice.

3.2.3 Local uniqueness and existence

We now briefly discuss how the different ways of specifying scalar field initial data relate to considerations of how the Hamiltonian and momentum constraint couple, and issues of local uniqueness.[7] First, we recall the more familiar case with fluid matter initial data, in

---

[7]We do not go into any detail here. See, e.g, [269, 316, 331, 42] for reviews on the uniqueness of constraint equations.

order to compare and contrast to the scalar field case. In the former, where the stress tensor is an algebraic function of the fluid variables, one typically specifies a conformal energy density $\tilde{\rho} \equiv \Psi^n \rho$ and a conformal momentum density $\tilde{p}^i \equiv \Psi^{10} p^i$. For the energy density, a value $n > 5$ is chosen based on uniqueness considerations, which we discuss below, while the exponent of the conformal momentum density is chosen to remove the Ψ dependence in the momentum equation (3.14) [342]. In the special case where K is chosen to be constant, the momentum constraint then becomes independent of Ψ, and the constraint equations decouple in the sense that one can first solve the momentum constraint for β^i, and then using the solution for β^i, solve the Hamiltonian constraint for the conformal factor.

In contrast, in the scalar field case matters are complicated by the fact that the energy and momentum depend on the gradient of the scalar field. As can be seen from eq. (3.18), specifying a conformal energy density would involve solving an additional nonlinear partial differential equation to determine the scalar field, and we are typically interested in specifying the initial scalar field profile as the quantity of physical interest anyway. However, noting that $\tilde{p}^i = -2\Psi^6 \eta \tilde{\gamma}^{ij} \partial_j \phi$ is fixed by choosing ϕ (and hence $\partial_j \phi$) and say $\hat{\eta} \equiv \eta \Psi^6$ at $t = 0$, then this choice of scalar field initial data achieves the same outcome as above, and (since we always choose K to be constant here) the momentum constraint decouples from the Hamiltonian constraint. This is the case considered above when constructing initial data such that the momentum constraints are analytically satisfied (3.28), and is also the case where there are uniqueness results in the mathematical literature for a scalar field on a compact manifold [97]. As discussed in Ref. [160], issues with the non-uniqueness of the momentum constraint can arise in this case when the kernel of the operator $\partial_j \mathbb{L}$ is non-trivial, which occurs with typical choices of initial data (e.g. a conformally flat metric). These are side-stepped with the analytical solution used here. Fixing $\partial_t \phi$, as in eq. (3.28), also removes the dependence of the momentum constraint on Ψ, since $\Psi^6 \eta = \left(\partial_t \phi + \beta^i \partial_i \phi \right) / \tilde{N}$. However, it introduces an extra term involving β^i, so that the previous analyses do not directly apply. For the conformal rescaling (3.26) that fixes the ratio of kinetic to gradient energy, the momentum constraint does not decouple and, again, previous analyses do not apply.

Finally, we consider the local uniqueness of the Hamiltonian constraint. For simplicity, we will ignore the momentum constraint and restrict to the choices for the metric free data discussed in Sec. 3.2.1 (e.g. conformally flat, and so on). Say we have some solution Ψ_0 to the CTS form of the Hamiltonian constraint (3.13), and we are interested in nearby solutions $\Psi = \Psi_0 + u$ where u is small compared to Ψ_0. Linearizing, we have

$$\left[\tilde{D}_i \tilde{D}^i - q(\vec{x}) \right] u = 0 \tag{3.31}$$

where, in terms of the functional derivative of the kinetic energy term,

$$q(\vec{x}) = \frac{7}{8} \Psi_0^{-8} (\mathbb{L}\beta)_{ij} (\mathbb{L}\beta)^{ij} + \frac{5}{12} \Psi_0^4 K^2 - \frac{5}{4} \Psi_0^4 (2 V_\phi) - \frac{1}{4} \tilde{\gamma}^{ij} \partial_i \phi \partial_j \phi - \frac{1}{4} \left. \frac{\delta(\eta^2 \Psi^5)}{\delta \Psi} \right|_{\Psi = \Psi_0} . \tag{3.32}$$

If $q(\vec{x}) > 0$, then, using the maximum principle, one can show that $u = 0$ everywhere, and Ψ_0 is (locally) unique [96, 98]. For the case of fluid matter mentioned above, the choice of

$\tilde{\rho}$ is motivated by ensuring that $\tilde{\rho}$ makes a positive contribution to q. In the scalar case, clearly, this will not be true in general. When fixing $\hat{\eta}$ or $\partial_t \phi$, the functional derivative term in eq. (3.32) becomes $7\Psi_0^{-8}\hat{\eta}^2/4$, and hence makes a positive contribution to q. When specifying $\tilde{\eta}$, the contribution is $-\tilde{\eta}^2/4$, and hence negative (as noted above, in this case the momentum constraint does not decouple as well). In either case, for the parameters considered here, we find that $q(\vec{x}) > 0$. In part, this can be attributed to our choice of K through eq. (3.17). A sufficient condition for $q > 0$ is that

$$\langle 2V_\phi + \tilde{\gamma}^{ij}\partial_i\phi\partial_j\phi + \hat{\eta}^2 \rangle \gtrsim \left(2V_\phi + \frac{1}{5}\gamma^{ij}\partial_i\phi\partial_j\phi - \frac{7}{5}\eta^2 \right) \tag{3.33}$$

when fixing $\hat{\eta}$ or $\partial_t \phi$, where here $\langle \ldots \rangle$ denotes the coordinate volume average. When fixing $\tilde{\eta}$ instead, the last term becomes $+\eta^2/5$. In all the cases we consider in this study, we find $\Psi_0 \sim 1$, and the gradient and kinetic energy terms, which appear with smaller prefactor on the right-hand side of (3.33) compared to the left-hand side, are approximately equal in magnitude, and either larger, or approximately equal, to the scalar potential energy term. This argument can also be straight-forwardly extend to multiple non-interacting scalar fields, in which case the kinetic, gradient and potential energy densities in (3.33) would simply be the sum of energy densities of individual fields.

Though the above discussion provides some motivation and guidance, in the end there is no mathematical result guaranteeing the existence and uniqueness of solutions to the constraint equations for all the cases we consider. However, the important thing for the purposes of this study is that we find we are able to numerically construct convergent solutions. In fact, there are several examples in the literature where the constraint equations have been solved without issue when it was known that more than one solution exists [343, 173, 340, 288, 45].

3.2.4 Numerical implementation

We construct initial data satisfying the constraint equations by numerically solving the CTS equations, discretized with second-order accurate finite differences, using a multigrid algorithm. Details can be found in [131]. We then evolve the Einstein equations in the generalized harmonic formulation using the code described in [292, 130], and assuming periodic boundary conditions. See appendix B.1 for more details on our numerical methods. In order to characterize our results we make use of the following diagnostic quantities. We compute the total and individual energy densities defined according to (3.18). We define a fiducial local Hubble expansion rate

$$H_K \equiv -\frac{K}{3} \tag{3.34}$$

which allows us to compute the corresponding local number of e-folds of expansion $\mathcal{N}$ as

$$\mathcal{N} \equiv \int H_K d\tau , \tag{3.35}$$

where the integration is along the integral curve of n^μ, and τ is the proper time given by the lapse through $d\tau = Ndt$ (see [336, 127]). Note that in a homogeneous (i.e. FLRW) spacetime this quantity is related to the initial and final scale factor as $\mathcal{N} = \int H d\tau = \log(a/a_0)$.

The average of a quantity over the spatial volume is denoted by

$$\langle X \rangle \equiv \frac{\int d^3x \sqrt{\gamma} X}{\int d^3x \sqrt{\gamma}} \tag{3.36}$$

where $\gamma = \det \gamma_{ij}$.

In some cases (in particular, for smaller values of k/H_0), there is prompt gravitational collapse in some regions and black holes form. To characterize the boundaries of black holes in our dynamical setting, we use the concept of an apparent horizon, defined as the outermost marginally outer trapped surface. We excise a region interior to the black hole from the computational domain, and do not evolve the equations there (see appendix B.1 for more details on the implementation). From the area of the apparent horizon $\mathcal{A}$ we define the irreducible mass, $M_{\mathrm{irr}} = \sqrt{\mathcal{A}/16\pi}$. We find that the angular momentum of the black holes is negligible, and hence the irreducible mass closely approximates the Christodoulou mass. We characterize the parameters we choose for the background cosmological solutions (to which we add large inhomogeneities) by computing the power spectrum of scalar fluctuations, which restoring Planckian units and assuming slow-roll inflation are given by

$$\Delta_{\mathcal{R}}{}^2 = \frac{1}{8\pi^2} \frac{H^2}{M_P{}^2} \frac{1}{\epsilon_V} \ , \tag{3.37}$$

We also quote the scalar spectral index and the tensor-to-scalar ratio (of background solution), which in the slow-roll approximation are given by

$$n_s - 1 = 2\eta_V - 6\epsilon_V, \quad r_{ts} = 16\epsilon_V \ . \tag{3.38}$$

Note that these definitions no longer apply in the non-perturbative, highly non-linear regime we consider.

3.3 Results

We examine the conditions under which an initially expanding universe, with either a single scalar field, or two non-interacting scalar fields (see section 3.2), transitions to exponential expansion. We construct initial data using the approach described in sections 3.2.1-3.2.2.

We study two regimes of interest, distinguished by the energy scale at which inflation takes place. We first consider single-field inflationary models where the universe is initially dominated by the gradient and kinetic energy of scalar field, $\eta^2 \sim \gamma^{ij}\partial_i\phi\partial_j\phi \sim 10^3 V(\phi_0)$, in which case the initial expansion rate is large compared to the inflationary Hubble rate

(we refer to this as "low energy" or sub-Planckian inflation, see section 3.3.1). We find that one or more (depending on the symmetry of the total energy density on the initial time slice) regions of the domain undergo gravitational collapse, leading to the formation of black holes. Ignoring the interior of the black hole(s), the spacetime is still expanding on average, and we find that, independently of the type of initial data, the gradient and kinetic energy dilute away until the numerical domain becomes dominated by inflationary energy.

We also explore inflationary models where the amount of kinetic, gradient, and potential energy are all comparable on the initial time slice, and their sum is order unity in units of the wavelength of the initial homogeneities (which is also comparable to the initial Hubble radius) $\rho L^2 \lesssim O(1)$ (see section 3.3.2). Here, we refer to this scenario as high energy, or nearly Planckian energy inflation, though, of course, our analysis is entirely classical and ignores quantum effects. We first consider single-field inflationary models, where we find that the solution quickly transitions to exponential expansion. Independently of the way initial data is constructed, the late-time evolution always consists of an exponentially expanding universe with a rapidly decreasing gradient energy and kinetic energy that asymptotes to its corresponding slow-roll value. We then extend our study to a two-field inflationary model where the energy content is such that the first stage of inflation may start at nearly Planckian energies, while the second phase will occur at sub-Planckian energies. For technical reasons discussed below, we are not able to evolve this scenario past the first stage of inflation. However, already at this stage we find large patches where gradients have become negligible and the spacetime is well described by a homogeneous evolution set by the local inflaton values. Extrapolating thusly indicates that these regions should undergo a prolonged period of inflation driven by the second field.

In the following, we quantify our results using the methods described in section 3.2.4, by computing, for instance, the ratio of kinetic and gradient energy to the potential energy. In all the cases we study, we consider perturbations such that the ratio of the wavenumber of the initial scalar field content to the expansion rate on the initial time slice k/H_0 is of the order of one, meaning our simulations probe the strong-field regime. As here we focus on models of large-field inflation, where ϕ_0 is large in Planckian units, and consider fluctuations of the the inflaton that are of order one, we note that we do not consider scenarios where the perturbations around the average scalar field value that exceed the distance in field space to the end of inflationary plateau. Previous studies [127, 105, 33] have found that inflation can fail to happen in such scenarios, depending on the potential.

3.3.1 Low energy inflation

We first consider solutions where the potential energy density is initially subdominant. To begin with, we describe an illustrative case where the time derivative of the scalar field is uniform on the initial time slice, i.e. given by eq. (3.25). We choose the potential to be given by an α-attractor potential eq. (3.23) with $\phi_0 = 3.1$, such that, in the absence

of inhomogeneities ($\delta\phi = 0$), and if the time derivative of the scalar field were zero, the combination of parameters (ϕ_0, m, α) would result in 60 e-folds of inflation, a scalar power spectrum of $\Delta_\mathcal{R}^2 \sim O(1)$, a scalar spectral index of $n_s = 0.97$, and a tensor-to-scalar ratio of $r_{ts} = 0.001$ for modes that cross the horizon 60 e-folds before the end of inflation. However, we pick an initial value of $\partial_t\phi$ such that, in a homogeneous Universe, the scalar field would evolve off the plateau of the inflationary potential without inflation occurring. The gradient and kinetic energy are chosen to be comparable on the initial time slice, but 800 times larger than the potential energy density. Figure 3.2 shows the individual volume-averaged energy densities (left panel) as a function of the effective scale factor $a = \exp(\langle\mathcal{N}\rangle)$. We also plot the kinetic $\dot\phi^2_{\mathrm{FLRW}}$ and potential energy $\rho_{\mathrm{V}_\phi,\mathrm{FLRW}}$ densities when solving the homogeneous FLRW equations in the absence of gradient energy and specifying the initial value of $\dot\phi_{\mathrm{FLRW}}$ to be the time derivative of the scalar field on the initial time slice given by eq. (3.25).

We find that in some regions, the maximum energy density quickly increases and black holes form (at the times indicated by the grey shaded areas in figure 3.2). As was pointed out in previous studies [127, 105], the formation of black holes can be motivated using the hoop conjecture [326]. Indeed, the hoop conjecture predicts that, if the mass of an overdensity exceeds the mass of a black hole of the same size, then the overdensity will collapse to a black hole. Following this argument, one can expect black holes to form when $\frac{4}{3}\pi k^{-3}\rho \sim k^{-1}/2$ which is equivalent to $k/H_0 \sim 1$, or $\delta\phi \sim 1$ in Planck units. Here, since the total energy density on the initial time slice is symmetric with respect to positive and negative values of the scalar field, two identical black holes form in the periodic domain. These black holes only create locally collapsing regions, and, after removing their interior from the domain of integration, the spacetime is still expanding on average. The gradient and kinetic energy are diluted until the spacetime is dominated by the potential energy, after which inflation starts. As the effective scale factor of the spacetime increases, the proper distance between the black holes also increases, as their density is also diluted by inflation.

Surprisingly, we find that the addition of gradient energy allows inflation to occur in cases where it would not in the equivalent homogeneous case. We will now demonstrate that the reasons are two-fold. On the one hand, there is some resistance from the gradient pressure, which acts as a restoring force, and hence tends to pull the scalar field up the potential and away from the minimum. On the other hand, the addition of gradient energy results in an increase in the initial expansion rate, as a result of which the oscillations of the inflaton are damped. We now confirm this picture, and propose a simple toy-model which allows us to reproduce our results and gain some intuition. Let us consider the Klein-Gordon equation on the background of an FLRW spacetime,

$$\ddot\phi + 3H\dot\phi - \gamma^{ij}\partial_i\partial_j\phi + V_\phi' = 0 \tag{3.39}$$

where we have included the gradient terms in addition to the usual friction term, and the *dot* here denotes the time derivative with respect to the proper time τ. We further assume
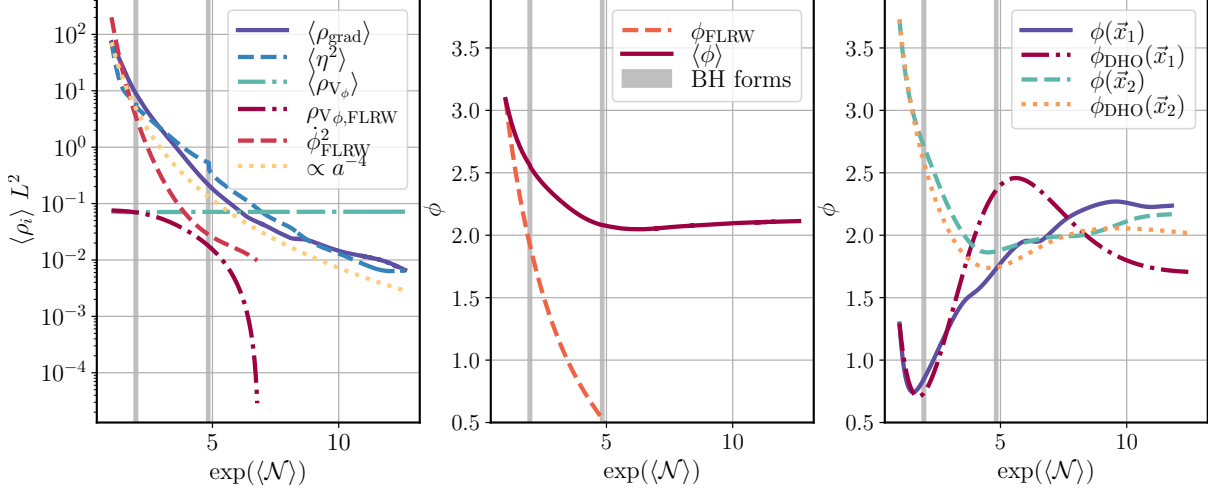
Figure 3.2: *Left*: The volume-averaged kinetic η^2, gradient ρ_{grad}, and potential ρ_{V_ϕ} energy densities plotted against the averaged measure of the effective scale factor for the case where the time derivative of the scalar field is uniform on the initial time slice and the potential has a T-shape (3.23) with $(\phi_0, m, \alpha, \omega, \delta\phi) = (3.0916, 0.14, 1/6, -7.1, 0.9)$. For comparison, we also show the evolution of the kinetic energy density $\dot{\phi}^2_{\text{FLRW}}$, and potential energy density $\rho_{V,\text{FLRW}}$ when solving the corresponding homogeneous FLRW equations in the absence of gradient energy and by specifying the initial value of $\dot{\phi}_{\text{FLRW}}$ to be the time derivative of the scalar field on the initial time slice. The energy density for a radiation dominated universe is shown by the dotted yellow line. *Middle*: The volume average of inflaton field value in comparison to the homogeneous solution. *Right*: The value of scalar field at the locations $\vec{x}_1 = L(0, -1/4, 1/4)$ and $\vec{x}_2 = L(1/8, -1/4, 1/4)$ when solving full equations of motion, and when solving equation for damped harmonic oscillator (3.41).

that the gradient energy can be approximated by a homogeneous energy density initially equal to the volume average, and that scales with an inverse power p of the scale factor

$$\rho_{\text{grad}} \approx 2V_0 r (a/a_0)^{-p} , \tag{3.40}$$

where $V_0 \equiv V_\phi(\phi = \phi_0)$ is the initial potential in the absence of inhomogeneities, and r gives the ratio of the initial value of gradient energy density to the inflationary energy density $r \equiv \frac{\langle \rho_{\text{grad},0} \rangle}{2V_0}$. In addition, we assume that the gradient energy redshifts in the same way as radiation, i.e. $p = 4$. In order to treat the spatial derivative term, we make the simplifying approximation that $\partial^2 \phi \sim (ik/a)^2 \Delta$, where a is the spatially homogeneous scale factor, and we have introduced the deviation from the background solution $\Delta \equiv \phi(t, x, y, z) - \chi_0(t)$, where $\chi_0(t)$ is the solution to the equation of motion (3.39) assuming the third term vanishes. Writing this in terms of the homogeneous number of e-folds, $d\mathcal{N} = Hd\tau$, the equation of motion (3.39) then becomes

$$H^2 \frac{d^2\phi}{d\mathcal{N}^2} + A \frac{d\phi}{d\mathcal{N}} + B\Delta = -V'_\phi \tag{3.41}$$

where, since $H^2 = \rho/3$ with ρ given by (3.18), using (3.40), and further assuming $\eta^2 \sim \rho_{\text{grad}}$, the coefficients are

$$H^2 = H_V^2 \left(\frac{V}{V_0} + 2re^{-p\mathcal{N}} \right), \tag{3.42}$$

and

$$A = 3H_V^2 \left[\frac{V}{V_0} + 2re^{-p\mathcal{N}} \left(1 + \frac{p}{6} \right) \right], \quad B = \frac{k^2}{e^{2\mathcal{N}}} \tag{3.43}$$

where $H_V^2 = 2V_0/3$ is the initial inflationary Hubble rate. This expression takes the form of a damped harmonic oscillator, where H^2 is analogous to the mass, A represents the Hubble friction, B the restoring pullback force, and the potential gradient the driving force pushing the inflaton down the potential. It is now clear that, for $r > 0$, the additional gradient energy not only increases the initial friction as well as the *mass* term, but also provides an additional pullback force for points away from the average value of the inflaton. Note that, as the universe expands, the contribution from the gradient energy to the friction and restoring terms is exponentially suppressed, such that if the scalar field remains within the inflationary part of the potential during the initial dynamical phase, then it can transition into slow-roll inflation.

In the right panel of figure 3.2, we compare the results of numerically integrating the damped harmonic equation (3.41) to the behavior of the full simulations at two arbitrarily located points. We find that the results are qualitatively the same and conclude that this simple toy-model can be used to build intuition about the dynamics of the full solution. Similarly, the left panel shows that the gradient and kinetic energy of the full evolution decreases as a^{-4}, as would be expected for a radiation dominated universe. We also note that the arguments given above suggest that other significant contributions to the expansion rate from inhomogeneities, for example from a gravitational wave energy density, as studied in [105], should also mitigate the disruptive effect of a small nonzero initial scalar field velocity.

We find that qualitatively similar results hold when starting from initial conditions constructed by specifying a rescaled version of the conjugate momentum such that $\tilde{\eta} = \Psi^2 \eta$ (3.27), or such that the momentum constraint constraint is analytically satisfied $\hat{\eta} = \Psi^6 \eta$ (3.29). In both cases, the rescaled conjugate momentum is chosen such that the gradient and kinetic energy are comparable on the initial time slice, but ~ 1000 times larger than the potential energy density. The former is demonstrated in the right panel of figure 3.3, where we choose the potential given by an α-attractor potential (3.23), and an initial scalar field profile given by (3.27), with parameters such that, in the absence of inhomogeneities ($\delta\phi = 0$), and if the conjugate momentum of the scalar field were zero, the combination of parameters (ϕ_0, m, α) would result in 60 e-folds of inflation, a scalar power spectrum of $\Delta_{\mathcal{R}}^2 \sim 0.05$, a scalar spectral index of $n_s = 0.97$, and tensor-to-scalar ratio of $r_{ts} = 0.006$ for modes that cross the horizon 60 e-folds before the end of inflation. We find that the gradient and kinetic energy decrease until the spacetime is dominated by the inflationary energy

after which inflation may start. Unlike for initial data with a constant velocity profile, here the energy density on the initial time slice is no longer symmetric with respect to positive and negative values of the scalar field, and therefore the black holes are no longer symmetric about the origin. Similarly, the left panel of figure 3.3 shows the individual energy densities for a solution constructed according to (3.29) and with quadratic potential such that in the absence of inhomogeneities and conjugate momentum, the combination of parameters (ϕ_0, m) would result in 60 e-folds of inflation, $\Delta_{\mathcal{R}}^2 \sim 1 \times 10^{-3}$, $n_s = 0.97$, and $r_{ts} = 0.13$ for modes that cross the horizon 60 e-folds before the end of inflation. Here, again, two regions collapse to black holes, but the universe keeps expanding, and eventually transitions to exponential expansion. These results emphasize that our conclusions are generic, and not sensitive to the particulars of how the scalar field momentum is chosen.
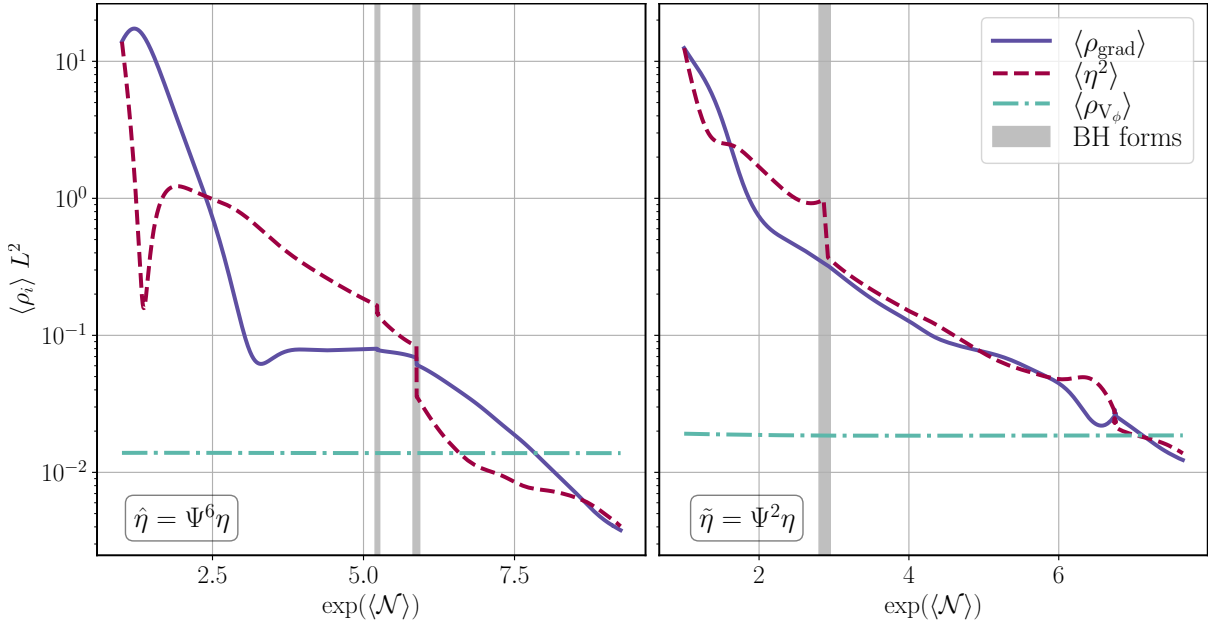
Figure 3.3: We show the gradient, kinetic, and potential energy contributions to the average energy density (similar to the left panel of figure 3.2) for two different cases. Gray regions indicate the formation of black holes. *Left*: A case with a quadratic potential given by (3.22) and initial data that automatically satisfies momentum constraint (3.29) with parameters $(\hat{\phi}_0, m, \sigma, \delta\hat{\phi}, \delta\hat{\eta}) = (\sqrt{2}11.0, 3.78 \times 10^{-3}, 0.1, 0.68, 2.21)$ *Right*: A case with initial data constructed according to (3.27) and with parameters $(\phi_0, m, \alpha, \delta\phi) = (5.42, 0.029, 1.0, 0.65)$ for the α-attractor potential (3.23).

3.3.2 High energy inflation

Single-field inflation

We next consider single-field inflationary models where inflation may naturally begin near the Planck scale. Thus, solutions where the sum of the kinetic, gradient and potential energy of the inflaton is order unity in Planck units. We further restrict our study to initial conditions where the kinetic, gradient, and potential energy are initially comparable, and the potential is quadratic in the scalar field, $V_\phi(\phi) = m^2\phi^2$. In figure 3.4, we show the volume-averaged total energy density (left panel) and the volume-averaged expansion rate (right panel) computed from (3.34), as a function of the effective scale factor, for the three types of initial data described in section 3.2.2. We specify the initial data such that, in the absence of gradient and kinetic energy, the homogeneous initial value of $\phi_0 = 11$ and other parameters would result in 60 e-folds of inflation, $\Delta_\mathcal{R}^2 \sim O(1)$, $n_s = 0.97$, and $r_{ts} = 0.13$ for modes that cross the horizon 60 e-folds before the end of inflation. Independent of the type of initial data used, as the scale factor increases, the average expansion rate and total energy density decreases (although at different rates depending on the initial data), until the kinetic and gradient energy is subdominant, leading to a universe dominated by the inflationary potential, hence undergoing exponential expansion. This is illustrated in figure 3.5, where we show the individual average energy densities. Although the gradient energy quickly becomes negligible, the kinetic energy asymptotes to a constant value, consistent with the value the kinetic energy would asymptote to when solving the homogeneous FLRW equations in the absence of gradient energy and specifying the initial value of $\dot{\phi}^2_{\mathrm{FLRW}}$ to be the volume average value of the kinetic energy of inhomogeneous solution on the initial time slice.

Though we evolve for long enough that the spacetime is dominated by the inflation potential energy and exponential expansion, we do not evolve to the end of inflation, as growing gradients from different regions in the domain inflating at different rates eventually lead to large truncation error.

We confirm that inhomogeneities do not prevent inflation in models of chaotic inflation occurring near the Planck scale [248, 249, 244]. Although the simplest models of inflation (including the quadratic potential we study here), are now strongly disfavored by the most recent observations from BICEP/Keck and Planck [16, 13], they could still appear in the context of more complicated inflationary models containing more than one scalar field. We discuss an example of such model in the following section.

Two-field inflation

Up to this point, we have only considered single field models. However, our methods can be applied equally well to more complicated inflationary models. To give an example, we consider a simple theory describing two non-interacting scalar fields, θ and ϕ, such that the potential is given by (3.24), which combines a quadratic dependence for ϕ with an
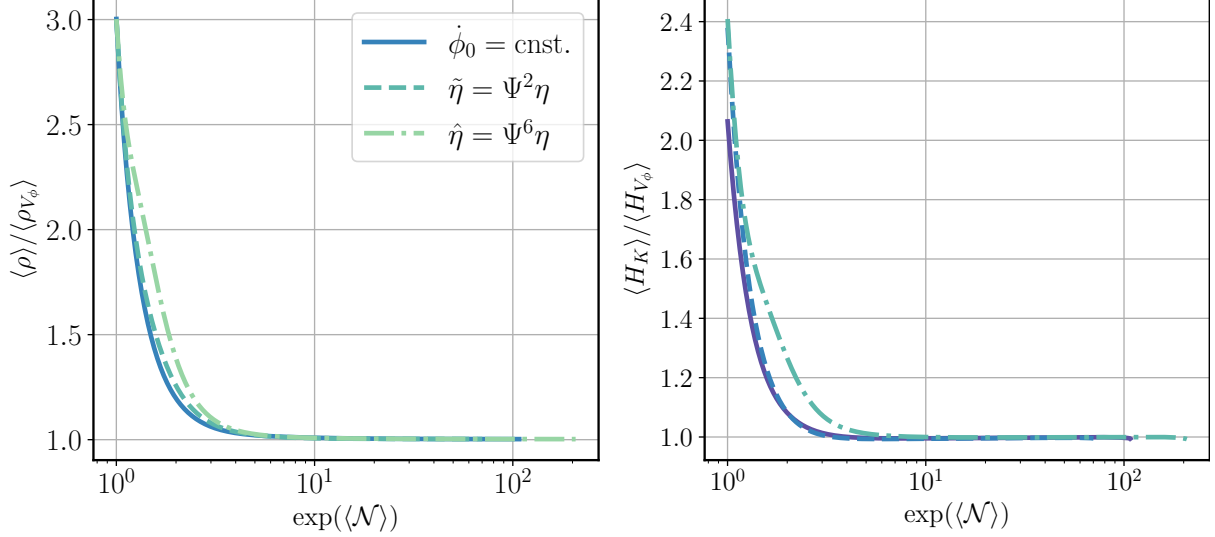
Figure 3.4: The volume-averaged total energy density (left) and expansion rate (right) plotted against a volume-averaged measure of the effective scale factor for cases with a quadratic potential given by (3.22). The quantities $\langle \rho_{V,\phi} \rangle$ and $\langle H_{V_\phi} \rangle$ respectively represent the volume-averaged measures of the potential energy density and inflationary expansion rate as a function of time. Both quantities can be seen to asymptote to the values expected for potential energy dominated inflation. The solid line represents a solution for initial data constructed using (3.25) and $(\phi_0, m, \omega, \delta\phi) = (11.0, 0.23, -5.83, 0.79)$. The dashed line represents initial data given by (3.26) with $(\phi_0, m, \delta\phi) = (11.0, 0.13, 0.85)$. Finally, the dash-dotted curve represents initial data given by (3.28) and $(\hat{\phi}_0, m, \sigma, \delta\hat{\phi}, \delta\hat{\eta}) = (\sqrt{2}\, 11.0, 0.12, 0.1, 0.68, 2.21)$.

α-attractor term for θ. We further assume that $M \gg m$. Here, the potential can give rise to two stages of inflation. The first stage of inflation is driven by the quadratic potential, and may start at nearly Planckian energies and be relatively short. Once inflation driven by ϕ ends, the second stage of inflation driven by the α-attractor potential, and lasting more than 60 e-folds, may begin. Here we are not able to evolve this model past the first stage of inflation, likely due to limited numerical resolution and the gauge choice. However, already at this stage we find that gradient energy has become subdominant, and by comparing the evolution in different regions to the homogeneous evolution with the same scalar field values, we can approximately extrapolate their later behavior.

We consider values for ϕ_0 and θ_0 such that, in the absence of inhomogeneities ($\delta\phi = 0$ and $\delta\theta = 0$) and kinetic energy on the initial time slice, the first stage of inflation would last one e-fold, and the second stage of inflation would last 60 e-folds and give rise to a scalar power spectrum with $\Delta_\mathcal{R}^2 \sim 0.1$, $n_s = 0.97$, and $r_{ts} = 0.006$. The remaining free data is chosen such that the total energy density is initially on the order of $1/L^2$, the potential energy is $1/7$ of the total energy, and the remaining fraction is provided by the kinetic and gradient energy of the fields θ and ϕ, with each term, for each field contributing equally to
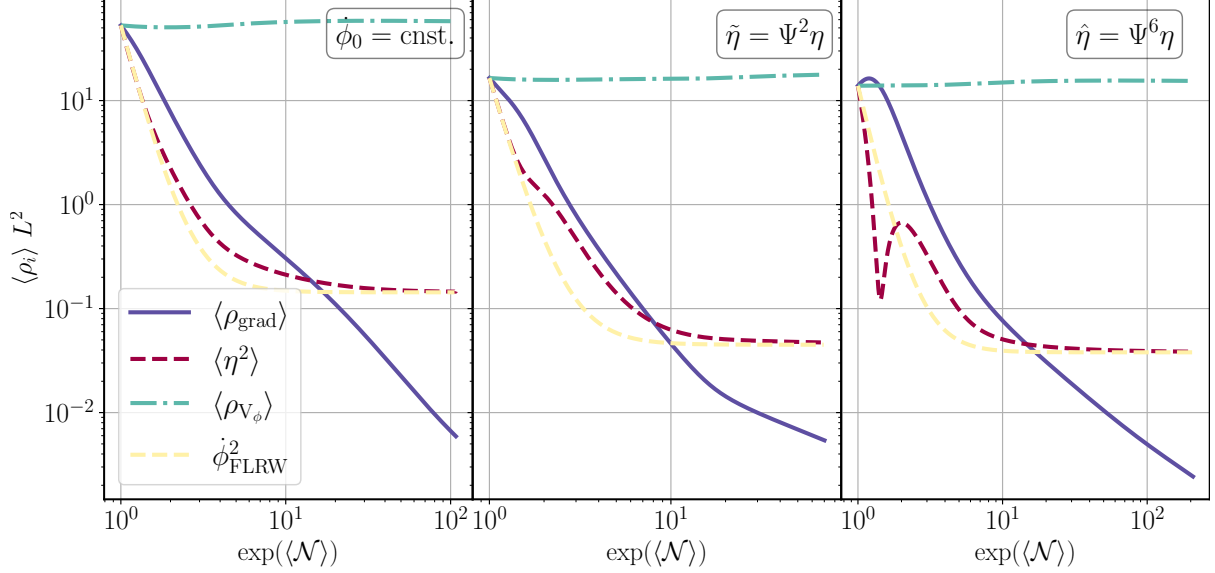
Figure 3.5: The volume-averaged kinetic η^2, gradient ρ_{grad} and potential ρ_{V_ϕ} energy densities plotted against the averaged measure of the effective scale factor for the cases shown in figure 3.4. For comparison, the evolution of the kinetic energy density when solving the FLRW equations in the absence of gradient energy and specifying the initial value of $\dot{\phi}^2_{\mathrm{FLRW}}$ to be the volume average value of the kinetic energy of inhomogeneous solution on the initial time slice, is also shown (dashed yellow line).

the total energy content. We choose an initially uniform time derivative of the scalar field for ease of implementation, but based on the previous section we do not expect our results to depend on the initial velocity profile of the scalar fields. The conjugate momentum on the initial time slice is such that, if one were to solve the FLRW equations in the absence of gradient energy, but specifying the initial values for $(\dot{\phi}_{\mathrm{FLRW}}, \dot{\theta}_{\mathrm{FLRW}})$ to be the volume average of conjugate momenta of the corresponding scalar fields on the initial time slice, then the first stage of inflation would only last half an e-fold and the second stage 35. The left panel of figure 3.6 shows the individual contributions to the total energy density for each scalar field in our simulation compared to when solving the FLRW equations in the absence of gradient energy and by specifying the initial value for the time derivative of scalar field to be the volume average value of the conjugate momentum of inhomogeneous solution on the initial time slice.

We first study the first stage of inflation driven by the quadratic potential, shown in the left panel of figure 3.6, in detail. In line with our earlier observations, we find that the average kinetic energy of the scalar field $\langle \eta^2_\phi \rangle$ (dashed red line) does not decrease as quickly as in the homogeneous case (dashed orange line). We also note that the average potential energy of ϕ (dash-dotted green line) increases at first, as does the average scalar field $\langle \phi \rangle$ initially, shown in figure 3.7, likely pulled up by the gradients in the field. As the universe expands, the gradient energy decreases and eventually, when the gradient energy is small

62

enough, the potential energy starts decreasing.
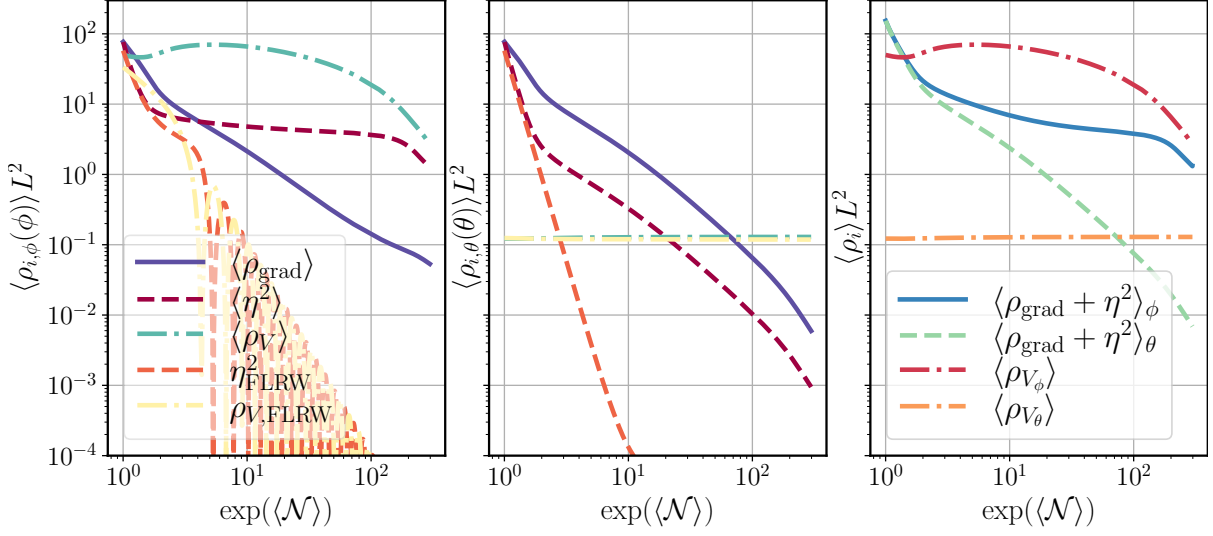
Figure 3.6: The gradient ρ_{grad}, kinetic η^2, and potential energy ρ_{V_ϕ} contributions to the volume average energy density as a function of the effective scale factor for each individual scalar field (ϕ left panel and θ middle panel) and both scalar fields combined (right panel). *Left*: Individual contributions to average energy density for scalar field with quadratic potential driving first stage of inflation. For comparison, the evolution of the kinetic energy density η^2_{FLRW} and potential energy density $\rho_{V,\mathrm{FLRW}}$ when solving the FLRW equations in the absence of gradient energy, and specifying the initial value for the time derivative of scalar field to be the volume average value of the conjugate momentum of inhomogeneous solution on the initial time slice, is also shown. *Middle*: Same as the left panel, but for a scalar field with the α-attractor potential driving second stage of inflation. *Right*: The sum of the volume-averaged gradient and kinetic energy densities for each scalar field separately $\langle \rho_{\mathrm{grad}} + \eta^2 \rangle$ and the volume-averaged potential energy densities for each scalar field.

Unfortunately, we were not able to able to evolve this scenario past the first stage of inflation. We attribute this to a lack of resolution to resolve large gradients developing between different regions of the domain inflating at different rates. We next illustrate these different regions and conjecture that if we had sufficiently large resolution, then the effectively causally disconnected Hubble patches will keep inflating, albeit at different rates, until the second stage of inflation kicks in. Figure 3.7 shows the range of values the scalar field driving the first stage of inflation and the conjugate momentum take, as a function of the effective scale factor. This already suggests that different patches will inflate at different rates, which in turn will lead to the formation of gradients in the field values across the numerical domain.

In particular, the region where sharp gradients develop in the field values, which we eventually can no longer resolve due to the finite numerical resolution of our grid, corresponds to where the scalar field ϕ stops inflating first. Figure 3.8 shows the scalar field ϕ,

its conjugate momentum η_ϕ, the extrinsic curvature K, and the gradient energy ρ_{grad} at the location where these unresolved features develop (indicated by $\tilde{\phi}_0$), but shortly before these become severe enough that the evolution must be halted (indicated by vertical dashed grey line in figure 3.10). We find that the extrinsic curvature is larger than in the rest of the domain, and that the gradient energy is negligible, as expected. We also show the value of the scalar field θ and its conjugate momentum η_θ for the field driving the second stage of inflation. These quantities indicate that the scalar field driving the second stage of inflation is still inflating at that location.

As the universe expands, the left and middle panels of figure 3.6 show that the average gradient energies of ϕ and θ are quickly diluted until they are negligible compared to the average inflationary energy of either field. This suggests that when the gradient energy becomes negligible in a neighbourhood surrounding a point of interest, then one can use the FLRW equations together with the local value of scalar field and its time derivative to compute the evolution of scalar field at that location. We first show that this approximation is valid for the location where unresolved gradients eventually develop. We then use this to extrapolate the behavior of both scalar fields, at different locations, past the point we are able to evolve.

In the left panel of figure 3.10, we plot the values of the respective scalar fields at the location where unresolved features eventually develop $(\tilde{\phi}_0, \tilde{\theta}_0)$ as a function of the local scale factor (purple dots). The smallest value of the scale factor for which we show the values of the scalar fields corresponds to the time at which the gradient energy becomes negligible in a neighbourhood surrounding the point of interest. We also show the evolution of the scalar field when solving the FLRW equations (dash-dotted lines), ignoring the gradient terms, and fixing the initial values for the scalar field and its time derivative to be the corresponding values for the inhomogeneous scalar fields and conjugate momenta at that spatial point. As expected, we find close agreement between the numerical and FLRW solution, and make use of the FLRW solution to extrapolate the behavior of scalar fields past the point we were able to numerically evolve. For the spatial point where ϕ stops inflating first, we find that θ will still inflate for ~ 250 e-folds at that particular point.

As another representative example, we also show the scalar field, its conjugate momentum, the extrinsic curvature, and the gradient energy at the location where ϕ obtains its maximum value (indicated by $\tilde{\phi}_{\max}$ in figure 3.9). Similarly, we find that the gradient energy is negligible in a neighbourhood of that point and plot the scalar field values and their corresponding FLRW solutions as a function of the local scale factor in the right panel of figure 3.10. We extrapolate the FLRW solution, and deduce that ϕ and θ will inflate for an additional 3 and 250 e-folds respectively. These results suggest that other parts of the domain will also keep inflating, although at different rates determined by the local value of the scalar field and its conjugate momentum at that location. We thus conjecture that, if we were able to continue the evolution, ϕ would fluctuate around zero in regions where it has reached the bottom of the potential (just like in the homogeneous case). We leave a more detailed analysis to confirm this to to future work.

Assuming the above picture, as the universe keeps expanding, the potential energy of the α-attractor potential eventually dominates the quadratic potential, after which the second stage of inflation starts. The middle panel of figure 3.6 shows that the gradient and kinetic energy of the scalar field driving the second stage of inflation becomes smaller than the potential energy even before the α-attractor potential dominates over the quadratic potential. Furthermore, we find that (shortly before large gradients make the evolution inaccurate) the wavelength of the perturbations $\sim L$ is about 60 times larger than the volume averaged Hubble radius of scalar field driving second stage of inflation. This suggests that by the time the first stage of inflation ends, the universe is effectively made up of patches that are homogeneous on Hubble scales and, at least in most regions, the second stage of inflation may generate a nearly-scale invariant spectrum consistent with observations.
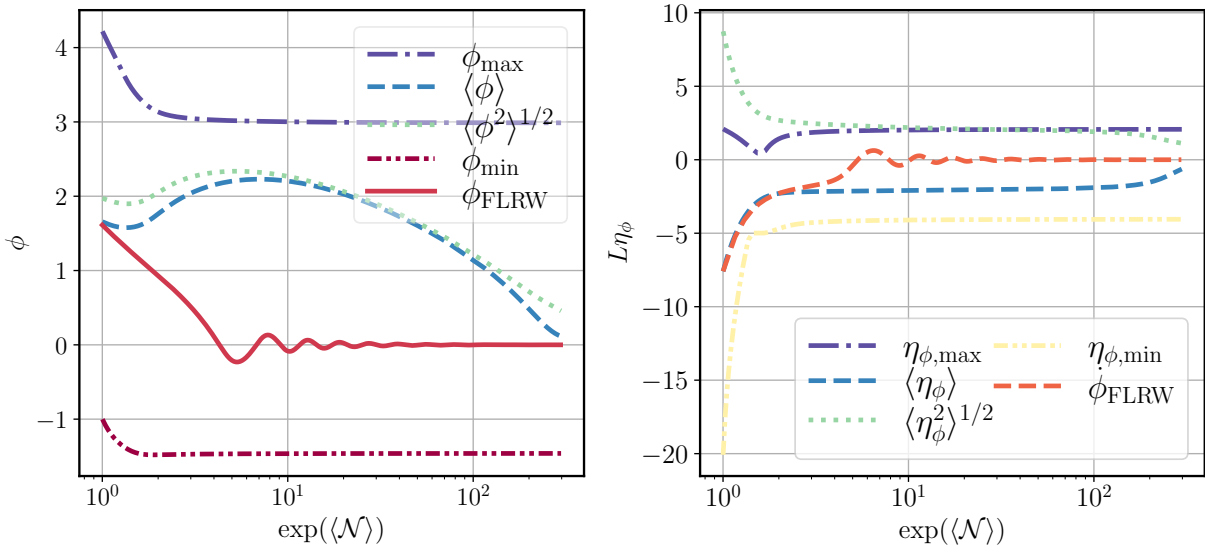
Figure 3.7: *Left*: The minimum $\phi_{\min}$, maximum $\phi_{\max}$, and volume-averaged values of the scalar $\langle\phi\rangle$ driving the first stage of inflation as a function of effective scale factor for the case shown in figure 3.6. For comparison, we also show the evolution of ϕ_{FLRW}, the scalar field when solving the FLRW equations in the absence of gradient energy, and specifying the initial value for the time derivative of scalar field to be the volume average value of the conjugate momentum of inhomogeneous solution on the initial time slice. *Right*: Similar quantities, but for the conjugate momentum of the scalar.

3.4 Discussion and conclusion

In this chapter, we have undertaken the first study of the robustness of large field models of inflation to large initial gradients and kinetic terms in the initial scalar field profile. We proposed three different ways of specifying scalar field configurations with non-vanishing momentum density when solving the Hamiltonian and momentum constraint equations
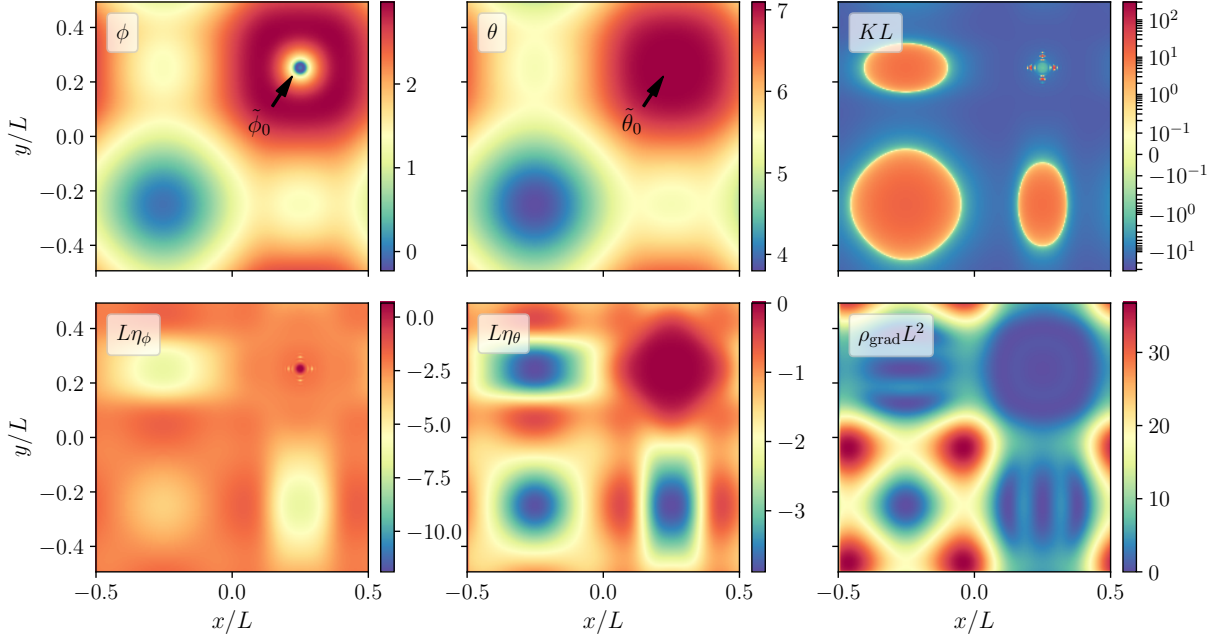
Figure 3.8: Two-dimensional spatial slices showing different quantities shortly before strong gradients (around the point indicated by the arrow) make the evolution inaccurate (at the time indicated by vertical dashed grey line in figure 3.10) for the case shown in figure 3.6. The first column shows the scalar field (top) driving the first stage of inflation and its conjugate momentum (bottom). The second column shows the corresponding quantities for the scalar driving the second stage of inflation. The third column shows the extrinsic curvature scalar (top) and total gradient energy.

using the CTS formalism. Solving the full system of coupled constraint equations allowed us to examine the effects of several initial conditions not previously studied in the literature. Our results are summarized as follows:

- We studied the evolution of single-field inflationary models where the initial gradient and kinetic energy densities of the inflaton are much larger than potential energy. We demonstrated that the presence of significant gradient energy can actually negate the effect of a large time derivative in the scalar field, allowing inflation to occur in cases where, in the homogeneous case, the kinetic energy would drive the scalar field off the inflationary plateau before exponential expansion occurred. We explained this in terms of the increased initial expansion rate and restoring pullback force in the presence of large gradients, deriving a simple toy-model to demonstrate this. This implies that rather natural initial gradients in the initial conditions will mitigate the effects of a non-zero initial field velocity of the inflaton.

- We also performed the first study of the impact of inhomogeneities on single-field inflationary models where inflation may start at nearly Planckian densities. We
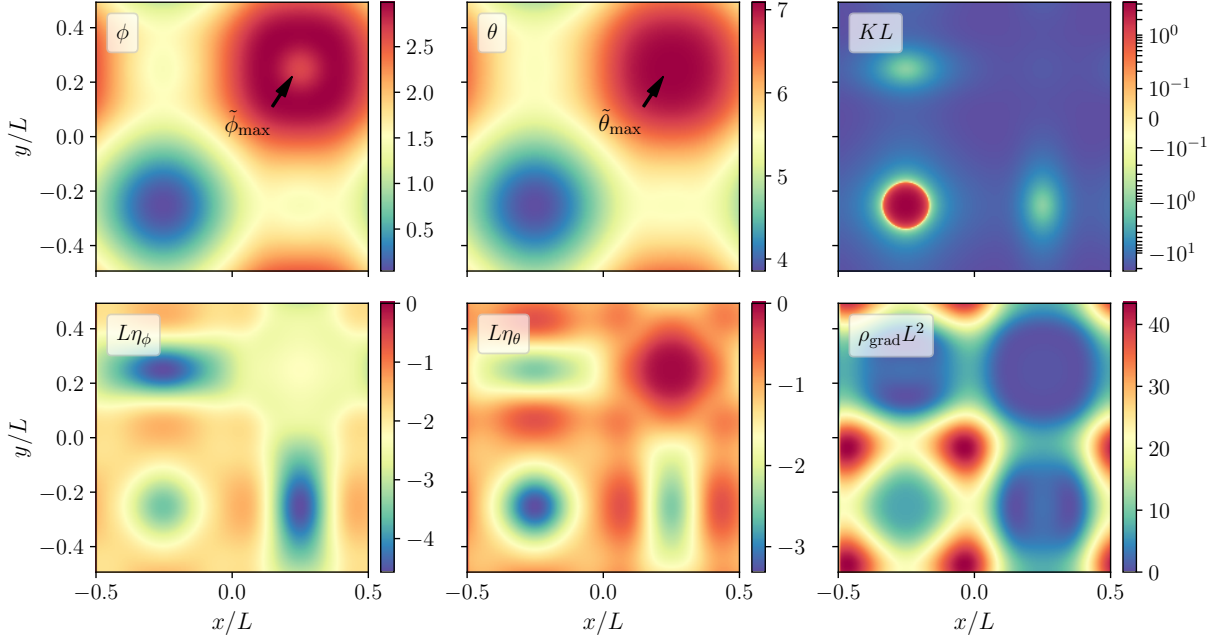
Figure 3.9: Same as figure 3.8, but for the two-dimensional spatial slices where ϕ is maximal.

found that, in cases where the gradient, kinetic and potential energy densities are all comparable at nearly Planckian densities, the universe will rapidly transition to exponential expansion. In these cases we did not find black hole formation.

- In addition to single-field inflationary models, we performed a preliminary study of the effects of inhomogeneities on cosmological scenarios where the universe undergoes two stages of inflation, the first one at nearly Planckian energies and the second one at sub-Planckian scales consistent with observations. Although we were not able to evolve the spacetime to the point where the second stage of inflation would start, and therefore make detailed conclusions, we find at this time large regions where the gradients are negligible and the spacetime is well approximated by the homogeneous evolution determined by the local inflaton values. We leave a more detailed study of these models for future work.

Exploring the two-field inflationary models considered here would require developing new numerical methods. As mentioned above, we believe one of the main difficulties lies in being able to resolve large gradients developing between different regions of the numerical domain inflating at different rates. A better choice of gauge, as well as working with higher resolution or adaptive mesh refinement may help address this, as well as allow us to evolve the single-field inflationary models for longer. This would also allow us to make contact with observations. More precisely, one could apply the methods for extracting cosmological observables from cosmological simulations introduced in [204] These methods would
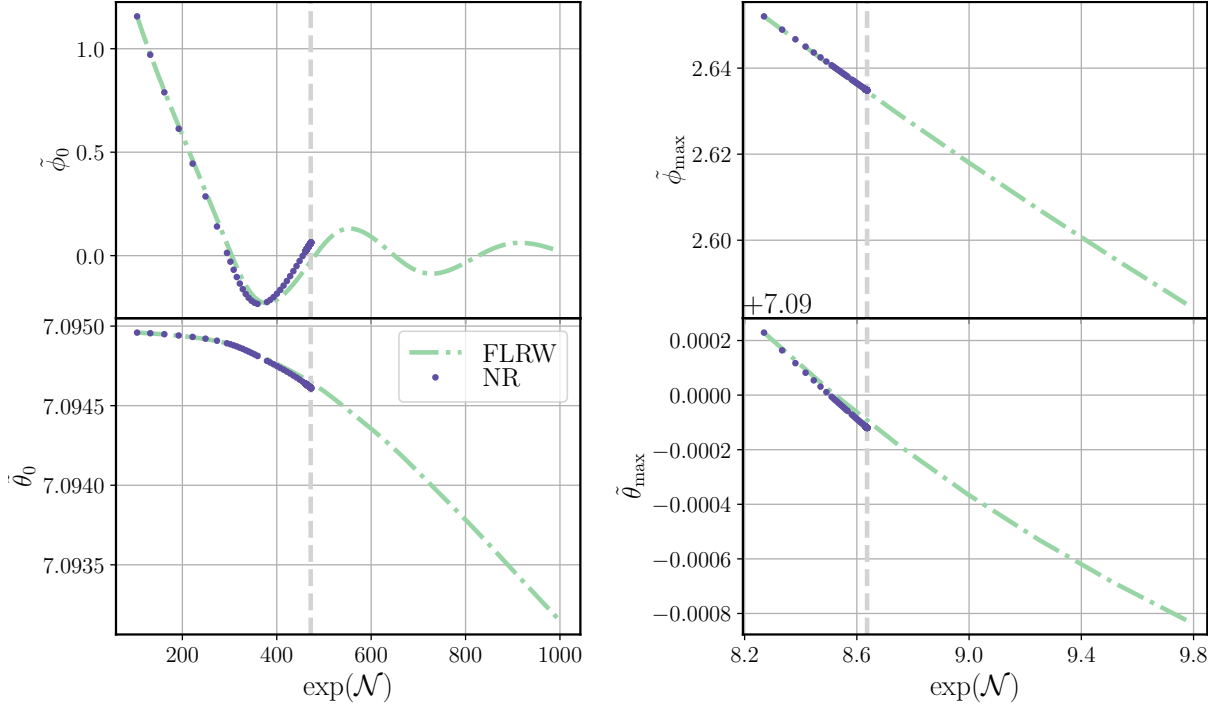
Figure 3.10: Scalar field and conjugate momentum values as a function of the local effective scale factor for two spatial points (indicated by $\tilde{\phi}_0$ and $\tilde{\phi}_{\max}$ on the spatial slices in figures 3.8 and 3.9, respectively), chosen such that gradient energy is negligible in surrounding neighbourhood (blue dots). The corresponding homogeneous FLRW solution using the same initial values plotted in the figure is also shown. The vertical dashed grey lines indicate the local scale factors corresponding to the two-dimensional spatial slices shown in figures 3.8 and 3.9.

allow us to predict the comoving curvature perturbation in the single-field inflationary models studied in this chapter. The leading observable in this case would be a non-zero contribution to the CMB quadrupole.

In this study, we only considered two families of inflationary potentials out of the multitude that have proposed in the literature. However, we verified that, starting from the same initial conditions, these two different potentials gave similar qualitative results and we do not expect our results to depend strongly on the details of the potential, since the key features are the flatness of the potential and the super-Planckian distance in field space that must be traversed to reach the minimum of the potential. For two-field inflationary models, for simplicity in this first study, we focused on theories where the scalar fields are non-interacting. It would be interesting to consider the evolution of two-field inflationary models where the scalar fields do interact and explore whether there are still robust to generic initial conditions (see e.g. [244] and [201]). Note however, that in the α-attractor generalization [213, 68] of the hybrid inflation scenario [250], the fields become decoupled in the large field limit, and the evolution of the initial conditions reduces to the one performed

in our chapter.

Another direction for future work would be to adapt the methods developed here to study the robustness inflation in the presence of other types of matter. One particular class of models of interest would be matter where the speed of sound of the fluctuations, or equivalently the Jeans length, goes to zero [308], as in, for example, dust. This would be a case especially prone to the gravitational collapse of initial perturbations.

The methods developed here for constructing general relativistic initial data are rather generic, and could be applied to a number of other cosmological scenarios where it is important to include momentum density. It would also be interesting to compare these methods to those proposed in the recent work of [34], where the authors construct initial data with non-trivial matter configurations by using a new scheme based on the Conformal Transverse-Traceless (CTT) formalism to solve for both constraint equations. In this so-called CTTK approach, rather than choosing a constant value for the trace of the extrinsic curvature K, one chooses an initial profile for the conformal factor, and solves an algebraic equation for a spatially varying K.

Chapter 4

Evolution of black holes through a nonsingular cosmological bounce

4.1 Introduction

In this chapter, we consider a proposed alternative to cosmic inflation namely the bouncing model. In a singular bounce, the universe passes through a classical singularity where the cosmological scale factor becomes small, curvature invariants blow up, and quantum gravity effects presumably become highly relevant to determining the future dynamics of the universe [327, 257, 41, 167].

   An alternative, which we focus on here, is a nonsingular bounce. For such cosmologies, so long as the spacetime curvature does not become Planckian, there is the possibility that quantum gravity effects could be subdominant to classical effects, in which case one may be able to describe the dynamics of the bounce using classical physics. Nonsingular bouncing cosmologies require violating the null convergence condition (NCC), which requires that $R_{\mu\nu}k^\mu k^\nu \geq 0$ for all null vectors k^μ, [261, 221, 43, 304, 70]. In Einstein gravity, the NCC is equivalent to the null energy condition (NEC) [1] which is satisfied by most standard classical field theories [304]. Nonsingular bouncing cosmologies hence require non-standard matter terms, or modifications to Einstein gravity, for example, Horndeski theories including ghost condensation [25, 79] or (cubic) Galileon/Horndeski models [124, 125, 82, 136, 193, 192]. While perturbative studies of these theories suggest they may be free of ghost or gradient instabilities [125, 193], less is known about which models will remain (strongly) hyperbolic through a bounce, when the solution is presumably not in the weakly coupled regime [277, 230, 229][2]

---

[1]The null energy condition requires that $T_{\mu\nu}k^\mu k^\nu \geq 0$ for all null vectors k^μ. Assuming the Einstein equations, which can be written as $R_{\alpha\beta} - \frac{1}{2}g_{\alpha\beta}R = 8\pi T_{\alpha\beta}$, it is straightforward to show that the NEC is equivalent to the NCC

[2]We note that the model proposed in [193] is known to break down shortly after the bounce has ended [121].

70

An important open question is what happens in bouncing cosmologies in the inhomogeneous and non-perturbative regime. While there are several analytical and numerical studies of the dynamics of bouncing cosmologies during their contraction phase [159, 190, 108, 191], there are relatively few studies of the dynamics of the bounce [286, 21, 83, 336, 193], and none that consider the dynamics of black holes beyond the restriction to spherical symmetry [142]. Previous studies of black hole–cosmological bounces have either constructed initial data for black hole bouncing solutions [101], worked in a perturbative limit [84, 94, 196, 172], or made use of analytic solutions (e.g. generalizations of the McVittie solutions [283, 282, 284]), that are limited by the fact that the metric evolution is prescribed ad-hoc, and from that the implied matter type and evolution is derived. The question of what happens to a black hole in a nonsingular cosmological bounce is particular salient for several reasons. On the one hand, the bounce necessarily requires a violation of the assumptions made in black hole singularity theorems and results on black hole horizons (namely the NCC) [181], so there is a question of whether the black hole will survive the bounce, or if the bounce mechanism will also reverse gravitational collapse, and if this will possibly lead to a naked singularity. On the other hand, one might also worry what the backreaction of the black hole's gravity will be on the bounce in the neighbourhood of the black hole. An extreme scenario would be if the bounce failed to happen in the vicinity of the black hole, possibly leading to a patch of contraction that grows into the expanding spacetime, as happens, e.g., in scenarios where the Higgs boson is destabilized during inflation, and goes to its true vacuum at negative energy densities [140, 126].

Here, we address these questions by studying the nonlinear dynamics and evolution of black holes in a particular nonsingular bouncing cosmology (details of which are described below). Black holes can be expected to form during the contraction of matter and radiation dominated universes [37, 94, 297], and will generally be present from previous eras in cyclic cosmologies [321, 195]. However, it is common to invoke a smoothing phase during contraction (e.g. ekpyrosis [222, 321, 139]), and argue that Hubble patches containing a black hole will be rare. Regardless, we view our work as serving two main purposes: (1) to study the dynamics and robustness of a nonsingular bouncing model when a very large perturbation, namely a black hole, is introduced, and (2) to explore the dynamics of the black hole and cosmological horizons during the bounce.

To avoid the difficulties related to finding a motivated theory that can give rise to bouncing solutions while also having well-posed evolution equations in the inhomogeneous regime, and thus being suitable for describing black hole dynamics, we will work with a bouncing cosmology model that incorporates a minimally coupled scalar field with a ghost field (i.e. a field which contributes to a negative cosmological energy density), to drive the bounce. While ghost fields are known to give problematic quantum mechanical theories (for a discussion of this in the context of cosmology see [102, 210]; see also [12]), we take the point of view of [286, 21, 336] and treat the ghost field as an *effective* model for NCC violation. Quantum stability and unitarity is a distinct issue requiring a separate analysis (see, e.g., [115]). Unlike earlier work with this model, we do not restrict ourselves to cosmological spacetimes that have planar symmetry [336], or to small linear perturbations about

a background bouncing spacetime [286, 21]. Instead, we consider contracting cosmological initial data that contains a black hole, and work in an axisymmetric spacetime. This allows us to examine the effect that a large inhomogeneity has on the dynamics of the spacetime near and during the bounce.

Following the growing number of studies making use of techniques from numerical relativity to study cosmological phenomena involving black hole dynamics (including the one in the previous chapter) [47, 341, 127, 126, 105, 33, 164, 202, 110], we use numerical solutions to follow the evolution of different size black holes, both non-spinning and spinning, through a bounce, considering those both bigger and smaller than the minimum Hubble radius. Our main results are that the black holes persist to the expanding phase, and that the nonsingular bouncing model under study is fairly robust under large perturbations, in the sense that the local spacetime expansion around the black hole successfully bounces for all of the cases we explored. For large enough black holes, we find the black hole apparent horizon collides with the cosmological horizon, and temporarily disappears during the contraction phase. Nevertheless, the black hole apparent horizon eventually reappears (with finite radius event horizon throughout) and this does not disrupt the bounce at late times.

In principle a nonsingular, *classical* bounce could occur at any characteristic length scale that is larger than the scale at which quantum gravity effects become important (presumably the Planck scale: $l_P \sim 10^{-33}$ cm in geometric units). Given this, the length scale of a classical nonsingular bounce can still be extremely small compared to the typical length scale of say, an astrophysical black hole (e.g. in [195] the bounce happens at a typical length scale of $\sim 10^{-25}$cm $\sim 10^8 l_P$). One may expect then that if any Hubble patch were to contain a black hole, that the black hole would be much larger than the minimum size of the Hubble patch. For example, even a black hole with a mass of $m_{BH} \sim 10^{15}$ g[3] at the bounce would still have a size of $\sim 10^{20} l_P$; this is orders of magnitude larger than the example bounce scale mentioned above. For this reason, we will be more interested in considering black holes whose size is comparable or larger than the bounce scale (which we take to be $1/|H_{\min}|$, where $H_{\min} < 0$ is the maximum contraction rate).

The remainder of this chapter is as follows. We discuss the nonsingular bouncing model we use in section 4.2. Our numerical methods and diagnostics for evolving the nonsingular bounce are outlined in section 4.3. Our numerical results are described in section 4.4, and we conclude in section 4.5. In appendix C.1, we discuss our numerical methodology in more detail, in appendix C.2, we define various quasi-local notions of black hole and cosmological horizons, and in appendix C.3, we provide an overview of the McVittie spacetime, an analytic solution to the Einstein equations of a black hole embedded in a cosmology, of which our numerical simulations can be seen as a generalization.

---

[3]Primordial black hole with masses smaller than $m_{BH} \sim 10^{15}$ g would have evaporated by now due to Hawking evaporation; this is then a reasonable lower bound for the mass of black holes that were present in the early universe [93, 85].

4.2 Ghost field model

We consider a theory that has two scalar fields ϕ and χ coupled to gravity:

$$S = \int d^4x \sqrt{-g} \left(\frac{1}{16\pi} R - \nabla_\alpha \phi \nabla^\alpha \phi - 2V(\phi) + \nabla_\alpha \chi \nabla^\alpha \chi \right). \tag{4.1}$$

This model has a canonically normalized scalar field ϕ with a potential $V(\phi) = V_0 e^{-c\phi}$, and a massless ghost field χ.

The covariant equations of motion for (4.1) are

$$\nabla^\alpha \nabla_\alpha \phi - \frac{dV}{d\phi} = 0, \tag{4.2a}$$

$$\nabla^\alpha \nabla_\alpha \chi = 0, \tag{4.2b}$$

$$\frac{1}{8\pi} \left(R_{\alpha\beta} - \frac{1}{2} g_{\alpha\beta} R \right) + 2\nabla_\alpha \chi \nabla_\beta \chi - 2\nabla_\alpha \phi \nabla_\beta \phi +$$
$$g_{\alpha\beta} \left(2V(\phi) + \nabla_c \phi \nabla^c \phi - \nabla_c \chi \nabla^c \chi \right) = 0. \tag{4.2c}$$

Nonlinear, inhomogeneous cosmological solutions to the model (4.1) were studied in [336]. There, the authors considered a toroidal universe with a planar perturbation in one of the spatial directions. In this work, we consider an *asymptotically* bouncing FLRW universe with an initial black hole; see section 4.3 and appendix C.1 for more details on our numerical methodology.

Strictly speaking, the ghost field should be stabilized by some mechanism at the quantum level. We choose to ignore this and treat (4.1) as a purely classical theory. As the equations of motion (4.2) have a well-posed initial value problem[4], we expect the model should admit at least short-time classical solutions from generic initial data.

4.2.1 Homogeneous bouncing cosmology

Here we briefly review homogeneous, isotropic bouncing solutions for the system (4.2) (see also [336, 21]), and discuss the values used for our asymptotic initial data. We work with harmonic coordinates ($g^{\mu\nu}\Gamma^\alpha_{\mu\nu} = 0$), so that the metric line element is

$$ds^2 = -a(t)^6 dt^2 + a(t)^2 \delta_{ij} dx^i dx^j. \tag{4.3}$$

---

[4]More specifically, the equations of motion form a strongly hyperbolic system when written in the generalized harmonic formulation we employ in our code.

The scalar field equations and Friedmann equations are then

$$\phi'' = - a^6 V_{,\phi},\tag{4.4a}$$

$$\chi'' = 0,\tag{4.4b}$$

$$\mathcal{H}' = 16\pi a^6 V(\phi),\tag{4.4c}$$

$$\mathcal{H}^2 = \frac{8\pi}{3}\left(\phi'^2 - \chi'^2 + 2a^6 V(\phi)\right).\tag{4.4d}$$

where the $'$ is the derivative with respect to the harmonic time coordinate t related to proper time by $d\tau \equiv a^3 dt$, and $\mathcal{H}$ is the harmonic Hubble parameter

$$\mathcal{H} \equiv \frac{a'}{a} \equiv a^3 H,\tag{4.5}$$

where remember H is the Hubble parameter defined with respect to the proper time $H \equiv (da/d\tau)/a$. We define effective energy densities ρ and pressures P for the two scalar fields:

$$\rho_\phi \equiv \dot{\phi}^2 + 2V, \qquad \rho_\chi \equiv -\dot{\chi}^2, \qquad P_\phi \equiv \dot{\phi}^2 - 2V, \qquad P_\chi = -\dot{\chi}^2,\tag{4.6}$$

where $\dot{f} \equiv df/d\tau$. The total effective equation of state is

$$w = \frac{P_\phi + P_\chi}{\rho_\phi + \rho_\chi} = -1 + \frac{16\pi}{3H^2}\left(\dot{\phi}^2 - \dot{\chi}^2\right),\tag{4.7}$$

so $w < -1$ if $|\dot{\chi}| > |\dot{\phi}|$. A requirement for having a nonsingular bounce is that $w < -1$, which coincides with violation of the NCC. For example, if we consider the null vector $k^\mu \partial_\mu \equiv \left((1/a^3)\partial_t + (1/a)\partial_x\right)/\sqrt{2}$, we then have

$$R_{\mu\nu}k^\mu k^\nu = -\dot{H} \quad \left(= 8\pi\left(\dot{\phi}^2 - \dot{\chi}^2\right)\right).\tag{4.8}$$

When the NCC holds, we see that $\dot{H} < 0$, so that we have cosmic deceleration during expansion $(H > 0)$, or cosmic acceleration during contraction $(H < 0)$. When the NCC is violated, $\dot{H} > 0$, and cosmic contraction can be slowed down, and even reversed to make a bounce.

We also define effective equations of state for the fields ϕ and χ:

$$w_\phi \equiv \frac{P_\phi}{\rho_\phi} = \frac{\dot{\phi}^2 - 2V}{\dot{\phi}^2 + 2V},\tag{4.9a}$$

$$w_\chi \equiv \frac{P_\chi}{\rho_\chi} = 1.\tag{4.9b}$$

From the Friedmann equations (4.4), one can determine that the energy density of the field f scales as $\rho_f \propto a^{-3(1+w_f)}$.

4.2.2 Initial conditions

For our initial conditions, we first set the free initial data by superimposing the homogeneous initial conditions for the cosmological scalar fields and metric with the metric of a (rotating) black hole spacetime. We then solve the constraint equations for the full metric using a conformal thin sandwich solver [131] (see appendix C.1 for more details).

For the cosmological free initial data, we consider an initially contracting FLRW universe dominated by the canonical scalar field ϕ (that is, with the initial condition $\rho_\chi \ll \rho_\phi$). In this limit, with the potential $V = V_0 e^{-c\phi}$, ϕ can obey a scaling solution such that the effective equation of state is roughly constant and equal to $w_\phi = \frac{c^2}{3\sqrt{16\pi}} - 1$ [21] (see more generally [252, 178, 80]). For $c > \sqrt{96\pi}$ and $V_0 < 0$, the scaling solution in a contracting universe is *ekpyrotic*: the contracting solution is a dynamical attractor, and density perturbations are smoothed out in each Hubble patch during contraction [159, 222, 139, 190, 108, 191]. In this limit $w_\phi \geq 1 = w_\chi$, so if $\rho_\phi > \rho_\chi$ initially during contraction, it remains so for all remaining time (recall $\rho_f \propto a^{-3(1+w_f)}$), and there cannot be a bounce. We instead consider the scenario where $c < \sqrt{96\pi}$ and $V_0 > 0$ so that $w_\phi < 1 = w_\chi$, which is required in order to obtain a nonsingular bounce with the massless ghost field we consider [21, 336]. As a result, the asymptotic, contracting, solution is *not* an attractor and the initial condition must be fine-tuned in order to keep w_ϕ constant during the contracting phase. We justify this by noting that our main goal is to just explore the bouncing phase, and not to give a completely realistic description of a bouncing cosmology.

Setting $c < \sqrt{96\pi}$ implies $w_\chi > w_\phi$, so the negative energy density of χ—which we choose to be initially negligible—grows faster than the positive energy density of the canonical field during the contraction. Because of this, the total scalar field energy density $\rho_\phi + \rho_\chi$ eventually goes through zero, and the sign of $\dot{a}$ switches from being negative to being positive. At this point, the universe goes from contraction to expansion. From the Friedmann equations (4.4), we see that once expansion has begun, the ghost field energy quickly diminishes and becomes negligible again compared to the energy density of ϕ [21, 336, 335].

In (4.10), we present our choice of asymptotic FLRW initial data, which, as discussed above, is fine-tuned to allow for the asymptotic cosmological value of w_ϕ to remain roughly constant during contraction up until the bouncing phase. The initial values for ϕ, ϕ', χ, χ', a, and a' are:

$$\phi(0) \equiv \phi_0 = 0, \quad \dot{\phi}_0 = -a_0{}^3 \sqrt{\frac{32\pi c^2 V_0}{96\pi - c^2}}, \tag{4.10a}$$

$$\chi(0) \equiv \chi_0 = 0, \quad \dot{\chi}_0 = a_0{}^3 \sqrt{\frac{12V_0}{(96\pi - c^2)\eta_0}}, \tag{4.10b}$$

$$a(0) \equiv a_0 = 1, \quad \dot{a}_0 = -a_0{}^4 \sqrt{\frac{2V_0(\eta_0 - 1)}{(96\pi - c^2)\eta_0}}. \tag{4.10c}$$

Here $\eta_0 \equiv \eta(0)$ is the initial value of the ratio between the energy densities of the two scalar fields [5]

$$\eta \equiv \left| \frac{\rho_\phi}{\rho_\chi} \right|. \tag{4.11}$$

We compute ρ_ϕ, ρ_χ in the code using formulas (4.12) and (4.14).

In a similar fashion to [336], we choose $c = \sqrt{48\pi}$ so that ϕ initially behaves like matter with $w_\phi = 0$. Such a matter-like contracting phase can generate scale invariant adiabatic perturbations that would seed structure formation in the early expansion phase.

4.3   Overview of numerical method and diagnostics

We evolve the system (4.2) nonlinearly using the harmonic formulation, and work with an axisymmetric spacetime. We spatially compactify our numerical domain, and evolve the boundary using the homogeneous FLRW equations of motion (4.4). See appendix C.1 for a more thorough discussion on our numerical methods.

In order to characterize our results, we make use of several diagnostic quantities. We define the following stress-energy tensors

$$T_{\mu\nu}{}^{(\phi)} = 2\nabla_\mu\phi\nabla_\nu\phi - g_{\mu\nu}\left(\nabla^\alpha\phi\nabla_\alpha\phi + 2V\right), \tag{4.12a}$$

$$T_{\mu\nu}{}^{(\chi)} = -2\nabla_\mu\chi\nabla_\nu\chi + g_{\mu\nu}\nabla^\alpha\chi\nabla_\alpha\chi, \tag{4.12b}$$

so that the Einstein equations read

$$R_{\mu\nu} - \frac{1}{2}g_{\mu\nu}R = 8\pi\left(T_{\mu\nu}^{(\phi)} + T_{\mu\nu}^{(\chi)}\right). \tag{4.13}$$

From $T_{\mu\nu}{}^{(\phi)}$ and $T_{\mu\nu}{}^{(\chi)}$ we define the corresponding energy densities

$$\rho = n^\mu n^\nu T_{\mu\nu} \tag{4.14}$$

where n^μ is the time-like unit normal vector to hypersurfaces of constant time. We additionally compute the local expansion rate

$$H_K \equiv -\frac{K}{3}, \tag{4.15}$$

where K is the trace of the extrinsic curvature on each constant t time slice (as in, e.g., [127, 126] or chapter 3). We note that H_K asymptotes to H at the boundary of our domain

$$H = \lim_{r\to\infty} H_K, \tag{4.16}$$

---

[5]Note that in chapter 3 η was used to refer to the conjugate momentum of scalar field

where r is the proper circumferential radius [6] (see equation (4.18)). We define an effective scale factor on each time slice

$$a_{\text{eff}}(t, \vec{x}) \equiv |\gamma_3|^{1/6} \tag{4.17}$$

where γ_3 is the determinant of the (three-dimensional) metric intrinsic to each constant time hypersurface. We are mainly interested in computing (4.14) to (4.17) on the black hole surface, and at different coordinate radii far away from the black hole. For non-rotating black holes, we track their values as a function of the distance from the center of the black hole. We compare the values to their homogeneous counterpart given by (4.6) and (4.4d). In axisymmetric spacetimes, the coordinate radius on the equator r_{co} is related to the proper circumferential radius r through the relation

$$r\left(t, \theta = \frac{\pi}{2}\right) = \sqrt{\gamma_{zz}\left(t, \theta = \frac{\pi}{2}\right)} \; r_{\text{co}}(t). \tag{4.18}$$

where γ_{zz} is the value of the spatial metric along the symmetry axis. In spherical symmetry, Eq. (4.18) reduces to the areal radius. To characterize the boundaries of black holes in our dynamical setting, we will consider two surfaces: event horizons and apparent horizons. The black hole event horizon is the boundary behind which null rays no longer escape to the asymptotic region. We compute its approximate location by integrating null surfaces backwards in time [22, 241, 325] (we restrict this to spherically symmetric cases, where it is sufficient to consider spherical null surfaces). We define the apparent horizon of the black hole, on the other hand, on each time slice, as the outermost marginally outer trapped surface, i.e. the surface for which the outgoing null expansion $\theta_{(l)}$ vanishes and the inward null expansion $\theta_{(n)}$ is negative and such that $\theta_{(l)} > 0$ immediately outside the black hole (and $\theta_{(l)} < 0$ immediately inside) [7].

In analogy to black hole apparent horizons, we will also use marginally trapped surfaces to define the location of the *cosmological apparent horizon*. We will refer to this simply as the cosmological horizon, but we note that this is not to be confused with the *event horizon* or the *particle horizon* commonly used in cosmology. During the contracting phase, the cosmological horizon is defined as the surface for which the outgoing null expansion $\theta_{(l)}$ vanishes, and the inward null expansion $\theta_{(n)}$ is negative, but $\theta_{(l)} > 0$ immediately inside the cosmological horizon. During the expanding phase, the cosmological horizon is defined as the surface for which the ingoing null expansion $\theta_{(n)}$ vanishes and the outward null expansion $\theta_{(l)}$ is positive and such that $\theta_{(n)} > 0$ outside the cosmological horizon.

As was already pointed out in chapter 2.2.2, in a homogeneous spacetime, the cosmological apparent horizon is simply the sphere with coordinate radius equal to the comoving Hubble radius, $R_H = (aH)^{-1}$, yielding an area $\mathcal{A}_{\text{C}} = 4\pi a^2 R_H^2 = 4\pi H^{-2}$. For our black hole spacetimes, we will always take the cosmological horizon to be centered on the black hole. This is because we are interested in the dynamics in the vicinity of the black hole,

---

[6]Note r is used to refer to the uncompactified coordinate radius in chapters 2 and 5

[7]In our particular setup, we define the outgoing (ingoing) direction as the direction pointing from the origin (asymptotically FLRW region) to the asymptotically FLRW region (the origin)

and it is this surface that is the most relevant to understanding the behavior of the black hole horizon. Figure 4.1 shows the outward null expansion (left) during the contracting phase (where $H < 0, \dot{H} < 0$) and the inward null expansion (right) during the expanding phase (where $H > 0, \dot{H} < 0$). See appendix C.1 for more details on our numerical implementation and appendix C.2 for more details on the various definitions of horizons we use.
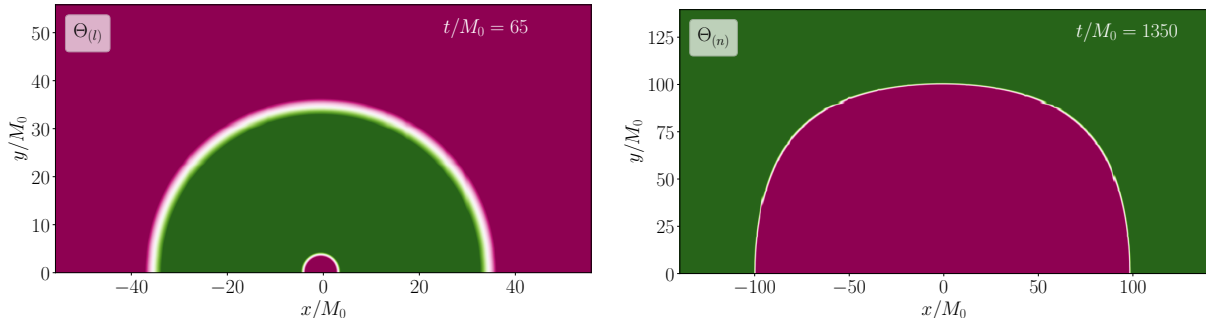
Figure 4.1: The outward null expansion, $\Theta_{(l)}$ at $t = 65M_0$, during the contracting phase (left) and the inward null expansion, $\Theta_{(n)}$ at $t = 1350M_0$, during the expanding phase (right) for a black hole with initial mass,M_0, such that the Hubble radius of the background cosmology $R_H \equiv |H^{-1}|$ shrinks from an initial value of $R_{H,0} = 75r_{BH,0}$ to $4.34r_{BH,0}$ (here $r_{BH,0} = 2M_0$ is the initial black hole radius). The color-scheme is such that white represents a vanishing expansion and pink (green) a negative (positive) value of corresponding null expansion.

From the area of the black hole apparent horizon $\mathcal{A}_{BH}$, we define an areal mass $M_A \equiv \sqrt{\mathcal{A}_{BH}/(16\pi)}$. The spacetime we study here violates the NCC, and thus we expect to find instances where M_A decreases. Similarly, the second law of black hole thermodynamics states that so long as the NCC is satisfied, the area of a black hole event horizon must increase into the future [179]. This can be extended to the cosmological setting assuming that the universe does not again collapse, and a notion of infinity can be defined [86]. However, here we are evolving a black hole in a spacetime that violates the NCC, and find that the event horizon does decrease in area.

The cosmological and black hole apparent horizons that we find on each time slice can also be thought of as foliations of three dimensional surfaces called holographic screens [62, 64, 65] or Marginally Trapped Tubes (MTTs) [29] in general, and dynamical horizons [182, 30, 31] if they obey certain extra conditions (we review the definitions of these concepts in appendix C.2). Though one can formulate area laws for these surfaces, in spherical symmetry they do not place any constraints on whether the area increases to the future. We keep track of the MTTs corresponding to the cosmological and black hole apparent horizons, and in particular, compute when they are spacelike or timelike in nature.

For the black holes, we compute the equatorial circumference of the horizons c_{eq}, and define their corresponding equatorial radii $r_{eq} = c_{eq}/2\pi$, which in the case of spherical

symmetry is also equal to the areal radius, $r_A = \sqrt{\frac{A_{\mathrm{BH}}}{4\pi}}$. When studying rotating black holes we can also associate an angular momentum to the apparent horizons

$$J_{\mathrm{AH}} \equiv \frac{1}{8\pi} \int \hat{\phi}_i K^{ij} dA_j, \tag{4.19}$$

where $\hat{\phi}_i$ is the axisymmetric Killing vector, and, using the Christodoulou formula, we can define a mass [99]

$$m_{\mathrm{BH}} \equiv \left(M_A{}^2 + \frac{J_{\mathrm{AH}}^2}{4M_A{}^2} \right)^{1/2} \tag{4.20}$$

Since the scalar fields do not carry any angular momentum in axisymmetry, the total angular momentum of the black hole remains constant throughout the evolution of our spacetime. Thus, we will only be interested in the total mass and circumferential radius of the black hole.

4.4 Results

We begin by studying the evolution of non-spinning black holes in an asymptotically bouncing universe (section 4.4.1-4.4.3) using the method described in section 4.3. Though we do not explicitly enforce spherical symmetry, we find no evidence of any instabilities that break that symmetry if our initial data respects it. We consider non-spinning black holes in section 4.4.4.

We find that the qualitative behavior of our solutions can be divided into two regimes, which can be distinguished by the ratio of the areal radius of the initial black hole horizon, $r_{\mathrm{BH},0}$ and the minimum size of the Hubble radius of the background cosmology $R_{\mathrm{H,min}} \equiv \min_t |1/H| = -1/H_{\mathrm{min}}$ (where $H_{\mathrm{min}} < 0$ is the maximum contraction rate). When $R_{\mathrm{H,min}}/r_{\mathrm{BH},0} \gtrsim 3.5$, the black holes pass through the bounce freely. When $R_{\mathrm{H,min}}/r_{\mathrm{BH},0} < 3.5$, we find that the locally defined cosmological and black hole apparent horizons merge, and cease to exist for a period of time during the contracting and bouncing phase. We note that the horizons merger at $R_{\mathrm{H,min}}/r_{\mathrm{BH},0} > 1$, as the black hole grows in size during the contraction phase (see figures 4.4,4.7; we will discuss this more in the following subsections).

For every initial data setup we considered, we find that the black hole continues to exist after the bounce phase ends: the late-time evolution always consists of a black hole in an expanding universe with the ghost field energy density decreasing at a faster rate than the canonical scalar field energy. Moreover, we find that the late time black hole mass remains similar to the initial black hole mass, regardless of the ratio of the initial black hole radius and minimum Hubble patch radius. In the following sections, we quantify these observations and extrapolate our findings to the regime where the Hubble radius shrinks to a much smaller size compared to the radius of the black hole.

4.4.1 Small black hole regime

We first consider solutions where $R_{\mathrm{H,min}}/r_{\mathrm{BH,0}} \gtrsim 3.5$ (see above for definitions). In figure 4.2, we show the Hubble parameter (left panel) computed from (4.15) and the ratio of scalar fields (right panel) computed from (4.11),(4.12) and (4.14) as a function of harmonic time for different coordinate radii. We also plot the value these quantities take at spatial infinity, where we assume homogeneous FLRW boundary conditions (see section 4.2.1). While the bounce seems to be pushed to slightly earlier harmonic times when the black hole is present, most of the local cosmological evolution remains unaffected by the presence of the black hole and follows the same qualitative evolution as the background cosmology (section 4.2.2). To determine how the cosmology is affected in a region close to the black hole, in figure 4.3 we plot the spatial dependence of η and $H_K/|H_{\mathrm{min}}|$ as a function of distance again along the equator at different times. Although the local expansion rate and the ratio of the energy densities can differ from their background values by up to $15-60\%$ and $9-16\%$ respectively, beyond $r \sim 10-25 r_{\mathrm{BH,0}}$ both quantities quickly asymptote to their respective background values. Note that the coordinate radius differs from the proper radius by the local scale factor; see eq. (4.18). The effective scale factor computed from (4.17) at different coordinate radii is plotted in figure C.2 (see appendix C.1). Again we find that far enough from the black hole, the value of scale factor remains largely unaffected by the presence of the black hole. We caution that these quantities will also be subject to gauge effects—in particular from our choice of the lapse function (see section C.1). As we describe below, towards the end of the simulations we find strong variation in the rate of which time advances at different spatial points.
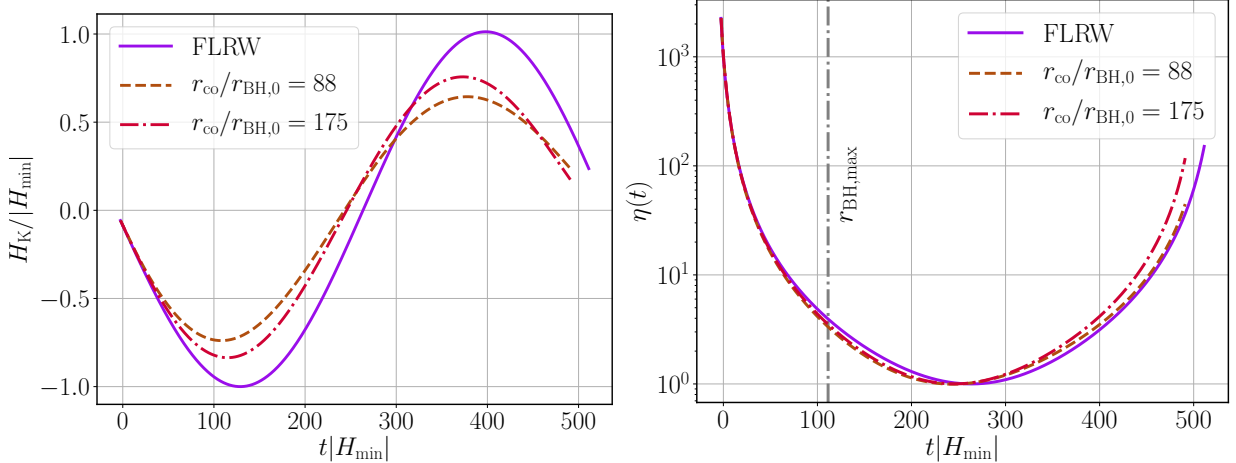
Figure 4.2: The expansion rate $H_K/|H_{\min}|$ computed from (4.15) (left) and the ratio of the matter to ghost field $\eta(t)$ given by (4.11) (right) for a black hole with initial mass such that the Hubble radius of the background cosmology $R_{\mathrm{H}} \equiv |H^{-1}|$ shrinks from an initial value of $R_{\mathrm{H},0} = 75 r_{\mathrm{BH},0}$ to $4.34 r_{\mathrm{BH},0}$ (here $r_{\mathrm{BH},0}$ is the initial black hole radius). The solid line shows the corresponding background solution, and the dashed and dash-dotted lines show the values at different coordinate radii. The vertical grey line is the time at which the black hole reaches its maximum areal radius as measured by the apparent horizon. Notice that the black hole reaches its maximum size slightly before the universe at large scales bounces, as the ghost field begins to dominate at an earlier time the closer one gets to the black hole horizon. The slight difference in the maximum absolute value of the FLRW value of $H_K/|H_{\min}|$ at $t|H_{\min}| \sim 120, 400$ is due to numerical error in our integration.

We next present several results regarding the behavior of the area of the black hole, as measured by either the event or apparent horizon. Naively, one expects the accretion of the canonical/ghost field to result in an increase/decrease in mass of the black hole [35]. That being said, it is less clear how a black hole embedded in a cosmology driven by a canonical/ghost field may behave [155, 156].

Figure 4.4 depicts the evolution of the black hole's areal radius. We find that during the contracting phase prior to the bouncing/NCC violation phase, the canonical scalar field energy density exceeds that of the ghost field; see figure 4.2 and the solid purple curve in figure 4.3. The black hole's proper area increases during this time; (first region in figure 4.4 where $H < 0, \dot{H} < 0$). Once the bouncing phase starts ($t|H_{\min}| \sim 120$ in figure 4.2), the black hole starts to shrink as one may expect since the ghost field energy in this regime is comparable to the canonical scalar field energy density (second region where $H < 0$ and $\dot{H} > 0$ in figures 4.2 and 4.3). Near the end of the bouncing phase the universe is expanding (region where $H > 0$ and $\dot{H} < 0$), yet the black hole's size is still shrinking in this region, as the ghost field energy density still dominates over the canonical scalar field energy density in the region near the black hole (in other words, $\eta < 1$ in the region close to the black hole, see figure 4.3), although at an increasingly slower rate as the ghost

81
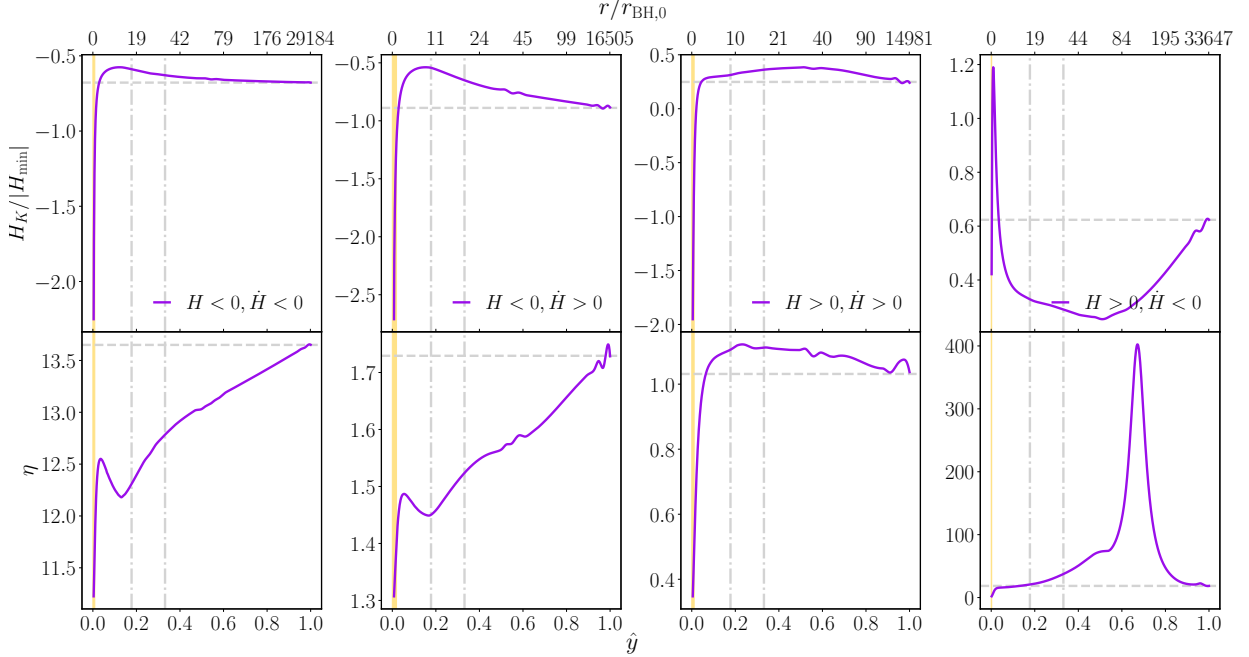
Figure 4.3: The expansion rate $H_K/|H_{\min}|$ (top) and the ratio of the energy densities of the matter to ghost field $\eta(t)$ given by (4.11) (bottom) for the black hole considered in figure 4.2 as a function of the compactified coordinate radius, $\hat{y}$ (see equation (C.1)), at different times during the evolution. Note that $\hat{y}$ lies along the "equator" of the black holes in our simulations. Also shown on the top axis is the proper radius of the spacetime computed from (4.18). The dashed horizontal grey lines indicate the corresponding background values at spatial infinity, the vertical dash-dotted lines correspond to the coordinate radii shown in figure 4.2, and the shaded region represents the black hole.

field energy density quickly diminishes in time. After the end of the bouncing phase, the universe continues to expand, the ghost field decays to dynamically irrelevant values, and the black hole begins growing in size (fourth region where $H > 0$ and $\dot{H} < 0$ and the dotted purple curve).

The left panel of figure 4.4 also shows the areal radius of the cosmological horizon. We see that during the contracting phase, the cosmological horizon shrinks from $r_{C,0} = 75 r_{BH,0}$ to a minimum radius of $r_{C,\min} = 4.34 r_{BH,0}$ at $t \sim 50 r_{BH,0}$. This is similar to the value the Hubble radius ($R_H \equiv |1/H|$), would shrink to in the absence of a black hole. This value is indicated by the diamond in figure 4.4. From this we conclude that—at least in this regime—the presence of the black hole does not qualitatively change the dynamics of the spacetime. Past this point of closest encounter, the cosmological horizon tends to $r_C \to +\infty$ which defines the location of the bounce ($\lim_{H\to 0} 1/H = \infty$). Once the universe switches from contraction to expansion, the cosmological horizon is defined as the location where the ingoing null expansion vanishes and outgoing null expansion is positive. After the bounce, the cosmological horizon at first shrinks to a minimum size before re-expanding
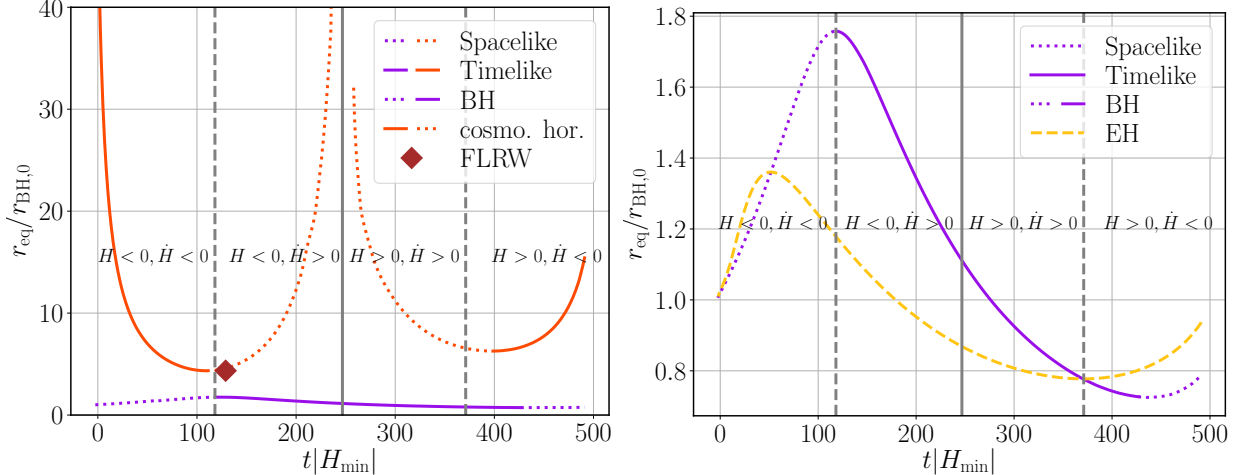
Figure 4.4: *Left*: The areal radii of the black hole (purple) and cosmological (orange) apparent horizons computed as described in section 4.3 for the black hole in figure 4.2. The line style reflects the signature of the marginally trapped tube or holographic screen (solid is timelike, dashed is spacelike). The diamond indicates the time and value to which the Hubble radius would shrink in the absence of a black hole. *Right*: The apparent horizon of the black hole (purple) and the corresponding event horizon (yellow dashed). The vertical solid line indicates the bounce, while the region between the dashed lines is the bouncing phase (where the NCC is violated).

to $+\infty$. We note that the areal radius of the cosmological horizon is no longer symmetric about the bounce once a black hole is present.

We also compute the signature of the MTTs associated with the horizons (see appendix C.2 for definitions), which we plot in figure 4.4.

First we study the properties of the black hole MTT in more detail. Using the terminology of appendix C.2, the black hole is a future marginally trapped tube foliated by future marginally outer trapped surfaces (alternatively called a future holographic screen). The area law of dynamical horizons states that if the MTT is spacelike (i.e. if it is a dynamical horizon), then the area of the black hole should increase in the outward radial direction, while if the MTT is timelike (i.e. we have a timelike membrane with $\Theta_{(n)} < 0$), then the area should increase into the past. Looking at figure 4.4 we find that (as expected) these laws are obeyed at all times, even during the bouncing phase.

We next look at the cosmological horizon. We consider the contracting and expanding phases separately. During the contracting phase, the cosmological horizon is a MTT foliated by future marginally inner trapped surfaces (alternatively, it is a future holographic screen). From the area law of future holographic screens [64, 65], we expect the cosmological horizon to obey the same area law as the black hole during the contracting phase. Our findings agree with this expectation: we find that the cosmological horizon is timelike when it decreases in time and spacelike when it increases in the outward direction. During the

83

expanding phase, however, the cosmological horizon ceases to be a MTT. Instead, we find that it satisfies the definition of a past holographic screen (as the ingoing null expansion now vanishes). From [64, 65], we still expect its area to increase in the future on timelike portions and in the outward direction on spacelike portions. Again we find that this is satisfied at all times during the expanding phase.

We conclude by looking at the event horizon shown in the right panel of figure 4.4. Our main finding here is that the event horizon no longer lies outside the apparent horizon at all times. This is a result of the violation of the NCC [181]. Interestingly, this behavior begins not during the bouncing phase of cosmological evolution (between the two dashed grey lines) when the NCC is violated, but *before* the bouncing phase has begun. This is because the event horizon is not a quasi-local quantity, so it can "anticipate" the bouncing/NCC violation phase. In general, we find that the event horizon always increase until it crosses the apparent horizon of the black hole, after which it decreases. Once the bouncing phase ends, the event horizon crosses the apparent horizon again, after which it starts increasing and remains larger than it for all future times.

We were not able to evolve the spacetime to arbitrarily large proper times. We ascribe this to gauge artefacts which impede the stable numerical evolution of the solution. In particular, the lapse function appears to become distorted in the spacetime region between the black hole and the asymptotically homogeneous regime, which causes that interior region to advance in time much faster compared to elsewhere in the simulation. (This is evident in the rightmost panels of figures 4.2, 4.5, and C.2.) That being said, based on the simulations we have run, we conjecture that the black hole asymptotes to close to its initial mass at $t \to \infty$ with no significant gain or loss of energy. That is, the end state is described by a black hole embedded in an expanding matter like FLRW universe with a negligible amount of ghost field and matter energy density. This is illustrated in figure C.3 of appendix C.1 where we consider a black hole with half the mass of the one depicted in figure 4.4, i.e. we consider a black hole such that the ratio of the minimum Hubble radius to the initial radius of the black hole is $R_{\mathrm{H,min}}/r_{\mathrm{BH,0}} = 8.69$. Figure C.3 shows that, overall, the black hole's size changes by a negligible amount. In this particular case, the final size of the apparent horizon of the black hole is $\sim 6\%$ larger that its initial value, the small difference being an artefact of the initial data. More importantly, figure C.3 also shows that the event horizon asymptotes to the apparent horizon at late times.

4.4.2 Large black hole regime

We next consider solutions where $R_{\mathrm{H,min}}/r_{\mathrm{BH,0}} < 3.5$. The nonlinear evolution of one particular case is shown in figure 4.5. As is the case for the lower initial mass evolutions (figure 4.2), we see that the cosmological evolution remains unaffected far away from the black hole. The bounce is pushed to even earlier times, as one may expect since a large black hole could presumably accelerate the rate of cosmological contraction. Figure 4.6 shows that in the region near the black hole apparent horizon, the local expansion rate

and the ratio of the energy densities now differ from their background value by up to 15–75% and 13–60%. Beyond $r \sim 2$–$12 r_{\text{BH},0}$, both quantities asymptote to their respective background values.
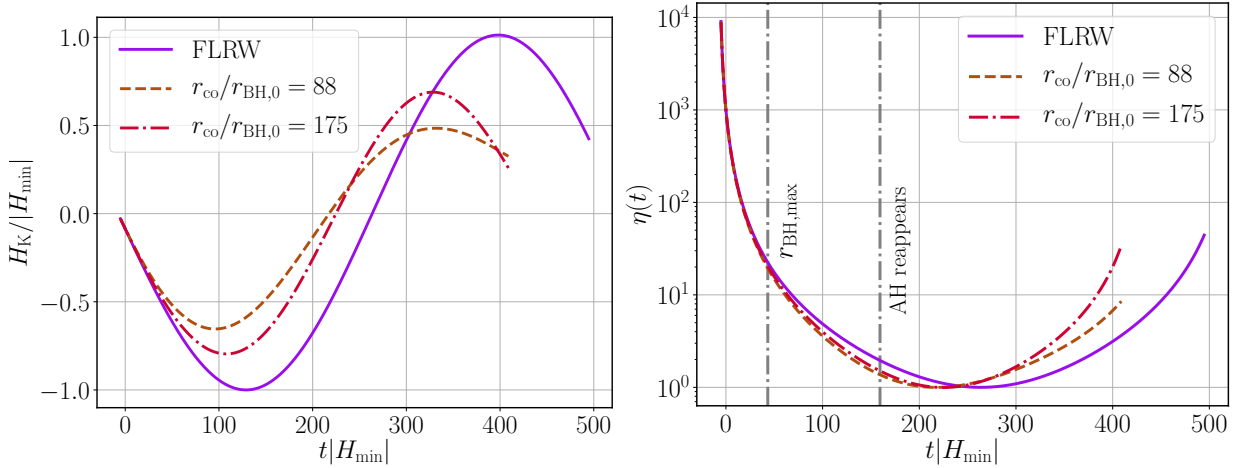
Figure 4.5: Same as figure 4.2, but for a black hole with initial mass such that the Hubble radius of the background cosmology $R_{\text{H}} \equiv |H^{-1}|$ shrinks from an initial value of $R_{\text{H},0} = 75 r_{\text{BH},0}$ to $2.17 r_{\text{BH},0}$ (here $r_{\text{BH},0}$ is the initial black hole radius).

The behavior of the black hole and cosmological apparent horizons, which is shown in figure 4.7, is qualitatively different for the large black hole initial data as compared to the small black hole initial data ($R_{\text{H,min}}/r_{\text{BH},0} \gtrsim 3.5$). Similar to the cases studied in the section 4.4.1, the cosmological horizon shrinks at first. Unlike those earlier cases though, it eventually merges with the expanding black hole apparent horizon. Following the merger, the spacetime has no apparent horizons for some time until they re-emerge. After that, the cosmological and black hole apparent horizons follow a similar trajectory to the horizons studied in section 4.4.1 during the cosmological expansion phase.

The merging of black hole and cosmological apparent horizons has been observed in McVittie spacetimes [144, 145] (see also appendix C.3) and can be interpreted the following way. As the apparent horizon of the black hole grows and the cosmological horizon shrinks during the contraction of the universe, we reach a point in time at which the black hole horizon coincides with the cosmological horizon. At this point, one cannot distinguish between the black hole and the cosmological horizon (recall that during the contraction the outward null expansion is negative outside of the cosmological horizon). A finite time later, before the bounce, but after the background Hubble radius reaches its minimum size, the effective Hubble radius has increased to a sufficiently large value so that the black hole solution again fits within the cosmological horizon. At this point, the cosmological and black hole apparent horizons reappear. We note that the black hole event horizon persists throughout the evolution of the spacetime, so in this sense the black hole never disappears; see figure 4.7. We next investigate the physical properties of this process in more detail.
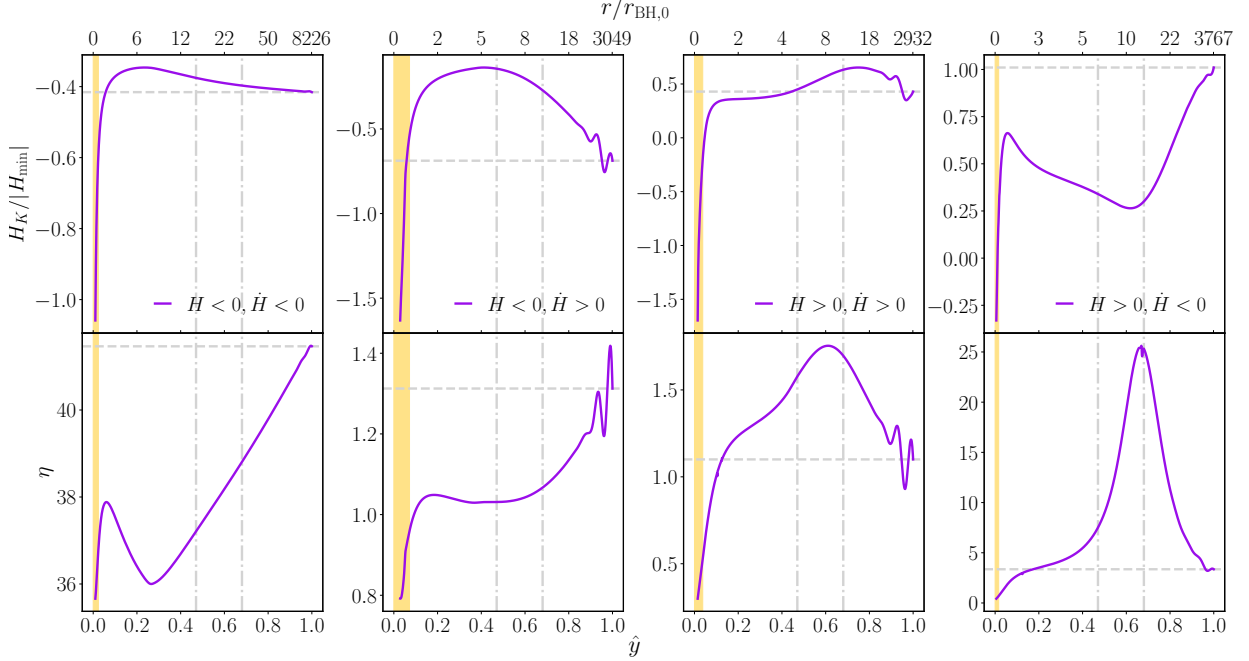
Figure 4.6: Same as figure 4.3, but for the case with $R_{\mathrm{H,min}}/r_{\mathrm{BH,0}} = 2.17$ also shown in figure 4.5.

We first address the question of whether a naked singularity forms after the black hole and cosmological horizons collide [155, 145, 144]. The formation of a naked singularity would signal a breakdown of the theory—either through the formation of a blowup in curvature, or through necessitating new boundary conditions to be set at the singularity boundary [280]. Our simulations suggest no naked singularity is formed. More concretely, the outward null expansion during this period is negative everywhere, so the entire spacetime is essentially trapped, and no new boundary conditions need to be specified. In particular, we can continue to excise a central region corresponding to the inside of the black hole. Additionally, considering the event horizon shown in figure 4.7, we see that it remains finite at all times. Note that just like in the case studied earlier in section 4.4.1, the event horizon is smaller than the apparent horizon before, and during the bouncing phase, and turns around when it crosses the apparent horizon.

We next consider the behavior of the marginally (anti-)trapped tubes and their signature, shown in figure 4.7. Note that while the black hole MTT is spacelike and increasing in time before it merges with the cosmological horizon, when it reappears from the merger, its signature remains spacelike even though its area continues to decrease in time. Since the area of the black hole always increases in the outward radial direction, this implies that while the outward direction points into the future before the merger, it points into the past when it reappears. The black hole apparent horizon undergoes another signature change at the bounce (indicated by the grey vertical solid line) after which it behaves like the case studied above (i.e. the signature of the horizon becomes timelike, and decreases as we
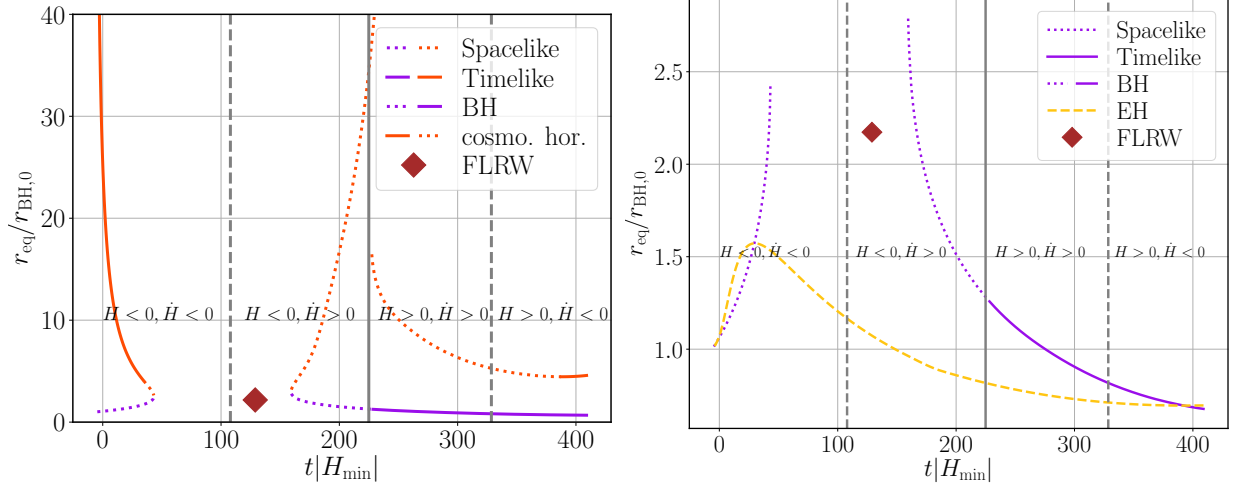
Figure 4.7: Same as figure 4.4 but for a black with initial mass such that the Hubble radius of the background cosmology $R_{\mathrm{H}} \equiv |H^{-1}|$ shrinks from an initial value of $R_{\mathrm{H},0} = 75 r_{\mathrm{BH},0}$ to $2.17 r_{\mathrm{BH},0}$ (here $r_{\mathrm{BH},0}$ is the initial black hole radius). Notice that the location where $H = 0$ (that is, where the Hubble radius diverges) does not exactly coincide to where the cosmological horizon blows up, as the cosmological horizon is measured locally (in the interior of the computational domain), while $H = 0$ is determined by the asymptotic cosmological evolution. For more discussion on how we define the cosmological horizon, see section 4.3

evolve forwards in time). Similarly, we find that the cosmological horizon follows the same trend as the case in section 4.4.1, except for a brief period of time just before it merges with the black hole apparent horizon: here the horizon signature becomes spacelike. We see that the cosmological horizon and black hole apparent horizons have the same signature when they annihilate and re-emerge.

A natural question to ask is whether the collision of the apparent horizons during the contraction phase is an artefact of the particular matter model we use, or is a more general consequence of a contracting universe. To explore this, we consider the same initial conditions as the ones used in figure 4.5, but now evolve only with the canonically normalized scalar field. The results of this are plotted in figure 4.8. We find that during contraction, the apparent horizons, with and without the presence of a ghost scalar field, behave in a similar fashion. In both cases, the black hole apparent horizon merges with the cosmological horizon at the same areal radius. This is in line with our earlier observation that the black hole horizon's size exceeds the cosmological horizon before the bouncing phase starts, (i.e. before the ghost field has a significant impact on the evolution of the system). The black hole and cosmological apparent horizon merge earlier by around $t \sim 2|H_{\mathrm{min}}|$ in the case of contraction without the ghost scalar field. This is consistent with the notion that the accretion of the ghost field should slow down the rate at which the black hole can grow in size, which would delay the time of merger of the two horizon.

Finally, we note that the signature of the cosmological horizon becomes spacelike in this setup just before merging with the black hole horizon for both cases. During this phase of evolution, the cosmological horizon is a dynamical horizon whose area *decreases* with time.
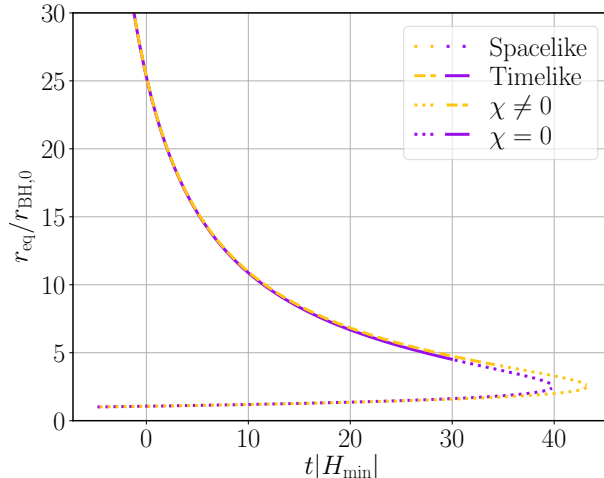
Figure 4.8: Cosmological and black hole apparent horizons from the contracting phase of the same case shown in figure 4.7 (labelled $\chi \neq 0$) compared to a similar case without a ghost field ($\chi = 0$).

4.4.3 Dependence on black hole size

In this section, we explore in more detail how the properties of the spacetime during the bounce change as a function of $R_{\mathrm{H,min}}/r_{\mathrm{BH,0}}$.

As described in section 4.4.1, for initial data where $R_{\mathrm{H,min}} \approx 4.34 r_{\mathrm{BH,0}}$ the black hole apparent horizon persists through the whole bounce, and the spacetime evolution near the black hole qualitatively resembles the asymptotic cosmological evolution. As this behavior will hold to an even greater degree for smaller black holes (relative to $R_{\mathrm{H,min}}$), we are more interested in the opposite regime, considering larger black holes. As mentioned in section 4.1, for astrophysical black holes we expect $R_{\mathrm{H,min}} \ll r_{\mathrm{BH}}$. We find that, when $R_{\mathrm{H,min}} \lesssim 3.5 r_{\mathrm{BH,0}}$, (see section 4.4.2), the black hole apparent horizon collides with the cosmological horizon while the universe is still contracting. In this section, we therefore explore how this behaviour changes as one increases the initial mass of the black hole. We note that for numerical reasons[8], we will restrict to evolutions where $R_{\mathrm{H,min}} > 0.86 r_{\mathrm{BH,0}}$.

---

[8]In particular, we see a large growth in constraint violation near the outer boundary when we increase the initial black hole mass to too large a size. This is likely related to the fact that we set our boundary conditions to be the homogeneous cosmological solutions, and that our runs lacked the resolution near the boundary to resolved the correct falloff of the fields to their asymptotic values.

However, as we argue below, we already see some consistent trends as $r_{\rm BH}$ is varied within this regime.

In the left panel of figure 4.9, we plot the radius of the black hole apparent horizon normalized by its initial value as a function of time. For evolutions where the black hole and cosmological MTTs do not collide, we find that although the area of the apparent horizon always reaches it maximum and minimum values at around the same harmonic time ($t \sim 110 R_{\rm H,min}$ for the maximum value, and $t \sim 440 R_{\rm H,min}$ for the minimum value), the value the maximum and minimum take does change as a function of initial black hole area. Independently of the black hole's initial size, the area of the apparent horizon is close to one around the bounce or in other words around the time where the total energy density of the background cosmology is zero. In the low mass regime, the variation in the black hole's size increases with increasing initial black hole area.

However as the initial size of the black hole increases, the maximum change in the radius of the apparent horizon eventually peaks at a value of $r_{\rm AH,max}/r_{\rm AH,0} \sim 2.6$. In this case, the ratio of the minimum Hubble radius of background cosmology to initial radius of the black hole corresponds to the threshold beyond which the horizons merge. Beyond this peak, although the horizons merge at successively earlier times (and always before the bouncing phase starts), with increasing initial black hole radius, the relative increase in the radius of the apparent horizon when the horizons merge saturates at a value of $r_{\rm AH,max}/r_{\rm AH,0} \sim 2.5$. Within the range of masses we were able to evolve, the apparent horizons always reappear, from which we conjecture that the presence of black holes in bouncing cosmologies do not disrupt the bounce. We were not able to evolve the space time to arbitrarily later proper time but based on all the simulations we have run, we conjecture that the black hole asymptotes to close to its initial radius as $t \to \infty$.

In the right panel of figure 4.9, we plot the radius of the black hole event horizon normalized by its initial value as a function of time. We do not compute the evolution of the event horizon past the bounce for black holes with initial black hole radius such that the minimum Hubble radius is smaller than $R_{\rm H,min} < 2.90 r_{\rm BH,0}$, as for those cases the event horizon cannot be located to the desired accuracy (see appendix C.1 for more details on the computation of the event horizon). For the set of initial radii we do compute, we find that the area of the event horizon reaches a maximum at successively earlier times with increasing initial black hole radius, always before the bouncing phase starts and always when the event horizon crosses the apparent horizon of the black hole. Beyond this point, the event horizon decreases in size, until it crosses the apparent horizon again, after which it starts increasing. This minimum happens at successively earlier times with increasing initial black hole radius. While the maximum size of the event horizon throughout the evolution increases with increasing initial black hole radius, the minimum decreases.

We next argue that the behavior of the event horizon in the region leading up to the bounce (where $H < 0$), can be at least qualitatively captured by studying null rays in the background FLRW spacetime. The reasoning is as follows: It is reasonable to assume that in the regime where $R_{\rm H}/r_{\rm BH,0} \gg 1$, the evolution of null rays near the black hole horizon will

not be greatly influenced by the background cosmological evolution. Likewise, we assume that in the regime where the black hole is "large" ($R_\mathrm{H}/r_{\mathrm{BH},0} \lesssim 1$), the trajectories of null rays exterior to the black hole are more influenced by the cosmological evolution[9], and in the background FLRW spacetime, during the contraction phase, outward radial null rays have decreasing proper radius when they are inside the Hubble radius. Following this line of thought, we integrate null rays backward in time in the background FLRW spacetime given by eq. 4.3, starting from the latest time for which $H < 0$ and $R_\mathrm{H} = r_{\mathrm{BH},0}$. Figure 4.10 shows the trajectories of a few such null rays for different ratios of $R_{\mathrm{H,min}}/r_{\mathrm{BH},0}$. We find that the proper radius of the null rays increases (as we go backwards in time) until the ray crosses R_H, after which it decreases. This is consistent with the behavior of the event horizon in the right panel of figure 4.9 and suggests that, at least for this part of the evolution, the size of the black hole is determined by the evolution of the background cosmology. This simple calculation also shows that as $R_{\mathrm{H,min}}/r_{\mathrm{BH},0}$ decreases, the maximum radius of the null ray increases. This agrees with what we see in our full numerical simulations. Extrapolating this trend to arbitrarily small $R_{\mathrm{H,min}}/r_{\mathrm{BH},0}$ suggests that for arbitrarily large black holes the peak of the event horizon will diverge. However, we are working with a cosmological solution that has undergone an infinite number of e-folds of contraction to the past (see section 4.2.2). If one were to consider a bouncing model that had only had a finite period of contraction (for example if we considered a cyclic cosmology [321]), then the maximum of the event horizon would always be finite.

Evolving forward in time, into the region where the universe is expanding ($H > 0$), we find that the event horizon continues to decrease until it crosses the apparent horizon, at which point it begins to increase in size. However, this behavior can not be captured by integrating the null geodesics in the background spacetime, which suggests that the influence of the black hole on the geometry is more relevant when $H > 0$, and for radii less than $r_{\mathrm{BH},0}$. Due to numerical issues, we are unable to evolve far enough in time to determine if the minimum of the event horizon keeps decreasing and eventually reaches a point where the event horizon ceases to exist as $R_{\mathrm{H,min}}/r_{\mathrm{BH},0} \to 0$.

Finally, we note that (as is shown in figure C.3) one expects the apparent and event horizons to converge to the same value at late times, but for reasons mentioned earlier in this section, we are not able to evolve long enough in time to show this happens for initial data with $R_{\mathrm{H,min}} < 4.34 r_{\mathrm{BH},0}$.

4.4.4 Spinning black holes

Up to this point, we have only considered non-spinning black holes (spherically symmetric spacetimes). However, our methods can be applied equally well to spinning black holes spacetimes. We have considered several such cases, finding the same qualitative behavior

---

[9]For example, we find that when the black hole and cosmological apparent horizons merge (and thus there is no boundary between a trapped and untrapped region), the spacetime dynamics qualitatively resemble that of the background cosmological evolution.
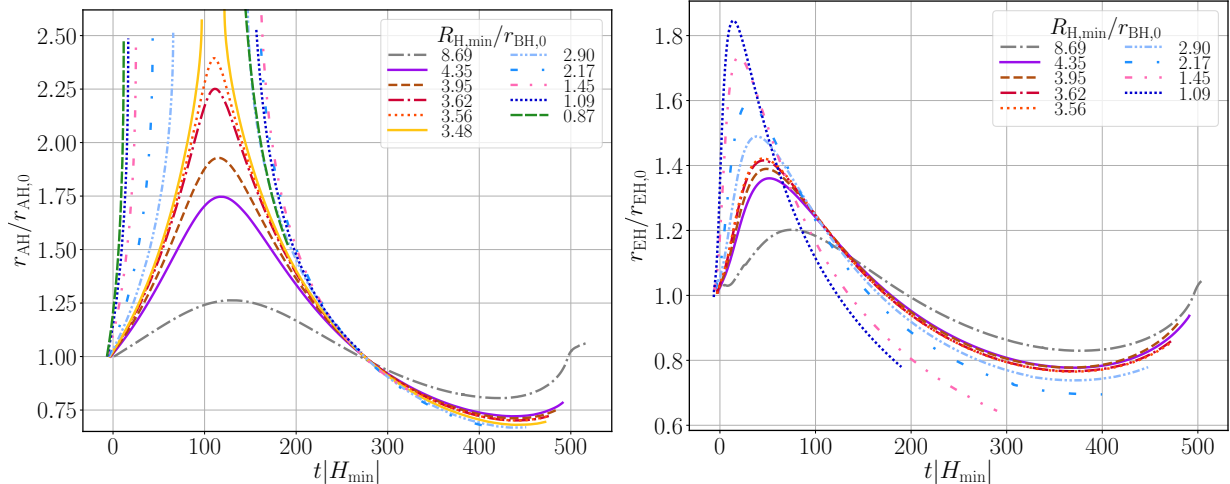
Figure 4.9: Radius of the apparent (left) and event (right) horizon of the black hole over time for different ratios of the minimum Hubble radius to initial black hole radius.

as for non-spinning black hole initial data. We illustrate this with a representative example case: initial data where the black hole is initially spinning with a dimensionless spin value of $a_0 = 0.5$. As we find little difference compared to the spacetimes with non-spinning black holes, here we only present the results for a black hole with $R_{\mathrm{H,min}} = 2.17 r_{\mathrm{BH,0}}$, and the same mass as in section 4.4.2. Figure 4.11 compares the circumferential radius of the black hole along the equator for the spinning and non-spinning cases. We find that the addition of spin causes the horizons to merge at a slightly later time as compared to a comparable non-spinning case. We do not plot the behavior of the asymptotic background cosmology as it is the same regardless of whether the black hole is spinning or not. As was mentioned in section 4.3, the angular momentum of the black hole is constant since the scalar field does not carry angular momentum.

4.5 Discussion and conclusion

We have considered the first numerical evolution of black holes through a nonsingular bouncing cosmology. As in [21, 336], we worked with a model that has two scalar fields: a canonically normalized field with an exponential potential and a ghost field. We have additionally considered asymptotically cosmological initial data that is tuned to allow for a matter-like (effective equation of state $w = 0$) contraction which is then followed by a bounce that ends with cosmological expansion. In [336], translational symmetries were assumed in two spatial directions, which precludes the formation of black holes. By contrast, in this work we considered axisymmetric spacetimes which allowed us to study the behavior of black holes through a bounce. While only a small fraction of Hubble patches are expected to have a black hole during the late stages of ekpyrotic contraction
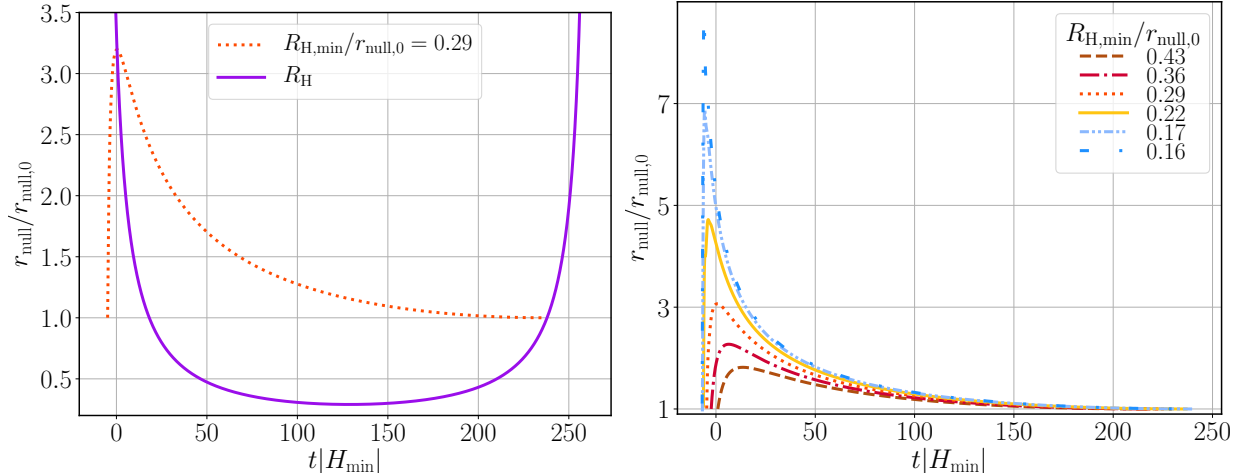
Figure 4.10: Proper radius of outward, radial null rays in the background FLRW spacetime (described in section 4.2.1). The left panel shows an example null ray that begins at a specified radius $r_{\mathrm{null},0}$, increases until it crosses the Hubble radius (during contraction), and then decreases until it reaches the Hubble radius again at $r_{\mathrm{null},0}$. The right panel shows the same thing for different ratios of the minimum Hubble radius to $r_{\mathrm{null},0}$.

[43, 94, 297], our setup allows us to examine the robustness of the ghost-field bounce, which in turn serves as an effective classical model of NCC violation.

We found two qualitatively different kinds of spacetime evolution, which depended on the ratio of the minimum Hubble radius of the background cosmology to the initial radius of the black hole. For black holes with initial radius smaller than ~ 3.5 times the minimum size of the Hubble radius of the background cosmology, the black hole passes through the bounce freely and the background cosmology remains largely unaffected (see section (4.4.1)). Beyond this limit, we found that while regions far away from the black hole still bounce freely, regions close to the black hole evolve differently (see section (4.4.2)). In particular, we found that during the contracting phase, the cosmological horizon and the black hole apparent horizon merge and cease to exist for a brief period of time. Some finite time later, before the bounce but after the background Hubble radius reached its minimum size, the cosmological and black hole apparent horizons separate. Within the range of masses we considered, we found that the black hole size (as measured by its horizon radius), varies significantly during its evolution. However, regardless of the initial mass of the black hole, we found that the late time evolution consists of a black hole in an expanding universe with a mass similar to its initial value. Although we were not able to evolve spacetimes where the Hubble radius shrinks to a much smaller size compared to the radius of the black hole, we conjecture that the black hole always survives through the bounce. This means that black holes created (or already present) in the contraction phase [94, 297] can persist to have observational consequences in the post-bounce era.

We found instances where the event and apparent horizons decrease as a result of our
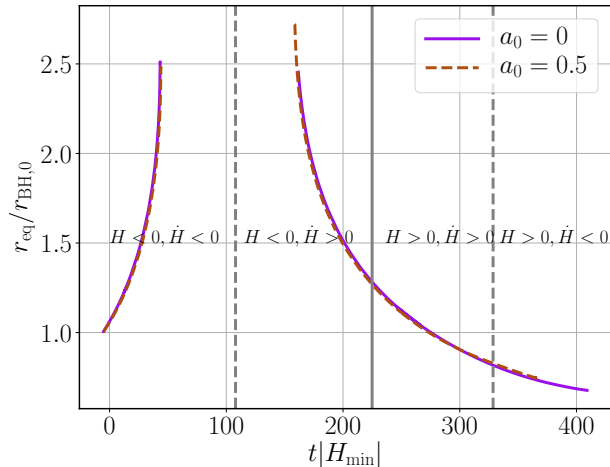
Figure 4.11: The circumferential radius of the black hole in figure 4.7 with zero spin $(a = 0)$ compared to dimensionless spin of $a = 0.5$.

spacetime violating the NCC. Independently of the NCC being violated, we found that in the regime where the black hole and cosmological apparent horizon collide, the latter becomes spacelike shortly before merging with the black hole. This is consistent with the observation that the signature of the marginally (anti-)trapped tubes changes such that any merging/reappearing pair of horizons always has the same signature.

Finally, we point out a few directions for future research. One would be to study the dynamics in a setup where the asymptotic cosmology is not prescribed. For example, this could be accomplished by considering a toroidal/periodic setup, and then considering a "lattice" of black holes [47, 101]. This setting would allow for the study of the impact of black holes, as well as other perturbations on the overall dynamics of the bounce. While small perturbations have not been found to appreciably change the dynamics of a nonlinear bounce when translational symmetries are assumed [336], it would be interesting to see if perturbations could be more disruptive in the presence of a black hole, and in a less-symmetric spacetime that does not preclude large-scale anisotropies. In addition, if the black holes survive the bounce, these could within this particular model contribute to a fraction of the total dark matter component in our Universe. A speculative, yet interesting question is whether their merger could lead to the formation of supermassive black holes, their origin still currently unknown. Using these simulations we could then predict observational signatures to confront the data with.

Another direction would be to consider other models of cosmological bounces. While we believe that the main conclusions we find here do not depend strongly on the details of the bounce model, it would be interesting to determine what differences would result from potentially more realistic models of a bounce. As we mention in the Introduction, the cosmological bounce scale may be many orders of magnitude smaller than the initial size of a primordial black hole. Due to the numerical instabilities (as described in Sec. 4.4.2), we were unable to carry out evolutions in the regime $R_{\mathrm{H,min}}/R_{\mathrm{BH,0}} \ll 1$. It would be

93

interesting to see if our results still hold in this limit.

Another interesting question is the degree to which a ghost field, which can reverse cosmic contraction, may similarly affect gravitational collapse and singularity formation in a black hole interior. NCC violating fields such as ghost fields have been used to construct singularity free black hole-like solutions, such as wormholes [262, 328, 251, 89], so it is not entirely implausible that there could be nontrivial dynamics near the center of a black hole that accretes a ghost field. In this study, we ignored the dynamics deep inside the black hole, excising that region from our domain. Exploring this would require coordinates better adapted to studying the interior of black hole spacetimes, such as null coordinates [67].

Chapter 5

Nonlinear studies of binary black hole mergers in Einstein-scalar-Gauss-Bonnet gravity

5.1 Introduction

As mentioned in chapter 1.1, GWs observed from the inspiral, merger, and ringdown of black hole binaries have greatly constrained the landscape of potential deviations from GR. However, in order to seek physics beyond GR, or to place the most stringent constraints on deformations of GR, one needs accurate predictions for specific modified gravity theories, in particular in the strong field and dynamical regime [344, 51, 53, 52]. As we know, this has been a major theoretical and technical challenge for many theories of interest [187, 272, 273, 270, 90, 91, 133, 301, 148, 54]. As a result, most tests of GR performed so far are model-independent or null tests, more commonly classified as consistency and parametrized tests [5, 6, 10, 11, 162]. Parametrized tests introduce deviations from GR to the gravitational waveform in a theory-agnostic way, and use the data to constrain the beyond GR parameters. Most current approaches, however, usually only constrain the deviations by considering one specific modification at a time and thus the interpretation of these constraints remains limited.

In this chapter, we study ESGB gravity, which introduces modifications to GR at small curvature length scales. ESGB gravity is an interesting class of theories to test against GR for the following reasons: As mentioned in the introduction, ESGB gravity is a representative example of a Horndeski theory of gravity, the most general class of scalar-tensor theories that lead to second order equations of motion in four dimensions. Moreover, ESGB gravity is inspired by the low energy limit of some string theories after compactification [61, 175, 218]. While we are interested in solving the fully nonlinear equations of motion of this theory, it is worth poiting out that ESGB gravity can also be motivated from an effective field theory argument. Variants of ESGB gravity allow for

95

scalar-charged black holes [219, 345, 318, 319], and hence can differ qualitatively from GR in the strong field regime, while still passing weak field tests. Because of all these reasons, much recent work has gone into modeling compact object mergers in ESGB gravity in both post-Newtonian (PN) theory [339, 309, 311, 312] and numerical relativity [334, 315, 270, 133, 133, 301, 129].

Perhaps one of the main motivations for studying ESGB gravity is that the equations of motion are strongly hyperbolic in the MGH formulation introduced in 1.2.2. As a result, in Ref. [133], the authors introduced a computational methodology to solve the equations of motion for binary black hole system in ESGB gravity without approximation (beyond that of numerical truncation error), by making use of this formulation. [1] Here we follow up on that work, and study the dynamics of the last stages of the inspiral phase of quasi-circular, non-spinning black holes in shift-symmetric ESGB (sGB) gravity, and investigate the accuracy of PN approximations [339, 309, 311, 312].

Remember that in general, the equations of motion for ESGB gravity can only be stably evolved in time for weakly-coupled solutions [302, 230, 229, 133, 301] which roughly means that the Gauss-Bonnet corrections to the spacetime geometry remain sufficiently small compared to the smallest curvature length scale in the solution. A binary black hole system in ESGB gravity can evolve from an initially weakly coupled state to a strongly coupled state, as the black holes become closer and eventually merge [206, 207]. We find that in a significant portion of the parameter space, our evolution breaks down as the black holes become closer, although approaching this limit does not appear to be preceded by dramatically different spacetime or scalar field dynamics compared to the weakly-coupled regime. Maintaining a weakly-coupled solution exterior to the black hole horizons through merger remains a major challenge in the numerical evolution of binary black holes in numerical relativity. While better addressing this issue remains an important issue for future work, for many cases here we focus on the properties of the late inspiral phase of binary evolution. Even when restricting to the inspiral phase, we show that the deviations from GR are significant in terms of the imprint on the resulting gravitational waves. One of our main results is that leading order PN approximations are not sufficient to model the gravitational signal in the late stages of the inspiral. For the cases we were able to evolve through merger, we find that the effects of ESGB gravity show up primarily in an nonlinear enhancement of the scalar field at merger, and in the dephasing of the gravitational waves, while the effect on the peak amplitude of the gravitational wave signal is small. This work also demonstrates the efficacy of the numerical relativity techniques utilized here—which should be applicable to any scalar-tensor theory with second order equations of motion—to quantify the impact on the gravitational wave signal of modified gravity in regimes where other approximations break down.

The remainder of the chapter is as follows. In Sec. 5.2, we review shift-symmetric ESGB gravity. In Sec. 5.3, we describe our numerical methods for evolving this theory and analyzing the results. Results from our study of quasi-circular binary black holes in

---

[1]These methods were recently extended to a modified version of the CCZ4 formulation in Ref. [24].

sGB are presented in Sec. 5.4. We discuss these results and conclude in Sec. 5.5. We discuss the accuracy of our simulations in Appendix D.1, collect PN results in sGB in Sec. D.2, outline our initial-data set-up in Appendix D.3, and review the accuracy of the perturbative approach to solving the equations of motion in Appendix D.4.

5.2   Shift-symmetric ESGB gravity

We briefly review shift-symmetric ESGB (sGB) gravity. The action is:

$$S = \frac{1}{16\pi} \int d^4x \sqrt{-g} \left(R - (\nabla\phi)^2 + 2\lambda\phi\mathcal{G} \right), \tag{5.1}$$

where $\mathcal{G}$ is the Gauss-Bonnet scalar:

$$\mathcal{G} \equiv R^2 - 4R_{\mu\nu}R^{\mu\nu} + R_{\alpha\mu\beta\nu}R^{\alpha\mu\beta\nu}. \tag{5.2}$$

Here, λ is a constant coupling parameter that, in geometric units, has dimensions of length squared. As the Gauss-Bonnet scalar $\mathcal{G}$ is a total derivative in four dimensions, we see that the action of sGB gravity is preserved up to total derivatives under constant shifts in the scalar field: $\phi \rightarrow \phi + \text{constant}$. Schwarzschild and Kerr black holes are not stationary solutions in this theory: if one begins with such vacuum initial data, the black holes will dynamically develop stable scalar clouds (hair). The end state then is a scalar-charged black hole, so long as the coupling normalized by the black hole mass m, λ/m^2, is sufficiently small [318, 319, 303, 133]. In particular, regularity of black hole solutions and hyperbolicity of the theory sets $\lambda/m^2 \lesssim 0.23$ for non-spinning black holes, [319, 303]. In contrast to stars, where the scalar field around them falls of more rapidly than $1/r$, black holes have a scalar charge, and thus black hole binaries emit scalar radiation, which increases the speed at which the binary inspirals and merges [338, 339]. The most stringent observational bounds on the theory come from unequal mass, or black hole-star binaries, as those emit scalar dipole radiation, which leads to a more rapid dephasing of the gravitational waveform than would be observed in GR. In PN theory, the scalar dipole radiation enters as a -1PN effect and can dominate over gravitational radiation at sufficiently wide separations (low frequencies). In this study, we will focus on late inspiral, where the gravitational waves are strongest and the scalar radiation is subdominant (the quadrupolar driven inspiral regime). Another feature of these solutions is that the scalar charge is inversely proportional to the square of the smallest mass black hole in the system. This suggests that the best way to probe EsGB gravity is by observing the smallest compact objects. We therefore expect stronger constraints on the theory will come from observing the merger of stellar mass black holes with ground-based detectors, as opposed to observations of supermassive black hole mergers with LISA (although long-duration observations of extreme mass-ratio insipirals with LISA may provide meaningful constraints [92]). Restoring dimensions, comparisons of gravitational wave observations from the LIGO-Virgo-KAGRA catalogue to PN results place constraints of $\sqrt{\lambda} \lesssim 2.5$ km, see Refs. [285, 253].

5.3   Methods

5.3.1   Evolution equations and code overview

The covariant equations of motion for sGB gravity are

$$\Box\phi + \lambda\mathcal{G} = 0, \qquad (5.3)$$

$$R_{\mu\nu} - \frac{1}{2}g_{\mu\nu}R - \nabla_\mu\phi\nabla_\nu\phi + \frac{1}{2}\left(\nabla\phi\right)^2 g_{\mu\nu} + 2\lambda\delta^{\alpha\beta\gamma\eta}_{\rho\sigma\kappa(\mu}g_{\nu)\eta}R^{\rho\sigma}{}_{\alpha\beta}\nabla^\kappa\nabla_\gamma\phi = 0, \qquad (5.4)$$

where $\delta^{\alpha\beta\gamma\eta}_{\rho\sigma\kappa\mu}$ is the generalized Kronecker delta tensor. We numerically evolve the full sGB equations of motion using the MGH formulation introduced in chapter 1.2.2. We use similar choices for the gauge and numerical parameters as in Ref. [133]. We worked with box-in-box adaptive mesh refinement as provided by the PAMR library [295]. We typically worked with eight levels of mesh refinement in our simulations, unless otherwise noted. We provide details on numerical resolution and convergence in Appendix D.1.

5.3.2   Puncture binary black hole initial data

On our initial time slice, we must satisfy the generalizations of the Hamiltonian and momentum constraint equations to sGB. Here, we do not implement a method to solve the equations for general ϕ, but instead consider initial data for which $\phi = \partial_t\phi = 0$. With this choice of ϕ, the constraint equations of sGB gravity reduce to those of vacuum GR [133, 301]. Even though $\phi = \partial_t\phi = 0$ on the initial time slice, scalar field clouds subsequently form on a timescale that is short compared with the orbital binary timescale (within $\sim 100M_0$). We construct quasi-circular binary black hole initial data via the black hole puncture method [74], using the `TwoPunctures` code [23, 279][2].

For puncture binary black hole initial data, we need to specify the initial black hole positions, and their approximate initial masses $m_{1,2}$ (with the convention that $m_1 \leq m_2$), linear momenta $P^\gamma_{1,2}$, and spins $S^\gamma_{1,2}$ (which we set to zero in this study). Given $m_{1,2}$ and the initial puncture (black hole) locations, we use the dynamics for a circular binary to 2PN order to determine the tangential components to $P^\gamma_{1,2}$, and the 2.5PN radiation reaction term to determine the initial radial component of $P^\gamma_{1,2}$ [278]. We review our initial data setup in more detail in Appendix D.3.

For the first $t = 50M_0$ (where $M_0 \equiv m_1 + m_2$) of evolution, we evolve the black holes purely in GR. We found this allowed for the junk radiation from the puncture initial data to disperse away from the black holes. After that initial evolution time, we turn on the Gauss-Bonnet coupling λ to a non-zero value. The constraints are satisfied in this procedure, as we can think of our initial data as starting at $t = 50M_0$ instead, with $\phi = \partial_t\phi = 0$ and a metric field that satisfies the constraints such that the initial data

---

[2]The particular version of the code we use can be accessed at [1].

satisfies the constraint equations for sGB gravity [133, 301]. While we use quasi-circular initial data based on PN approximations for the initial orbital velocities from GR, we found that the scalarization process does not appreciably impact the eccentricity of our runs, and instead the eccentricity of our runs is dominated by the truncation error of the simulations. For more discussion, see Appendix D.1.

5.3.3 Diagnostic Quantities

We use many of the same diagnostics as in Ref. [133], which we briefly review here. We measure the scalar and gravitational radiation by extracting the scalar field ϕ and Newman-Penrose scalar Ψ_4 on finite-radius coordinate spheres. Due to the coupling between the scalar field and metric through the Gauss-Bonnet coupling, in general scalar and gravitational radiation will couple together through the term $\delta \times Riemm \times \nabla\nabla\phi$. For asymptotically flat spacetimes that have an asymptotically flat future null infinity (that is spacetimes for which the peeling theorem holds, so the Weyl scalar fall of sufficiently fast [264]), this coupling falls off as $1/r^4$ as $r \to \infty$. For those spacetimes, in the wave zone, we can treat the gravitational and scalar radiation as two uncoupled quantities (for related discussions, see [324, 133]). We discuss how we estimate the finite-radius extraction error of our waveforms in Appendix D.1.

We decompose Ψ_4 and ϕ into their spin-weighted spherical harmonic components

$$\Psi_{4,\ell m}(t,r) \equiv \int_{\mathbb{S}_2} {}_{-2}\bar{Y}_{\ell m}(\vartheta,\varphi) \, \Psi_4(t,r,\vartheta,\varphi), \tag{5.5a}$$

$$\phi_{\ell m}(t,r) \equiv \int_{\mathbb{S}_2} {}_{0}\bar{Y}_{\ell m}(\vartheta,\varphi) \, \phi(t,r,\vartheta,\varphi). \tag{5.5b}$$

The gravitational wave luminosity is

$$P_{\text{GW}}(t) = \lim_{r\to\infty} \frac{r^2}{16\pi} \int_{\mathbb{S}_2} \left| \int_{-\infty}^{t} \Psi_4 \right|^2. \tag{5.6}$$

The scalar wave luminosity is P_{SF}

$$P_{\text{SF}} \equiv - \lim_{r\to\infty} r^2 \int_{\mathbb{S}_2} N t^\mu \left(T^{\text{SF}}\right)_\mu^\nu dA_\nu, \tag{5.7}$$

where $N = 1/\sqrt{-g^{tt}}$ is the lapse and t^μ is the asymptotic timelike Killing vector, the integral is over a sphere, and

$$T^{\text{SF}}_{\mu\nu} \equiv \frac{1}{8\pi} \left(\nabla_\mu\phi\nabla_\nu\phi - \frac{1}{2}g_{\mu\nu}\nabla_\alpha\phi\nabla^\alpha\phi \right). \tag{5.8}$$

We assume the scalar radiation is outgoing, so that Eq. (5.7) reduces to

$$P_{\text{SF}}(t) = \lim_{r\to\infty} \frac{r^2}{8\pi} \int_{\mathbb{S}_2} (\partial_t\phi)^2. \tag{5.9}$$

To compare our numerical waveforms, we must estimate the orbital frequency of the binary Ω. We do so using the approximate relation [287, 49, 254]

$$\Omega \approx \frac{1}{2} \frac{d\Phi_{22}(t)}{dt},$$ (5.10)

where $\Phi_{22}/2$ is the definition of orbital phase computed from half the complex phase of $\Psi_{4,22}$. We track the apparent horizons (AHs) associated with the black holes, and measure their areas and associated angular momentum J_{BH}. From this, we compute the black hole mass m_{BH} via the Christodoulou formula (4.20). We note that while the areal mass always increases in vacuum GR [179], it can decrease in sGB gravity as the theory can violate the NCC [302, 303]. In our simulations, $J_{\mathrm{AH}} \approx 0$ to numerical precision for the constituents of the binary black hole. We measure the average value of the scalar field on the black hole apparent horizons

$$\langle \phi \rangle_{AH} \equiv \frac{1}{\mathcal{A}_{\mathrm{BH}}} \int_{AH} \phi.$$ (5.11)

5.3.4 Cases considered

We focus on quasi-circular black hole binaries with no spin. We classify our runs by two dimensionless numbers: their mass ratio q[3] and by the relative Gauss-Bonnet scalar coupling strength ζ_1 (compare to Refs. [339, 285, 253]):

$$q \equiv \frac{m_1}{m_2} \leq 1, \qquad \zeta_1 \equiv \frac{\lambda}{m_1^2}.$$ (5.12)

As m_1 is the smaller black hole mass, it roughly quantifies the smallest curvature scale in our simulations. We consider the mass ratios $q = 1, 2/3$, and $1/2$, with an initial separation of $10M_0$, approximately 8 orbits before merger in GR. For the equal mass ratios, we consider ESGB coupling parameters $\zeta_1 = 0, 0.01, 0.05$, and 0.1; while for the mass ratios $q = 2/3$ and $q = 1/2$, we consider smaller values of $\zeta_1 = 0, 0.025, 0.05$, and 0.075; and $\zeta_1 = 0, 0.05$, and 0.075, respectively. When comparing waveforms ($\Psi_{4,\ell m}$ or $\phi_{\ell m}$) with different values of the coupling, we compute the time t_{align} at which the gravitational wave frequency is $0.01M_0$, and apply this as a time offset. This alleviates the effect of any dephasing or shift in frequency due to the scalarization process. We then rotate the waveforms by a constant, complex phase so that their initial phases align. For comparisons with other works, our coupling λ corresponds to $\alpha_{\mathrm{GB}} \equiv \lambda/\sqrt{8\pi}$ used in, e.g. [285, 253].[4] Restoring physical units, we have

$$\sqrt{\alpha_{GB}} \approx 3.97 \text{ km} \left(\frac{\sqrt{\lambda}}{m_1} \right) \left(\frac{m_1}{6 \ M_\odot} \right)$$ (5.13)

---

[3]Note q was used to refer to the number of compactified dimensions in chapter 2

[4]However, several other studies (e.g. [334, 59, 289, 290]) take conventions leading to a value of α_{GB} that is $16\sqrt{\pi}\times$ times larger.

where 6 $M_\odot$ is approximately the value of smallest black hole observed in the LIGO-Virgo-Kagra third observing run [8]. For reference, Ref. [253] sets a constraint of $\sqrt{\alpha_{\mathrm{GB}}} \lesssim 1.2$ km by comparing gravitational wave observations of black hole-neutron star binaries to PN results of ESGB. In comparison, the largest coupling we consider in our simulations (our equal-mass $\zeta = 0.1$ run) corresponds to $\sqrt{\alpha_{\mathrm{GB}}} \sim 1.25$ km for a 6 $M_\odot$ black hole, which is roughly within observational bounds.

5.3.5 Challenges in modeling the merger phase of black hole evolution

As we discuss in Sec. 5.4, we are unable to evolve the binaries through merger for many of our simulations. For some of our runs, we turned off the scalar Gauss-Bonnet coupling inside a compact ellipsoidal region centered at the black hole binaries center of mass at a finite time before merger. This allowed us to evolve through merger, and extract gravitational and scalar radiation from the inspiral up until the causal future of the excised region intersected where we measured the radiation (typically at $r/M_0 = 90$).

For one case, namely $q = 1$ and $\zeta_1 = 0.05$, we only turn off the Gauss-Bonnet coupling slightly before finding a common apparent horizon, and only in a localized region that is encompassed by the final black hole. We have verified that varying the size of this region has no appreciable impact on the resulting radiation, and so we include the full results from this case, though a careful tracking of the propagation of information along characteristics would be needed to more rigorously justify this.

We believe the main difficulty with evolving through merger in our simulations may be elliptic regions that form around merger. These regions may possibly be hidden behind the final event horizon, and so could possibly be excised from the computational domain if an apparent horizon is located quickly enough. Higher resolution runs, with excision surfaces that lie closer to the apparent horizons of the inspiraling black holes or a different choice of the auxiliary metrics in the modified generalized harmonic formulation, may allow for the successful merger of black holes in sGB gravity with unequal mass ratios. We leave a further investigation of this to future work.

5.4 Results

We present results for binary black holes with several mass ratios, beginning roughly eight orbits before merger, focusing on how the orbital dynamics and radiation changes as a function of the sGB coupling. We compare both the scalar radiation, and the modified gravity induced dephasing of the orbit and gravitational wave signal to the PN prediction.

5.4.1 Scalar radiation and dynamics

In Fig. 5.1, we compare the leading order scalar waveforms $\phi_{\ell m}$ from our numerical evolution to the PN formulas given in Eq. (D.5). The PN formulas are accurate to 0.5PN order for the mode ϕ_{11}, and to leading PN order for the remaining modes. As in the comparisons of scalar waveforms computed in Refs. [334, 311, 312], the frequency we use in the PN expressions are obtained from our numerical evolutions using Eq. (5.10), so our comparison is measuring the accuracy of the PN approximation in determining the amplitude of the scalar field, given its frequency. We see that the fractional difference between the 0.5PN order PN theory for the $\ell = 1, m = 1$ mode, and the numerical scalar waveform is about 30% initially, and grows as the binary inspirals. We also note that the inclusion of higher PN terms increases the overall amplitude of the scalar waveforms, making the agreement between the PN and numerical waveforms worse than at leading order at the frequencies we consider. This result holds for all three mass ratios we considered. Comparing other values of the coupling constant shows similar behaviour and thus, we do not show the plots here.

Comparing our results to Fig. 7 of Ref. [334], where the leading order PN scalar waveforms were compared to numerical waveforms obtained in a test field approximation (valid to first order in the coupling parameter ζ_1), we find close agreement between our waveforms, suggesting the test field scalar waveform computed from a prescribed orbital evolution is fairly accurate at least during the early inspiral phase. This is further emphasized in Fig. 5.2, where we plot the scalar waveforms, rescaled by ζ_1. In the decoupling limit, the amplitude of the emitted waveforms is directly proportional to ζ_1 [339, 334]. From Fig. 5.2, we see that, at least during the inspiral phase of binary black hole evolution, this relation holds up well for the full theory. This is to be expected, as nonlinear corrections to ϕ only enter at order ζ_1^3 in sGB gravity; see Appendix D.4.

In Fig. 5.3, we plot the average value of ϕ on the black hole apparent horizon for the two initial black holes, and the final remnant black hole, for runs with ($q = 1, \zeta_1 = 0.01$ and 0.05) and ($q = 1/2, \zeta_1 = 0.05$). We see that after the black holes have acquired a scalar charge, the average value of the scalar field on the two black hole horizons increases as they inspiral towards each other, in general qualitative agreement with the predictions of Refs. [206, 207]. The remnant black hole for the equal mass runs (BH3 in the left panel) has a smaller average scalar field value on its horizon than the two original black holes, as it has a larger mass (so $\lambda/m_3^2 < \lambda/m_{1,2}^2$), and it is spinning [133]. As we discuss in Sec. 5.3.5, we are unable to evolve through merger for any of the unequal mass ratio cases we consider, so there is no remnant apparent horizon in the right panel.

5.4.2 Gravitational Waves

We next estimate the relative dephasing of the gravitational waveforms, taking into account various sources of numerical error in our simulations. Accurately computing the phase of

(a) $q = 1$

(b) $q = 2/3$

(c) $q = 1/2$
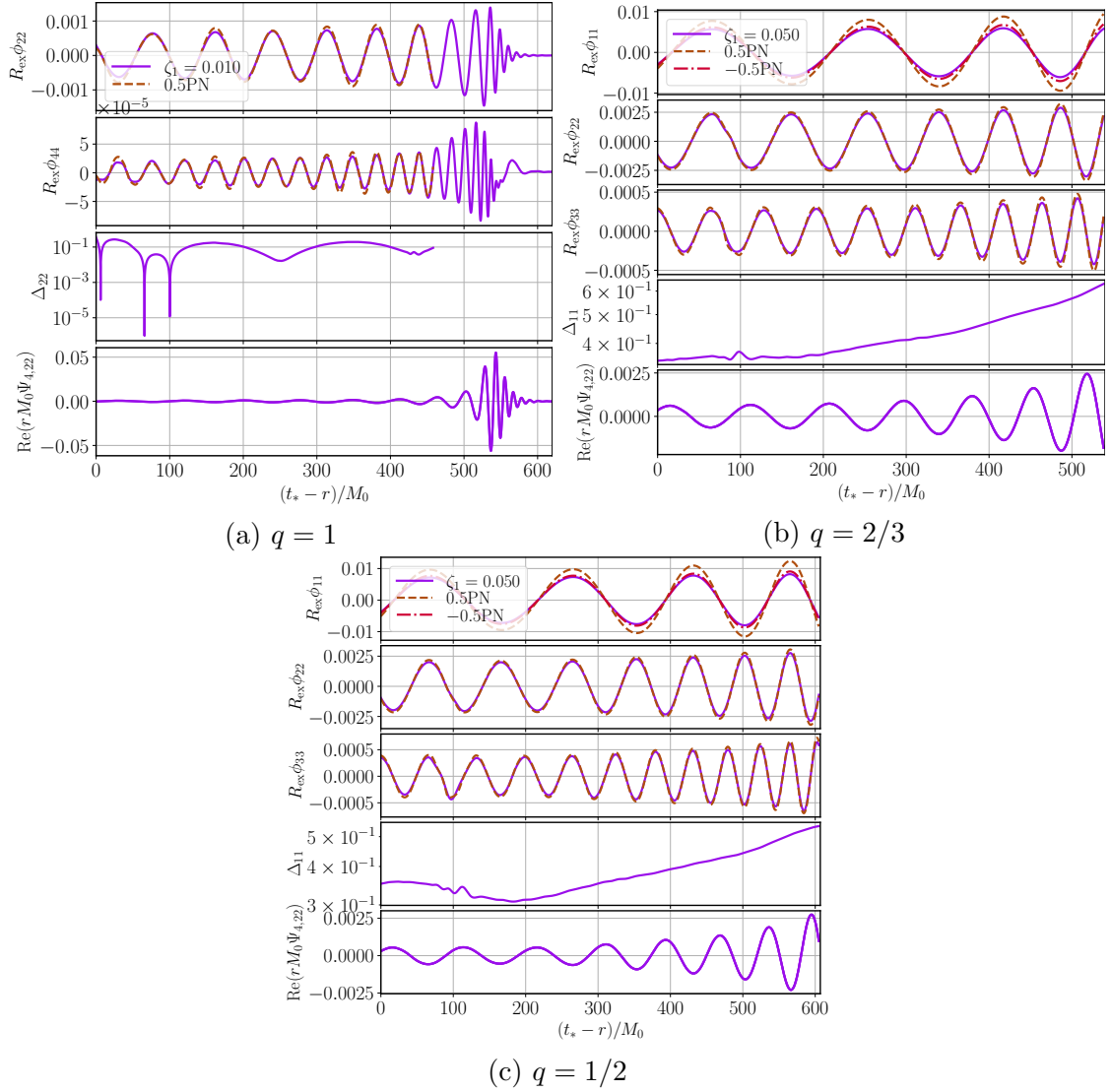
Figure 5.1: Scalar waveforms as a function of retarded time, $t_* - r = t - t_{\mathrm{align}} - r$, rescaled by the extraction radius $R_{\mathrm{ex}} = r/M_0 = 90$, sourced by nonspinning BH binaries of mass ratio $q = \{1, 2/3, 1/2\}$ (clockwise from the top left). The corresponding waveform $\Psi_{4,22}$ is displayed in the bottom for comparison. We show the $(\ell, m) = (2, 2)$ and $(4, 4)$ spherical harmonic components for the equal mass ratio and the $(\ell, m) = (1, 1)$, $(2, 2)$, and $(3, 3)$ components for unequal mass ratios. During the inspiral, we also display the PN waveform (brown dashed lines), derived to 0.5PN order, and the leading order waveform at -0.5PN for the $(\ell, m) = (1, 1)$ mode (red dash-dotted lines). We also show the relative difference between the amplitude of the PN and numerical waveform Δ_{lm} for the leading order mode.
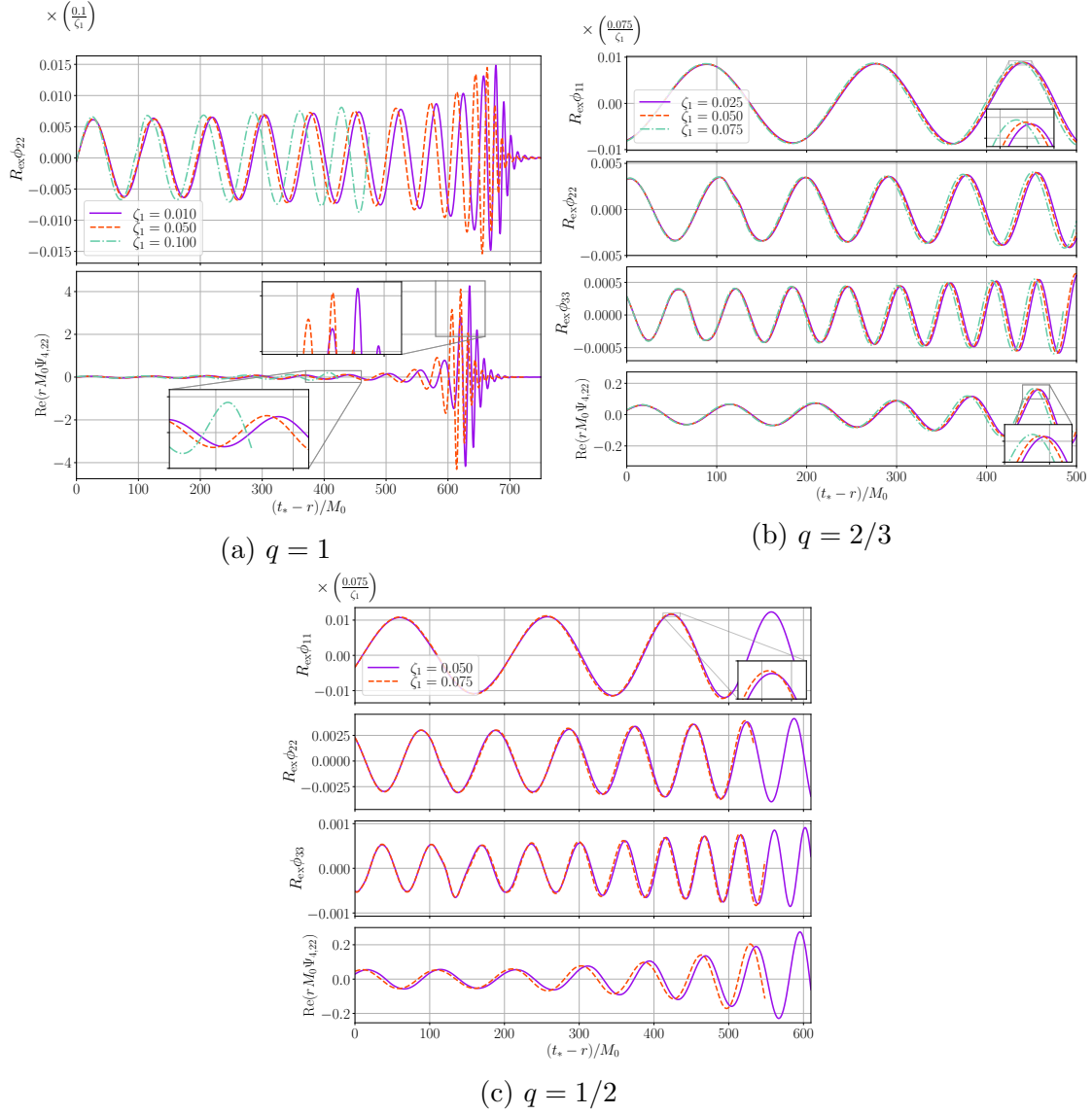
Figure 5.2: Scalar waveforms as a function of retarded time, $t_* - r = t - t_{\text{align}} - r$, rescaled by the extraction radius $R_{\text{ex}} = r/M_0 = 90$ and test field dependence on coupling constant λ, sourced by nonspinning binary black holes of mass ratio $q = \{1, 2/3, 1/2\}$ (clockwise from top left) and different coupling constants ζ_1. The corresponding gravitational waveforms $\Psi_{4,22}$ are displayed in the bottom of each panel for comparison. We show the leading order (ℓ, m) mode for each mass ratio.

(a) $q = 1, \zeta_1 = 0.01$ and 0.05

(b) $q = 1/2, \zeta_1 = 0.05$
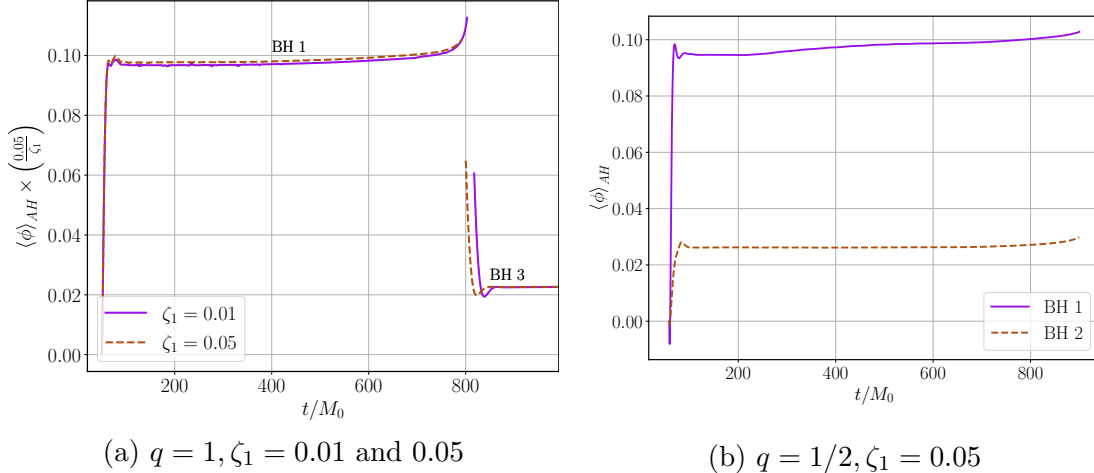
Figure 5.3: Average value of the scalar field, rescaled by the test field dependence, over the black hole horizons for different mass ratios. For the equal mass ratio binary (left panel), we were able to evolve through merger, and thus determine the average value of the scalar field on the third, remnant black hole. While we were unable to evolve through merger for the unequal mass ratio binaries, on the right panel we show the average scalar field for a $q = 1/2$ run. The dips in the average scalar field near the end of the evolution for that run are due to numerical error.

a gravitational signal is crucial, given this will be the most salient effect of sGB gravity that current gravitational wave detectors are able to measure [346, 53, 253]. Due to the presence of scalar charge around each black hole in sGB gravity, black holes will emit scalar radiation as they inspiral each other, so they will inspiral faster as compared to what would be the case in GR. In Fig. 5.4, we plot the gravitational waveforms $\Psi_{4,22}$, after matching their frequency at a time t_{align}, and applying a rotation in the complex plane, so that their phases align initially. We see that there is a noticeable dephasing of binaries with different values of ζ_1. In Fig. 5.5, we quantify the dephasing for the $\ell = 2$, $m = 2$ mode of Ψ_4 [see Eq. (D.3)]

$$\delta\Phi(f) \equiv \Phi_{\text{sGB}}(f) - \Phi_{\text{GR}}(f), \tag{5.14}$$

by comparing the orbital phase [computed from Eq. (D.3)] of the waveforms at a given frequency smaller than $M_0 f < 0.018$ which corresponds to the empirically found transition from the inspiral to merger-ringdown phase in GR [189, 220], along with the corresponding PN predictions for a quadrupolar driven inspiral [309, 253] (see also Appendix D.2). We find $\delta\Phi < 0$, and the dephasing grows as we increase the coupling λ, which is in general qualitative agreement with PN predictions for sGB gravity. This being said, at least for the last few orbits of the inspiral that we study, we find that our results do not agree quantitatively with PN predictions. A possible reason for this is because we are comparing to PN theory close to the merger phase of binary evolution, where more orders of the PN expansion are needed to match to numerical relativity simulations even in GR. These

105

differences also need to be compared to the various sources of numerical error in the simulations, which in some cases exceed the small phase differences, as we discuss below. In Fig. 5.6, we show the dephasing at consecutive orders up to 2PN for for a range of gravitational wave frequencies we sample in our simulations (the last few orbits before merger), yet within the regime where the PN approximation should be valid in GR, $M_0 f < 0.018$ [189, 220]. The PN formulas we plot were first presented including terms of up to 2PN order in Ref. [253]; we review their computation in Appendix D.2. As noted in Ref. [253], we mention that the dephasing for ESGB gravity has only been computed to 2PN order, with only partial results at 0.5 PN order onwards. We see that there are still noticeable differences in the PN approximation with the addition of the highest order terms in the near-merger regime studied here, and thus the expansion will likely have to be continued to higher order to achieve a highly accurate prediction in that regime, although we cannot rule out that the inclusion of the currently missing terms to the 0.5 through 2 PN contributions in the phase may lead to a faster convergence in the PN expansion than observed here.

Finally, we compare the orbital dephasing to the numerical errors in the simulations. A detailed error analysis is given in Appendix D.1, which we briefly summarize here. The error in the Richardson extrapolated phase is ~ 0.25 radians, which is comparable to the ESGB dephasing, and larger than the relative error in the 2PN computation. However, if the dominant truncation error in our simulations does not depend strongly on the value of ζ_1, and thus partially cancels out when calculating the difference $\delta\Phi$ in the phase between the sGB and GR simulations using the same resolution, this will lead to noticeable smaller truncation error in this quantity compared to the overall phase. We see evidence that this is the case, for example, by comparing a measure of the truncation error in $\delta\Phi$, computed by comparing a $q = 1/2$ GR simulation to an equivalent sGB simulation with $\zeta_1 = 0.075$ at two different resolutions, to an estimate of the overall truncation error in Φ for the same sGB case. We find the former to be $\sim 50\times$ smaller than the latter (see Appendix D.1). We also find similar results for the GW amplitude. Thus, for a number of cases (see Fig. 5.5), the difference in errors is smaller than the dephasing $\delta\Phi$ we measure.

Lastly, we note that the dephasing between the sGB and GR simulations may be caused by small differences in the eccentricity of our simulations, which would be caused by the orbit being slightly perturbed by the rapid development of the scalar field around the black holes at early times, as an artifact of using initial conditions with $\phi = \partial_t\phi = 0$. If this were the case, one would expect the eccentricity of the modified waveforms to increase with coupling. We estimate the orbital eccentricity in our simulations to be $\lesssim 0.01$, and we find that it decreases with increasing resolution, with only a mild dependence on coupling. This suggests that residual eccentricity from the initial data is subdominant to finite-resolution numerical errors, and does not significantly affect the dephasing of the binary. The eccentricity of the binary system is not much affected by the value of the Gauss-Bonnet coupling, as even for the largest couplings we consider the energy contained in the scalar cloud is only a small fraction of the total binary binding energy, and an even smaller fraction of that energy is radiated away during the scalarization process.
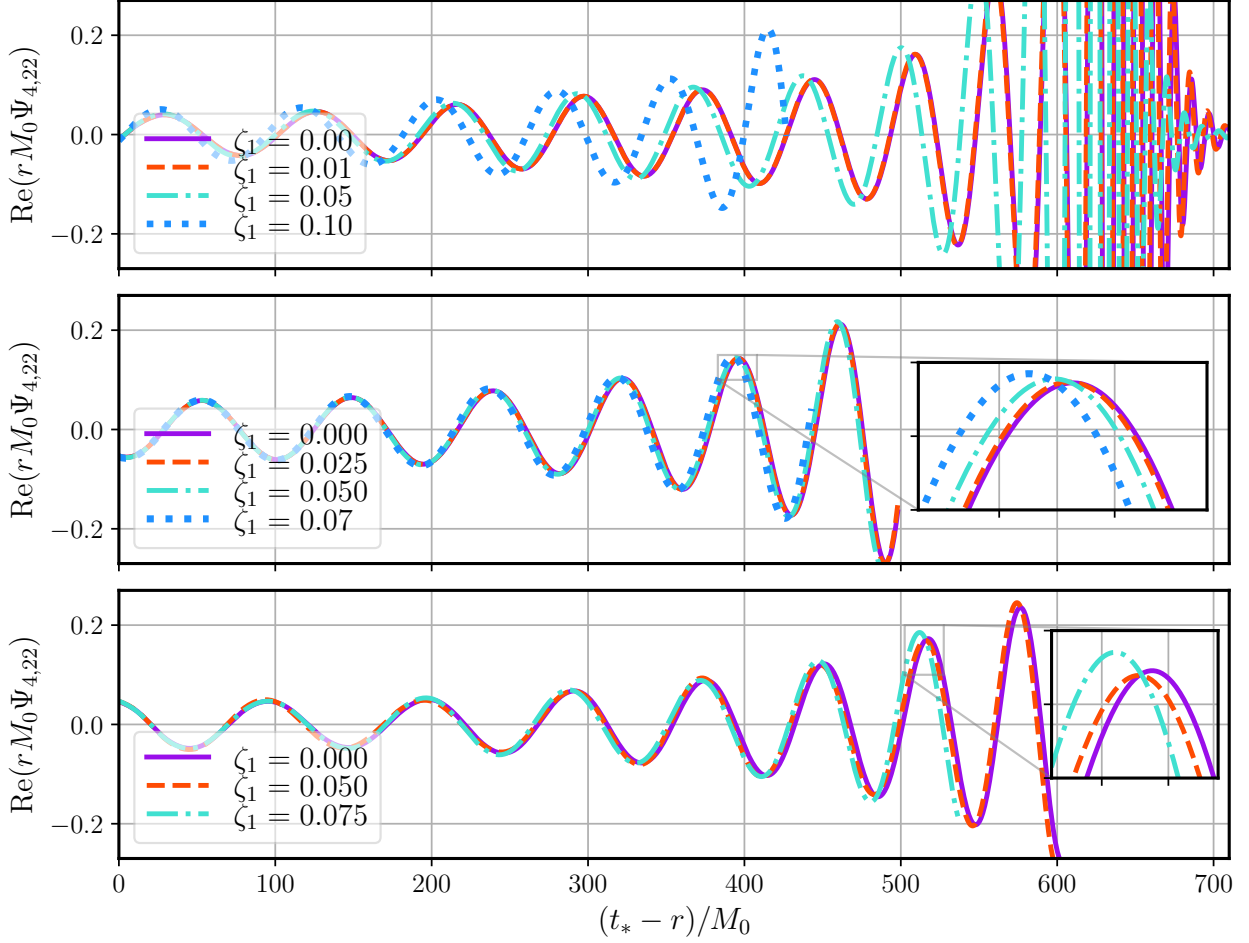
Figure 5.4: The radially rescaled value of $\Psi_{4,22}$ as a function of retarded time, $t_* - r = t - t_{\text{align}} - r$, for different values of ζ_1. The top, middle, and bottom panels show the waveforms for the $q = 1$, $2/3$, and $1/2$ mass ratio binaries. Here we measure $\Psi_{4,22}$ at a radius of $R_{\text{ex}} = r/M_0 = 90$.
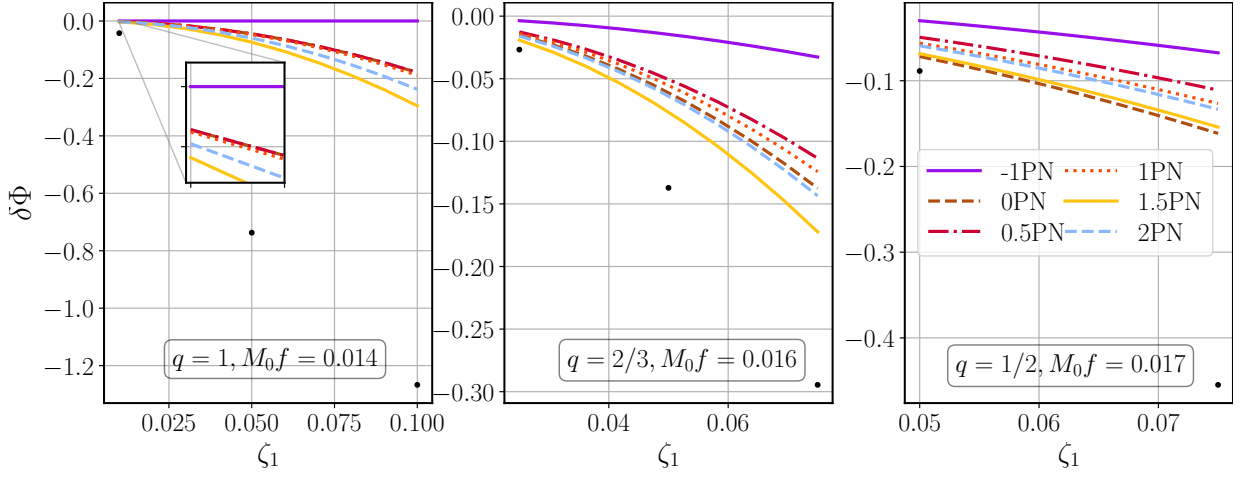
Figure 5.5: Difference between the orbital phase of gravitational waveform in sGB and GR, $\delta\Phi$ [see Eq. (D.7)], accumulated as the binary evolves from a frequency $f_0 = 0.01/M_0$ to a frequency f. The left, middle, and right panels display results for the $q = 1, 2/3$, and $1/2$ mass ratio binaries, respectively, with $M_0 f = 0.014, 0.016$, and 0.017. We plot the PN predictions for orders -1PN through 2PN (with each curve including all terms up to that order).
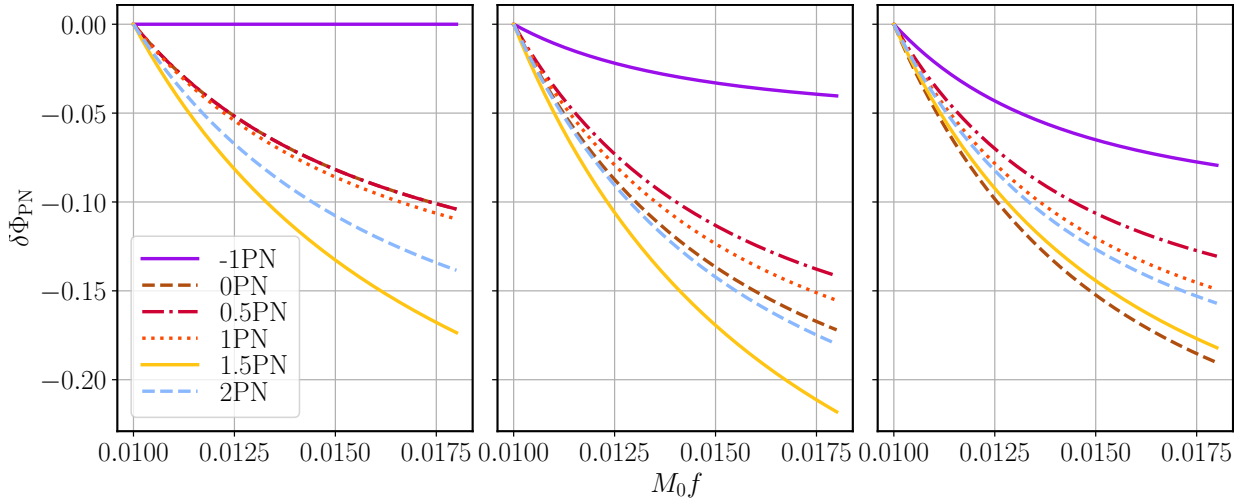
Figure 5.6: The shift in the gravitational wave phase for the orbital phase, summed to each PN order up to 2PN. In the left, middle, and right panels we set $\zeta_1 = 0.05, 0.075$, and 0.075, respectively. As in Fig. 5.4, the left panel is for a $q = 1$ binary, the middle panel is for a $q = 2/3$ binary, and the right panel is for a $q = 1/2$ binary.
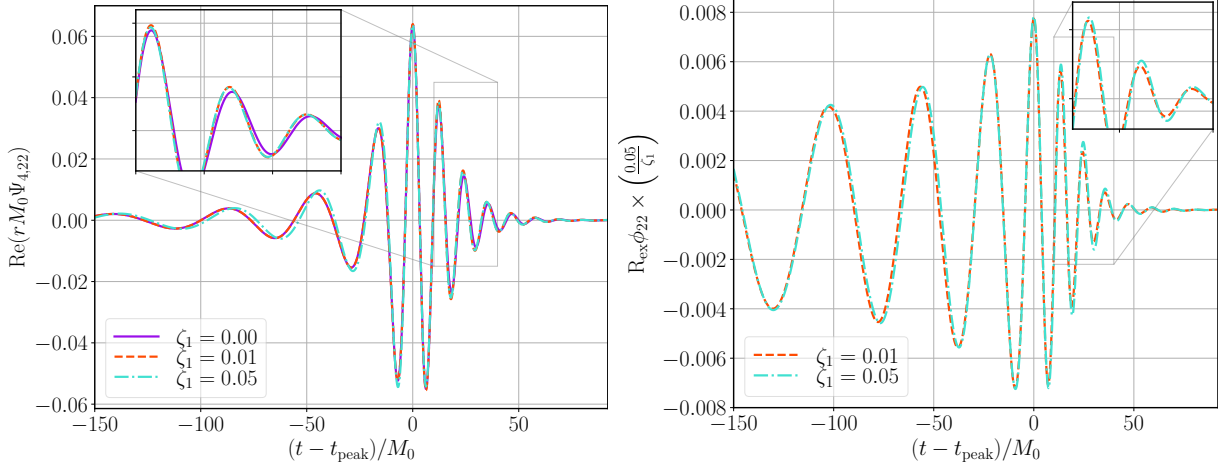
Figure 5.7: Gravitational wave radiation (left) and scalar radiation (right) for equal mass ratio binaries with coupling $\zeta_1 = 0$, 0.01, and 0.05. We show the real part of the $\ell = m = 2$ spherical harmonics of the Newman-Penrose scalar Ψ_4 and ϕ. Time is measured with respect to the time where the complex amplitude of $\Psi_{4,22}/\phi_{22}$ peaks. We add an overall phase so that the waveforms are real and positive at $t = t_{\text{peak}}$.

5.4.3 Merger dynamics

Lastly, we mention the effects of ESGB on the merger dynamics of equal mass binaries with couplings $\zeta_1 = 0.01$ and 0.05, compared to GR. Figure 5.7 shows the gravitational wave emission starting slightly before merger, and including the ringdown, for different values of ζ_1. We find that while the ESGB waveforms have a noticeable dephasing relative to GR, consistent with the fact that ESGB binaries should merge faster due to the additional energy loss through scalar radiation, the peak amplitude of the gravitational wave at merger depends only very weakly on ζ_1. The effect of modified gravity on the frequency and decay rate of the quasinormal modes is also too small to reliably quantify with our current numerical data, so we defer a more detailed study of the ringdown to future work.

In the right panel of Fig. 5.7 we show the leading $\ell = m = 2$ mode of the scalar waveform after rescaling for the test-field dependence on the coupling, which implies that the amplitude of ϕ scales linearly with ζ_1. For the $\zeta_1 = 0.05$ case, we find an additional nonlinear enhancement in the scalar field amplitude at merger, with $|\phi|/\lambda$ roughly 5% higher compared to the $\zeta_1 = 0.01$ case.

The negligible effect on the GW amplitude with varying ESGB coupling that we find here contrasts with the large effect found in order-reduced simulations. In particular, the correction to Ψ_4, which scales quadratically with ζ_1 in the perturbative approach taken in Ref. [270], gives an order-one correction to the amplitude for the highest couplings used here (see Fig. 2 of Ref. [270]); though we note that Ref. [270] also uses a slightly different mass-ratio ($q = 0.82$) and non-zero spins for the constituent black holes. We speculate that this qualitative difference behavior in the waveform is due to the presence of secularly growing

109

errors terms, which are known to be present in such a perturbative approach to evolving modifications to GR. For more discussion of this phenomena, see Refs. [273, 270, 153].

5.5   Discussion and Conclusion

In this work, we have performed the first systematic study of the nonlinear dynamics of binary black hole inspiral and merger in sGB gravity. We considered several values of the sGB coupling and the binary mass ratio, and compared our results to PN theory. Solving the full equations of motion allowed us to directly measure the increased dephasing of the inspiral due to the emission of scalar radiation, and to determine the relative effects of nonlinearity on the scalar and gravitational waveforms. We argue that, at least in the last few orbits of the inspiral phase before merger, PN theory is currently not accurate enough to determine the dephasing of the binary due to the modified gravity, even taken as a correction to a more accurate to GR waveform.

In addition to measuring the dephasing of binary black holes, we find that leading order PN theory (in the GB coupling λ) does well in matching the amplitude of scalar radiation emitted during the inspiral phase, given the frequency of observed gravitational radiation. This is in general qualitative agreement with earlier numerical relativity work that compared simulations of sGB gravity in the decoupling limit to PN predictions [334]. The success of leading order PN theory in matching the scalar waveform can be partially explained by the fact that corrections to the scalar field amplitude in the GB coupling enter at order ζ_1^3 for sGB gravity (see Appendix D.4).

We have studied the dynamics of the merger for a limited number of cases, where we found that when the black holes merge the effect due to the ESGB modifications on the peak amplitude of the gravitational wave signal is small, in contrast to what results using perturbative treatments of the merger would suggest. We leave a detailed study of the detectability of these effects and their degeneracy with different intrinsic parameters to future work.

In this first study, for computational expediency, and given that the ESGB equations of motion are more complicated to solve than the GR ones, we have focused on the roughly last 8 orbits before merger. However, an obvious direction for future work is to consider binaries that start at wider separations (and hence lower orbital and gravitational wave frequencies), in order to determine at what point leading order PN theory becomes accurate. Modeling the merger is arguably the most important contribution numerical relativity can make to our understanding of binary black hole evolution. As we were unable to evolve through merger for larger coupling values understanding this limitation of our code/methods remains an important task for future work. Different choices of gauge or auxiliary metrics, as well developing better diagnostics for monitoring the breakdown of hyperbolicity may help address this. As mentioned above, we believe one of the main difficulties lie in being able to excise elliptic regions near merger, around the time the final

remnant black hole forms from the merger. Our algorithm may be improved by implementing a more complicated excision surface (currently we only excise an ellipsoidal region), and working with higher resolution, to more stably excise closer to the surface of the apparent horizons. We note that recent work [24] reports evolutions of non-spinning, equal mass ratio black hole binaries through merger using a modified CCZ4 formulation of the equations of motion with puncture-like coordinates, for ζ_1 values as large as $\zeta_1 = 0.1/\sqrt{2} \sim 0.07$ (converting to our conventions). In that work, the authors make use of an effective excision algorithm by letting the modified gravity coupling go to zero at small values of the spatial metric conformal factor, as in Refs. [146, 147]; such a method may be useful in conjunction with our direct excision method to stabilize the evolution near the excision boundary.

In this work, we only considered binary black hole systems where the individual black holes were initially nonspinning. As black hole spin can significantly impact the dynamics of binaries in GR, a natural next step to this work would be to consider black hole spin. Furthermore, introducing spin may lead to novel gravitational wave signatures as, for example, in black hole spin-induced spontaneous scalarization [120, 185, 50].

We have only simulated the dynamics of arguably the simplest of the ESGB gravity theories that gives scalar hairy black holes. Other kinds of scalar Gauss-Bonnet couplings (i.e. more general terms of the form $\beta(\phi)\mathcal{G}$ in the action) can allow for a rich range of phenomena, most notably the effect of spontaneous (de)scalarization, which so far has only been studied either perturbatively [315, 137], or in symmetry-reduced settings [122, 314, 259, 313, 120, 185, 50, 132]. As well, including a term of the form $f(\phi) X^2$ in the action is also "natural" from an effective-field theoretic point of view, as this is another four derivative term that is also parity-invariant [332, 230], and may have some effect on the binary evolution. Simulating nonlinear effects such as spontaneous black hole scalarization requires understanding the backreaction of the scalar field on the background geometry, as that affects the saturation of the instability and end state black hole, and determines which effects occur in the regime where the theory remains hyperbolic [132]. Accurately simulating theories with high precision that exhibit spontaneous black hole scalarization will additionally require the development of initial data solvers that solve the constraint equations in sGB gravity that have an initially nontrivial scalar field profile [228, 301]. It would also be interesting to extend recent work on binary neutron star mergers [129] to study black hole–neutron star binaries in ESGB gravity (earlier work on spontaneous scalarization in ESGB gravity for single neutron star solutions include Ref. [235]).

Chapter 6

Conclusions and further outlook

In this thesis, we used and developed the tools of numerical relativity to test our understanding of gravity in the strong field regime which would otherwise be inacessible. We used numerical simulations as a theoretical laboratory for gravity, addressing several problems in early universe cosmologies, high energy physics and spacetimes surrounding black holes. We explored the possible role of extra dimensions in determining the physical mechanisms responsible for the accelerated expansion of the Universe within the context of string theory and presented the first study of the dynamics associated with extra dimensions. Of course, here we only studied a very simple model but that retains many of the important features of the low energy limit of string theory and figures prominently in the AdS/CFT correspondence [256], has been employed to study the cosmological constant problem [116, 88, 77, 28], and dimension-changing transitions [106, 234, 88, 58], among other phenomena. More importantly, this study showed the power of using numerical techniques to probe the inhomogeneous and strong field regime in high energy physics. The general methods developed in this work could be used and extended to explore other higher dimensional string inspired scenarios as well as black holes in higher dimensions [138, 300]. One particular avenue which would be interesting to pursue would be to extend this study to the case where the external space is anti-de Sitter as this would have applications to the AdS/CFT correspondence.

In this thesis, we also applied numerical relativity techniques to study early universe paradigms that could account for the observable universe and solve the problem of initial conditions in cosmology. We focused on studying the robustness of inflation and nonsingular bouncing models. It would be interesting and extremely useful to our understanding of the early universe if our numerical methods could be further developed to make predictions that can be confronted with observations of the cosmic microwave background and large-scale structure datasets. The code used in our investigations (as well as many others cosmology codes in the literature e.g. [103]) is limited by gauge dynamics. A better gauge, as well as working with higher resolution or adaptive mesh refinement may help allow us to run cosmology codes for longer than is currently possible when starting from generic initial conditions. One could also use a different formulation of the Einstein equations such as

the tetrad formulation, which is better suited to follow the evolution of spacetime across many *e*-folds in both contracting and inflating spacetimes [159, 108, 158, 190, 191, 197]. A particularly promising avenue for future work would be to extend the methods developed for computing cosmological observables from numerical relativity simulations of bubble collisions in one space and one time dimension [205] to the spacetimes studied here. Succesfully applying this procedure would be an important step towards making quantitative constraints on various early universe paradigms. The predictions obtained could be used to forecast the ability of cosmological datasets to place constraints on the mechanism that operated in the early universe and explains the large scale structure we observe today.

Finally, in this thesis we used a new formulation of the Einstein equations to study the nonlinear dynamics of binary black hole mergers in ESGB gravity. In this first study, we have taken a crucial first step towards using GWs emitted during the merger of compact objects to test the strong field limit of GR, fulfilling the promise of GW astronomy. However, there are still a lot of challenges to overcome before one can confidently claim a deviation from GR with GWs, and fully leverage the science potential of these exquisite detections. Clearly, the modeling of merger of compact objects in modified theories of gravity represents one of the most important challenges for present and future numerical studies, still it is essential to make contact between theoretical models and upcoming observations. Several areas of focus for follow-up work were already identified in the conclusion of the previous chapter, some of which are already underway. Ultimately, all of them are geared towards computing faithful and accurate theoretical models of the predicted gravitational waveforms in a large class of modified theories of gravity and covering a significant portion of the parameter space of potential binaries.

As was mentioned several times already, the main technical challenge when attempting to predict the GW signal in alternative theories of gravity is to formulate a well-posed initial value formulation. As a result, most groups have so far mainly focused: (i) on a very limited number of theories that preserve the mathematical structure of the field equations in GR e.g subclass of scalar-tensor theories that lead to neutron stars developing a scalar charge [310, 38] (ii) on treating the modifications to GR perturbatively [272, 270], (iii) or on reformulating the field equations in the spirit of Israel-Stewart theory in hydrodynamics [90, 91]. One particularly iteresting work which is already underway, is to compare our solutions to the full equations to these less computationally challenging aproaches.
The focus of this thesis was black hole spacetimes as they provide a very clean and elegant way of probing the highly dynamical regime of gravity. However, in the next few years, both the sensitivity and size of current ground-based GW detectors will increase. With a five-site GW network operating at design sensitivity, we expect 10-180 binary neutron star and black hole-neutron star (BHNS) detections per year with a significant fraction localized to within a few square degrees facilitating follow-up observations in the electromagnetic spectrum [4]. It is therefore interesting to consider whether the electromagnetic and GW transients of these sources can be used as an alternative and potentially more powerful probe to test our theory of gravity. The code used for our study of binary black holes is also able to numerically evolve hydrodynamics coupled to the Einstein equations. Work is

currently underway to study BHNS mergers in ESGB gravity. From an observational point of view, an interesting aspect of EsGB gravity is that unlike black holes, neutron stars do not carry scalar charge. Since the amount of scalar emission leading to a phase-shift in the gravitational signal as compared to GR in such theories scales with the difference between the scalar charges of component masses in binary, GW detections from BHNS binaries will give the strongest constraints on these theories. This shows the potential for discovery if one were to accurately model the gravitational signal emitted by these systems.

References

[1] Standalone TwoPunctures. https://github.com/JLRipley314/Standalone-TwoPunctures-C-Cpp.

[2] B. P. Abbott et al. Tests of general relativity with GW150914. *Phys. Rev. Lett.*, 116(22):221101, 2016. [Erratum: Phys.Rev.Lett. 121, 129902 (2018)].

[3] B. P. Abbott et al. GW170817: Observation of Gravitational Waves from a Binary Neutron Star Inspiral. *Phys. Rev. Lett.*, 119(16):161101, 2017.

[4] B. P. Abbott et al. Prospects for observing and localizing gravitational-wave transients with Advanced LIGO, Advanced Virgo and KAGRA. *Living Rev. Rel.*, 21(1):3, 2018.

[5] B. P. Abbott et al. Tests of General Relativity with GW170817. *Phys. Rev. Lett.*, 123(1):011102, 2019.

[6] B. P. Abbott et al. Tests of General Relativity with the Binary Black Hole Signals from the LIGO-Virgo Catalog GWTC-1. *Phys. Rev. D*, 100(10):104036, 2019.

[7] B. P. Abbott et al. GW190425: Observation of a Compact Binary Coalescence with Total Mass $\sim 3.4 M_\odot$. *Astrophys. J. Lett.*, 892(1):L3, 2020.

[8] R. Abbott et al. GWTC-3: Compact Binary Coalescences Observed by LIGO and Virgo During the Second Part of the Third Observing Run. 11 2021.

[9] R. Abbott et al. Observation of Gravitational Waves from Two Neutron Star–Black Hole Coalescences. *Astrophys. J. Lett.*, 915(1):L5, 2021.

[10] R. Abbott et al. Tests of general relativity with binary black holes from the second LIGO-Virgo gravitational-wave transient catalog. *Phys. Rev. D*, 103(12):122002, 2021.

[11] R. Abbott et al. Tests of General Relativity with GWTC-3. 12 2021.

[12] Allan Adams, Nima Arkani-Hamed, Sergei Dubovsky, Alberto Nicolis, and Riccardo Rattazzi. Causality, analyticity and an IR obstruction to UV completion. *JHEP*, 10:014, 2006.

[13] P. A. R. Ade et al. Improved Constraints on Primordial Gravitational Waves using Planck, WMAP, and BICEP/Keck Observations through the 2018 Observing Season. *Phys. Rev. Lett.*, 127(15):151301, 2021.

[14] N. Aghanim et al. Planck 2018 results. I. Overview and the cosmological legacy of Planck. *Astron. Astrophys.*, 641:A1, 2020.

[15] Anthony Aguirre, Matthew C Johnson, and Magdalena Larfors. Runaway dilatonic domain walls. *Phys. Rev. D*, 81:043527, 2010.

[16] Y. Akrami et al. Planck 2018 results. X. Constraints on inflation. *Astron. Astrophys.*, 641:A10, 2020.

[17] Andreas Albrecht, Robert H. Brandenberger, and R. Matzner. Numerical Analysis of Inflation. *Phys. Rev. D*, 32:1280, 1985.

[18] Andreas Albrecht, Robert H. Brandenberger, and Richard Matzner. Inflation With Generalized Initial Conditions. *Phys. Rev. D*, 35:429, 1987.

[19] Andreas Albrecht and Paul J. Steinhardt. Cosmology for Grand Unified Theories with Radiatively Induced Symmetry Breaking. *Phys. Rev. Lett.*, 48:1220–1223, 1982.

[20] Artur Alho and Filipe C. Mena. Pre-inflationary homogenization of scalar field cosmologies. *Phys. Lett. B*, 703:537–542, 2011.

[21] Laura E. Allen and David Wands. Cosmological perturbations through a simple bounce. *Phys. Rev. D*, 70:063515, 2004.

[22] Peter Anninos, David Bernstein, Steven Brandt, Joseph Libson, Joan Masso, Edward Seidel, Larry Smarr, Wai-Mo Suen, and Paul Walker. Dynamics of apparent and event horizons. *Phys. Rev. Lett.*, 74:630–633, 1995.

[23] Marcus Ansorg, Bernd Bruegmann, and Wolfgang Tichy. A Single-domain spectral method for black hole puncture data. *Phys. Rev. D*, 70:064011, 2004.

[24] Llibert Aresté Saló, Katy Clough, and Pau Figueras. Well-posedness of the four-derivative scalar-tensor theory of gravity in singularity avoiding coordinates. 8 2022.

[25] Nima Arkani-Hamed, Hsin-Chia Cheng, Markus A. Luty, and Shinji Mukohyama. Ghost condensation and a consistent infrared modification of gravity. *JHEP*, 05:074, 2004.

[26] Nima Arkani-Hamed, Savas Dimopoulos, and G.R. Dvali. The Hierarchy problem and new dimensions at a millimeter. *Phys.Lett.*, B429:263–272, 1998.

[27] K. G. Arun, Luc Blanchet, Bala R. Iyer, and Moh'd S. S. Qusailah. The 2.5PN gravitational wave polarisations from inspiralling compact binaries in circular orbits. *Class. Quant. Grav.*, 21:3771–3802, 2004. [Erratum: Class.Quant.Grav. 22, 3115 (2005)].

[28] Cesar Asensio and Antonio Segui. Exploring a simple sector of the Einstein-Maxwell landscape. *Phys. Rev. D*, 87(2):023503, 2013.

[29] Abhay Ashtekar and Gregory J. Galloway. Some uniqueness results for dynamical horizons. *Adv. Theor. Math. Phys.*, 9(1):1–30, 2005.

[30] Abhay Ashtekar and Badri Krishnan. Dynamical horizons: Energy, angular momentum, fluxes and balance laws. *Phys. Rev. Lett.*, 89:261101, 2002.

[31] Abhay Ashtekar and Badri Krishnan. Dynamical horizons and their properties. *Phys. Rev. D*, 68:104030, 2003.

[32] Abhay Ashtekar and Badri Krishnan. Isolated and dynamical horizons and their applications. *Living Rev. Rel.*, 7:10, 2004.

[33] Josu C. Aurrekoetxea, Katy Clough, Raphael Flauger, and Eugene A. Lim. The Effects of Potential Shape on Inhomogeneous Inflation. *JCAP*, 05:030, 2020.

[34] Josu C. Aurrekoetxea, Katy Clough, and Eugene A. Lim. CTTK: A new method to solve the initial data constraints in numerical relativity. 7 2022.

[35] E. Babichev, V. Dokuchaev, and Yu. Eroshenko. Black hole mass decreasing due to phantom energy accretion. *Phys. Rev. Lett.*, 93:021102, 2004.

[36] T. Baker, E. Bellini, P. G. Ferreira, M. Lagos, J. Noller, and I. Sawicki. Strong constraints on cosmological gravity from GW170817 and GRB 170817A. *Phys. Rev. Lett.*, 119(25):251301, 2017.

[37] T. Banks and W. Fischler. Black crunch. 12 2002.

[38] Enrico Barausse, Carlos Palenzuela, Marcelo Ponce, and Luis Lehner. Neutron-star mergers in scalar-tensor theories of gravity. *Phys. Rev. D*, 87:081506, 2013.

[39] James M. Bardeen, B. Carter, and S. W. Hawking. The Four laws of black hole mechanics. *Commun. Math. Phys.*, 31:161–170, 1973.

[40] J. D. Barrow and F. J. Tipler. Closed universe - Their future evolution and final state. *Mon. Not. Roy. Astron. Soc.*, 216:395–402, September 1985.

[41] Itzhak Bars, Shih-Hung Chen, Paul J. Steinhardt, and Neil Turok. Antigravity and the Big Crunch/Big Bang Transition. *Phys. Lett. B*, 715:278–281, 2012.

[42] Robert Bartnik and Jim Isenberg. The Constraint equations. In *50 Years of the Cauchy Problem in General Relativity: Summer School on Mathematical Relativity and Global Properties of Solutions of Einstein's Equations*, 2002.

[43] D. Battefeld and Patrick Peter. A Critical Review of Classical Bouncing Cosmologies. *Phys. Rept.*, 571:1–66, 2015.

[44] Daniel Baumann. Inflation. In *Theoretical Advanced Study Institute in Elementary Particle Physics: Physics of the Large and the Small*, pages 523–686, 2011.

[45] Thomas W. Baumgarte, Niall O Murchadha, and Harald P. Pfeiffer. The Einstein constraints: Uniqueness and non-uniqueness in the conformal thin sandwich approach. *Phys. Rev. D*, 75:044009, 2007.

[46] Thomas W. Baumgarte and Stuart L. Shapiro. *Numerical Relativity: Solving Einstein's Equations on the Computer*. Cambridge University Press, 2010.

[47] Eloisa Bentivegna and Mikolaj Korzynski. Evolution of a periodic eight-black-hole lattice in numerical relativity. *Class. Quant. Grav.*, 29:165007, 2012.

[48] Marsha J. Berger and Joseph Oliger. Adaptive Mesh Refinement for Hyperbolic Partial Differential Equations. *Journal of Computational Physics*, 53(3):484–512, March 1984.

[49] Emanuele Berti, Vitor Cardoso, Jose A. Gonzalez, Ulrich Sperhake, Mark Hannam, Sascha Husa, and Bernd Bruegmann. Inspiral, merger and ringdown of unequal mass black hole binaries: A Multipolar analysis. *Phys. Rev. D*, 76:064034, 2007.

[50] Emanuele Berti, Lucas G. Collodel, Burkhard Kleihaus, and Jutta Kunz. Spin-induced black-hole scalarization in Einstein-scalar-Gauss-Bonnet theory. *Phys. Rev. Lett.*, 126(1):011104, 2021.

[51] Emanuele Berti et al. Testing General Relativity with Present and Future Astrophysical Observations. *Class. Quant. Grav.*, 32:243001, 2015.

[52] Emanuele Berti, Kent Yagi, Huan Yang, and Nicolás Yunes. Extreme Gravity Tests with Gravitational Waves from Compact Binary Coalescences: (II) Ringdown. *Gen. Rel. Grav.*, 50(5):49, 2018.

[53] Emanuele Berti, Kent Yagi, and Nicolás Yunes. Extreme Gravity Tests with Gravitational Waves from Compact Binary Coalescences: (I) Inspiral-Merger. *Gen. Rel. Grav.*, 50(4):46, 2018.

[54] Miguel Bezares, Ricard Aguilera-Miret, Lotte ter Haar, Marco Crisostomi, Carlos Palenzuela, and Enrico Barausse. No Evidence of Kinetic Screening in Simulations of Merging Binary Neutron Stars beyond General Relativity. *Phys. Rev. Lett.*, 128(9):091103, 2022.

[55] Luc Blanchet. Gravitational Radiation from Post-Newtonian Sources and Inspiralling Compact Binaries. *Living Rev. Rel.*, 17:2, 2014.

[56] Jose J. Blanco-Pillado, Handhika S. Ramadhan, and Benjamin Shlaer. Decay of flux vacua to nothing. *JCAP*, 1010:029, 2010.

[57] Jose J. Blanco-Pillado, Delia Schwartz-Perlov, and Alexander Vilenkin. Quantum Tunneling in Flux Compactifications. *JCAP*, 0912:006, 2009.

[58] Jose J. Blanco-Pillado, Delia Schwartz-Perlov, and Alexander Vilenkin. Transdimensional Tunneling in the Multiverse. *JCAP*, 1005:005, 2010.

[59] Jose Luis Blázquez-Salcedo, Caio F. B. Macedo, Vitor Cardoso, Valeria Ferrari, Leonardo Gualtieri, Fech Scen Khoo, Jutta Kunz, and Paolo Pani. Perturbed black holes in Einstein-dilaton-Gauss-Bonnet gravity: Stability, ringdown, and gravitational-wave emission. *Phys. Rev. D*, 94(10):104024, 2016.

[60] Ivan Booth, Lionel Brits, Jose A. Gonzalez, and Chris Van Den Broeck. Marginally trapped tubes and dynamical horizons. *Class. Quant. Grav.*, 23:413–440, 2006.

[61] David G. Boulware and S. Deser. String-generated gravity models. *Phys. Rev. Lett.*, 55:2656–2660, Dec 1985.

[62] Raphael Bousso. Holography in general space-times. *JHEP*, 06:028, 1999.

[63] Raphael Bousso, Oliver DeWolfe, and Robert C. Myers. Unbounded entropy in space-times with positive cosmological constant. *Found. Phys.*, 33:297–321, 2003.

[64] Raphael Bousso and Netta Engelhardt. New Area Law in General Relativity. *Phys. Rev. Lett.*, 115(8):081301, 2015.

[65] Raphael Bousso and Netta Engelhardt. Proof of a New Area Law in General Relativity. *Phys. Rev. D*, 92(4):044031, 2015.

[66] Jonathan Braden, Matthew C. Johnson, Hiranya V. Peiris, and Anthony Aguirre. Constraining cosmological ultralarge scale structure using numerical relativity. *Phys. Rev. D*, 96(2):023541, 2017.

[67] Patrick R. Brady and John D. Smith. Black hole singularities: A Numerical approach. *Phys. Rev. Lett.*, 75:1256–1259, 1995.

[68] Matteo Braglia, Andrei Linde, Renata Kallosh, and Fabio Finelli. Hybrid α-attractors, primordial black holes and gravitational wave backgrounds. 11 2022.

[69] Robert Brandenberger. Initial conditions for inflation — A short review. *Int. J. Mod. Phys. D*, 26(01):1740002, 2016.

[70] Robert Brandenberger and Patrick Peter. Bouncing Cosmologies: Progress and Problems. *Found. Phys.*, 47(6):797–850, 2017.

[71] Robert H. Brandenberger. Conceptual problems of inflationary cosmology and a new approach to cosmological structure formation. In *Inflationary Cosmology*, pages 393–424. Springer Berlin Heidelberg.

[72] Robert H. Brandenberger. The Matter Bounce Alternative to Inflationary Cosmology. 6 2012.

[73] Robert H. Brandenberger and Hume A. Feldman. Effects of Gravitational Perturbations on the Evolution of Scalar Fields in the Early Universe. *Phys. Lett. B*, 220:361–367, 1989.

[74] Steven Brandt and Bernd Bruegmann. A Simple construction of initial data for multiple black holes. *Phys. Rev. Lett.*, 78:3606–3609, 1997.

[75] Adam R. Brown and Alex Dahlen. Small Steps and Giant Leaps in the Landscape. *Phys.Rev.*, D82:083519, 2010.

[76] Adam R. Brown and Alex Dahlen. Spectrum and stability of compactifications on product manifolds. *Phys. Rev. D*, 90(4):044047, 2014.

[77] Adam R. Brown, Alex Dahlen, and Ali Masoumi. Compactifying de Sitter space naturally selects a small cosmological constant. *Phys. Rev. D*, 90(12):124048, 2014.

[78] J.David Brown. Generalized Harmonic Equations in 3+1 Form. *Phys. Rev. D*, 84:124012, 2011.

[79] Evgeny I. Buchbinder, Justin Khoury, and Burt A. Ovrut. New Ekpyrotic cosmology. *Phys. Rev. D*, 76:123503, 2007.

[80] A. B. Burd and John D. Barrow. Inflationary Models with Exponential Potentials. *Nucl. Phys. B*, 308:929–945, 1988. [Erratum: Nucl.Phys.B 324, 276–276 (1989)].

[81] Rong-Gen Cai and Sang Pyo Kim. First law of thermodynamics and Friedmann equations of Friedmann-Robertson-Walker universe. *JHEP*, 02:050, 2005.

[82] Yi-Fu Cai, Damien A. Easson, and Robert Brandenberger. Towards a Nonsingular Bouncing Cosmology. *JCAP*, 08:020, 2012.

[83] Yi-Fu Cai, Taotao Qiu, Robert Brandenberger, Yun-Song Piao, and Xinmin Zhang. On Perturbations of Quintom Bounce. *JCAP*, 03:013, 2008.

[84] B. J. Carr and A. A. Coley. Persistence of black holes through a cosmological bounce. *Int. J. Mod. Phys. D*, 20:2733–2738, 2011.

[85] Bernard Carr, Kazunori Kohri, Yuuiti Sendouda, and Jun'ichi Yokoyama. Constraints on primordial black holes. *Rept. Prog. Phys.*, 84(11):116902, 2021.

[86] Bernard J. Carr and S. W. Hawking. Black holes in the early Universe. *Mon. Not. Roy. Astron. Soc.*, 168:399–415, 1974.

[87] Sean M Carroll. *Spacetime and geometry.* Cambridge University Press, 2019.

[88] Sean M. Carroll, Matthew C. Johnson, and Lisa Randall. Dynamical compactification from de Sitter space. *JHEP*, 11:094, 2009.

[89] Belen Carvente, Víctor Jaramillo, Juan Carlos Degollado, Darío Núñez, and Olivier Sarbach. Traversable ℓ-wormholes supported by ghost scalar fields. *Class. Quant. Grav.*, 36(23):235005, 2019.

[90] Juan Cayuso, Néstor Ortiz, and Luis Lehner. Fixing extensions to general relativity in the nonlinear regime. *Phys. Rev. D*, 96(8):084043, 2017.

[91] Ramiro Cayuso and Luis Lehner. Nonlinear, noniterative treatment of EFT-motivated gravity. *Phys. Rev. D*, 102(8):084008, 2020.

[92] Katie Chamberlain and Nicolas Yunes. Theoretical Physics Implications of Gravitational Wave Observation with Future Detectors. *Phys. Rev. D*, 96(8):084039, 2017.

[93] George F. Chapline. Cosmological effects of primordial black holes. *Nature*, 253(5489):251–252, Jan 1975.

[94] Jie-Wen Chen, Junyu Liu, Hao-Lan Xu, and Yi-Fu Cai. Tracing Primordial Black Holes in Nonsingular Bouncing Cosmology. *Phys. Lett. B*, 769:561–568, 2017.

[95] Matthew W. Choptuik and Frans Pretorius. Ultra Relativistic Particle Collisions. *Phys. Rev. Lett.*, 104:111101, 2010.

[96] Yvonne Choquet-Bruhat, James Isenberg, and Vincent Moncrief. Solutions of constraints for einstein equations. *Comptes rendus de l'Académie des sciences. Série 1, Mathématique*, 315(3):349–355, 1992.

[97] Yvonne Choquet-Bruhat, James Isenberg, and Daniel Pollack. The Constraint equations for the Einstein-scalar field system on compact manifolds. *Class. Quant. Grav.*, 24:809–828, 2007.

[98] Yvonne Choquet-Bruhat, James Isenberg, and James W. York, Jr. Einstein constraints on asymptotically Euclidean manifolds. *Phys. Rev. D*, 61:084034, 2000.

[99] D. Christodoulou. Reversible and irreversible transforations in black hole physics. *Phys. Rev. Lett.*, 25:1596–1597, 1970.

[100] Michele Cicoli, Senarath De Alwis, Anshuman Maharana, Francesco Muia, and Fernando Quevedo. De Sitter vs Quintessence in String Theory. *Fortsch. Phys.*, 67(1-2):1800079, 2019.

[101] Timothy Clifton, Bernard Carr, and Alan Coley. Persistent Black Holes in Bouncing Cosmologies. *Class. Quant. Grav.*, 34(13):135005, 2017.

[102] James M. Cline, Sangyong Jeon, and Guy D. Moore. The Phantom menaced: Constraints on low-energy effective ghosts. *Phys. Rev. D*, 70:043543, 2004.

[103] Katy Clough, Pau Figueras, Hal Finkel, Markus Kunesch, Eugene A Lim, and Saran Tunyasuvunakool. Grchombo: Numerical relativity with adaptive mesh refinement. *Classical and Quantum Gravity*, 32(24):245011, dec 2015.

[104] Katy Clough, Raphael Flauger, and Eugene A. Lim. Robustness of Inflation to Large Tensor Perturbations. *JCAP*, 05:065, 2018.

[105] Katy Clough, Eugene A. Lim, Brandon S. DiNunno, Willy Fischler, Raphael Flauger, and Sonia Paban. Robustness of Inflation to Inhomogeneous Initial Conditions. *JCAP*, 09:025, 2017.

[106] Carlo R. Contaldi, Lev Kofman, and Marco Peloso. Gravitational instability of de Sitter compactifications. *JCAP*, 0408:007, 2004.

[107] Gregory B. Cook. Initial data for numerical relativity. *Living Rev. Rel.*, 3:5, 2000.

[108] William G. Cook, Iryna A. Glushchenko, Anna Ijjas, Frans Pretorius, and Paul J. Steinhardt. Supersmoothing through Slow Contraction. *Phys. Lett. B*, 808:135690, 2020.

[109] Maxence Corman and William E. East. Starting inflation from inhomogeneous initial conditions with momentum. 12 2022.

[110] Maxence Corman, William E. East, and Matthew C. Johnson. Nonlinear dynamics of flux compactification. *JHEP*, 09:021, 2021.

[111] Maxence Corman, William E. East, and Justin L. Ripley. Evolution of black holes through a nonsingular cosmological bounce. 6 2022.

[112] Maxence Corman, Justin L. Ripley, and William E. East. Nonlinear studies of binary black hole mergers in Einstein-scalar-Gauss-Bonnet gravity. *Phys. Rev. D*, 107(2):024014, 2023.

[113] Paolo Creminelli, Or Hershkovits, Leonardo Senatore, and András Vasy. A de Sitter no-hair theorem for 3+1d Cosmologies with isometry group forming 2-dimensional orbits. 4 2020.

[114] Alex Dahlen and Claire Zukowski. Flux Compactifications Grow Lumps. *Phys. Rev.*, D90(12):125013, 2014.

[115] Claudia de Rham and Scott Melville. Unitary null energy condition violation in P(X) cosmologies. *Phys. Rev. D*, 95(12):123523, 2017.

[116] Frederik Denef, Michael R. Douglas, and Shamit Kachru. Physics of String Flux Compactifications. *Ann. Rev. Nucl. Part. Sci.*, 57:119–144, 2007.

[117] Nathalie Deruelle and Dalia S. Goldwirth. Conditions for inflation in an initially inhomogeneous universe. *Phys. Rev. D*, 51:1563–1568, 1995.

[118] Oliver DeWolfe, Daniel Z. Freedman, Steven S. Gubser, Gary T. Horowitz, and Indrajit Mitra. Stability of AdS(p) x M(q) compactifications without supersymmetry. *Phys.Rev.*, D65:064033, 2002.

[119] Oliver DeWolfe and Steven B. Giddings. Scales and hierarchies in warped compactifications and brane worlds. *Phys.Rev.*, D67:066008, 2003.

[120] Alexandru Dima, Enrico Barausse, Nicola Franchini, and Thomas P. Sotiriou. Spin-induced black hole spontaneous scalarization. *Phys. Rev. Lett.*, 125(23):231101, 2020.

[121] David A. Dobre, Andrei V. Frolov, José T. Gálvez Ghersi, Sabir Ramazanov, and Alexander Vikman. Unbraiding the Bounce: Superluminality around the Corner. *JCAP*, 03:020, 2018.

[122] Daniela D. Doneva and Stoytcho S. Yazadjiev. New Gauss-Bonnet Black Holes with Curvature-Induced Scalarization in Extended Scalar-Tensor Theories. *Phys. Rev. Lett.*, 120(13):131103, 2018.

[123] Michael R. Douglas and Shamit Kachru. Flux compactification. *Rev. Mod. Phys.*, 79:733–796, 2007.

[124] S. Dubovsky, T. Gregoire, A. Nicolis, and R. Rattazzi. Null energy condition and superluminal propagation. *JHEP*, 03:025, 2006.

[125] Damien A. Easson, Ignacy Sawicki, and Alexander Vikman. G-Bounce. *JCAP*, 11:021, 2011.

[126] William E. East, John Kearney, Bibhushan Shakya, Hojin Yoo, and Kathryn M. Zurek. Spacetime Dynamics of a Higgs Vacuum Instability During Inflation. *Phys. Rev. D*, 95(2):023526, 2017.

[127] William E. East, Matthew Kleban, Andrei Linde, and Leonardo Senatore. Beginning inflation in an inhomogeneous universe. *JCAP*, 09:010, 2016.

[128] William E. East and Frans Pretorius. Ultrarelativistic black hole formation. *Phys. Rev. Lett.*, 110(10):101101, 2013.

[129] William E. East and Frans Pretorius. Binary neutron star mergers in Einstein-scalar-Gauss-Bonnet gravity. 8 2022.

[130] William E. East, Frans Pretorius, and Branson C. Stephens. Hydrodynamics in full general relativity with conservative AMR. *Phys. Rev. D*, 85:124010, 2012.

[131] William E. East, Fethi M. Ramazanoglu, and Frans Pretorius. Conformal Thin-Sandwich Solver for Generic Initial Data. *Phys. Rev. D*, 86:104053, 2012.

[132] William E. East and Justin L. Ripley. Dynamics of Spontaneous Black Hole Scalarization and Mergers in Einstein-Scalar-Gauss-Bonnet Gravity. *Phys. Rev. Lett.*, 127(10):101102, 2021.

[133] William E. East and Justin L. Ripley. Evolution of Einstein-scalar-Gauss-Bonnet gravity using a modified harmonic formulation. *Phys. Rev. D*, 103(4):044040, 2021.

[134] William E. East, Radosław Wojtak, and Tom Abel. Comparing Fully General Relativistic and Newtonian Calculations of Structure Formation. *Phys. Rev. D*, 97(4):043509, 2018.

[135] Richard Easther, Layne C. Price, and Javier Rasero. Inflating an Inhomogeneous Universe. *JCAP*, 08:041, 2014.

[136] Benjamin Elder, Austin Joyce, and Justin Khoury. From Satisfying to Violating the Null Energy Condition. *Phys. Rev. D*, 89(4):044027, 2014.

[137] Matthew Elley, Hector O. Silva, Helvi Witek, and Nicolás Yunes. Spin-induced dynamical scalarization, descalarization, and stealthness in scalar-Gauss-Bonnet gravity during a black hole coalescence. *Phys. Rev. D*, 106(4):044018, 2022.

[138] Roberto Emparan and Harvey S. Reall. Black holes in higher dimensions. *Living Reviews in Relativity*, 11(1), sep 2008.

[139] Joel K. Erickson, Daniel H. Wesley, Paul J. Steinhardt, and Neil Turok. Kasner and mixmaster behavior in universes with equation of state w >= 1. *Phys. Rev. D*, 69:063514, 2004.

[140] Jose R. Espinosa, Gian F. Giudice, Enrico Morgante, Antonio Riotto, Leonardo Senatore, Alessandro Strumia, and Nikolaos Tetradis. The cosmological Higgstory of the vacuum instability. *JHEP*, 09:174, 2015.

[141] L.C. Evans. *Partial Differential Equations*. Graduate studies in mathematics. American Mathematical Society, 2010.

[142] V. Faraoni. *Cosmological and Black Hole Apparent Horizons*. Lecture Notes in Physics. Springer International Publishing, 2015.

[143] Valerio Faraoni and Audrey Jacques. Cosmological expansion and local physics. *Phys. Rev. D*, 76:063510, 2007.

[144] Valerio Faraoni, Andres F. Zambrano Moreno, and Roshina Nandra. Making sense of the bizarre behaviour of horizons in the McVittie spacetime. *Phys. Rev. D*, 85:083526, 2012.

[145] Valerio Faraoni, Andres F. Zambrano Moreno, and Angus Prain. The charged McVittie spacetime. *Phys. Rev. D*, 89(10):103514, 2014.

[146] Pau Figueras and Tiago França. Gravitational Collapse in Cubic Horndeski Theories. 6 2020.

[147] Pau Figueras and Tiago França. Black hole binaries in cubic Horndeski theories. *Phys. Rev. D*, 105(12):124004, 2022.

[148] Nicola Franchini, Miguel Bezares, Enrico Barausse, and Luis Lehner. Fixing the dynamical evolution in scalar-Gauss-Bonnet gravity. 5 2022.

[149] Peter G. O. Freund and Mark A. Rubin. Dynamics of Dimensional Reduction. *Phys. Lett.*, 97B:233–235, 1980. [,80(1980)].

[150] Andrew R. Frey. Warped strings: Selfdual flux and contemporary compactifications. Other thesis, 8 2003.

[151] Andrew R. Frey, Gonzalo Torroba, Bret Underwood, and Michael R. Douglas. The Universal Kahler Modulus in Warped Compactifications. *JHEP*, 0901:036, 2009.

[152] Andrei V. Frolov and Lev Kofman. Inflation and de Sitter thermodynamics. *JCAP*, 05:009, 2003.

[153] José T. Gálvez Ghersi and Leo C. Stein. Numerical renormalization-group-based approach to secular perturbation theory. *Phys. Rev. E*, 104(3):034219, 2021.

[154] Jose Tomas Galvez Ghersi, Ghazal Geshnizjani, Federico Piazza, and Sarah Shandera. Eternal inflation and a thermodynamic treatment of Einstein's equations. *JCAP*, 06:005, 2011.

[155] Changjun Gao, Xuelei Chen, Valerio Faraoni, and You-Gen Shen. Does the mass of a black hole decrease due to the accretion of phantom energy. *Phys. Rev. D*, 78:024008, 2008.

[156] Changjun Gao, Xuelei Chen, You-Gen Shen, and Valerio Faraoni. Black Holes in the Universe: Generalized Lemaitre-Tolman-Bondi Solutions. *Phys. Rev. D*, 84:104047, 2011.

[157] David Garfinkle. Harmonic coordinate method for simulating generic singularities. *Phys. Rev. D*, 65:044029, 2002.

[158] David Garfinkle, Anna Ijjas, and Paul J. Steinhardt. Initial conditions problem in cosmological inflation revisited. 2023.

[159] David Garfinkle, Woei Chet Lim, Frans Pretorius, and Paul J. Steinhardt. Evolution to a smooth universe in an ekpyrotic contracting phase with w > 1. *Phys. Rev. D*, 78:083537, 2008.

[160] David Garfinkle and Lawrence Mead. Cosmological initial data for numerical relativity. *Phys. Rev. D*, 102(4):044022, 2020.

[161] M. Gasperini and G. Veneziano. The Pre - big bang scenario in string cosmology. *Phys. Rept.*, 373:1–212, 2003.

[162] Abhirup Ghosh. Summary of Tests of General Relativity with GWTC-3. In *56th Rencontres de Moriond on Gravitation*, 4 2022.

[163] Gary W. Gibbons and Kei-ichi Maeda. Black Holes in an Expanding Universe. *Phys. Rev. Lett.*, 104:131101, 2010.

[164] John T. Giblin, James B. Mertens, Glenn D. Starkman, and Chi Tian. Cosmic expansion from spinning black holes. *Class. Quant. Grav.*, 36(19):195009, 2019.

[165] Steven B. Giddings, Shamit Kachru, and Joseph Polchinski. Hierarchies from fluxes in string compactifications. *Phys. Rev. D*, 66:106006, 2002.

[166] Steven B. Giddings and Anshuman Maharana. Dynamics of warped compactifications and the shape of the warped landscape. *Phys.Rev.*, D73:126003, 2006.

[167] Steffen Gielen and Neil Turok. Perfect Quantum Cosmological Bounce. *Phys. Rev. Lett.*, 117(2):021301, 2016.

[168] Dalia S. Goldwirth. On inhomogeneous initial conditions for inflation. *Phys. Rev. D*, 43:3204–3213, 1991.

[169] Dalia S. Goldwirth and Tsvi Piran. Spherical Inhomogeneous Cosmologies and Inflation. 1. Numerical Methods. *Phys. Rev. D*, 40:3263, 1989.

[170] Dalia S. Goldwirth and Tsvi Piran. Inhomogeneity and the Onset of Inflation. *Phys. Rev. Lett.*, 64:2852–2855, 1990.

[171] Dalia S. Goldwirth and Tsvi Piran. Initial conditions for inflation. *Phys. Rept.*, 214:223–291, 1992.

[172] N. N. Gorkavyi and Sergei Tyul'bashev. Black Holes and Neutron Stars in an Oscillating Universe. *Astrophys. Bull.*, 76(3):229–247, 2021.

[173] Eric Gourgoulhon, Philippe Grandclement, Keisuke Taniguchi, Jean-Alain Marck, and Silvano Bonazzola. Quasiequilibrium sequences of synchronized and irrotational binary neutron stars in general relativity: 1. Method and tests. *Phys. Rev. D*, 63:064029, 2001.

[174] Ruth Gregory and Raymond Laflamme. The Instability of charged black strings and p-branes. *Nucl.Phys.*, B428:399–434, 1994.

[175] David J. Gross and John H. Sloan. The quartic effective action for the heterotic string. *Nuclear Physics B*, 291:41–89, 1987.

[176] Carsten Gundlach, Jose M. Martin-Garcia, Gioel Calabrese, and Ian Hinder. Constraint damping in the Z4 formulation and harmonic gauge. *Class. Quant. Grav.*, 22:3767–3774, 2005.

[177] Alan H. Guth. The Inflationary Universe: A Possible Solution to the Horizon and Flatness Problems. *Phys. Rev. D*, 23:347–356, 1981.

[178] J.J. Halliwell. Scalar fields in cosmology with an exponential potential. *Physics Letters B*, 185(3):341–344, 1987.

[179] S. W. Hawking. Gravitational radiation from colliding black holes. *Phys. Rev. Lett.*, 26:1344–1346, May 1971.

[180] Stephen Hawking. Gravitational radiation in an expanding universe. *J. Math. Phys.*, 9:598–604, 1968.

[181] S.W. Hawking, G.F.R. Ellis, and P.V. Landshoff. *The Large Scale Structure of Space-Time*. Cambridge Monographs on Mathematical Physics. Cambridge University Press, 1973.

[182] Sean A. Hayward. Marginal surfaces and apparent horizons. 3 1993.

[183] Sean A. Hayward. Gravitational energy in spherical symmetry. *Phys. Rev. D*, 53:1938–1949, 1996.

[184] Sean A. Hayward, Shinji Mukohyama, and M. C. Ashworth. Dynamic black hole entropy. *Phys. Lett. A*, 256:347–350, 1999.

[185] Carlos A. R. Herdeiro, Eugen Radu, Hector O. Silva, Thomas P. Sotiriou, and Nicolás Yunes. Spin-induced scalarized black holes. *Phys. Rev. Lett.*, 126(1):011103, 2021.

[186] Kurt Hinterbichler, Janna Levin, and Claire Zukowski. Kaluza-Klein Towers on General Manifolds. *Phys. Rev. D*, 89(8):086007, 2014.

[187] Eric W. Hirschmann, Luis Lehner, Steven L. Liebling, and Carlos Palenzuela. Black Hole Dynamics in Einstein-Maxwell-Dilaton Theory. *Phys. Rev.*, D97(6):064032, 2018.

[188] Gregory Walter Horndeski. Second-order scalar-tensor field equations in a four-dimensional space. *Int. J. Theor. Phys.*, 10:363–384, 1974.

[189] Sascha Husa, Sebastian Khan, Mark Hannam, Michael Pürrer, Frank Ohme, Xisco Jiménez Forteza, and Alejandro Bohé. Frequency-domain gravitational waves from nonprecessing black-hole binaries. I. New numerical waveforms and anatomy of the signal. *Phys. Rev. D*, 93(4):044006, 2016.

[190] Anna Ijjas, William G. Cook, Frans Pretorius, Paul J. Steinhardt, and Elliot Y. Davies. Robustness of slow contraction to cosmic initial conditions. *JCAP*, 08:030, 2020.

[191] Anna Ijjas, Frans Pretorius, Paul J. Steinhardt, and Andrew P. Sullivan. The Effects of Multiple Modes and Reduced Symmetry on the Rapidity and Robustness of Slow Contraction. 4 2021.

[192] Anna Ijjas and Paul J. Steinhardt. Classically stable nonsingular cosmological bounces. *Phys. Rev. Lett.*, 117(12):121304, 2016.

[193] Anna Ijjas and Paul J. Steinhardt. Fully stable cosmological solutions with a non-singular classical bounce. *Phys. Lett. B*, 764:289–294, 2017.

[194] Anna Ijjas and Paul J. Steinhardt. Bouncing Cosmology made simple. *Class. Quant. Grav.*, 35(13):135004, 2018.

[195] Anna Ijjas and Paul J. Steinhardt. A new kind of cyclic universe. *Phys. Lett. B*, 795:666–672, 2019.

[196] Anna Ijjas and Paul J. Steinhardt. Entropy, black holes, and the new cyclic universe. *Phys. Lett. B*, 824:136823, 2022.

[197] Anna Ijjas, Andrew P. Sullivan, Frans Pretorius, Paul J. Steinhardt, and William G. Cook. Ultralocality and slow contraction. *Journal of Cosmology and Astroparticle Physics*, 2021(06):013, jun 2021.

[198] Maximiliano Isi, Will M. Farr, Matthew Giesler, Mark A. Scheel, and Saul A. Teukolsky. Testing the black-hole area law with GW150914. 12 2020.

[199] Maximiliano Isi, Matthew Giesler, Will M. Farr, Mark A. Scheel, and Saul A. Teukolsky. Testing the no-hair theorem with GW150914. *Phys. Rev. Lett.*, 123(11):111102, 2019.

[200] Ted Jacobson. Thermodynamics of space-time: The Einstein equation of state. *Phys. Rev. Lett.*, 75:1260–1263, 1995.

[201] Cristian Joana. Gravitational dynamics in Higgs inflation: Preinflation and preheating with an auxiliary field. *Phys. Rev. D*, 106(2):023504, 2022.

[202] Cristian Joana and Sébastien Clesse. Inhomogeneous preinflation across Hubble scales in full general relativity. *Phys. Rev. D*, 103(8):083501, 2021.

[203] Matthew C. Johnson, Hiranya V. Peiris, and Luis Lehner. Determining the outcome of cosmic bubble collisions in full General Relativity. *Phys. Rev. D*, 85:083516, 2012.

[204] Matthew C. Johnson, Carroll L. Wainwright, Anthony Aguirre, and Hiranya V. Peiris. Simulating the Universe(s) III: Observables for the full bubble collision spacetime. *JCAP*, 07:020, 2016.

[205] Matthew C. Johnson, Carroll L. Wainwright, Anthony Aguirre, and Hiranya V. Peiris. Simulating the universe(s) III: observables for the full bubble collision spacetime. *Journal of Cosmology and Astroparticle Physics*, 2016(07):020–020, jul 2016.

[206] Félix-Louis Julié and Emanuele Berti. Post-Newtonian dynamics and black hole thermodynamics in Einstein-scalar-Gauss-Bonnet gravity. *Phys. Rev. D*, 100(10):104061, 2019.

[207] Félix-Louis Julié, Hector O. Silva, Emanuele Berti, and Nicolás Yunes. Black hole sensitivities in Einstein-scalar-Gauss-Bonnet gravity. *Phys. Rev. D*, 105(12):124031, 2022.

[208] Shamit Kachru, Renata Kallosh, Andrei D. Linde, Juan Martin Maldacena, Liam P. McAllister, et al. Towards inflation in string theory. *JCAP*, 0310:013, 2003.

[209] Shamit Kachru, Renata Kallosh, Andrei D. Linde, and Sandip P. Trivedi. De Sitter vacua in string theory. *Phys. Rev. D*, 68:046005, 2003.

[210] Renata Kallosh, Jin U Kang, Andrei D. Linde, and Viatcheslav Mukhanov. The New ekpyrotic ghost. *JCAP*, 04:018, 2008.

[211] Renata Kallosh and Andrei Linde. Universality Class in Conformal Inflation. *JCAP*, 07:002, 2013.

[212] Renata Kallosh and Andrei Linde. BICEP/Keck and Cosmological Attractors. 10 2021.

[213] Renata Kallosh and Andrei Linde. Hybrid cosmological attractors. *Phys. Rev. D*, 106(2):023522, 2022.

[214] Renata Kallosh, Andrei Linde, and Diederik Roest. Superconformal Inflationary α-Attractors. *JHEP*, 11:198, 2013.

[215] Renata Kallosh, Andrei Linde, and Alexander Westphal. Chaotic Inflation in Supergravity after Planck and BICEP2. *Phys. Rev. D*, 90(2):023534, 2014.

[216] Nemanja Kaloper, Matthew Kleban, and Damien Martin. McVittie's Legacy: Black Holes in an Expanding Universe. *Phys. Rev. D*, 81:104044, 2010.

129

[217] Th. Kaluza. Zum Unitätsproblem der Physik. *Sitzungsber. Preuss. Akad. Wiss. Berlin (Math. Phys.)*, 1921:966–972, 1921.

[218] P. Kanti, N. E. Mavromatos, J. Rizos, K. Tamvakis, and E. Winstanley. Dilatonic black holes in higher curvature string gravity. *Phys. Rev. D*, 54:5049–5058, Oct 1996.

[219] P. Kanti, N.E. Mavromatos, J. Rizos, K. Tamvakis, and E. Winstanley. Dilatonic black holes in higher curvature string gravity. 2: Linear stability. *Phys. Rev. D*, 57:6255–6264, 1998.

[220] Sebastian Khan, Sascha Husa, Mark Hannam, Frank Ohme, Michael Pürrer, Xisco Jiménez Forteza, and Alejandro Bohé. Frequency-domain gravitational waves from nonprecessing black-hole binaries. II. A phenomenological model for the advanced detector era. *Phys. Rev. D*, 93(4):044007, 2016.

[221] Justin Khoury, Burt A. Ovrut, Nathan Seiberg, Paul J. Steinhardt, and Neil Turok. From big crunch to big bang. *Phys. Rev. D*, 65:086007, 2002.

[222] Justin Khoury, Burt A. Ovrut, Paul J. Steinhardt, and Neil Turok. The Ekpyrotic universe: Colliding branes and the origin of the hot big bang. *Phys. Rev. D*, 64:123522, 2001.

[223] Shunichiro Kinoshita. New branch of Kaluza-Klein compactification. *Phys. Rev. D*, 76:124003, 2007.

[224] Shunichiro Kinoshita and Shinji Mukohyama. Thermodynamic and dynamical stability of Freund-Rubin compactification. *JCAP*, 06:020, 2009.

[225] Matthew Kleban and Leonardo Senatore. Inhomogeneous Anisotropic Cosmology. *JCAP*, 10:022, 2016.

[226] O. Klein. Quantum Theory and Five-Dimensional Theory of Relativity. (In German and English). *Z.Phys.*, 37:895–906, 1926.

[227] Prashant Kocherlakota et al. Constraints on black-hole charges with the 2017 EHT observations of M87*. *Phys. Rev. D*, 103(10):104047, 2021.

[228] Aron D. Kovacs. On the construction of asymptotically flat initial data in scalar-tensor effective field theory. 3 2021.

[229] Aron D. Kovacs and Harvey S. Reall. Well-posed formulation of Lovelock and Horndeski theories. *Phys. Rev. D*, 101(12):124003, 2020.

[230] Aron D. Kovacs and Harvey S. Reall. Well-posed formulation of scalar-tensor effective field theory. *Phys. Rev. Lett.*, 124(22):221101, 2020.

[231] H. O. Kreiss and J. Oliger. Comparison of accurate methods for the integration of hyperbolic equations. *Tellus*, 24:199, January 1972.

[232] Heinz-Otto Kreiss and Jens Lorenz. *Initial-Boundary Value Problems and the Navier-Stokes Equations.* Society for Industrial and Applied Mathematics, 2004.

[233] Heinz-Otto Kreiss and Joseph Oliger. Comparison of accurate methods for the integration of hyperbolic equations. *Tellus*, 24(3):199–215, 1972.

[234] C. Krishnan, S. Paban, and M. Zanic. Evolution of gravitationally unstable de Sitter compactifications. *JHEP*, 05:045, 2005.

[235] Hao-Jui Kuan, Daniela D. Doneva, and Stoytcho S. Yazadjiev. Dynamical Formation of Scalarized Black Holes and Neutron Stars through Stellar Core Collapse. *Phys. Rev. Lett.*, 127(16):161103, 2021.

[236] J. H. Kung and Robert H. Brandenberger. The Initial Condition Dependence of Inflationary Universe Models. *Phys. Rev. D*, 40:2532, 1989.

[237] H. Kurki-Suonio, R. A. Matzner, J. Centrella, and J. R. Wilson. Inflation From Inhomogeneous Initial Data in a One-dimensional Back Reacting Cosmology. *Phys. Rev. D*, 35:435–448, 1987.

[238] Hannu Kurki-Suonio, Pablo Laguna, and Richard A. Matzner. Inhomogeneous inflation: Numerical evolution. *Phys. Rev. D*, 48:3611–3624, 1993.

[239] P. Laguna, H. Kurki-Suonio, and R. A. Matzner. Inhomogeneous inflation: The Initial value problem. *Phys. Rev. D*, 44:3077–3086, 1991.

[240] Zhong-Heng Li and Anzhong Wang. Existence of black holes in Friedmann-Robertson-Walker universe dominated by dark energy. *Mod. Phys. Lett. A*, 22:1663–1676, 2007.

[241] Joseph Libson, Joan Masso, Edward Seidel, Wai-Mo Suen, and Paul Walker. Event horizons in numerical relativity. 1: Methods and tests. *Phys. Rev. D*, 53:4335–4350, 1996.

[242] Yen-Kheng Lim. Warped branches of flux compactifications. *Phys. Rev.*, D85:064027, 2012.

[243] Lee Lindblom and Bela Szilagyi. An Improved Gauge Driver for the GH Einstein System. *Phys. Rev. D*, 80:084019, 2009.

[244] Andrei Linde. Inflationary Cosmology after Planck 2013. In *100e Ecole d'Ete de Physique: Post-Planck Cosmology*, pages 231–316, 2015.

[245] Andrei Linde. On the problem of initial conditions for inflation. *Found. Phys.*, 48(10):1246–1260, 2018.

[246] Andrei D. Linde. A New Inflationary Universe Scenario: A Possible Solution of the Horizon, Flatness, Homogeneity, Isotropy and Primordial Monopole Problems. *Phys. Lett. B*, 108:389–393, 1982.

[247] Andrei D. Linde. Chaotic Inflation. *Phys. Lett. B*, 129:177–181, 1983.

[248] Andrei D. Linde. The Inflationary Universe. *Rept. Prog. Phys.*, 47:925–986, 1984.

[249] Andrei D. Linde. Initial conditions for Inflation. *Phys. Lett. B*, 162:281–286, 1985.

[250] Andrei D. Linde. Hybrid inflation. *Phys. Rev. D*, 49:748–754, 1994.

[251] Francisco S. N. Lobo. *Exotic solutions in General Relativity: Traversable wormholes and 'warp drive' spacetimes*. 10 2007.

[252] F. Lucchin and S. Matarrese. Power-law inflation. *Phys. Rev. D*, 32:1316–1322, Sep 1985.

[253] Zhenwei Lyu, Nan Jiang, and Kent Yagi. Constraints on Einstein-dilation-Gauss-Bonnet gravity from black hole-neutron star gravitational wave events. *Phys. Rev. D*, 105(6):064001, 2022.

[254] Michele Maggiore. *Gravitational Waves. Vol. 1: Theory and Experiments*. Oxford Master Series in Physics. Oxford University Press, 2007.

[255] Andrew J. Majda, Di Qi, and Themistoklis P. Sapsis. Blended particle filters for large-dimensional chaotic dynamical systems. *Proceedings of the National Academy of Sciences*, 111(21):7511–7516, 2014.

[256] Juan Martin Maldacena. The Large N limit of superconformal field theories and supergravity. *Int. J. Theor. Phys.*, 38:1113–1133, 1999.

[257] Paul L. McFadden, Neil Turok, and Paul J. Steinhardt. Solution of a braneworld big crunch / big bang cosmology. *Phys. Rev. D*, 76:104038, 2007.

[258] G. C. McVittie. The Mass-Particle in an Expanding Universe. *Monthly Notices of the Royal Astronomical Society*, 93(5):325–339, 03 1933.

[259] Masato Minamitsuji and Taishi Ikeda. Scalarized black holes in the presence of the coupling to Gauss-Bonnet gravity. *Phys. Rev. D*, 99(4):044017, 2019.

[260] Charles W. Misner and David H. Sharp. Relativistic equations for adiabatic, spherically symmetric gravitational collapse. *Phys. Rev.*, 136:B571–B576, Oct 1964.

[261] Carmen Molina-Paris and Matt Visser. Minimal conditions for the creation of a Friedman-Robertson-Walker universe from a 'bounce'. *Phys. Lett. B*, 455:90–95, 1999.

[262] Michael S. Morris and Kip S. Thorne. Wormholes in spacetime and their use for interstellar travel: A tool for teaching general relativity. *American Journal of Physics*, 56(5):395–412, 1988.

[263] Abdul H. Mroue, Harald P. Pfeiffer, Lawrence E. Kidder, and Saul A. Teukolsky. Measuring orbital eccentricity and periastron advance in quasi-circular black hole simulations. *Phys. Rev. D*, 82:124016, 2010.

[264] Ezra Newman and Roger Penrose. An approach to gravitational radiation by a method of spin coefficients. *Journal of Mathematical Physics*, 3(3):566–578, 1962.

[265] B. C. Nolan. A Point mass in an isotropic universe. 2. Global properties. *Class. Quant. Grav.*, 16:1227–1254, 1999.

[266] Brien C. Nolan. A Point mass in an isotropic universe: Existence, uniqueness and basic properties. *Phys. Rev. D*, 58:064006, 1998.

[267] Brien C. Nolan. A Point mass in an isotropic universe. 3. The region R less than or = to 2m. *Class. Quant. Grav.*, 16:3183–3191, 1999.

[268] M. Novello and S. E. Perez Bergliaffa. Bouncing Cosmologies. *Phys. Rept.*, 463:127–213, 2008.

[269] Niall Ó Murchadha and James W. York. Initial-value problem of general relativity. ii. stability of solutions of the initial-value equations. *Phys. Rev. D*, 10:437–446, Jul 1974.

[270] Maria Okounkova. Numerical relativity simulation of GW150914 in Einstein dilaton Gauss-Bonnet gravity. *Phys. Rev. D*, 102(8):084046, 2020.

[271] Maria Okounkova, Will M. Farr, Maximiliano Isi, and Leo C. Stein. Constraining gravitational wave amplitude birefringence and Chern-Simons gravity with GWTC-2. *Phys. Rev. D*, 106(4):044067, 2022.

[272] Maria Okounkova, Leo C. Stein, Mark A. Scheel, and Daniel A. Hemberger. Numerical binary black hole mergers in dynamical Chern-Simons gravity: Scalar field. *Phys. Rev. D*, 96(4):044020, 2017.

[273] Maria Okounkova, Leo C. Stein, Mark A. Scheel, and Saul A. Teukolsky. Numerical binary black hole collisions in dynamical Chern-Simons gravity. *Phys. Rev. D*, 100(10):104026, 2019.

[274] T. Padmanabhan. Classical and quantum thermodynamics of horizons in spherically symmetric space-times. *Class. Quant. Grav.*, 19:5387–5408, 2002.

[275] Eran Palti. The Swampland: Introduction and Review. *Fortsch. Phys.*, 67(6):1900037, 2019.

[276] Giuseppe Papallo. On the hyperbolicity of the most general Horndeski theory. *Phys. Rev. D*, 96(12):124036, 2017.

[277] Giuseppe Papallo and Harvey S. Reall. On the local well-posedness of Lovelock and Horndeski theories. *Phys. Rev. D*, 96(4):044019, 2017.

[278] Vasileios Paschalidis. private communication.

[279] Vasileios Paschalidis, Zachariah B. Etienne, Roman Gold, and Stuart L. Shapiro. An efficient spectral interpolation routine for the TwoPunctures code. 4 2013.

[280] Roger Penrose. Gravitational Collapse: the Role of General Relativity. *Nuovo Cimento Rivista Serie*, 1:252, January 1969.

[281] A. A. Penzias and R. W. Wilson. A Measurement of Excess Antenna Temperature at 4080 Mc/s. *Astrophys. J. Lett.*, 142:419–421, July 1965.

[282] Daniela Pérez, Santiago E. Perez Bergliaffa, and Gustavo E. Romero. Black hole in asymmetric cosmological bounce. *Astron. Nachr.*, 342(1-2):69–74, 2021.

[283] Daniela Pérez, Santiago E. Perez Bergliaffa, and Gustavo E. Romero. Dynamical black hole in a bouncing universe. *Phys. Rev. D*, 103(6):064019, 2021.

[284] Daniela Pérez and Gustavo E. Romero. Survival of black holes through a cosmological bounce. 5 2022.

[285] Scott E. Perkins, Remya Nair, Hector O. Silva, and Nicolas Yunes. Improved gravitational-wave constraints on higher-order curvature theories of gravity. *Phys. Rev. D*, 104(2):024060, 2021.

[286] Patrick Peter and Nelson Pinto-Neto. Primordial perturbations in a non singular bouncing universe model. *Phys. Rev. D*, 66:063509, 2002.

[287] P. C. Peters and J. Mathews. Gravitational radiation from point masses in a keplerian orbit. *Phys. Rev.*, 131:435–440, Jul 1963.

[288] Harald P. Pfeiffer and James W. York, Jr. Uniqueness and non-uniqueness in the Einstein constraints. *Phys. Rev. Lett.*, 95:091101, 2005.

[289] Lorenzo Pierini and Leonardo Gualtieri. Quasi-normal modes of rotating black holes in Einstein-dilaton Gauss-Bonnet gravity: the first order in rotation. *Phys. Rev. D*, 103:124017, 2021.

[290] Lorenzo Pierini and Leonardo Gualtieri. Quasi-normal modes of rotating black holes in Einstein-dilaton Gauss-Bonnet gravity: the second order in rotation. 7 2022.

[291] J. Polchinski. *String theory. Vol. 2: Superstring theory and beyond.* Cambridge Monographs on Mathematical Physics. Cambridge University Press, 12 2007.

[292] Frans Pretorius. Numerical relativity using a generalized harmonic decomposition. *Class. Quant. Grav.*, 22:425–452, 2005.

[293] Frans Pretorius. Simulation of binary black hole spacetimes with a harmonic evolution scheme. *Class. Quant. Grav.*, 23:S529–S552, 2006.

[294] Frans Pretorius and Matthew W. Choptuik. Adaptive mesh refinement for coupled elliptic-hyperbolic systems. *J. Comput. Phys.*, 218:246–274, 2006.

[295] Frans Pretorius, Branson Stephens, and Matthew W. Choptuik. PAMR. http://laplace.physics.ubc.ca/Group/Software.html.

[296] Dimitrios Psaltis et al. Gravitational Test Beyond the First Post-Newtonian Order with the Shadow of the M87 Black Hole. *Phys. Rev. Lett.*, 125(14):141104, 2020.

[297] Jerome Quintin and Robert H. Brandenberger. Black hole formation in a contracting universe. *JCAP*, 11:029, 2016.

[298] Lisa Randall and Raman Sundrum. A Large mass hierarchy from a small extra dimension. *Phys.Rev.Lett.*, 83:3370–3373, 1999.

[299] Lisa Randall and Raman Sundrum. An Alternative to compactification. *Phys.Rev.Lett.*, 83:4690–4693, 1999.

[300] Harvey S. Reall. Higher dimensional black holes. *International Journal of Modern Physics D*, 21(12):1230001, nov 2012.

[301] Justin L. Ripley. Numerical relativity for Horndeski gravity. 7 2022.

[302] Justin L. Ripley and Frans Pretorius. Gravitational collapse in Einstein dilaton-Gauss–Bonnet gravity. *Class. Quant. Grav.*, 36(13):134001, 2019.

[303] Justin L. Ripley and Frans Pretorius. Scalarized Black Hole dynamics in Einstein dilaton Gauss-Bonnet Gravity. *Phys. Rev. D*, 101(4):044015, 2020.

[304] V. A. Rubakov. The Null Energy Condition and its violation. *Phys. Usp.*, 57:128–142, 2014.

[305] Olivier Sarbach and Manuel Tiglio. Continuum and Discrete Initial-Boundary-Value Problems and Einstein's Field Equations. *Living Rev. Rel.*, 15:9, 2012.

[306] Erik Schnetter, Badri Krishnan, and Florian Beyer. Introduction to dynamical horizons in numerical relativity. *Phys. Rev. D*, 74:024028, 2006.

[307] E Schuecking. Das schwarzschildsche linienelement und die expansion des weltalls. *Eur. Phys. J. A*, 137(5):595–603, October 1954.

[308] Leonardo Senatore. Lectures on Inflation. In *Theoretical Advanced Study Institute in Elementary Particle Physics: New Frontiers in Fields and Strings*, pages 447–543, 2017.

[309] Noah Sennett, Sylvain Marsat, and Alessandra Buonanno. Gravitational waveforms in scalar-tensor gravity at 2PN relative order. *Phys. Rev. D*, 94(8):084003, 2016.

[310] Masaru Shibata, Keisuke Taniguchi, Hirotada Okawa, and Alessandra Buonanno. Coalescence of binary neutron stars in a scalar-tensor theory of gravity. *Phys. Rev. D*, 89(8):084005, 2014.

[311] Banafsheh Shiralilou, Tanja Hinderer, Samaya Nissanke, Néstor Ortiz, and Helvi Witek. Nonlinear curvature effects in gravitational waves from inspiralling black hole binaries. *Phys. Rev. D*, 103(12):L121503, 2021.

[312] Banafsheh Shiralilou, Tanja Hinderer, Samaya Nissanke, Néstor Ortiz, and Helvi Witek. Post-Newtonian Gravitational and Scalar Waves in Scalar-Gauss-Bonnet Gravity. 5 2021.

[313] Hector O. Silva, Caio F. B. Macedo, Thomas P. Sotiriou, Leonardo Gualtieri, Jeremy Sakstein, and Emanuele Berti. Stability of scalarized black hole solutions in scalar-Gauss-Bonnet gravity. *Phys. Rev. D*, 99(6):064011, 2019.

[314] Hector O. Silva, Jeremy Sakstein, Leonardo Gualtieri, Thomas P. Sotiriou, and Emanuele Berti. Spontaneous scalarization of black holes and compact stars from a Gauss-Bonnet coupling. *Phys. Rev. Lett.*, 120(13):131104, 2018.

[315] Hector O. Silva, Helvi Witek, Matthew Elley, and Nicolás Yunes. Dynamical Descalarization in Binary Black Hole Mergers. *Phys. Rev. Lett.*, 127(3):031101, 2021.

[316] Larry L. Smarr, editor. *Proceedings, Sources of Gravitational Radiation: Seattle, WA, USA, July 24 - August 4, 1978*, Cambridge, 1979. Cambridge Univ. Press.

[317] George F. Smoot et al. Structure in the COBE differential microwave radiometer first year maps. *Astrophys. J. Lett.*, 396:L1–L5, 1992.

[318] Thomas P. Sotiriou and Shuang-Yong Zhou. Black hole hair in generalized scalar-tensor gravity. *Phys. Rev. Lett.*, 112:251102, 2014.

[319] Thomas P. Sotiriou and Shuang-Yong Zhou. Black hole hair in generalized scalar-tensor gravity: An explicit example. *Phys. Rev. D*, 90:124063, 2014.

[320] Alexei A. Starobinsky. A New Type of Isotropic Cosmological Models Without Singularity. *Phys. Lett. B*, 91:99–102, 1980.

[321] Paul J. Steinhardt and Neil Turok. Cosmic evolution in a cyclic universe. *Phys. Rev. D*, 65:126003, 2002.

[322] Leonard Susskind. The anthropic landscape of string theory. In *Universe or Multiverse*. Cambridge University Press, 2003.

[323] Roberto A Sussman. Conformal structure of a schwarzschild black hole immersed in a friedman universe. *Gen. Relativ. Gravit.*, 17(3):251–291, March 1985.

[324] Oliver J. Tattersall, Pedro G. Ferreira, and Macarena Lagos. Speed of gravitational waves and black hole hair. *Phys. Rev. D*, 97(8):084005, 2018.

[325] Jonathan Thornburg. Event and apparent horizon finders for 3+1 numerical relativity. *Living Rev. Rel.*, 10:3, 2007.

[326] K. S. Thorne. In J. Klauder, editor, *Magic Without Magic: John Archibald Wheeler*, page 231, San Francisco, 1972. Freeman.

[327] Andrew J. Tolley, Neil Turok, and Paul J. Steinhardt. Cosmological perturbations in a big crunch / big bang space-time. *Phys. Rev. D*, 69:106005, 2004.

[328] Matt Visser. *Lorentzian wormholes: From Einstein to Hawking.* 1995.

[329] Sebastian H. Völkel, Enrico Barausse, Nicola Franchini, and Avery E. Broderick. EHT tests of the strong-field regime of general relativity. *Class. Quant. Grav.*, 38(21):21LT01, 2021.

[330] Carroll L. Wainwright, Matthew C. Johnson, Hiranya V. Peiris, Anthony Aguirre, Luis Lehner, and Steven L. Liebling. Simulating the universe(s): from cosmic bubble collisions to cosmological observables with numerical relativity. *JCAP*, 03:030, 2014.

[331] Darragh M. Walsh. Non-uniqueness in conformal formulations of the Einstein constraints. *Class. Quant. Grav.*, 24:1911–1926, 2007.

[332] Steven Weinberg. Effective Field Theory for Inflation. *Phys. Rev. D*, 77:123541, 2008.

[333] Clifford M. Will. The Confrontation between General Relativity and Experiment. *Living Rev. Rel.*, 17:4, 2014.

[334] Helvi Witek, Leonardo Gualtieri, Paolo Pani, and Thomas P. Sotiriou. Black holes and binary mergers in scalar Gauss-Bonnet gravity: scalar field dynamics. *Phys. Rev. D*, 99(6):064035, 2019.

[335] BingKan Xue. *Nonsingular Bouncing Cosmology.* PhD thesis, Princeton U., 2013.

[336] BingKan Xue, David Garfinkle, Frans Pretorius, and Paul J. Steinhardt. Nonperturbative analysis of the evolution of cosmological perturbations through a nonsingular bounce. *Phys. Rev. D*, 88:083509, 2013.

[337] Kent Yagi. A New constraint on scalar Gauss-Bonnet gravity and a possible explanation for the excess of the orbital decay rate in a low-mass X-ray binary. *Phys. Rev. D*, 86:081504, 2012.

[338] Kent Yagi, Leo C. Stein, and Nicolas Yunes. Challenging the Presence of Scalar Charge and Dipolar Radiation in Binary Pulsars. *Phys. Rev. D*, 93(2):024010, 2016.

[339] Kent Yagi, Leo C. Stein, Nicolás Yunes, and Takahiro Tanaka. Post-Newtonian, Quasi-Circular Binary Inspirals in Quadratic Modified Gravity. *Phys. Rev. D*, 85:064022, 2012. [Erratum: Phys.Rev.D 93, 029902 (2016)].

[340] Hwei-Jang Yo, James N. Cook, Stuart L. Shapiro, and Thomas W. Baumgarte. Quasi-equilibrium binary black hole initial data for dynamical evolutions. *Phys. Rev. D*, 70:084033, 2004. [Erratum: Phys.Rev.D 70, 089904 (2004)].

[341] Chul-Moon Yoo, Hirotada Okawa, and Ken-ichi Nakao. Black Hole Universe: Time Evolution. *Phys. Rev. Lett.*, 111:161102, 2013.

[342] James W. York, Jr. Conformal 'thin sandwich' data for the initial-value problem. *Phys. Rev. Lett.*, 82:1350–1353, 1999.

[343] Shijun Yoshida and Yoshiharu Eriguchi. Rotating boson stars in general relativity. *Phys. Rev. D*, 56:762–771, 1997.

[344] Nicolás Yunes and Xavier Siemens. Gravitational-Wave Tests of General Relativity with Ground-Based Detectors and Pulsar Timing-Arrays. *Living Rev. Rel.*, 16:9, 2013.

[345] Nicolas Yunes and Leo C. Stein. Non-Spinning Black Holes in Alternative Theories of Gravity. *Phys. Rev. D*, 83:104002, 2011.

[346] Nicolas Yunes, Kent Yagi, and Frans Pretorius. Theoretical Physics Implications of the Binary Black-Hole Mergers GW150914 and GW151226. *Phys. Rev. D*, 94(8):084002, 2016.

APPENDICES

Appendix A

Nonlinear dynamics of flux compactification

A.1 Dimensional reduction

In this section, we illustrate the properties of dimensional reduction with several examples. Recall that in our units $M_D \equiv (8\pi G_D)^{-1/(D-2)} = 1$.

A.1.1 Time-dependent Freund-Rubin Solution

We start with a simple example, where identifying scale factor and moduli fields in the four-dimensional effective theory is straightforward. Consider solutions of the form:

$$ds^2 = -N(t)^2 dt^2 + a(t)^2 d\vec{x}_{p-1}^2 + L(t)^2 d\Omega_q^2 \ . \tag{A.1}$$

This metric ansatz encompasses the static Freund-Rubin solutions of section 2.2.3, as well as the time-dependent solutions resulting from total-volume ($\ell = 0$) perturbations of the static Freund-Rubin solutions. For such solutions, we have

$$\frac{K - K^x{}_x}{2} \ = \ \frac{\dot{a}}{Na} + \frac{q}{2}\frac{\dot{L}}{NL} \ . \tag{A.2}$$

Defining

$$\tilde{N} = (L/L_0)^{q/2}\, N, \quad \tilde{a} = (L/L_0)^{q/2}\, a \ , \tag{A.3}$$

where $L_0 \equiv L(t=0)$ we have that

$$\int d^q y \sqrt{\gamma_q} N \gamma_{xx}^{3/2} \left(\frac{K^x{}_x - K}{2}\right)^2 = \left(L_0^q \int d\Omega_q\right) \tilde{N}\tilde{a}^3 \left(\frac{\dot{\tilde{a}}}{\tilde{N}\tilde{a}}\right)^2 \ . \tag{A.4}$$

From this expression we can identify $\tilde{N}$ as the four dimensional lapse, $\tilde{a}$ as the four dimensional scale factor and therefore:

$$M_4^2 = L_0^q \int d\Omega_q, \quad \sqrt{-g(t)} = \tilde{N}\tilde{a}^3, \quad H^2 = \left(\frac{\dot{\tilde{a}}}{\tilde{N}\tilde{a}}\right)^2 . \tag{A.5}$$

Note that the change of variables defined by eq. (A.3) is precisely the conformal transformation of the four-dimensional metric that brings us to the four-dimensional Einstein frame (e.g. the conformal frame in which the Planck mass is constant in time); for comparison, see, e.g., refs. [88, 114].

Evaluating the area of the cosmological apparent horizon using eq. (2.17), we obtain:

$$\mathcal{A}_H = 4\pi \int d\Omega_q L_0^q \left(\frac{\tilde{N}\tilde{a}}{\dot{\tilde{a}}}\right)^2 = M_4^2 \frac{4\pi}{H^2} . \tag{A.6}$$

The entropy, eq. (2.19), is given by $\mathcal{S} = 16\pi M_4^2/H^2$, which is the value one would have assigned based purely on the four dimensional effective theory.

For the time-dependent Freund-Rubin solutions, it is possible to derive the full dimensionally reduced action. This can be found, e.g., in refs. [88, 114], which we reproduce here for completeness. Expanding the terms in the action we obtain

$$\begin{aligned}
S &= \frac{1}{2} \int d^4x \, d^q y \, \sqrt{-g} \left[-6 \left(\frac{K^x{}_x - K}{2}\right)^2 \right. \\
&+ \frac{1}{2}(K^\theta{}_\theta)^2 + \frac{(q+3)(q-1)}{4}(K^\phi{}_\phi)^2 + (K^\theta{}_\theta + \frac{q-1}{2}K^\phi{}_\phi)^2 \\
&+ \left. {}^{(D-1)}R - 2\Lambda_D - \frac{1}{q!}\mathbf{F}_q^2 \right] .
\end{aligned} \tag{A.7}$$

Evaluating the various terms in the action for the metric ansatz eq. (A.1) we have:

$$\frac{1}{2}(K^\theta{}_\theta)^2 + \frac{(q+3)(q-1)}{4}(K^\phi{}_\phi)^2 + (K^\theta{}_\theta + \frac{q-1}{2}K^\phi{}_\phi)^2 = \frac{q(q+2)}{2}\left(\frac{\dot{L}}{L}\right)^2 , \tag{A.8}$$

$$^{(D-1)}R = \frac{q(q-1)}{L^2} \tag{A.9}$$

and

$$\frac{1}{q!}\mathbf{F}_q^2 = \frac{Q_B^2}{L^{2q}} = \frac{1}{M_4^4}\frac{n^2}{L^{2q}} . \tag{A.10}$$

Using the relations eqs. (A.3) and (A.5), we have

$$S = \int d^4x \, \tilde{N}\tilde{a}^3 \left[-\frac{M_4^2}{2}6H^2 + \frac{M_4^2}{2}\frac{L_0^q q(q-1)}{2L^{q+2}}\dot{L}^2 - V(L) \right] \tag{A.11}$$

141

where we have defined the effective potential

$$\frac{V(L)}{M_4^4} \equiv \frac{1}{2}\left(\frac{L_0}{L}\right)^q\left(-\frac{q(q-1)}{L^2} + 2\Lambda_D + \frac{1}{M_4^4}\frac{n^2}{L^{2q}}\right) \ . \tag{A.12}$$

We see that the dimensionally-reduced theory is that of an FLRW Universe with a scalar field L (with a non-canonical kinetic term) evolving in the effective potential $V(L)$ (plotted in figure 2.2).

A.1.2 Factorizable warped metrics

Another illustrative example is given by solutions of the form:

$$ds^2 = e^{2A(y,t)}\left[-\left(N(t)^2 - e^{-\frac{2(q+2)}{(q-2)}A(y,t)}\tilde{g}_{\gamma\delta}\beta^\gamma(y,t)\beta^\delta(y,t)\right)dt^2 + a(t)^2 d\vec{x}_{p-1}^2\right] \tag{A.13}$$

$$+ \ 2e^{-\frac{8}{q-2}A(y,t)}\tilde{g}_{\gamma\delta}(y)\beta^\gamma(y,t)dtdy^\delta + e^{-\frac{8}{q-2}A(y,t)}\tilde{g}_{\gamma\delta}(y)dy^\gamma dy^\delta \ . \tag{A.14}$$

For $q = 6$, this ansatz is characteristic of warped solutions to Type IIB string theory [165, 166, 151]. We have that

$$\frac{K_x^x - K}{2} = \frac{e^{-A}}{N}\left(\frac{\dot{a}}{a} - \frac{q+2}{q-2}\partial_0 A - \frac{1}{4}\tilde{g}^{\gamma\delta}\mathcal{L}_\beta\tilde{g}_{\gamma\delta}\right) \tag{A.15}$$

where $\partial_0 \equiv \partial_t - \mathcal{L}_\beta$. Defining

$$\tilde{N}(y,t) = e^{-\frac{q+2}{q-2}A(y,t)}N(t), \quad \tilde{a}(y,t) = e^{-\frac{q+2}{q-2}A(y,t)}a(t) \tag{A.16}$$

we have

$$\int d^q y \sqrt{\gamma_q}\, N\gamma_{xx}^{3/2}\left(\frac{K_x^x - K}{2}\right)^2 = \int d^q y \sqrt{\tilde{g}}\, \tilde{N}\tilde{a}^3\left[\left(\frac{\dot{\tilde{a}}}{\tilde{N}\tilde{a}}\right)^2 + F(\beta)\right] \ . \tag{A.17}$$

Although the change of variables proposed above allows one to decompose the action in a suggestive form, it is not immediately clear how to identify the four-dimensional Planck mass, scale factor and lapse. This is due both to the presence of terms involving the shift (written above as $F(\beta)$), as well as the average of a product of y-dependent factors over the compact space. The latter problem arises because eq. (A.16) defines a conformal transformation of the four dimensional metric that depends on both time and the coordinates on the compact space. This can be contrasted with the standard approach to dimensional reduction in the presence of warping, where one defines a purely time dependent conformal transformation to the four-dimensional metric.

Ignoring terms evolving the shift for the remainder of the calculation (i.e. setting $\beta^\gamma = 0$ and denoting the neglected terms with an ellipsis) for simplicity, we can make contact with

142

the standard approach as follows. First, we decompose the action as follows:

$$
\begin{aligned}
\sqrt{-g_4} M_4^2 H^2 &= \int d^q y \sqrt{\tilde{g}} \, N a^3 \left[\frac{\dot{a}}{Na} - \frac{q+2}{q-2} \frac{\dot{A}}{N} + \ldots \right]^2 e^{-2\frac{q+2}{q-2}A} \\
&= N a^3 \left(\int d^q y \sqrt{\tilde{g}} \, e^{-\frac{4q}{q-2}A(y,t=0)} \right) \times \\
&\quad \left[\left(\frac{\dot{a}}{Na} \right)^2 e^{\phi(t)} + \left(\frac{\dot{a}}{N^2 a} \right) \frac{de^{\phi(t)}}{dt} + \left(\frac{1}{2N} \frac{de^{\phi(t)}}{dt} \right)^2 \right] + \Delta + \ldots \\
&= \bar{N} \bar{a}^3 \left(\int d^q y \sqrt{\tilde{g}} e^{-\frac{4q}{q-2}A(y,t=0)} \right) \left[\frac{\dot{\bar{a}}}{\bar{N}\bar{a}} \right]^2 + \Delta + \ldots
\end{aligned}
\tag{A.18}
$$

where we have made the following definitions:

$$
e^{\phi(t)} \equiv \frac{\int d^q y \sqrt{\tilde{g}} e^{-2\frac{q+2}{q-2}A}}{\int d^q y \sqrt{\tilde{g}} \, e^{-\frac{4q}{q-2}A(y,t=0)}} , \tag{A.19}
$$

and

$$
\bar{N}(t) \equiv N(t) e^{\phi(t)/2}, \quad \bar{a}(t) \equiv a(t) e^{\phi(t)/2} \tag{A.20}
$$

and

$$
\Delta \equiv \frac{(q+2)^2}{(q-2)^2} \frac{a^3}{N} \int d^q y \sqrt{\tilde{g}} \, \dot{A} e^{-2\frac{q+2}{q-2}A} \left[\dot{A} - \langle \dot{A} \rangle \right] , \tag{A.21}
$$

where

$$
\langle \dot{A} \rangle \equiv \frac{\int d^q y \sqrt{\tilde{g}} \, \dot{A} e^{-2\frac{q+2}{q-2}A}}{\int d^q y \sqrt{\tilde{g}}} = -\frac{q-2}{2(q+2)} \frac{de^{\phi}}{dt} e^{-\frac{4q}{q-2}A(y,t=0)} . \tag{A.22}
$$

To the extent that Δ is small (and again, we are neglecting terms involving the shift), we can identify

$$
M_4^2 = \int d^q y \sqrt{\tilde{g}} \, e^{-\frac{4q}{q-2}A(y,t=0)}, \quad \sqrt{-g_4} = \bar{N}\bar{a}^3, \quad H^2 = \left[\frac{\dot{\bar{a}}}{\bar{N}\bar{a}} \right]^2 . \tag{A.23}
$$

This definition for M_4 is not the same as in previous literature [165, 166, 151], but rather chosen to be consistent with our convention eq. (2.21). Note that eq. (A.20) defines the conformal transformation typically used in the literature to transform to the Einstein frame.

Evaluating the cosmological apparent horizon area using eq. (2.17)

$$
\mathcal{A}_H = 4\pi \int d^q y \sqrt{\tilde{g}} \, e^{-2\frac{q+2}{q-2}A} \left(\frac{\dot{a}}{Na} - \frac{q+2}{q-2} \frac{\dot{A}}{N} + \ldots \right)^{-2} . \tag{A.24}
$$

In the case where we make the approximation that $\dot{A} \simeq \langle \dot{A} \rangle$ (and neglecting terms involving the shift) we find:

$$
\mathcal{A}_H = 4\pi \int d^q y \sqrt{\tilde{g}} \, e^{-2\frac{q+2}{q-2}A} \left(\frac{\dot{\bar{a}}}{\bar{N}\bar{a}} \right)^{-2} e^{-\phi} = M_4^2 \frac{4\pi}{H^2} . \tag{A.25}
$$

143

Though, for general warped metrics of the form eq. (A.13), the cosmological apparent horizon cannot be precisely associated with the Hubble parameter as defined by dimensional reduction in previous literature. However, we note that for the static warped solutions discussed in the text, $\dot{A} = \beta^\gamma = 0$, and the correspondence does hold.

A.2 $(D-1)+1$ equations

A.2.1 Maxwell equations

Plugging in our metric and flux ansatz into the Maxwell equations (2.4), the evolution equations for the electric and magnetic fluxes become

$$
\begin{aligned}
\dot{Q}_E &= \beta^\theta Q_E \left(\frac{Q'_E}{Q_E} + (q-1) \cot\theta \right) + NKQ_E + 2N(q-1)K^{\phi_1}_{\phi_1} Q_E - N\gamma_{\theta\theta}^{-1} Q'_B \\
&\quad + N\gamma_{\theta\theta}^{-1} Q_B \left(-(p-1)\frac{\gamma'_{xx}}{2\gamma_{xx}} + \frac{\gamma'_{\theta\theta}}{2\gamma_{\theta\theta}} + (q-1)\frac{\widetilde{\gamma}'_{\phi_1\phi_1}}{2\widetilde{\gamma}_{\phi_1\phi_1}} \right) - \gamma_{\theta\theta}^{-1}(\partial_\theta N)Q_B
\end{aligned}
\tag{A.26}
$$

and

$$
\begin{aligned}
\dot{Q}_B &= \beta^\theta Q_B \left(\frac{Q'_B}{Q_B} + (q-1) \cot\theta \right) + Q_B \partial_\theta \beta^\theta - N \left(Q'_E + (q-1)Q_E \cot\theta \right) \\
&\quad - (\partial_\theta N)Q_E
\end{aligned}
\tag{A.27}
$$

where the dot represents differentiation with respect to time.

A.2.2 Generalized harmonic equations

We evolve the solutions using a space-time decomposition of the generalized harmonic formulation [157, 292]. Here we write down the field equations for completeness. In this formulation, the lapse and shift are evolution variables, in addition to the spatial metric and extrinsic curvature. We also introduce the auxiliary fields π and $\rho^{\bar{m}}$ that are directly related to the time derivative of N and $\beta^{\bar{m}}$. We fix the coordinate degrees of freedom by specifying a so-called source vector, H^M such that the constraint vector

$$
C^M \equiv H^M + \left({}^{(D)}\Gamma^M{}_{NK} - {}^{(D)}\bar{\Gamma}^M_{NK} \right) g^{NK} = 0
\tag{A.28}
$$

vanishes. Here ${}^{(D)}\bar{\Gamma}^M_{NK}$ denotes a background connection which we set to zero in the usual generalized harmonic formulation (1.13). The generalized harmonic equations are

$$
{}^{(D)}R_{MN} - \nabla_{(M}C_{N)} = -\kappa \left[n_{(M}C_{N)} - \frac{1}{(D-2)}g_{MN}n^L C_L \right] + \left[T_{MN} - \frac{1}{D-2}g_{MN}T \right] .
\tag{A.29}
$$

As was mentioned in 1.2.2, these are hyperbolic, provided the source functions are specified directly as a function of the spacetime coordinates x^M and the metric g_{MN}.

We evolve the $(D-1)+1$ form of the generalized harmonic evolution equations [78] as follows

$$\partial_t \gamma_{xx} = -2NK_{xx} + \gamma'_{xx}\beta^\theta \tag{A.30a}$$

$$\partial_t \gamma_{\theta\theta} = -2K_{\theta\theta} + 2\gamma_{\theta\theta}\partial_\theta\beta^\theta + \beta^\theta \gamma'_{\theta\theta} \tag{A.30b}$$

$$\partial_t \widetilde{\gamma}_{\phi_1\phi_1} = -2N\widetilde{K}_{\phi_1\phi_1} + \beta^\theta(\widetilde{\gamma}'_{\phi_1\phi_1} + 2\cot\theta\widetilde{\gamma}_{\phi_1\phi_1}) \tag{A.30c}$$

$$\partial_t K_{xx} = -\frac{\gamma'_{xx}}{2\gamma_{\theta\theta}}\partial_\theta N + N\left(^{(D-1)}R_{xx} - 2K_x^x K_{xx} + KK_{xx}\right) + N\left(\frac{1}{D-2}\gamma_{xx}(S-\rho) - S_{xx}\right)$$
$$+\beta^\theta\partial_\theta K_{xx} - NC_\perp K_{xx} - N\frac{1}{2}\gamma'_{xx}C^\theta - \kappa N\gamma_{xx}C_\perp/2 \tag{A.31a}$$

$$\partial_t K_{\theta\theta} = -\partial_\theta^2 N + \frac{\gamma'_{\theta\theta}}{2\gamma_{\theta\theta}}\partial_\theta N + N\left(^{(D-1)}R_{\theta\theta} - 2K_\theta^\theta K_{\theta\theta} + KK_{\theta\theta}\right) + N\left(\frac{1}{D-2}\gamma_{\theta\theta}(S-\rho) - S_{\theta\theta}\right)$$
$$+\beta^\theta\partial_\theta K_{\theta\theta} + 2K_{\theta\theta}\partial_\theta\beta^\theta - NC_\perp K_{\theta\theta} - N\frac{1}{2}\gamma'_{\theta\theta}C^\theta - N\gamma_{\theta\theta}\partial_\theta C^\theta - \kappa N\gamma_{\theta\theta}C_\perp/2 \tag{A.31b}$$

$$\partial_t \widetilde{K}_{\phi_1\phi_1} = -\left(\cot\theta\frac{\widetilde{\gamma}_{\phi_1\phi_1}}{\gamma_{\theta\theta}} + \frac{\widetilde{\gamma}'_{\phi_1\phi_1}}{2\gamma_{\theta\theta}}\right)\partial_\theta N + N\left(\frac{^{(D-1)}R_{\phi_1\phi_1}}{\sin^2\theta} - 2\widetilde{\gamma}^{\phi_1\phi_1}(\widetilde{K}_{\phi_1\phi_1})^2 + K\widetilde{K}_{\phi_1\phi_1}\right)$$
$$+\frac{1}{p+q-2}N\widetilde{\gamma}_{\phi_1\phi_1}\left(-2\Lambda_D + \widetilde{\gamma}_{\phi_1\phi_1}^{-(q-1)}(p-1)\left[Q_E^2 - \gamma_{\theta\theta}^{-1}Q_B^2\right]\right) \tag{A.31c}$$
$$+\left(\partial_\theta\widetilde{K}_{\phi_i\phi_i} - \frac{\widetilde{\gamma}'_{\phi_1\phi_1}}{\widetilde{\gamma}_{\phi_1\phi_1}}\widetilde{K}_{\phi_i\phi_i}\right)\beta^\theta - NC_\perp\widetilde{K}_{\phi_1\phi_1} - N\left[\cot\theta\widetilde{\gamma}_{\phi_1\phi_1} + \frac{1}{2}\widetilde{\gamma}'_{\phi_1\phi_1}\right]C^\theta - \kappa N\widetilde{\gamma}_{\phi_1\phi_1}C_\perp/2$$

$$\partial_t N = N^2\pi - N^2 H_\perp + \beta^\theta\partial_\theta N \tag{A.32a}$$
$$\partial_t\beta^\theta = \beta^\theta\partial_\theta\beta^\theta + N^2\rho^\theta - N\gamma^{\theta\theta}\partial_\theta N + N^2 H^\theta \tag{A.32b}$$

and

$$\partial_t\pi = -N\left((p-1)K_{xx}K^{xx} + K_{\theta\theta}K^{\theta\theta} + (q-1)K_{\phi_1\phi_1}K^{\phi_1\phi_1}\right) + D_{\bar{m}}D^{\bar{m}}N$$
$$+C^\theta\partial_\theta N - \frac{(D-3)}{(D-2)}\kappa NC_\perp - N\frac{1}{D-2}((D-3)\rho + S) + \beta^\theta\partial_\theta\pi \tag{A.33a}$$

$$\partial_t\rho^\theta = \gamma^{\bar{n}\bar{l}}\bar{D}_{\bar{n}}\bar{D}_{\bar{l}}\beta^{\bar{\theta}} + N\gamma^{\theta\theta}\partial_\theta\pi - \pi\gamma^{\theta\theta}\partial_\theta N - 2K^{\theta\theta}\partial_\theta N$$
$$+2N\left[-(p-1)\frac{\gamma'_{xx}}{2\gamma_{\theta\theta}}K^{xx} + \frac{\gamma'_{\theta\theta}}{2\gamma_{\theta\theta}}K^{\theta\theta} + (q-1)\left[-(\cot\theta\frac{\widetilde{\gamma}_{\phi_1\phi_1}}{\gamma_{\theta\theta}} + \frac{\widetilde{\gamma}'_{\phi_1\phi_1}}{2\gamma_{\theta\theta}}) + \cot\theta\right]\widetilde{K}^{\phi_1\phi_1}\right]$$
$$+\kappa NC^\theta - 2Nj^\theta + (\beta^\theta\partial_\theta\rho^\theta - \rho^\theta\partial_\theta\beta^\theta) + (q-1)\beta\widetilde{\gamma}_{\phi_1\phi_1}^{-1} \tag{A.33b}$$

145

with the non-trivial constraints

$$C_\perp \equiv \pi + K = 0 \tag{A.34a}$$

$$
\begin{aligned}
C^\theta &= -\rho^\theta - (p-1)\frac{\gamma'_{xx}}{2\gamma_{\theta\theta}}\gamma^{xx} + \frac{\gamma'_{\theta\theta}}{2\gamma_{\theta\theta}}\gamma^{\theta\theta} = 0 \\
&\quad + (q-1)\left[-(\cot\theta\frac{\widetilde{\gamma}_{\phi_1\phi_1}}{\gamma_{\theta\theta}} + \frac{\widetilde{\gamma}'_{\phi_1\phi_1}}{2\gamma_{\theta\theta}}) + \cot\theta \right]\widetilde{\gamma}^{\phi_1\phi_1}
\end{aligned} \tag{A.34b}
$$

$$\mathcal{H} = {}^{(D-1)}R - 3K_{xx}K^{xx} - K_{\theta\theta}K^{\theta\theta} - (q-1)K_{\phi_i\phi_i}K^{\phi_i\phi_i} + K^2 - 2\rho = 0 \tag{A.34c}$$

$$\mathcal{M}_\theta = D_{\bar{m}}K^{\bar{m}}{}_\theta - D_\theta K - j_\theta = 0 \tag{A.34d}$$

where $K \equiv \gamma^{\bar{m}\bar{n}}K_{\bar{m}\bar{n}}$, $^{(D-1)}R = \gamma^{\bar{m}\bar{n}}R_{\bar{m}\bar{n}}$, $\bar{D}_{\bar{m}}$ denotes the covariant derivative associated with the background metric $\bar{g}_{MN}$ which we assume to have a lapse of one, shift of zero and a time-independent spatial metric under $(D-1)+1$ splitting. We also define $H_\perp \equiv n^M H_M$, $H^{\bar{m}} \equiv \gamma^{\bar{m}}{}_N H^N$ and the various projections of stress-energy tensor T_{MN} as $S_{\bar{m}\bar{n}} = \gamma^M_{\bar{m}}\gamma^N_{\bar{n}}T_{MN}$, $\rho = n^M n^N T_{MN}$ and $j_{\bar{m}} = -\gamma^K_{\bar{m}}T_{KN}n^N$.

We find that our solutions are more stable if we choose a gauge such that the shift vector is driven to zero, and the lapse is constant in time for the stationary background solutions,

$$H^\theta = -\frac{\eta}{N^2}\beta^\theta, \quad H^\perp = -K_0 \tag{A.35}$$

where K_0 is the initial value of the trace of the extrinsic curvature and η is some constant controlling the rate at which the shift is driven to zero. We typically set $\kappa = 15$ and $\eta = 10$ in units where $\Lambda_D = 1$, although their exact values are not too important.

A.3 Type IIB supergravity

In this section, we review the action of the low energy limit of type IIB string theory, namely 10-dimensional type IIB supergravity (SUGRA). We refer the reader to [150, 291] for a more detailed review. The fields of type IIB SUGRA are the higher dimensional metric g_{MN}, the dilaton-axion (complex) scalar $\tau = C_0 + i\exp^{-\phi}$, two 2-form potentials $C_2 = C_{MN}$ and $B_2 = B_{MN}$ with 3-form field strengths $F_3 = dC_2$ and $H_3 = dB_2$, and a self-dual 5-form field strength $F_5 = dC_4 = \star F_5$. It is often convenient to introduce the 5-form $\tilde{F}_5 = dC_4 - C_2 \wedge H_3$, where self-duality $\star\tilde{F}_5 = \tilde{F}_5$ must be imposed as an added constraint on the solutions. It cannot be imposed on the action or else the wrong equations of motion result. Working in the 10-dimensional string frame, the action for type IIB SUGRA is,

$$
\begin{aligned}
S = {}&\frac{1}{2\kappa_{10}^2}\int d^{10}x\sqrt{-g}\left\{ \exp^{-2\phi}\left[R + 4\left(\partial\phi\right)^2 - \frac{1}{2}|H_3|^2 \right] - \frac{1}{2}\left(\partial C\right)^2 - \frac{1}{2}\left|\tilde{F}_3\right|^2 - \frac{1}{4}\left|\tilde{F}_5\right|^2 \right\} \\
&+ \frac{1}{4\kappa_{10}^2}\int \left(C_4 - \frac{1}{2}B_2 \wedge C_2 \right) \wedge F_3 \wedge H_3,
\end{aligned} \tag{A.36}
$$

where the last term only contributes as a boundary term and $2\kappa_{10}^2 = (2\pi)^7 \alpha'^4$ where α' is the Regge slope [291]. Similarly to the theory studied in Chapter 2, type IIB SUGRA consist of q-forms to stabilize the extra dimensions. However, the action we considered in Chapter 2 does not contain a dilaton. Clearly, Freund-Rubin compactifications are too simple to be realistic candidates for any string theory, yet they serve as a good illustration of the kind of dynamics one may expect in string theories with flux compactifications.

A.4 Convergence tests

As mentioned in 1.2.2, ensuring that the constraints converge to zero with increasing numerical resolution, and at the expected order, provides a consistency check that the numerical solution obtained is converging to a solution of the field equations. Our numerical scheme converges at fourth order with temporal resolution and exponentially with spatial resolution. Figure (A.1) shows the integrated norm of the constraint violation given by eq. (A.28) for several resolutions, demonstrating that this quantity is converging to zero at the expected rate. The highest temporal resolution used in the resolution study is equivalent to the resolution we use for the other solutions. The spatial resolution required depends on whether the solution has inhomogeneous features that needs to be resolved or not. For homogeneous solutions we typically use $N_\theta \sim 20$, for stationary oblate solutions $N_\theta \sim 72$ and finally the prolate solutions typically require up to $N_\theta \sim 152$. For unstable solutions, we perturb the solutions with a sufficiently small amplitude to ensure that we are in the linear regime. In figure A.1, we plot the evolution of the metric variable $\gamma_{\theta\theta}$ for a Freund-Rubin solution unstable to the warped instability, and perturbed with an initial amplitude of $\bar{h} = 10^{-5}$ and $\bar{h} = 5 \times 10^{-5}$. Both solutions undergo a clear exponential growth phase before entering the nonlinear regime, with the time of saturation being set by the amplitude of the initial perturbation.
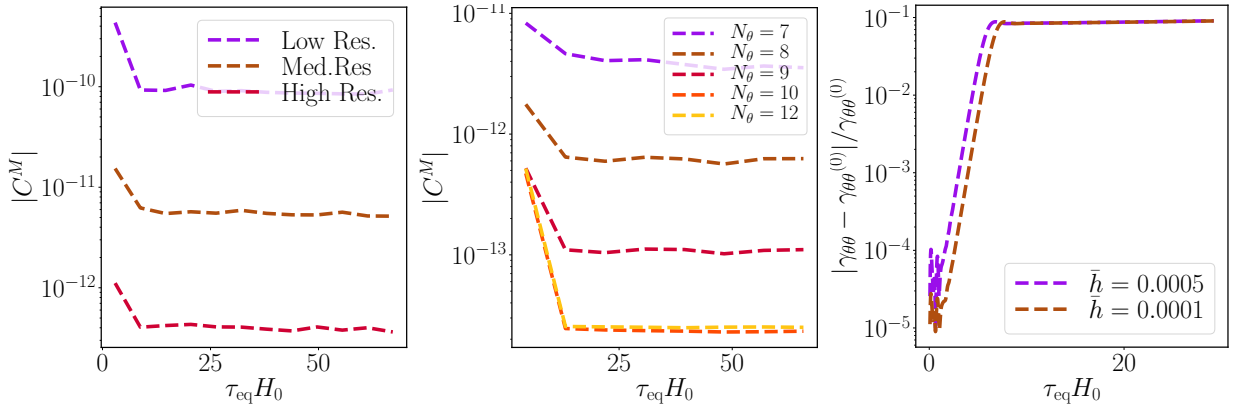
Figure A.1: Integrated norm of the constraint violation eq. (A.28) for different temporal (left) and spatial (middle) resolutions as a function of proper time (in units of the background Hubble expansion) for $q = 4$, $\Lambda_D = 1$, $H/M_4 = 0.0078$ and an initial $\ell = 2$ perturbation. The medium and high temporal resolutions have $2\times$ and $4\times$ the resolution of the low resolution run. N_θ in the middle indicates the number of collocation points used. We find that the constraint violations converge at fourth order in time and exponentially in space. (Right) The time evolution of spatial average of relative difference of $\gamma_{\theta\theta}$ from its background solution for $q = 4$, $H/M_4 = 0.0050$ and an initial $\ell = 2$ perturbation of magnitude $\bar{h} = 10^{-4}$ and $\bar{h} = 5 \times 10^{-4}$. The linear warped instability is evident.

Appendix B

Starting inflation from inhomogeneous initial conditions with momentum

B.1 Numerical methodology

We solve the equations of motion (1.1) and (3.4) using the generalized harmonic formulation, as described in chapter 1.2.2. The numerical scheme we use follows that of [130], which we briefly summarize here. We discretize the partial differential equations in space, using standard fourth-order finite difference stencils, and in time, using fourth-order Runge-Kutta integration. We control high frequency numerical noise using Kreiss-Oliger dissipation [231]. We use constraint damping to control the constraint violating modes sourced by truncation error, with damping parameter values similar to those used in black hole formation using the generalized harmonic formulation [292]. We fix the gauge freedom through specifying the source functions H^α, choosing damped harmonic coordinates [95, 243], as in [128, 127]. During the expansion phase, we dynamically adjust the time step size in proportion to the decreasing global minimum of $1/N$ where N is the lapse (this would be $N = 1/a^3$ in a homogeneous FLRW universe with harmonic time) in order to avoid violating the Courant-Friedrichs-Lewy condition [127, 134, 111].

Following [292], we track the evolution of any apparent horizons by finding the surfaces where the outer null expansion vanishes, and excise an ellipsoid-shaped region interior to the horizon. We typically set the ratio of the maximum ellipsoid axis to the maximum black hole radial value to be 0.78.

The simulation domain is three dimensional with length D in each direction. The simulations are performed with between 384 and 512 points across each linear dimension. Each single-field inflationary model run typically requires ~ 12 core years. The two-field inflationary scenario takes ~ 21 core years. We construct initial data describing an

149

inhomogeneous cosmology as described in section 3.2.2 and 3.2.1 using the the conformal thin sandwich formalism, as described in [131]. The elliptic equations are solved using a second-order accurate multigrid scheme with a typical resolution of 384 points across each linear dimension.

Finally, we present a convergence test of our code and setup. In figure B.1, we show the time evolution of the norm of the constraint violation $C^\alpha \equiv \Box x^\alpha - H^\alpha$ for the strong-field case considered in figure 3.3 for different numerical resolutions. For this case, the lowest resolution is 256 across each linear dimension for the evolution and 192 for the initial data code. The medium and high resolutions correspond, respectively, to an increased resolution of 3/2 and 2× that of the lowest resolution, both in the initial data and evolution code. We find that the constraints initially converge to zero at roughly second order and then eventually transition to fourth order convergence. This is because the truncation error is dominated by the second order convergence of the initial data code at first, but eventually the truncation error of fourth order evolution code takes over. The high resolution in the convergence study is equivalent to the resolution we use for most of the cases studied here.
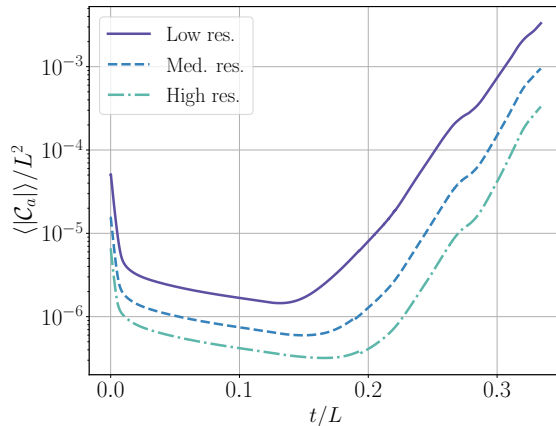
Figure B.1: Volume integrated norm of the constraint violation as a function of time for the case shown in right panel of figure 3.3. The medium and high resolution have 3/2× and 2× the resolution of the low resolution. We observe second order convergence at first, followed by fourth order convergence, which is consistent with the second order convergence of our initial data code and fourth order convergence of our evolution code.

B.2   Modified CTS formalism

In some cases studied here, instead of solving both the momentum and Hamiltonian constraint using the the CTS formalism [131], we construct initial data by following a similar approach to [159, 336], generalized to three dimensions, and choosing initial data such that the momentum constraint is automatically satisfied. We then solve for the conformal factor using the Hamiltonian constraint. Starting from the constraint equations in the CTS form

(3.10), choosing conformally flat initial data $\tilde{\gamma}_{ij} = \delta_{ij}$, choosing the lapse and shift vector to be $N = 1$ and $\beta^i = 0$, and letting the extrinsic curvature scalar be a constant given by (3.17), the Hamiltonian and momentum constraint equations for a stress energy tensor given by (2.3) become

$$
\begin{aligned}
\partial_i \partial^i \Psi &= -\left(\frac{1}{8}\hat{A}_{ij}\hat{A}^{ij} + \frac{1}{4}\hat{\eta}^2\right)\Psi^{-7} + \left(\frac{1}{12}K^2 - \frac{1}{2}V\right)\Psi^5 + \frac{1}{4}\partial_i\phi\partial^i\phi\Psi, \\
\partial_j \hat{A}^{ij} &= -2\hat{\eta}\delta^{ij}\partial_j\phi
\end{aligned}
\tag{B.1}
$$

where

$$
\hat{\eta} = \Psi^6\eta = \Psi^6\partial_t\phi \tag{B.2}
$$

and in last step we assumed $N = 1$ and $\beta^i = 0$. Let us consider the case where we have inhomogeneities along all spatial dimensions. Then the momentum constraint is solved by the following ansatz:

$$
\begin{aligned}
\hat{\eta}(x) &= \frac{1}{\sqrt{2}}\left[\hat{\eta}_0 + f_0\cos(kx) + e_0\cos(ky) + d_0\cos(kz)\right], \\
\phi(x) &= \frac{1}{\sqrt{2}}\left[\hat{\phi}_0 + f_1\cos(kx) + e_1\cos(ky) + d_1\cos(kz)\right],
\end{aligned}
\tag{B.3}
$$

and the particular solution

$$
\hat{A}^{ij} = \begin{pmatrix}
\hat{A}^{11}(x,y,z) & \hat{A}^{12}(x,y) & \hat{A}^{13}(x,z) \\
\hat{A}^{12}(x,y) & \sigma\hat{A}^{11}(x,y,z) & \hat{A}^{23}(y,z) \\
\hat{A}^{13}(x,z) & \hat{A}^{23}(y,z) & -(1+\sigma)\hat{A}^{11}(x,y,z)
\end{pmatrix},
\tag{B.4}
$$

where f_0, f_1, e_0, e_1, d_0, d_1, and σ are parameters to choose and

$$
\begin{aligned}
\hat{A}^{11}(x,y,z) &= -\hat{\eta}_0 f_1\cos(kx) - \frac{1}{4}f_0 f_1\cos(2kx) - \hat{\eta}_0\frac{e_1}{\sigma}\cos(ky) - \frac{1}{4}\frac{e_0 e_1}{\sigma}\cos(2ky) \\
&\quad +\hat{\eta}_0\frac{d_1}{1+\sigma}\cos(kz) + \frac{1}{4}\frac{d_0 d_1}{1+\sigma}\cos(2kz)
\end{aligned}
\tag{B.5}
$$

$$
\begin{aligned}
\hat{A}^{12}(x,y) &= e_0 f_1\sin(kx)\sin(ky), & \text{where } e_0 f_1 = e_1 f_0 & \tag{B.6} \\
\hat{A}^{13}(x,z) &= d_0 f_1\sin(kx)\sin(kz), & \text{where } d_0 f_1 = d_1 f_0 & \tag{B.7} \\
\hat{A}^{23}(x,z) &= d_0 e_1\sin(ky)\sin(kz), & \text{where } d_0 e_1 = d_1 e_0 & \tag{B.8}
\end{aligned}
$$

The conditions on the constants f_0, f_1, e_0, e_1, d_0, and d_1 come from substituting the ansatz into (B.1).

Appendix C

Evolution of black holes through a nonsingular cosmological bounce

C.1   Numerical methodology

We solve the equations of motion (4.2) using the generalized harmonic formulation as described in chapter 1.2.2. The numerical scheme we use is the same as in chapter 3 and follows that of [130]. We fix the gauge freedom by working in harmonic coordinates, $\Box x^\alpha = 0$. Just like in chapter 3 and [127, 134], we dynamically adjust the time step size in proportion to the decreasing global minimum of $1/\alpha$ during the expanding phase (where $\alpha = 1/a^3$ in a homogeneous FLRW universe, see eq. (4.3)).

We dynamically track the outer apparent horizon of the black hole, and excise an ellipsoid-shaped region interior the horizon. We typically set the ratio of the maximum ellipsoid axis to the maximum black hole radial value to be 0.6.

We compute the event horizon by integrating null surfaces backwards in time [22, 241, 325] (we restrict this to spherically symmetric cases, where it is sufficient to consider spherical null surfaces). Since we are not able to evolve the spacetime to infinite proper time (at which point the event and apparent horizon would coincide), we cannot precisely determine the final position of the event horizon. Instead, we use the apparent horizon as the approximate location of the event horizon and choose a range of initial guesses around this value. For two surfaces initially separated by $2.5r_{\mathrm{BH},0}$, we find that their separation decreases to $0.1r_{\mathrm{BH},0}$ within $\sim 4 \times 10^{-3}|H_{\min}|^{-1}$ when evolving the null surfaces backwards in time, after which we consider the location of the event horizon to be accurate to the desired accuracy. Note that the separation rapidly decreases when integrating backwards in time, a direct consequence of the divergence of the null geodesics going forward in time [241].

We additionally make the use of compactified coordinates so that physical boundary

conditions can be placed at spatial infinity [292]:

$$x^i = \tan\left(\frac{\pi \hat{x}^i}{2}\right), \tag{C.1}$$

so that $\hat{x}^i = 1$ corresponds to $x^i = \infty$. Unlike in [292] though, we work in an asymptotically FLRW spacetime instead of an asymptotically flat spacetime, similar to what is done in [126]. That is, at our spatial boundary we set

$$g_{tt} = -\alpha(t)^2, \qquad g_{ti} = 0, \qquad g_{ij} = a(t)^2 \delta_{ij}, \tag{C.2}$$

where the lapse $\alpha(t) = a(t)^3$; and the scale factor $a(t)$ satisfies the Friedmann equations, eq. (4.4).

We use Berger-Oliger [48] style adaptive mesh refinement (AMR) supported by the PAMR/AMRD library [294, 295]. Typically our simulations have 9–12 AMR levels (using a 2 : 1 refinement ratio), with each nested box centered on the initial black hole and between 128 and 256 points across the x-direction on the coarsest AMR level. The interpolation in time for the AMR boundaries is only third-order accurate, which can reduce the overall convergence to this order in some instances. As we restrict to axisymmetric spacetimes, we use the modified Cartoon method to reduce our computational domain to a two-dimensional Cartesian half-plane [292]. Each of our production runs typically takes one core year to complete.

We construct initial data describing a black hole of mass $M(t = 0) = M_0$ in an initially contracting FLRW spacetime described in section 4.2.2. We solve the constraint equations using the conformal thin sandwich formalism, as described in [131]. More precisely, we choose the initial time slice to have constant extrinsic curvature $K = -3H_0$ where $H_0 = \mathcal{H}_0 a_0^{-3}$ is given by (4.4d), and the initial values for $\{\phi, \phi', \chi, \chi', a, a'\}$ are fixed by (4.10) (a similar approach was employed in [127, 126]). Without loss of generality, we choose the initial value of the ratio between the energy density of the ϕ and χ fields and V_0 to be such that during the contraction phase, the Hubble radius of the background cosmology $R_H \equiv |H^{-1}|$ shrinks from an initial value of $R_H(t = 0) = 75 r_{\mathrm{BH},0}$ to $4.34 r_{\mathrm{BH},0}$ (here $r_{\mathrm{BH},0}$ is the initial black hole radius). We considered a range of initial black hole masses, keeping the initial ratio of Hubble to black hole radius to be 75, but changing the minimum Hubble to initial black hole radius ratio from $4.34 r_{\mathrm{BH},0}$ all the way to $0.87 r_{\mathrm{BH},0}$. We also study some black holes with an initial dimensionless spin of $a_0 = 0.5$.

Finally, we present a convergence test of our code and setup. In figure C.1, we present the time evolution of the apparent horizon of the black hole and the norm of the constraint violations $C^\alpha \equiv \Box x^\alpha$ integrated over the coordinate radius $r \leq 265 M_0$, for a non-spinning black hole with initial mass such that $R_{\mathrm{H,min}} = 1.45 r_{\mathrm{BH},0}$, for different numerical resolutions. For this case, the lowest resolution is 128 points across the x-direction on the coarsest AMR level with 10 levels of mesh refinement and a spatial resolution of $dx/M_0 \approx 0.004$ on the finest level. The medium and high resolutions correspond, respectively, to an increased resolution of $3/2$ and $2\times$ that of the lowest resolution run. We find that the constraints

converge to zero at roughly third order. This is because the convergence is dominated by the third order time interpolation on the AMR boundaries. The medium resolution in the convergence study is equivalent to the resolution we use for all the other cases studied here. We place the mesh refinement such that the radius of the black hole resides inside the finest AMR level initially. During the evolution, the mesh refinement is adjusted according to truncation error estimates to maintain roughly the same level of error.
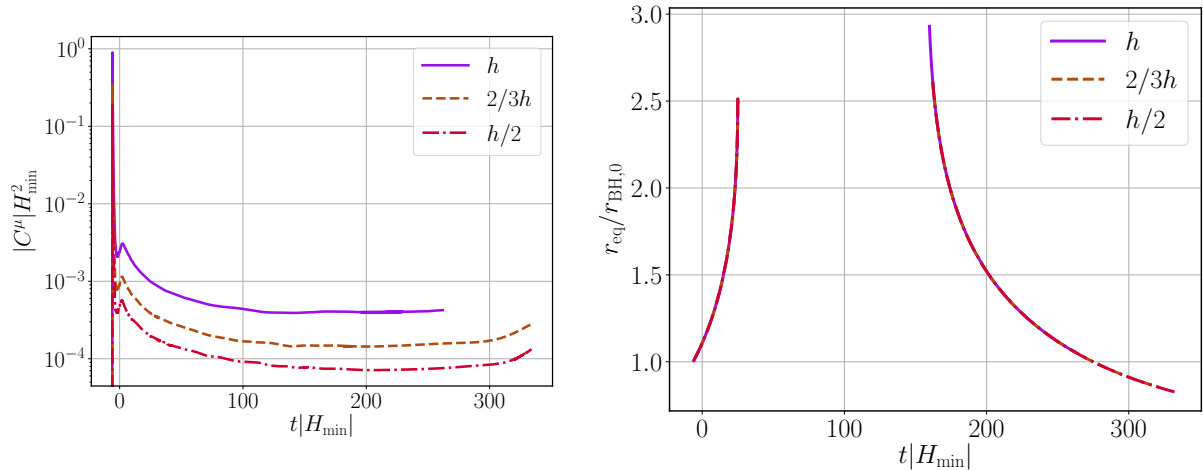
Figure C.1: The integrated norm (left) of the constraint violations $C^\alpha \equiv \Box x^\alpha$ integrated over the coordinate radius $r \leq 265M_0$ and the apparent horizon (right), for a black hole with initial radius such that $R_{\mathrm{H,min}} = 1.45 r_{\mathrm{BH},0}$, for different resolutions. The medium (high) resolution case has $1.5\times$ $(2\times)$ the resolution of the low resolution, and the convergence is consistent with third order.

C.2 Various notions of black hole and cosmological horizons

C.2.1 General definitions and properties

Nonsingular classically bouncing cosmologies require the violation of the NCC [261, 221, 21, 43, 70]. The NCC plays a fundamental fundamental role in the classical area law for black holes [181, 39]. Given this, we pay particular attention to the dynamics of the black hole horizon in our simulations. In addition to the event horizon (which can only be computed once the whole spacetime is known [325]), there are several other quasi-local definitions of black hole horizons which we measure: dynamical horizons [32, 31, 30], apparent horizons [32, 60, 182, 31, 30, 306, 142], and holographic screens [62, 64, 65] (also called marginally trapped tubes [29]).

For completeness, we collect the definitions and some of the basic properties of these horizons in this appendix. Wherever applicable, we also discuss how these definitions can
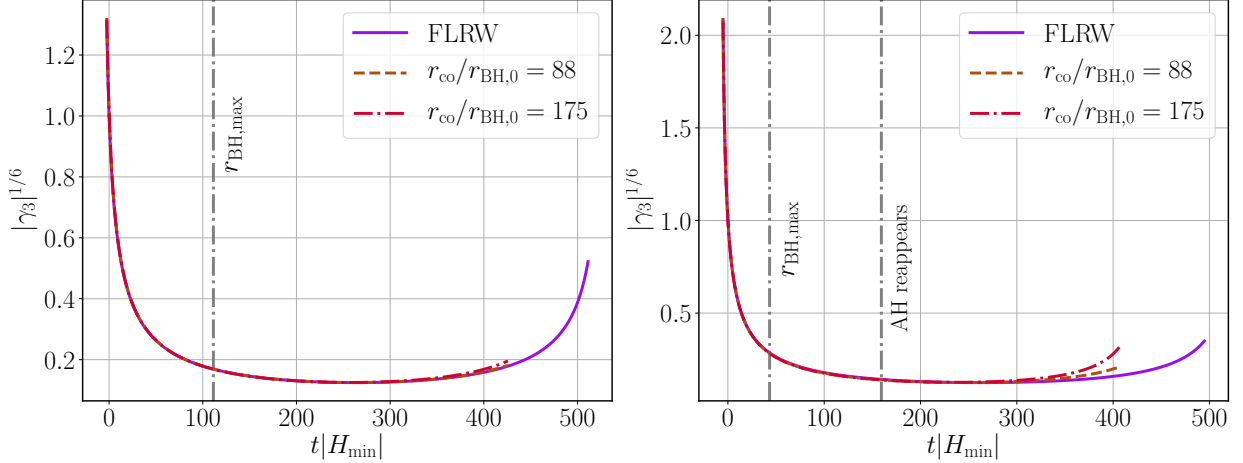
Figure C.2: The effective scale factor $|\gamma_3|^{1/6}$ computed from (4.17) for a black hole with initial mass such that the Hubble radius of the background cosmology $R_H \equiv |H^{-1}|$ shrinks from an initial value of $R_{H,0} = 75 r_{BH,0}$ to $4.34 r_{BH,0}$ (left)/$2.17 r_{BH,0}$ (right). The solid line shows the corresponding background solution and the dashed and dash-dotted lines the values at different coordinate radii. The vertical grey line is the time at which the black hole reaches its maximum mass as observed by the apparent horizon.

be extended to define cosmological horizons. We refer the reader to [32, 60, 182, 31, 30, 306, 142, 62, 64, 65] for more thorough reviews on this subject.

Trapped surfaces and apparent horizons

Let $\mathcal{S}$ be a smooth, closed, orientable spacelike two-dimensional submanifold in a four-dimensional spacetime $(\mathcal{M}, g_{ab})$. We then define two linearly independent, future-directed, null vectors normal to $\mathcal{S}$, normalized[1] such that

$$g_{\alpha\beta} l^\alpha n^\beta = -1 \tag{C.3}$$

where by convention l^α and n^β are respectively the outgoing and ingoing[2] null normals. The two-metric induced on $\mathcal{S}$ is

$$\tilde{q}_{\alpha\beta} = g_{\alpha\beta} + l_\alpha n_\beta + n_\alpha l_\beta, \tag{C.4}$$

and the null expansions are defined as

$$\Theta_{(l)} \equiv \tilde{q}^{\alpha\beta} \nabla_\alpha l_\beta, \qquad \Theta_{(n)} \equiv \tilde{q}^{\alpha\beta} \nabla_\alpha n_\beta. \tag{C.5}$$

---

[1]This convention varies across the literature. We follow [306], which is different from [30].

[2]In asymptotically flat or AdS spacetimes, the notions of *outward* and *inward* are the intuitive ones but in cosmological spacetimes–where an independent notion of "outward" such as conformal infinity do not exist–this is no longer true. In the context of our numerical simulations, we naturally define the outgoing (ingoing) direction as the direction from the origin (spatial infinity) to spatial infinity (the origin).
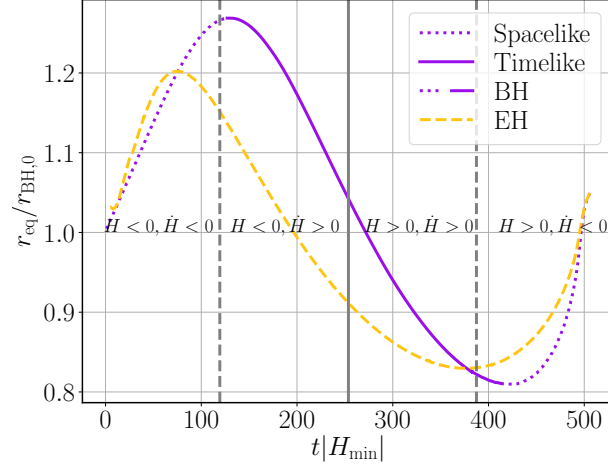
Figure C.3: The apparent horizon of the black hole (purple) and the corresponding event horizon (yellow dashed) for a black hole with initial mass such that the Hubble radius of the background cosmology $R_{\mathrm{H}} \equiv |H^{-1}|$ shrinks from an initial value of $R_{\mathrm{H},0} = 75 r_{\mathrm{BH},0}$ to $8.69 r_{\mathrm{BH},0}$. The vertical solid line indicates the bounce, while the region between the dashed lines is the bouncing phase (where the NCC is violated). The line style of the apparent horizon reflects the signature of the marginally trapped tube or holographic screen (solid is timelike, dashed is spacelike).

The closed two-surface $\mathcal{S}$ is a *trapped surface* if the outgoing and ingoing expansions are strictly negative i.e. if $\{\Theta_{(l)} < 0, \Theta_{(n)} < 0\}$ and a *marginal trapped surface* if the outgoing null expansion vanishes i.e if $\{\Theta_{(l)} = 0, \Theta_{(n)} < 0\}$. Conversely, the closed two-surface $\mathcal{S}$ is am *anti-trapped surface* if the outgoing and ingoing expansions are strictly positive i.e. if $\{\Theta_{(l)} > 0, \Theta_{(n)} > 0\}$ and a *marginal anti-trapped surface* if the ingoing null expansion vanishes i.e if $\{\Theta_{(l)} > 0, \Theta_{(n)} = 0\}$.

A marginal trapped surface ($\Theta_{(l)} = 0$) is *future* if $\Theta_{(n)} < 0$, *past* if $\Theta_{(n)} > 0$, *outer* if $\mathcal{L}_{(n)}\Theta_{(l)} < 0$ and *inner* if $\mathcal{L}_{(n)}\Theta_{(l)} > 0$. Conversely, a marginal anti-trapped surface ($\Theta_{(n)} = 0$) is *future* if $\Theta_{(l)} < 0$, *past* if $\Theta_{(l)} > 0$, *outer* if $\mathcal{L}_{(l)}\Theta_{(n)} < 0$ and *inner* if $\mathcal{L}_{(l)}\Theta_{(n)} > 0$.

A black hole *apparent horizon* is a *future marginally outer trapped surface*. Within the context of cosmology, the *cosmological apparent horizon* of an expanding FLRW spacetime is a *past marginally inner anti-trapped surface*. For a contracting FLRW spacetime, the *cosmological apparent horizon* is a *future marginally inner trapped surface*.

Dynamical horizons and holographic screens

We now have all the ingredients to introduce the concept of a *Marginally Trapped Tube* (MTT): A MTT is a smooth, three-dimensional submanifold that is foliated by MTSs. If a MTT is everywhere spacelike, it is referred to as a *dynamical horizon*

156

[30, 31]. If it is everywhere timelike, it is called a *timelike membrane* (TLM)[3]. Finally, if it is everywhere null then we have an isolated horizon.

We next outline the various ingredients that go into the area law of dynamical horizons (the quasi-local horizon that appears the most frequently in our numerical solutions). It is straightforward to derive an area law for purely spacelike or purely timelike dynamical horizons. Consider first the spacelike case. Let H be a dynamical horizon and $\mathcal{S}$ be a member of the foliation of *future marginally trapped surfaces*. Since H is spacelike, we can define a future-directed unit timelike vector normal to H, $\hat{\tau}^a$ and a unit outward pointing spacelike vector tangent to H and normal to the cross-sections of H, $\hat{r}^\alpha$. A suitable set of null normals is then

$$l^\alpha = \frac{1}{\sqrt{2}}(\hat{\tau}^\alpha + \hat{r}^\alpha), \quad n^\alpha = \frac{1}{\sqrt{2}}(\hat{\tau}^\alpha - \hat{r}^\alpha). \tag{C.6}$$

Then since (by the definition of a dynamical horizon) $\Theta_{(l)} = 0$ and $\Theta_{(n)} < 0$, it follows that the extrinsic curvature scalar of $\mathcal{S}$ is

$$\tilde{K} = \tilde{q}^{\alpha\beta} D_\alpha \hat{r}_\beta = -\frac{\Theta_{(n)}}{\sqrt{2}} > 0, \tag{C.7}$$

where D_α is the covariant derivative operator on H. This shows that the area of the cross-sections of a spacelike dynamical horizon increases along $\hat{r}^\alpha$. We emphasize that this does not necessarily imply that the area increases in time. In spherical symmetry, we explicitly show below (section C.2.2) that the outward vector points in the future when the area increases in time and in the past when the area decreases in time. For a timelike dynamical horizon, the roles of $\hat{\tau}^\alpha$ and $\hat{r}^\alpha$ are interchanged. In this case, $\hat{r}^\alpha$ is no longer tangential to H, and is instead the unit spacelike vector normal to H. Additionally, $\hat{\tau}^\alpha$ is instead the unit timelike vector tangent to H and orthogonal to the cross-sections of H. The area law then becomes

$$\tilde{K} = \tilde{q}^{\alpha\beta} D_\alpha \hat{\tau}_\beta = +\frac{\Theta_{(n)}}{\sqrt{2}} < 0, \tag{C.8}$$

i.e. the area of a timelike dynamical horizons decreases along $\hat{\tau}^\alpha$. Note this law does not rely on any energy conditions, such as the NCC.

Finally, we note that the area law defined in [30, 31] only applies to dynamical horizons and timelike membranes. The definition does not include marginally anti-trapped tubes, which are often present in cosmological settings, or marginally trapped tubes which may not have a definite signature at a given time. To remedy this, Bousso and Engelhardt [64, 65] formulated and proved a new area theorem applicable to an entire hypersurface H of indefinite signature. The area theorem is based on a few technical assumptions but should be applicable to most hypersurfaces foliated by marginally trapped or anti-trapped surfaces $\mathcal{S}$, called *leaves*. In this context,

---

[3]More recently this surface has also been called a *timelike dynamical horizon*; see appendix B of [31].

marginally (anti-)trapped tubes are referred to as *future (or past) holographic screens*. More precisely, the Bousso-Engelhardt area theorem is: the area of the leaves of any future (past) holographic screen, H, increases monotonically along H. The direction of increase along a future (past) holographic screen is the past (future) on timelike portions of H or exterior on spacelike portions of H. Thus H only evolves into the past (future) and/or exterior of each leaf.

C.2.2 Dynamical horizons and timelike membranes in spherical symmetry

As most of our simulations are performed in an essentially spherically symmetric spacetime, here we consider the properties of dynamical horizons for these spacetimes in more detail. The main purpose of this section is to illustrate how the area law for dynamical horizons [30, 31] reduces to an essentially tautological statement about the dynamics of the horizon area.

We use r to denote the areal radius, and we will work with a gauge such that r is also a coordinate of the spacetime, that is we will consider a metric of the form

$$ds^2 = \alpha_{ab}dx^a dx^b + r^2 \left(d\vartheta^2 + \sin^2\theta d\varphi^2\right), \tag{C.9}$$

where α_{ab} is a two-dimensional metric that is function of (t,r) (here t is the timelike coordinate). We recall that in spherical symmetry the expansion for a null vector v^μ is [46]

$$\Theta_{(v)} = \frac{1}{4\pi r^2} v^\alpha \partial_\alpha \left(4\pi r^2\right) = \frac{2}{r} v^r. \tag{C.10}$$

The last expression follows from our imposing a gauge such that the areal radius is also a coordinate of our spacetime.

We consider the level sets of a function

$$F(t,r) \equiv \mathfrak{r}(t) - r. \tag{C.11}$$

Case 1: the level sets of F are spacelike.

We define a unit timelike vector orthogonal to the level set of F:

$$\hat{\tau}_\alpha \equiv \frac{1}{\sqrt{-\nabla^\beta F \nabla_\beta F}} \nabla_\alpha F = \frac{1}{\mathcal{N}_{\hat{\tau}}} \left(\dot{\mathfrak{r}}, -1, 0, 0\right), \tag{C.12}$$

where we have defined $\mathcal{N}_{\hat{\tau}} \equiv \sqrt{-\nabla_\alpha F \nabla^\alpha F}$. We next find the unit spacelike vector orthogonal to $\hat{\tau}_\alpha$, $\hat{r}_\alpha \hat{r}^\alpha = 1, \hat{r}_\alpha \hat{\tau}^\alpha = 0$. We write $\hat{r}^\alpha$ as

$$\hat{r}^\alpha = \frac{1}{\mathcal{N}_{\hat{r}}} \left(\frac{1}{\dot{\mathfrak{r}}}, 1, 0, 0\right), \tag{C.13}$$

158

where $\mathcal{N}_{\hat{r}}$ is the normalization. Defining the null vectors according to (C.6), a surface $\mathfrak{r}(t)$ is trapped if $\Theta_{(l)} = 0, \Theta_{(n)} < 0$, and it is anti-trapped if $\Theta_{(l)} > 0, \Theta_{(n)} = 0$. The area law for dynamical horizons states that the area of the dynamical horizon must increase in the direction of $\hat{r}^{\alpha}$ as we evolve along $\hat{r}^{\alpha}$ [30, 31]. From the form of $\hat{r}^{\alpha}$, we see that this reduces to: if $\dot{\mathfrak{t}} > 0$, then the dynamical horizon area increases in the direction of increasing time, and if $\dot{\mathfrak{t}} < 0$, then the dynamical horizon areas increases in the direction of decreasing time.

Case 2: the level sets of F are timelike.

Analogous to the case when the level set is spacelike, we define a unit spacelike vector orthogonal to the level set of F:

$$\hat{r}_{\alpha} \equiv \frac{1}{\sqrt{-\nabla^{\beta}F\nabla_{\beta}F}}\nabla_{\alpha}F = \frac{1}{\mathcal{N}_{\hat{r}}}\left(\dot{\mathfrak{t}}, -1, 0, 0\right), \tag{C.14}$$

and a unit timelike vector orthogonal to $\hat{r}_{\alpha}$,

$$\hat{\tau}^{\alpha} = \frac{1}{\mathcal{N}_{\hat{\tau}}}\left(\frac{1}{\dot{\mathfrak{t}}}, 1, 0, 0\right), \tag{C.15}$$

where $\mathcal{N}_{\hat{\tau}}$ is the normalization. Again, a surface $\mathfrak{r}(t)$ is trapped if $\Theta_{(l)} = 0, \Theta_{(n)} < 0$, and it anti-trapped if $\Theta_{(l)} > 0, \Theta_{(n)} = 0$. The area law for timelike membranes states that the area of the timelike membrane must decrease in the direction of $\hat{\tau}^{\alpha}$ as we evolve along $\hat{\tau}^{\alpha}$ [30, 31]. From the form of $\hat{\tau}^{\alpha}$, we see that this statement then reduces to: if $\dot{\mathfrak{t}} > 0$, then the membrane area increases in the direction of increasing time, and if $\dot{\mathfrak{t}} < 0$, then the membrane area increases in the direction of decreasing time.

C.3   The McVittie spacetime

Here we briefly review the McVittie spacetime [258] (see also [266, 265, 267, 240, 143, 216, 144]), which is an analytic solution to the Einstein equations that describes a spherically symmetric black hole embedded in an asymptotically cosmological spacetime provided the cosmology asymptotes (in time: $t \to \infty$) to a de-Sitter cosmology–for more discussion on this point, see [216][4]. The two most salient properties of the McVittie spacetime are that the spacetime is spherically symmetric and satisfies the *no-accretion condition*, $G^{r}{}_{t} = 0$, which in turn implies that the stress-energy component $T^{r}{}_{t} = 0$. Thus, there is no radial flow of cosmic fluid in the McVittie solution (this assumption can be dropped for some generalizations of the McVittie spacetime [143]). We relax all of these assumptions in our numerical simulations, in addition to working in a set of coordinates that allows us

---

[4]We note that while other spacetimes that describe black holes embedded within an asymptotically FLRW universe have been proposed [307, 323, 163], here we only focus on the McVittie spacetime as it remains the most widely studied exact spacetime of this form.

to extend our spacetime past the black hole horizon, which to our knowledge has not yet been accomplished for the McVittie spacetime or its generalizations. While our numerical solutions differ in many of their properties from the McVittie spacetime, the McVittie spacetime serves as a useful analytic example to understand some of the properties of dynamical, apparent, and event horizons in spacetimes that have a black hole and an asymptotic cosmological expansion (see section C.2).

We consider only spatially flat McVittie solutions. The spacetime metric in isotropic coordinates is

$$g_{\alpha\beta}dx^\alpha dx^\beta = -\frac{\left(1 - \frac{m(t)}{2\bar{r}}\right)^2}{\left(1 + \frac{m(t)}{2\bar{r}}\right)^2}dt^2 + a^2(t)\left(1 + \frac{m(t)}{2\bar{r}}\right)^4\left(d\bar{r}^2 + \bar{r}^2 d\Omega^2\right). \tag{C.16}$$

where the McVittie no-accretion condition requires that the mass function $m(t)$ satisfies

$$\frac{\dot{m}}{m} = -\frac{\dot{a}}{a} \tag{C.17}$$

or

$$m(t) = \frac{m_H}{a(t)} \tag{C.18}$$

where $a(t)$ is the scale factor of the FLRW background, an overdot denotes differentiation with respect to comoving time, and $m_H \geq 0$ is an integration constant. The Misner-Sharp [260] (or Hawking-Hayward [180, 183]) quasi-local mass M_{MS}—which is a coordinate invariant notion of energy for spherically symmetric spacetimes—is defined to be

$$1 - \frac{2M_{MS}}{r_A} \equiv (\nabla r_A)^2, \tag{C.19}$$

where $r_A = a\left(1 + m/2\bar{r}\right)^2\bar{r}$ is the areal radius. From (C.19), one can show that the Misner-Sharp mass for the McVittie spacetime is (see e.g. [142])

$$M_{MS} = m_H + \frac{1}{2}H^2 r_A^3. \tag{C.20}$$

Here $H \equiv \frac{1}{a(t)}\frac{da(t)}{dt}$ is the asymptotic Hubble expansion. When H is constant, this is the Schwarzschild-de Sitter metric in coordinates analogous to outgoing Eddington-Finkelstein coordinates. This metric is a solution to the Einstein equations provided H satisfies the Friedmann equation

$$H(t)^2 = \frac{8\pi}{3}\rho(t), \tag{C.21}$$

where $\rho(t) \equiv \hat{\tau}^\alpha\hat{\tau}^\beta T_{\alpha\beta}$ is the energy density of background fluid and $\hat{\tau}_\alpha$ the unit timelike normal to hypersurfaces of constant t. In principle, one may consider arbitrary FLRW backgrounds generated by cosmic fluids satisfying any equation of state. However, the McVittie spacetime only describes a *black hole* embedded in a cosmology if the spacetime asymptotes to a de Sitter background as $r \to \infty, t \to \infty$ [216]. With this caveat in mind, from eq. (C.20) we can think of m_H as the mass of the black hole, and $\frac{1}{2}H^2 r_A^3 = (4\pi r_A^3/3)\rho$ as the mass of the cosmological fluid encapsulated within a sphere of radius r_A.

160

C.3.1 Apparent horizons and event horizons in the McVittie spacetime

Here we briefly review different notions of horizons in the McVittie spacetime [216, 144] for reference and comparison to our numerical study. To do so, we rewrite the McVittie line element (C.16) in terms of the areal radius such that the line element becomes

$$g_{\alpha\beta}dx^\alpha dx^\beta = -\left(1 - \frac{2m_H}{r_A} - H^2 r_A^2\right)dt^2 - \frac{2Hr_A}{\sqrt{1 - \frac{2m_H}{r_A}}}dt dr_A + \frac{1}{1 - \frac{2m_H}{r_A}}dr_A^2 + r_A^2 d\Omega^2,$$

(C.22)

We now use the notions introduced in section C.2 to derive the location of the black hole and cosmological apparent horizons in McVittie spacetimes given by (C.22). We define the following orthonormal timelike and spacelike vectors, (that is $\hat{r}_\alpha \hat{r}^\alpha = 1, \hat{\tau}^\alpha \hat{r}_\alpha = 0$):

$$\hat{\tau}_\alpha dx^\alpha \equiv \left(1 - \frac{2m_H}{r_A}\right)^{1/2} dt,$$

(C.23)

$$\hat{r}_\alpha dx^\alpha \equiv -Hr_A dt + \left(1 - \frac{2m_H}{r_A}\right)^{-1/2} dr_A.$$

(C.24)

With the unit timelike vector $\hat{\tau}_\alpha$ and unit spacelike vector $\hat{r}_\alpha$ we can define the following metrics

$$h_{\alpha\beta} \equiv g_{\alpha\beta} + \hat{\tau}_\alpha \hat{\tau}_\beta, \qquad \tilde{q}_{\alpha\beta} \equiv g_{\alpha\beta} + \hat{\tau}_\alpha \hat{\tau}_\beta - \hat{r}_\alpha \hat{r}_\beta,$$

(C.25)

The tensor $h_{\alpha\beta}$ can be identified with the spatial Riemannian metric of constant t slices, and $\tilde{q}_{\alpha\beta}$ can be identified with the angular metric. In the coordinates eq. (C.22), the null expansions (C.5) associated with the null vectors (C.6) reduce to

$$\Theta_{(l)} = \frac{1}{r_A}l^\alpha \partial_\alpha r_A = \frac{1}{r_A}l^{\hat{r}} = \frac{1}{r_A}\left(Hr_A + \sqrt{1 - \frac{2m_H}{r_A}}\right),$$

(C.26)

$$\Theta_{(n)} = \frac{1}{r_A}n^\alpha \partial_\alpha r_A = \frac{1}{r_A}n^{\hat{r}} = \frac{1}{r_A}\left(Hr_A - \sqrt{1 - \frac{2m_H}{r_A}}\right).$$

(C.27)

At the apparent horizons we have $\Theta_{(l)}\Theta_{(n)} = 0$. For the McVittie solution the apparent horizons are then located at the zeros of

$$H(t)^2 r_A^3 - r_A + 2m_H = 0.$$

(C.28)

In general, there are at most two real solutions. The smaller root $r_- = r\left(\Theta_{(l)} = 0, \Theta_{(n)} < 0\right)$ is called the black hole apparent horizon, since it reduces to the Schwarzschild horizon $r_- = 2m_H$ in the limit where there is no background expansion $H \to 0$, while the larger root is called the cosmological apparent horizon, as it reduces to the static de Sitter horizon

$r_+ = r\left(\Theta_{(n)} = 0, \Theta_{(l)} > 0\right) = 1/H_0$ in the limit $m \to 0$ and $H = H_0 > 0$ [216, 144, 142]. In [216], the authors further showed that the surface defined by $\Theta_{(l)} = 0$, $t \to 0$ in fact defines the surface of the event horizon for a black hole, provided that $\lim_{t \to \infty} H = H_0 > 0$ and $H > 0$ for all t. In this limit the black hole asymptotes to a Schwarzschild de-Sitter solution as $t \to \infty$. However, when the spacetime asymptotes to an FLRW cosmology with a scale factor obeying a power law, so that $\lim_{t \to \infty} H = 0$, then the authors showed that the surface defined by $\Theta_{(l)} = 0$ asymptotes to a region with a weak curvature singularity, essentially due to the divergence of the radial pressure (together with the Ricci scalar) required to keep the matter density on $t = const.$ slice constant .

Although the Schwarzschild-de Sitter black hole does not change size, it is not unreasonable to expect that in more general FLRW spacetimes, black holes could expand or contract in size. In particular, if one were to relax the no-accretion condition, then this would allow for the black hole to accrete matter from the surrounding cosmic fluid. There are many generalizations of the McVittie spacetime in the literature and we refer the interested reader to [142] for a review. However most generalizations of this spacetime are limited to either a no-flux condition, or to specific kinds of matter fields. For example, to work around the no-flux condition, in [143] the authors had to use a fluid model that includes a "heat" current vector. Because of this, it may be difficult to draw general conclusions from the generalized McVittie models. For example, there are conflicting claims about whether a black hole expands/contracts in a universe filled with matter/phantom energy, where studies making use of the McVittie model reach the opposite conclusion of studies that do not make use of the model [35, 155, 156].

Appendix D

Nonlinear studies of binary black hole mergers in Einstein-scalar-Gauss-Bonnet gravity

D.1 Convergence tests and accuracy of our simulations

Here we quantify the main sources of error in our simulations, which include the numerical truncation error, finite radius extraction effects, and residual orbital eccentricity.

D.1.1 Truncation error and convergence

We first consider the truncation error, which is due to the finite resolution of the simulations. The simulations of the binary black hole systems with mass ratio $q = 1$ and $q = 2/3$ presented in this work use eight levels of adaptive mesh refinement with a refinement ratio of $2 : 1$, and have a linear grid spacing of $dx = 0.012 M_0$ on the finest level containing the smallest back hole. The results for the mass ratio $q = 1/2$ use nine levels of adaptive mesh refinement and a grid spacing of $dx = 0.006 M_0$ around the smallest black hole. Each binary black hole simulation takes between ~ 9 and ~ 13 cpu core years.
In Fig. D.1, we plot the integrated constraint violation for a $q = 2/3$, $\zeta_1 = 0.075$ binary with grid spacing that is $4/3$ and $\times 2/3$ as large as default resolution. We also perform a resolution study of a $q = 1/2$, $\zeta_1 = 0.075$ binary, where the linear spacing of the medium resolution is $dx = 0.005 M_0$ and covers the smallest black hole. The integrated constraints shown in Fig. D.1 have grid spacing $4/3$ and $\times 2/3$ as large as medium resolution. We see roughly third order convergence in the constraint violation. Though we use fourth order finite difference stencils and Runge-Kutta time integration, this level of convergence
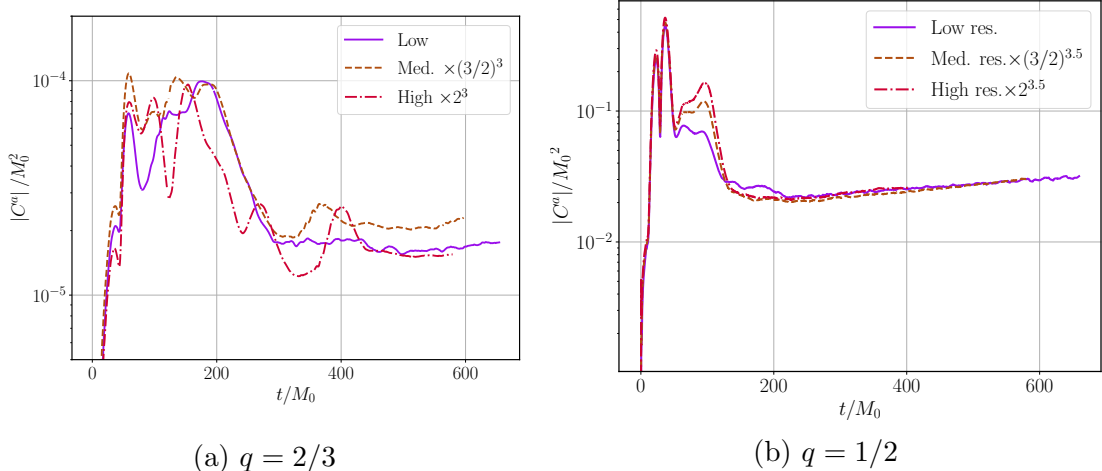
(a) $q = 2/3$ (b) $q = 1/2$

Figure D.1: Volume integrated norm of the constraint violation as a function of time for a nonspinning $q = 2/3$ and $q = 1/2$ binary black hole merger with $\zeta_1 = 0.075$ at three resolutions. The medium and high resolutions have $1.5 \times$ and $2\times$ the resolution of the low resolution on the coarsest grid. We observe roughly third order convergence of our runs, which is consistent with the third order in time interpolation used on the boundaries of adaptive mesh refinement grids [130, 295].

is consistent with the third order interpolation in time used to set values on the boundaries of adaptive mesh refinement levels.

In Fig. D.2, we plot the self-convergence of the amplitude and phase for $\Psi_{4,22}$ and ϕ_{11} for the $q = 1/2$, $\zeta_1 = 0.075$ run. Unlike the integrated constraint violation, we find that $\Psi_{4,22}$ and ϕ_{11} converge at roughly fourth order for $q = 1/2$. For the same run, we show the Richardson extrapolated error in the phase and amplitude for $\Psi_{4,22}$ and ϕ_{11} (Fig. D.3).

As discussed in Sec. 5.4, because we use the same numerical resolution for carrying out the GR and sGB simulations, which we then compare to compute the dephasing $\delta\Phi$, there is a cancellation which leads to a smaller truncation error in this quantity compared to the overall truncation error in Φ. This is illustrated in Fig. D.4, where we estimate the truncation error in $\delta\Phi$ by comparing a $q = 1/2$ GR simulation to an equivalent sGB simulation with $\zeta_1 = 0.075$ at two different resolutions. We compare this to an estimate of the overall truncation error in Φ for the same sGB case, and carry out a similar comparison for the GW amplitude.

D.1.2 Extraction error of waveforms

We next consider the extraction error, that is, the errors in our waveforms due to extracting them at a finite radius. To estimate the extraction error we compute the complex amplitude and phase of the $(\ell = 2, m = 2)$ multipole of Ψ_4 defined in Eq. (D.3) and the $(\ell = 1, m = 1)$ multipole of ϕ defined in Eq. (5.5b) at several extraction radii, and extrapolate the

(a) Amplitude A of ϕ_{11} , $q = 1/2$

(b) Amplitude A of $\Psi_{4,22}$, $q = 1/2$

(c) Phase Φ of ϕ_{11}, $q = 1/2$

(d) Phase Φ_{22} of $\Psi_{4,22}$, $q = 1/2$
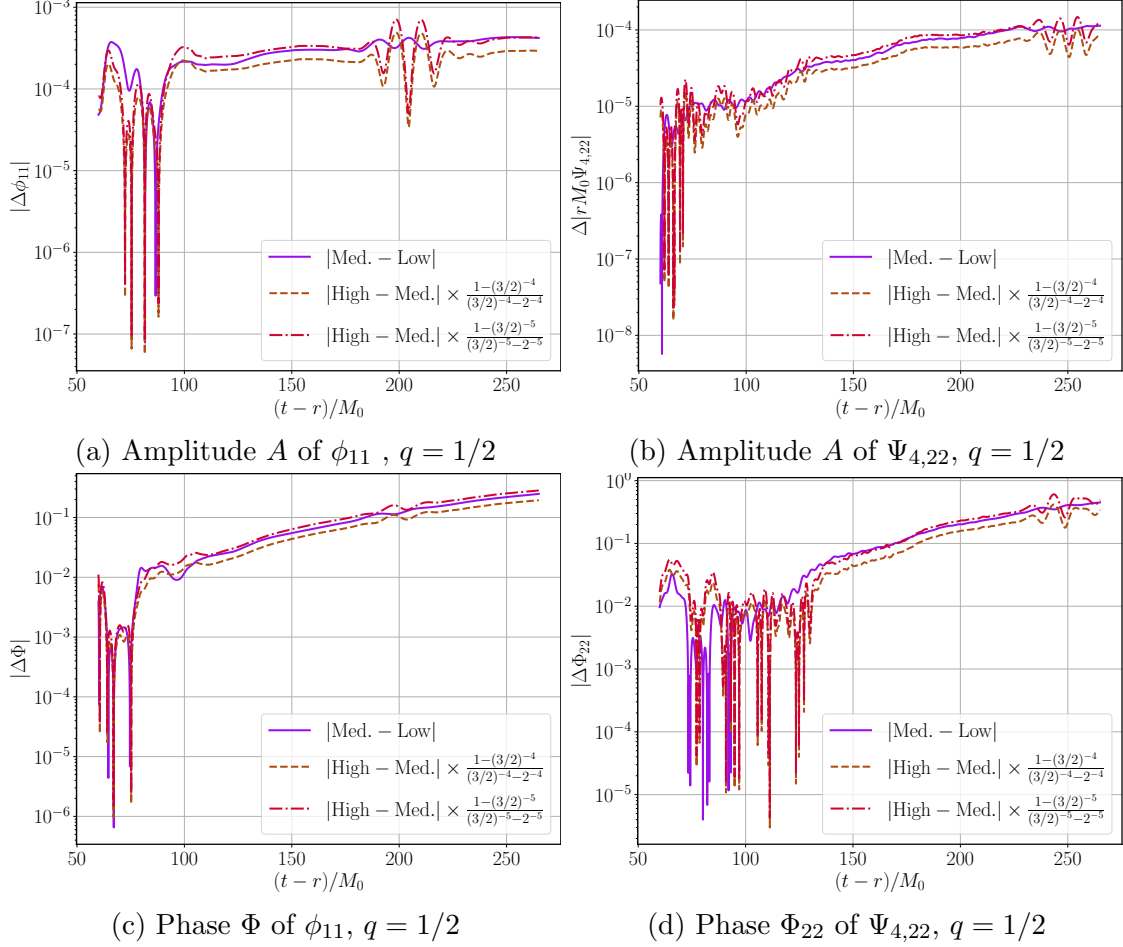
Figure D.2: We show the absolute differences between the low, medium, and high resolutions of the amplitude and phase of the scalar (left) and tensor (right) waveforms for a nonspinning BH binary with mass ratios $q = 1/2$ and coupling $\zeta_1 = 0.075$. We see that the waveform converges at between fourth order and fifth order (corresponding to the scaling used for the dashed and the dashed-dotted lines, respectively). Note that we only show the scalar waveform from $50M_0$ onwards as the scalar field is zero before then.

(a) Phase Φ of ϕ_{11}

(b) Phase Φ_{22} of $\Psi_{4,22}$

(c) Amplitude A of ϕ_{11}

(d) Amplitude A of $\Psi_{4,22}$

Figure D.3: Truncation error estimate of the medium resolution obtained from the Richardson extrapolation of the phase $\Phi(t)$ and amplitude $A(t)$ of the scalar (left) and tensor (right) waveform extracted at $100M_0$ for a nonspinning BH binary with mass ratio $q = 1/2$ and coupling $\zeta_1 = 0.075$.

166

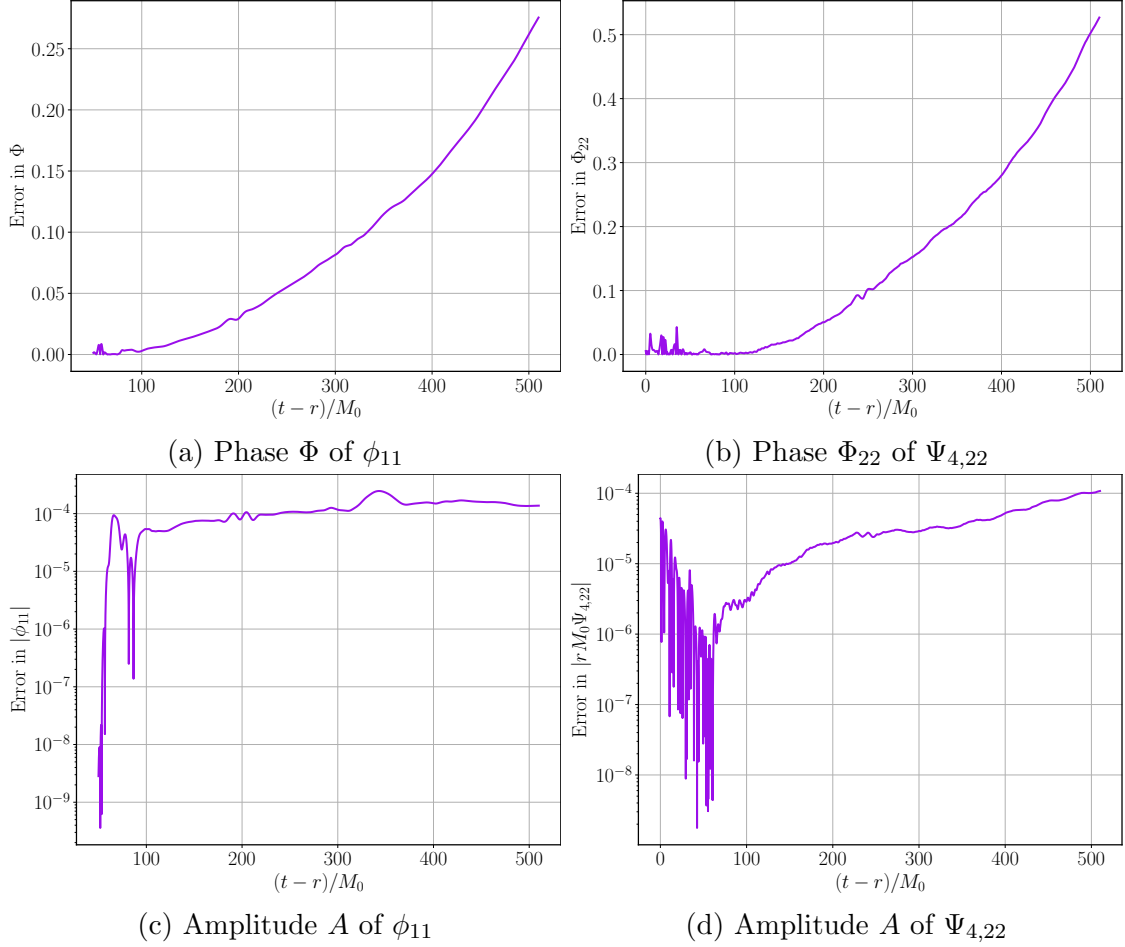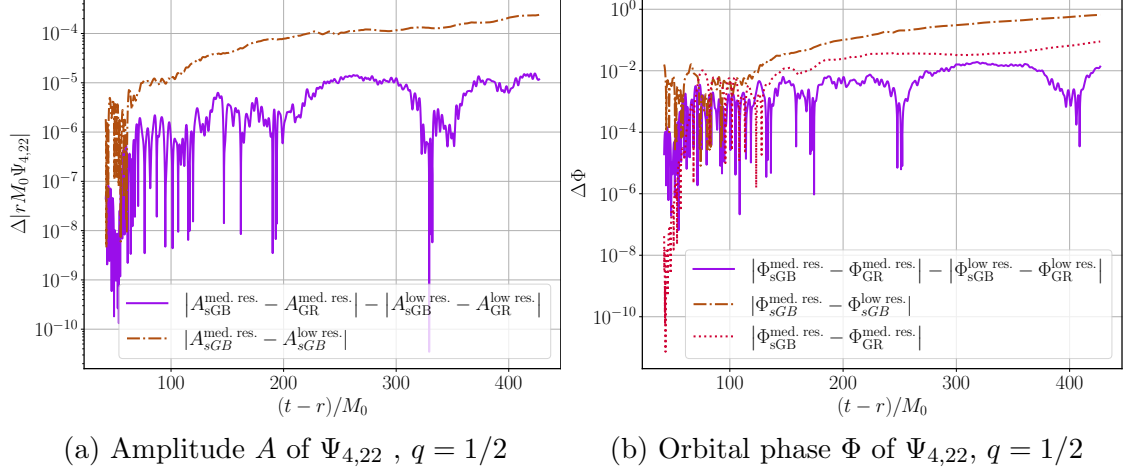(a) Amplitude A of $\Psi_{4,22}$, $q = 1/2$ (b) Orbital phase Φ of $\Psi_{4,22}$, $q = 1/2$

Figure D.4: We show the difference between the low and medium resolutions of the amplitude (left) and phase (right) of the gravitational waveform for a nonspinning BH binary with mass ratio $q = 1/2$ and coupling $\zeta_1 = 0.075$ (solid purple) and the difference of the difference between the sGB and GR amplitude and phase at low and medium resolutions (dashed brown line). This provides evidence that the truncation error roughly cancels between the sGB and GR runs.

quantities to infinity by fitting them to polynomials in $1/r$

$$A(r, t_{\mathrm{ret}}) = \sum_{n=0}^{N} \frac{A^{(n,N)}(t_{\mathrm{ret}})}{r^n}, \tag{D.1a}$$

$$\xi(r, t_{\mathrm{ret}}) = \sum_{n=0}^{N} \frac{\xi^{(n,N)}(t_{\mathrm{ret}})}{r^n}. \tag{D.1b}$$

where $t_{\mathrm{ret}} = t - r$ refers to the retarded time, A is the amplitude of the waveform, and ξ is the phase. The time-dependent $n = 0$ coefficients are then used as the amplitude and phase of the asymptotic waveform. The error from computing a field quantity $u(t_{\mathrm{ret}}, r)$ at a finite radius r_i is then

$$\epsilon(u, r_i, N) = |u(t_{\mathrm{ret}}, r_i) - u^{(0,N)}(t_{\mathrm{ret}})|. \tag{D.2}$$

In Fig. D.5 and D.6, we plot our estimates for the error due to the extraction of the gravitational and scalar waveforms at a finite radius. Comparing these to the estimate of the truncation error in Fig. D.3 we conclude that the finite resolution of the code is the dominant source of error.

D.1.3 Orbital eccentricity

To estimate the orbital eccentricity of the binary system, introduced by imperfect initial data, we use the gravitational wave phase [263]. We write the $(\ell, m) = (2, 2)$ component

167

(a) Phase Φ_{22}

(b) Amplitude A

Figure D.5: Deviation of the phase, $\epsilon(\Phi_{22}, r_i, 1)$ (left) and relative deviation of the amplitude, $\epsilon(A, r_i, 1)/A_{0,1}$ (right) of the waveform $r\Psi_{4,22}(t,r)M_0 = A(t,r)e^{i\Phi_{22}(t,r)}$ obtained at finite extraction radius from the values extrapolated according to Eq. (D.1) for a nonspinning BH binary with mass ratio $q = 1/2$ and coupling $\zeta_1 = 0.075$.

(a) Phase Φ

(b) Amplitude A
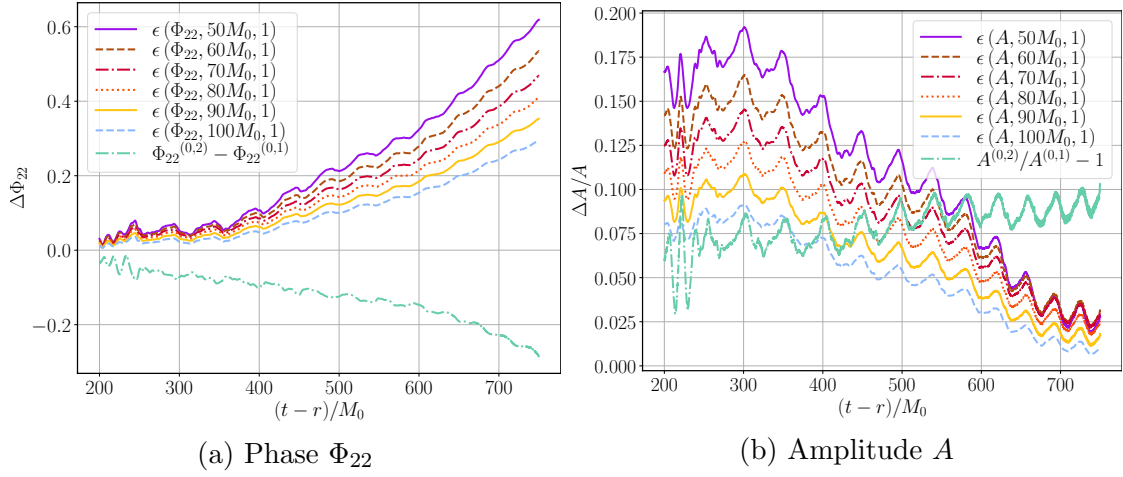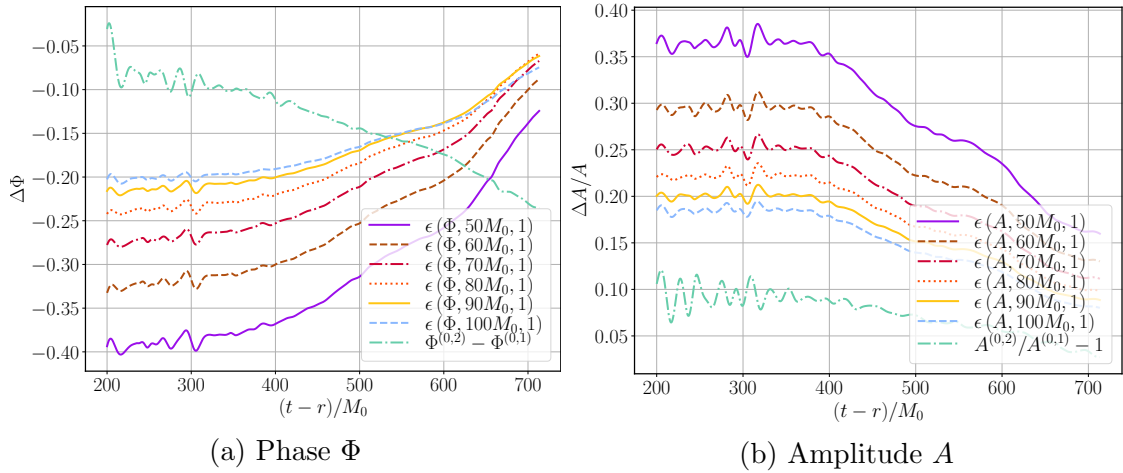
Figure D.6: Deviation of the phase, $e(\Phi, r_i, 1)$ (left) and relative deviation of the amplitude, $e(A, r_i, 1)/A_{0,1}$ (right) of the waveform $(r/M_0)\phi_{11}(t,r) = A(t,r)e^{i\Phi(r,t)}$ obtained at finite extraction radius from the values extrapolated according to Eq. (D.1) for a nonspinning BH binary with mass ratio $q = 1/2$ and coupling $\zeta_1 = 0.075$.

of Ψ_4 in the wave zone as:

$$r \ M_0 \times \Psi_{4,22} \equiv A_{22}(t,r)e^{-i\Phi_{22}} + \mathcal{O}\left(\frac{1}{r}\right). \tag{D.3}$$

We fit a 5th order polynomial to the orbit-averaged Φ to obtain Φ_{fit}, and define the eccentricity to be the amplitude of the oscillating function

$$e_\Phi(t) \equiv \frac{\Phi_{22}(t) - \Phi_{\text{fit},22}(t)}{4}. \tag{D.4}$$

We plot the eccentricity [see Eq. (D.4)] of our simulations in Fig. D.7 for different values of ζ_1 and resolution. Ideally, an eccentricity estimator will plot a sinusoidal wave as a function of time [263]. Our eccentricity measurements have higher harmonics, which we attribute to the junk radiation from the choice of puncture initial data, and from the black hole scalarization process, and from the fact that we only measure the eccentricity over a relatively short inspiral time ($t/M_0 < 1000$). While the eccentricity does slightly increase with increasing ζ_1, we find that our eccentricity is mostly limited by resolution, and not from perturbations caused by our initial data. This suggests that the dephasing between the sGB and GR simulations is not dominated by small differences in the eccentricity of our simulations caused by the rapid development of the scalar field around the black holes at early times.

D.2   Post-Newtonian results in sGB gravity

Due to the presence of monopole scalar charge around each black hole in sGB gravity, black hole inspirals can emit scalar radiation, which enters at -1PN order as dipole emission for unequal mass black hole binaries. The calculation of the leading PN correction to the gravitational and scalar radiation for binary black holes in sGB gravity was carried out in Ref. [339]. In the limit of an exactly equal mass, nonspinning binary, the dipole radiation vanishes. More generally it is straightforward to see that any odd multipole of a scalar is zero in this case as the spherical harmonics are odd under parity inversion ($\vec{r} \to -\vec{r}$), but the spacetime in this case is even under this transformation. Thus, for equal mass black hole binaries, the scalar waveform enters at higher PN order [339, 311, 312].

The PN calculations initiated in Ref. [339] were recently extended to higher PN order in Refs. [311, 312]. In those works, the authors additionally considered more general Gauss-Bonnet couplings $f(\phi)\mathcal{G}$. Here we only present the leading-order PN results. To leading order in ζ_1, spherical harmonic components of the scalar radiation of the binary system go

(a) $q = 1$

(b) $q = 2/3$

(c) $q = 1/2$

(d) $q = 2/3, \zeta_1 = 0.075$, resolution study
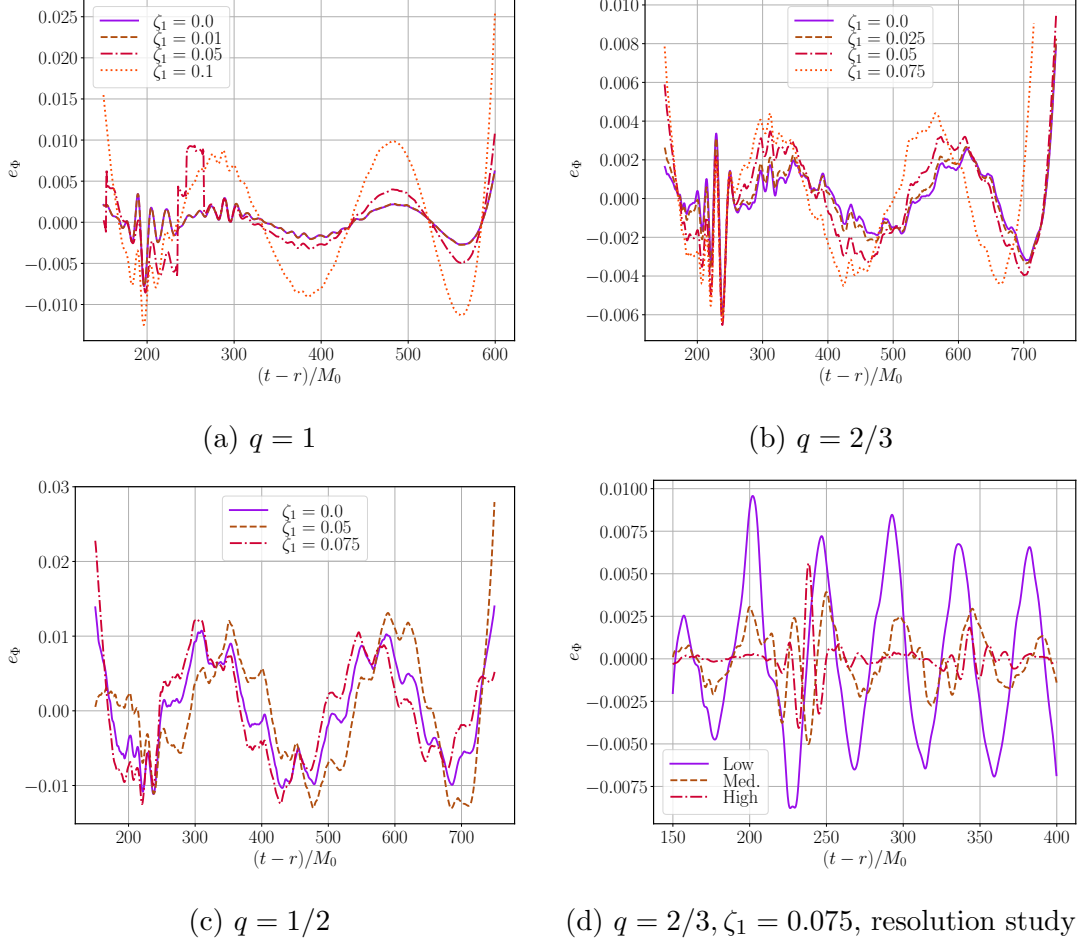
Figure D.7: Eccentricity estimator of the $q = 1$, $q = 2/3$, and $q = 1/2$ mass ratio inspirals for several different values of ζ_1, and for the $q = 2/3$ mass ratio at different resolutions. We see that the eccentricity of the binaries we study is affected by both the form of our initial data (the formation of scalar charge from vacuum initial conditions), and, to a greater extent, from the resolution of our runs. We measure the eccentricity using the radially extrapolated Weyl scalar $\Psi_{4,22}$. The low and high resolution have $2/3$ and $4/3\times$ the resolution of the medium resolution which has a linear grid spacing of $dx = 0.006M_0$ on finest level.

as [339, 334, 311, 312])

$$\phi_{00} \approx \left(\frac{2\lambda}{r}\right)(8\pi)^{1/2}\frac{M_0}{m_1 m_2}, \tag{D.5a}$$

$$\phi_{11} \approx -\left(\frac{2\lambda}{r}\right)\left(\frac{2\pi}{3}\right)^{1/2}\left(1 + \frac{3m_1^2 + 3m_2^2 + 4m_1 m_2}{M_0^2}x\right)\frac{\Delta M_0}{m_1 m_2}x^{1/2}, \tag{D.5b}$$

$$\phi_{22} \approx -\left(\frac{2\lambda}{r}\right)\left(\frac{8\pi}{15}\right)^{1/2}\frac{m_1^2 - m_1 m_2 + m_2^2}{M_0 m_1 m_2}x, \tag{D.5c}$$

$$\phi_{33} \approx \left(\frac{2\lambda}{r}\right)\left(\frac{1296\pi}{35}\right)^{1/2}\frac{\Delta M\left(m_1^2 + m_2^2\right)}{8M_0^2 m_1 m_2}x^{3/2}, \tag{D.5d}$$

$$\phi_{44} \approx \left(\frac{2\lambda}{r}\right)\left(\frac{2048\pi}{315}\right)^{1/2}\frac{m_1^4 - m_1^3 m_2 + m_1^2 m_2^2 - m_1 m_2^3 + m_2^4}{3m_1 m_2 M_0^3}x^2, \tag{D.5e}$$

where $m_{1,2}$ are the masses of the two black holes, with the convention $m_1 \leq m_2$ (see Sec. 5.3.2), Ω is the angular velocity of the binary in the center of mass frame, and

$$\phi_{\ell m} \equiv \lim_{r\to\infty}\int_{\mathbb{S}_2}\bar{Y}_{lm}\phi, \tag{D.6a}$$

$$M_0 \equiv m_1 + m_2, \tag{D.6b}$$

$$\Delta M \equiv m_2 - m_1, \tag{D.6c}$$

$$x \equiv (M_0\Omega)^{2/3}. \tag{D.6d}$$

Note that the second terms in Eq. (D.5), which are raised to the 1/2 power, come from the integral over the sphere of $\bar{Y}_{lm}$. The scalar waveforms Eq. (D.5) are presented to leading order in the PN expansion, except for the $\ell = m = 1$ waveform, which has been computed to 0.5PN order [311, 312].

We next consider the dephasing of gravitational waves in PN theory. We write the orbital phase in the time domain as a function of the PN parameter x,

$$\Phi(x) = \Phi_{\mathrm{GR}}(x) + \delta\Phi(x). \tag{D.7}$$

Here, Φ_{GR} is the orbital phase when setting $\lambda = 0$, and $\delta\Phi$ is the additional phase shift that comes from the emission of scalar radiation. In the PN expansion of scalarized compact objects, there are two limits considered in the literature: the *dipole driven regime* and the *quadrupole driven regime* [309, 312]. In the dipole driven regime, the dipole scalar emission is the dominant source of radiated energy, while in the quadrupole driven regime, the dominant source of radiated energy is the gravitational wave emission. The system is in the quadrupole driven regime when

$$x \gtrsim \frac{5}{24}\mathcal{S}_-^{\ 2} \tag{D.8}$$

171

where we introduced the scalar dipole

$$\mathcal{S}_{\pm} \equiv \frac{\alpha_2 \pm \alpha_1}{2\sqrt{\bar{\alpha}}}, \tag{D.9}$$

where $\bar{\alpha} \equiv (1 + \alpha_1\alpha_2)$, and α_i are the *black hole sensitivities* for sGB gravity [206, 207] (for their explicit values, see Eq. (D.10) below). Notice, for equal mass ratio binaries, the system is always in the quadrupole driven regime as there is no dipole radiation ($\mathcal{S}_- = 0$). We see that the system is in the dipole driven regime only for unequal mass ratio binaries that are far apart (that is, when x is small). Given the experimental constraints on $\zeta_1 \ll 1$ and $\mathcal{S}_-$, the binary systems of interest for ground- and space-based GW detectors are driven by the quadrupolar driven regime for sGB gravity. We thus compare our numerical waveforms to gravitational waveforms for systems in which quadrupolar radiation is dominant.

The leading order contribution to the GW phase in ESGB gravity was computed in Refs. [339, 337] using the stationary-phase-approximation [254], and later extended to higher orders in PN theory in Refs. [311, 312, 253]. The highest order PN corrections to the phase so far have been computed by Lyu et al. [253], who mapped results obtained partially to 2PN order in scalar-tensor theories [309] to sGB gravity. Here, we review their calculation, and present results for the time-domain orbital phase $\delta\Phi$ as a function of the PN parameter x.

The results of Ref. [309] were presented in the Jordan frame, and ESGB gravity is written in the Einstein frame. Thus, the first step Lyu et al. took was to transform the results of Ref. [309] to the Einstein frame. After this transformation, Lyu et al. noticed that the results of Ref. [309] were expressed in terms of the black hole sensitivities α_i, and their derivatives β_i. These were computed for black holes in ESGB gravity by Julié et al. [206, 207], and for non-spinning black holes are given by (here we used the conversion $\varphi \to \phi/\sqrt{2}$, $f(\varphi) \to 2\sqrt{16\pi}\varphi$, and $\alpha_{\mathrm{GB}} \to \lambda/\sqrt{8\pi}$)

$$\alpha_i \equiv -\frac{\alpha_{\mathrm{GB}} f'(\varphi_0)}{2m_i{}^2} = -\frac{\sqrt{2}\lambda}{m_i{}^2}, \tag{D.10}$$

$$\beta_i \equiv \frac{d\alpha_i}{d\varphi}\Big|_{\varphi_0} = -\frac{\alpha_{\mathrm{GB}}{}^2 f'(\varphi_0)^2}{2m_i{}^2} = -\frac{4\lambda^2}{m_i{}^2}, \tag{D.11}$$

where φ_0 is the asymptotic value of scalar field at infinity (we set $\varphi_0 = 0$). We see that $\beta_i \propto \lambda^2$, so it is negligible compared to α_i. Using these expressions, and keeping terms up to $\mathcal{O}(\lambda^2)$, sGB corrections to the orbital phase in the quadrupolar driven regime can be expressed as

$$\delta\Phi(x) = \sum_i \delta\Phi_{i,\mathrm{PN}} = \frac{\lambda^2}{8\pi m_1^4 m_2^4 \eta} \sum_i c_i x^{(-5+2i)/2}, \tag{D.12}$$

172

where

$$c_{-1} = \frac{25\pi}{1344}\left(m_2^2 - m_1^2\right)^2 \tag{D.13}$$

$$c_0 = \frac{5\pi}{32256}\left[(659 + 728\eta)(m_2^2 - m_1^2)^2\right] + \frac{5\pi}{12}m_2^2 m_1^2 \tag{D.14}$$

$$c_{0.5} = -\frac{25\pi}{384}\left(m_2^2 - m_1^2\right)^2\left(3\pi + f_3^{\mathrm{ST}}\right) \tag{D.15}$$

$$c_1 = \frac{5\pi}{585252864}\left[55883520(m_2^3 m_1 + m_2 m_1^3) + 25(1640783 + 2621304\eta + 2095632\eta^2)(m_2^4 + m_1^4)\right.$$
$$\left.-2m_1^2 m_2^2(83960375 + 43179192\eta + 52390800\eta^2)\right] - \frac{25\pi}{288}\left(m_2^2 - m_1^2\right)^2 f_4^{ST} \tag{D.16}$$

$$c_{1.5} = -\frac{5\pi^2}{12}\left(m_2^4 - 14m_1^2 m_2^2 + m_1^4\right) - \frac{5\pi}{96}\left(m_2^4 - 6m_1^2 m_2^2 + m_1^4\right)f_3^{\mathrm{ST}} + \frac{1}{\lambda^2}\frac{5\pi}{8}m_1^4 m_2^4 f_3^{\mathrm{ST}} \tag{D.17}$$

$$c_2 = \frac{5\pi}{48771072}\left[-24385536(m_2^3 m_1 + m_2 m_1^3) + (4341025 - 65553264\eta + 684432\eta^2)(m_1^4 + m_2^4)\right.$$
$$\left.+54m_1^2 m_2^2(-12500965 + 19310256\eta + 366128\eta^2)\right] \tag{D.18}$$

$$-\frac{5\pi}{48}\left(m_2^4 - 14m_1^2 m_2^2 + m_1^4\right)f_4^{\mathrm{ST}} + \frac{1}{\lambda^2}\frac{5\pi}{4}m_1^4 m_2^4 f_4^{\mathrm{ST}}. \tag{D.19}$$

and $\eta \equiv m_1 m_2/M_0^2$ is the symmetric mass ratio [1]. Our calculation of these coefficients are presented in an ancillary Mathematica notebook. As noted in Ref. [253], the leading -1PN term here agrees with the one found in Refs. [339, 337]. We note that we have *not* included black hole spin dependence here (in the notation of Ref. [253], we have set $s_i = 1$, although the notebook presents results for general s_i. The terms at 0.5 PN onwards contain currently unknown coefficients f_{2n}^{ST}, which represent our ignorance of the new scalar contributions at relative $n = 1.5$ and $n = 2$ PN order in the non-dipolar flux (part of the flux that does not vanish for an equal mass binary) beyond 1PN order [309]; we see that f_{2n}^{ST} must scale as λ^{2+n}, $n > 0$ in order for these terms to not be important as $\lambda \to 0$. In the quadrupolar driven regime, experimental constraints on the weak-field parameters of scalar-tensor gravity suggest that these contributions should be much smaller than the 2PN GR terms [309], so f_{2n}^{ST} is set to zero in Ref. [253] and in this work.

D.3 Puncture initial data for sGB binary black hole evolution

As we discuss in Sec. 5.3.2, the Hamiltonian and momentum constraint equations in sGB gravity reduce to those of GR when $\phi = \partial_t\phi = 0$ on the initial data hypersurface [133, 301],

---

[1] η is used to refer to conjugate momentum of scalar field in chapter 3 and ratio of energy densities of scalar fields in chapter 4

and we make use of GR puncture initial data in our simulations. While puncture initial data is well known [107] and the `TwoPunctures` implementation of that formalism is widely used [23], to our knowledge it has never been implemented in conjunction with black hole excision and a (modified) generalized harmonic formulation. Here, we review puncture initial data, and how we incorporated the `TwoPunctures` initial data in our MGH code.

First we write the metric in ADM variables:

$$ds^2 = -N^2 dt^2 + \gamma_{ij} \left(dx^i + \beta^i dt \right) \left(dx^j + \beta^j dt \right). \tag{D.20}$$

The extrinsic curvature is

$$K_{ij} = -\frac{1}{2N} \left(\partial_t \gamma_{ij} - D_i \beta_j - D_j \beta_i \right), \tag{D.21}$$

where D_i is the extrinsic curvature with respect to the spatial slice.

Puncture initial data is spatially conformally flat and maximally sliced ($K = 0$), and sets $\gamma_{ij} = \psi^4 \delta_{ij}$, that is the initial spatial metric is conformally flat. The extrinsic curvature is specified by choosing a set of effective black hole masses $m_{(n)}$, spins $S^\gamma_{(n)}$, momenta $P^\gamma_{(n)}$, and locations. One then solves the Hamiltonian constraint for ψ, which then gives us γ_{ij} (the momentum constraint is solved using an analytic formula). Puncture initial data does not specify the lapse N and shift β^i. We set $\beta^i = 0$, and choose N to be (we set the `initial-lapse` parameter to `twopunctures-averaged` in the `TwoPunctures` code [23])

$$N = \left(1 + \frac{m_1}{2r_1} + \frac{m_2}{2r_2} \right)^{-1}, \tag{D.22}$$

where r_i is the radial (Euclidean) distance from the ith puncture. To recover the metric initial data from the ADM variables, we invert the definitions to get

$$\begin{aligned} g_{tt} &= -N^2, & g_{ti} &= 0, \\ g_{ij} &= \gamma_{ij}, & \partial_t g_{tt} &= -2N\partial_t N, \\ \partial_t g_{ti} &= 0, & \partial_t g_{ij} &= -2NK_{ij}. \end{aligned} \tag{D.23}$$

In puncture coordinates, the black hole apparent horizon is located at $r = m_i/2$. We then initially excise an ellipsoid inside that surface on our $t = 0$ slice after the `TwoPunctures` code has solved for the conformal factor and interpolated the result on the initial Cartesian grid we use. The MGH parameters $\hat{g}^{\mu\nu}$, $\tilde{g}^{\mu\nu}$, and H_μ determine $\partial_t N$ and $\partial_t \beta_i$.

We set $S^\gamma_{(1,2)} = 0$, so that the black holes are initially nonspinning. We choose quasi-circular initial data for the momenta $P^\gamma_{(1,2)}$. In particular, given r and $m_{(n)}$, we set (here using spherical polar coordinates)

$$P^\gamma_{(n)} \partial_\gamma = m_{(n)} \times \left(\dot{r} \partial_r + r\Omega \partial_\phi \right). \tag{D.24}$$

We choose $\dot{r}$ to be accurate to 2.5PN order for a quasi-circular binary, that is it incorporates the leading-order radiation reaction term, and we choose Ω to be accurate to 2PN order for a quasi-circular binary [55, 27, 278].

We note that Kovacs [228] has recently constructed a more general set of puncture initial data for black holes in sGB gravity, which reduces to the original puncture data for GR that we use here when one chooses the initial values of $\phi = \partial_t \phi = 0$.

D.4   Perturbative solutions to sGB gravity

Here, we briefly review the perturbative approach to solving the equations of motion in shift-symmetric ESGB (sGB) gravity. While we do not employ the perturbative method in this work (instead, we solve the full sGB equations of motion), all previous numerical relativity work comparing to PN theory has [334, 311, 312]. As in those earlier results, we find that at a given frequency, the amplitude of our scalar waveforms are very similar to the scalar waveforms produced in the decoupling limit; however, here we are able to directly measure the extra dephasing of the binary black holes due to the emission of scalar radiation. This can be traced to the fact that corrections to the scalar amplitude beyond the leading order decoupling limit scale as the coupling to the third power, which we show here.

In the perturbative approach, the scalar field and tensor field are expanded order by order in a small parameter ϵ:

$$g_{\mu\nu} = \sum_{k=0}^{\infty} \epsilon^k g_{\mu\nu}^{(k)}, \tag{D.25a}$$

$$\phi = \sum_{k=0}^{\infty} \epsilon^k \phi^{(k)}. \tag{D.25b}$$

We assume $\epsilon \sim \lambda/m_1^2 = \zeta_1$, and set $\phi^{(0)} = 0$, so that the "background" spacetime is vacuum GR. To zeroeth order in the coupling, the tensor and scalar equations of motion are

$$G_{\mu\nu}^{(0)} - \nabla_\mu \phi^{(0)} \nabla_\nu \phi^{(0)} + \frac{1}{2} g_{\mu\nu}^{(0)} \left(\nabla \phi^{(0)} \right)^2 = 0, \tag{D.26a}$$

$$\Box^{(0)} \phi^{(0)} = 0, \tag{D.26b}$$

where $G_{\mu\nu}$ is the Einstein tensor. We see that if for initial data we set $\phi^{(0)} = \partial_t \phi^{(0)} = 0$, then $\phi^{(0)} = 0$ for all time, and the metric field satisfies the Einstein equations. From now on we assume $\phi^{(0)} = 0$. To linear order in ϵ, the equations of motion are

$$G_{\mu\nu}^{(1)} = 0, \tag{D.27a}$$

$$\Box^{(0)} \phi^{(1)} + \lambda \mathcal{G}^{(0)} = 0. \tag{D.27b}$$

We see that the equation of motion for $g_{\mu\nu}^{(1)}$ is also the vacuum Einstein equations. We can then consistently set $g_{\mu\nu}^{(1)} = 0$. The scalar field $\phi^{(1)}$ is no longer zero, even if one initially sets $\phi^{(1)} = \partial_t \phi^{(1)} = 0$ for initial data, as generically $\mathcal{G}^{(0)} \neq 0$. Solving for $\phi^{(1)}$ to this order, while solving for $g_{\mu\nu}^{(0)}$ from the Einstein equations, is called the decoupling approximation [334]. To second order in ϵ, we have

$$G_{\mu\nu}^{(2)} - \nabla_\mu \phi^{(1)} \nabla_\nu \phi^{(1)} + \frac{1}{2} g_{\mu\nu}^{(0)} \left(\nabla \phi^{(1)} \right)^2 + 2\lambda \delta_{\rho\sigma\kappa(\mu}^{\alpha\beta\gamma\eta} g_{\nu)\eta} \left(R^{\rho\sigma}{}_{\alpha\beta} \right)^{(0)} \nabla^\kappa \nabla_\gamma \phi^{(1)} = 0, \quad \text{(D.28a)}$$

$$\Box^{(0)} \phi^{(2)} = 0. \quad \text{(D.28b)}$$

The scalar equation follows from $g_{\mu\nu}^{(1)} = 0$. Note that the scalar equation for $\phi^{(2)}$ would have corrections if the Gauss-Bonnet coupling was nonlinear in ϕ; for more discussion see for example Sec II.B.5 in [334]. We see that we can consistently set $\phi^{(2)} = 0$. To third order in perturbation theory, we have

$$G_{\mu\nu}^{(3)} = 0, \quad \text{(D.29a)}$$

$$\Box^{(0)} \phi^{(3)} + \Box^{(2)} \phi^{(1)} + \lambda \mathcal{G}^{(2)} = 0. \quad \text{(D.29b)}$$

We can set $g_{\mu\nu}^{(3)} = 0$, but there is a nontrivial correction to $\phi^{(3)}$ (there would be corrections to $g_{\mu\nu}^{(3)}$ if the scalar Gauss-Bonnet coupling was nonlinear in ϕ, due to corrections in $\phi^{(2)}$; see the discussion below Eqs .(D.28)). Thus, once one can computed $\phi^{(1)}$, corrections to the scalar waveform do not appear until $\phi^{(3)}$. We considered $\zeta_1 \sim 0.1$ at the largest, so the largest correction due to nonlinear effects to the amplitude would be of relative order $\zeta_1^3/\zeta_1 = \zeta_1^2 \sim 0.01$, a 1% effect. This is consistent with what we see in Figs. 5.1 and 5.2.

While nonlinear effects in ζ_1 are not expected to dramatically change the amplitude of the scalar field during inspiral for sGB gravity, nonlinear effects must be incorporated to determine the long-time dephasing of the binary due to the emission of scalar radiation. Nonlinear effects may additionally change the spacetime geometry of the merger in ways not captured in the perturbative approach. Finally, if the scalar Gauss-Bonnet coupling is not linear in ϕ, higher order corrections in the coupling can enter in the scalar waveform at order ζ_1^2, and so could be more important in determining the properties of black hole binaries.